Universality of Long-Term Correlations in Thermal Fluctuations in Pool Boiling

A DISSERTATION
SUBMITTED TO THE FACULTY OF THE GRADUATE SCHOOL
OF THE UNIVERSITY OF MINNESOTA
BY

Ankit Saini

IN PARTIAL FULFILLMENT OF THE REQUIREMENTS
FOR THE DEGREE OF
DOCTOR OF PHILOSOPHY

Dr. Vinod Srinivasan, Advisor

December, 2024

Acknowledgements

There are many people that have earned my gratitude for their contributions to my time in graduate school. I will try to put into words my gratitude for all those who have held me up through the years.

Prof. Vinod Srinivasan: I will forever be grateful for your inspiring and patient guidance through the long years of my PhD. You are one of the most inspiring and influential teachers that I have had in my life. It was an honor for me to have you as my advisor.

My lab-mates past and present: Sankar, Merin, Vikas, Reece, Preston, Xijun, Manish, Krishna, Jin-Wei, and Chujun. Thank you for all your support through the years which meant that I felt less alone and kept pushing when things seemed hard.

Peter Ness and his staff at the CSE Research Shop: You are the ones who make it all possible. Thank you for all your hard work, and kindness and patience.

To Prof. Matt Anderson: For showing me the way and giving me multiple opportunities to teach heat transfer as a grad student instructor. You helped me find my passion in teaching.

To John Gardner, Jennifer Dahal, and the rest of the admin staff at the mechanical engineering department: Thank you for having infinite patience for us, the grad students.

To the friends I made along the way: Daniel & Catalina, Sharey, Biswa, Guru, Stein, Ian, and Zak. Your friendships were invaluable in getting me through the years. Thank you for all the fun and hope to have a lot more throughout the years.

To my parents, my sister, and my extended family: Words cannot describe how thankful I am to all of you for always having my back. I am where I am today because of you, and the values that you have instilled in me.

To my family away from home: Kelley, Kristi, Sara, Dave, Theo and Amie. Thank you for giving me a sense of belonging. I love you all.

To my partner, Ruth: Thank you so much for being by my side through this journey, and encouraging me every step of the way. You are what makes all this, and life, worth it.

Best of luck to Vikas and others who continue this work...

Dedication

In memory of my grandparents, with love and gratitude.

Abstract

Boiling systems are characterized by Critical Heat Flux (CHF), the maximum level of applied heat flux beyond which the near-surface liquid is displaced by a thin vapor film leading to a sharp rise in the surface temperature and heater failure. Operation close to CHF is avoided because its behavior gets altered unpredictably as the surface undergoes oxidation and/or particle deposition over time. Reliable mechanistic models that can accurately predict dynamic changes to CHF do not exist. Furthermore, all surface/fluid combinations exhibit different CHFs and are represented on boiling curves with dimensional axes. The lack of a universal dimensionless quantity makes it difficult to compare across boiling systems and is indicative of how poorly the physics governing CHF is understood.

In this context, non-linear dynamical analysis of boiling systems may yield information about conditions just prior to CHF. This idea is based on the fact that boiling is a non-linear, complex dynamical system that is governed by mass, momentum and energy transport in three subsystems, namely the bulk fluid, the heater surface, and the heater-fluid interface. Previous studies have demonstrated that as a result of interactions between these subsystems, local surface temperature, contact line length and surface void fraction exhibit fluctuations on a wide range of time scales and are characterized by scaling exponents. This is promising because such scaling laws can serve as characteristic fingerprints of the state in which a system is operating and act as a precursor to transition to a different state or an impending catastrophic event (like CHF).

Building on the above-mentioned framework, this study investigated the statistics of local temperature fluctuations on surfaces undergoing boiling using surface-deposited,

micro-scale Resistance Temperature Detectors (RTDs). Scale-free behavior of temperature fluctuations is established, and analysis of the Auto-Correlation Functions (ACF) reveals the presence of long-term correlations of temperature fluctuations when operating close to dry-out. The time series are then characterized using the Hurst Exponent, a measure of long-term memory of a time series, along the boiling curve. It is demonstrated that the trend in evolution of Hurst Exponent along the boiling ccurve is common across all experiments performed. Specifically, temperature fluctuations have a high degree of persistence and exhibit short-term correlations at low heat flux and have a lower degree of persistence and exhibit long-term correlations at high heat flux.

Next, surface-averaged temperature fluctuations of a platinum wire undergoing boiling were investigated along similar lines. The observed values of CHF spanned one order of magnitude. Scale-free behavior and long-term correlations through analysis of ACF were observed again. It is shown that the evolution of the Hurst Exponent for surface-averaged temperature fluctuations also follows the same trend as that for local temperature fluctuations on plane surface experiments.

Finally, the above analysis was extended to publicly available data of heat flux fluctuations on temperature-controlled surfaces undergoing boiling in micro-gravity. While the specific values of the Hurst Exponent along the boiling curve were lower for the micro-gravity data, the same trend as before is observed. From the spatial uniformity of this behavior as well as its universality, it may be possible to determine the proximity of a system to CHF using the Hurst Exponent, even as the surface undergoes changes in surface condition due to fouling.

Contents

Acknowledgements **i**

Dedication **iii**

Abstract **iv**

Contents **vi**

List of Tables **x**

List of Figures **xi**

1 Introduction **1**

1.1 Motivation & Objectives 1

1.2 Organization of this Work 5

2 Background **7**

2.1 Fundamentals of Boiling 7

2.1.1 Pool Boiling 7

2.1.2 The Boiling Curve 9

2.1.3 Bubble Ebullition Cycle 12

2.1.4 Heat Transfer Mechanisms in Pool Boiling 18

2.2 Mechanistic Models for CHF on a Plain Surface 20
2.3 Roughness Effects on Pool Boiling CHF 26
2.4 Non-Hydrodynamic and Non-Linear Features of Pool Boiling 28
2.5 On the Study of Long-Term Correlations in Boiling 31

3 Experimental Facilities **35**
3.1 Facility for Surface Pool Boiling Experiments 35
3.1.1 Estimating Heat Losses from Boiling Platform 40
3.1.2 Electrical Circuit 44
3.1.3 Signal Conditioning of RTD Signals 46
3.1.4 Calibration of the RTDs 49
3.1.5 Experimental Procedure 56
3.1.6 Digital Filtering and Post-Processing 64
3.2 Facility for Wire Pool Boiling Experiments 70
3.2.1 Calibration of Wires 72
3.2.2 Experimental Procedure 77
3.2.3 Post-Processing 86

4 Results: Surface Pool Boiling Experiments **91**
4.1 Experimental Runs 91
4.2 Statistical Distributions 94
4.2.1 PDFs of RTD Temperature Fluctuations 97
4.2.2 Variation of Statistical Moments with Segment Size 101
4.2.3 Variation of Statistical Moments with q^* 104
4.3 Frequency Spectrum Analysis 106
4.4 Autocorrelation Function Analysis 111
4.5 Hurst Exponent Analysis 114
4.5.1 Interpretation and Estimation of the Hurst Exponent 115

4.5.2 Crossover in Scaling of Structure Functions and Range of Segment Sizes in Evaluation of H 119
4.5.3 Results of Hurst Exponent Analysis 122
4.5.4 Relationship of Hurst Exponent to Autocorrelation Decay 124

5 Results - Wire Pool Boiling Experiments 126
5.1 Experimental Runs 126
5.2 Statistical Distributions 129
5.2.1 Variation of Statistical Moments with Segment Size 132
5.3 Frequency Spectrum Analysis 135
5.4 Auto-Correlation Function Analysis 137
5.5 Hurst Exponent Analysis 138
5.6 Comparison of Hurst Exponent Evolution for Surface and Wire Experiments 141

6 Results - Boiling Experiments in Microgravity 142
6.1 Statistical Distributions 144
6.2 Frequency Spectrum Analysis 146
6.3 Auto-Correlation Function Analysis 148
6.4 Hurst Exponent Analysis 150

7 Conclusion 154
7.1 Recommended Future Work 156

References 158

Appendix A. Calibrating the Standard Platinum Resistance Thermometer 169
A.1 Triple Point of Water 172
A.2 Transition Temperature of Decahydrate of Sodium Sulfate 176

A.3 Error Propagation and Uncertainty Analysis 178

Appendix B. Calibrating type-T Thermocouples 180

Appendix C. Micro-Fabrication of RTDs on Sapphire Subtrates 186

Appendix D. Acronyms 190

D.1 Acronyms 190

List of Tables

3.1 Conductive Thermal Resistance Calculations 42

3.2 Convective Thermal Resistance Calculations 43

4.1 List of Surface Pool Boiling Experiments 92

4.2 RTD Temperature Fluctuations with Gaussian PDF. 98

5.1 List of Wire Pool Boiling Experiments 127

A.1 Values of constants in Equations (A.4) and (A.5). 171

B.1 Regression Analysis for Thermocouple Calibration. 183

D.1 Acronyms 190

List of Figures

1.1 Sensitive dependence of CHF on surface fouling and liquid salinity. . . . 2
2.1 Schematic representing pool boiling on a heated surface. 7
2.2 Order of magnitude estimates of HTCs associated with different convective techniques. 8
2.3 Representative Boiling Curve. 10
2.4 Life-cycle of a Bubble. 14
2.5 Heat Transfer Mechanisms in Pool Boiling. 19
2.6 Schematic of Zuber's Hydrodynamic Instability Model. 21
2.7 Schematic of Haramura and Katto's Macrolayer Dryout Model. 22
2.8 Schematic of Kandlikar's Static Force Model. 24
2.9 Enhancements in Pool Boiling Performance. 26
2.10 SEM images of Textured Surfaces for CHF Enhancement. 27
2.11 Temperature Gradients on Boiling Surfaces. 29
2.12 Conjuagte Problem in Pool Boiling. 32
3.1 Surface Pool Boiling Facility Schematic. 36
3.2 Resistance Temperature Detectors. 37
3.3 Printed Circuit Board. 38
3.4 Boiling Platform. 39
3.5 Estimating Heat Loss from Boiling Platform. 41

3.6 Power Spectra of RTD Signal without Signal Conditioning. 47
3.7 Role of Offset Resistors. 48
3.8 Effect of Using In-Amp. 50
3.9 Calibration Curves for RTDs 53
3.10 TCR Values of calibrated RTDs. 55
3.11 Process Flow of Surface Boiling Experiments. 57
3.12 Electrical Circuit Schematic for Surface Experiments. 59
3.13 Power Adjustment Flowchart. 62
3.14 Digital Filtering Process. 65
3.15 Effect of Digital Filtering. 66
3.16 Temperature Conversion of RTD Signal. 66
3.17 Boiling Curves using Backside T/C vs Mean RTD Temperature. 68
3.18 Wire Pool Boiling Facility Schematic. 70
3.19 Calibration Curves for a Platinum Wire 75
3.20 TCR Values from Calibration Runs. 76
3.21 Process Flow of Wire Boiling Experiments. 78
3.22 Electrical Circuit Schematic for Wire Experiments. 80
3.23 Power Adjustment Flowchart. 84
3.24 Post-Processing of Wire Voltage Fluctuations. 87
3.25 Representative Boiling Curves for Wire Experiments. 90
4.1 CHF Values of Surface Experiments. 93
4.2 CHF Values of Surface Experiments by Surface. 93
4.3 Boiling Curves for Surface Experiments. 94
4.4 Stationarity Analysis of White Noise. 95
4.5 Probability Density Estimation (PDF) of RTD Temperature Fluctuations. 97
4.6 PDFs across all Experiments. 99
4.7 PDFs of all RTDs from Parylene-C in Novec 7100. 100
4.8 Stationarity Analysis of RTD Temperature Fluctuations - Instance 1. . . 102

4.9 Stationarity Analysis of RTD Temperature Fluctuations - Instance 2. . . 103
4.10 Evolution of Statistical Moments for Surface Experiments. 105
4.11 PSD of RTD Temperature Fluctuations - Instance 1. 107
4.12 PSD of RTD Temperature Fluctuations - Instance 2. 107
4.13 Representative PSD Evolution Curve. 108
4.14 PSD Evolution Curves for Surface Experiments. 109
4.15 PSD of RTD Temperature Fluctuations with Noise. 110
4.16 Auto-Correlation Function (ACF) Decay for RTD Temperature Fluctuations. 111
4.17 Decay in Auto-Correlation Functions (ACF) across All Experiments. . . 113
4.18 PSDs of RTD Temperature Fluctuations with Noise. 114
4.19 Scaling of Distributions for Random Walk. 116
4.20 Examples of Structure Function Scaling. 118
4.21 Deviation from Structure Function Scaling Law at Small Segment Sizes. 120
4.22 Deviation from Structure Function Scaling Law at Small Segment Sizes. 121
4.23 Evolution of H with q^* for All Surface Experiments. 123
4.24 Comparison of Evolution of H across all Surface Experiments. 124
5.1 CHF Values of Wire Experiments. 127
5.2 Boiling Curves for Wire Experiments. 128
5.3 PDFs across all Wire Experiments. 130
5.4 Evolution of Statistical Moments for Wire Experiments. 131
5.5 Stationarity Analysis of Wire Temperature Fluctuations - Instance 1. . . 133
5.6 Stationarity Analysis of Wire Temperature Fluctuations - Instance 2. . . 134
5.7 PSD of Wire Temperature Fluctuations - Instance 1. 136
5.8 PSD of Wire Temperature Fluctuations - Instance 1. 136
5.9 PSD Evolution Curves for Wire Experiments. 137
5.10 Auto-Correlation Function (ACF) Decay for Wire Temperature Fluctuations. 138

5.11 Decay in Auto-Correlation Functions (ACF) across All Wire Experiments. 139
5.12 Comparison of Evolution of H across all Wire Experiments. 140
5.13 Comparison of Hurst Exponent Evolution in Surface and Wire Experiments. 141
6.1 Representative Time-Average Heat Map and Power Fluctuations in MABE. 143
6.2 PDFs and Evolution of Statistical Moments for MABE. 145
6.3 PSDs of MABE Experiments. 147
6.4 Decay in Auto-Correlation Functions (ACF) across MABE Experiments. 149
6.5 Evolution of H for Minimum and Maximum Heat Flux Dissipating Heaters in MABE Experiments. 150
6.6 Evolution of H in MABE Experiments across Different Pressure Levels. 151
6.7 Overlap in evolution of H in Microgravity and Terrestrial MABE Experiments. 152
7.1 Decrease in the Hurst Exponent along the Boiling Curve. 155
A.1 Triple Point Cell. 173
A.2 Phase Diagram of the Na_2SO_4:H_2O system. 176
A.3 Resistance measurements of the SPRT at $T_{salt} = 305.5148$ K. 177
B.1 Thermocouple Calibration Curve. 183
C.1 Micro-fabrication of RTDs. 187

Chapter 1

Introduction

1.1 Motivation & Objectives

Boiling is a highly efficient phase-change process that is capable of transferring large amounts of thermal energy per unit area per unit time. As a result, boiling is used in the thermal management of electronic chips, where extremely high heat fluxes must be transported away from small surfaces while maintaining the peak surface temperature below some threshold. Boiling is also used in the generation of electricity from nuclear fuel, coal and natural gas[1] in boilers operating on the Rankine cycle. Together, nuclear fuel, coal and natural gas are projected to make up 74% of the U.S. electricity production in 2025, respectively. [1]

All boiling systems are characterized by an upper bound on the heat flux called the Critical Heat Flux (CHF). CHF is a level of applied heat flux beyond which the near-surface liquid is displaced by a vapor film, restricting the liquid from access to the surface. As a result, thermal energy begins to accumulate in the surface, causing a

[1] In natural gas powered electric plants, a Rankine cycle is used as a bottoming cycle for the gas engine to improve the overall thermal efficiency of the combined power cycle.

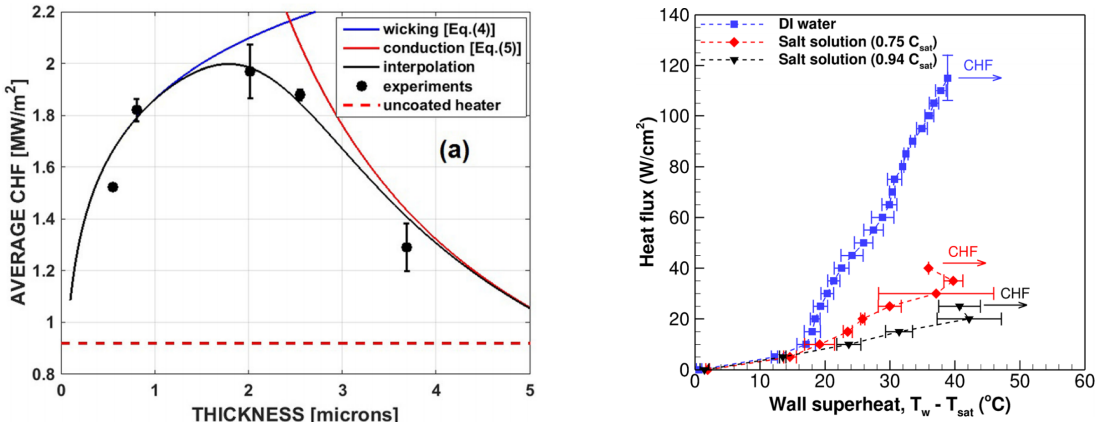

(a) Non-monotonic behavior of CHF with nanoparticle deposition thickness [2].

(b) 6-fold reduction in CHF due to salinity [3].

Figure 1.1: Sensitive dependence of CHF on surface fouling and liquid salinity.

sharp rise in the surface temperature and ultimate failure. This phenomenon is known as dry-out. The highest heat transfer coefficients (HTCs) are observed at heat fluxes close to the CHF, making it desirable to operate any boiling system close to it. However, obtaining reliable values of CHF for boiling systems is difficult because CHFs have a sensitive dependence on surface and liquid characteristics. Surface fouling can change the surface chemistry and/or geometry due to incremental changes over time in particle deposition or surface oxidation and alter CHF (Figure 1.1a) while changes in liquid salinity can also drastically reduce CHF (1.1b). This renders CHF unpredictable and as a result, operation close to it is avoided. Operating at a lower heat flux is undesirable because it places a lower bound on the surface area of a heat exchanger which increases the initial cost of the plant (with a given power rating), and in electronics cooling, it places an upper bound on the computational power of a chip with a given surface area.

Although many mechanistic models that predict CHF have been proposed over the last 70 years (Section 2.2), the conditions that bring about the onset of dry-out are not well understood. The aforementioned models are mostly hydrodynamic and are based on simplified assumptions of uniform and constant surface temperature and heat flux.

They fail to capture the dynamic effects of surface fouling on CHF. These models also propose different dry-out triggering mechanisms and are not universally applicable to all boiling systems. In the absence of reliable predictions of CHF, power plant operators rely on lookup tables [4] while relying on a factors of safety ranging up to 1.45 [5].

A solution to operation at higher heat fluxes and higher HTC has been to enhance CHF through surface or fluid modification. Over the past two decades, novel ways of enhancing CHF and HTC have been proposed which use micro/nano-scale structures, microporous surface coatings, nanofluids and micro-channels (Section 2.3). These have demonstrated the importance of surface chemistry and geometry in reducing contact angle, increasing nucleation site density, enhancing wicking flow and facilitating liquid-vapor pathways, thereby promoting rewetting of a dry spot on the heater surface and delaying dry-out. Although enhancing CHF does allow for operation at higher heat fluxes than before, it is also plagued by surface fouling and CHF remains difficult to predict. Therefore, it is necessary to understand the effects of surface fouling on CHF. This may be achieved by performing lab experiments but due to the sensitive dependence of CHF on surface chemistry and/or geometry (which are application-specific), the results of these experiments will have high uncertainties associated with them. Therefore, it is essential that some predictive techniques are developed that can indicate changes in the value of CHF based on the dynamic conditioning of the surface.

In this context, operation close to CHF requires some indicator of a surface's proximity to dry-out. Such an indicator should be capable of detecting an imminent, but not incipient, dry-out and allow for control measures to be taken in time. It should also be universal across all surfaces regardless of the extent of fouling. In recent years, several studies have demonstrated that boiling is a chaotic and complex dynamical system by examining fluctuations in surface temperature, contact line length and surface void fraction [6–8]. From the study of non-linear, complex dynamical systems, it is known that such systems undergo catastrophic changes with small changes in certain

input parameters, akin to dry-out in boiling. Data series generated by such systems have information embedded in them which can be used for short term forecasting of a catastrophic event [9]. This suggests that in boiling, there should be a focus on the aforementioned dynamical quantities to look for an indicator to presage dry-out.

Non-linear, complex dynamical systems are known to generate data series exhibiting fluctuations on a wide range of time scales that follow scaling laws over several orders of magnitude. These scaling relations cause the dynamics of the system to appear self-similar (Section 2.5). In the last 20 years, scaling behavior in self-similar data series has been reported in many natural time series generated by complex systems, including geophysical, medical and physiological, astrophysical, and financial systems [10–13]. Phase transitions in complex systems are often associated with changes in their fractal dynamics, allowing for a detection of such transitions (or corresponding states) by fractal analysis. While the fractal nature of boiling has been demonstrated by studies, the use of this property in estimating the system's proximity to CHF remains unexplored. Particularly, self-similar data series exhibit long-term correlations which can be quantified using a measure called Hurst Exponent (see Section 5.5 for details). This motivates the objective of the present study: to demonstrate the use of Hurst Exponent calculated for time series generated in boiling system as an indicator of a surface's proximity to dry-out.

The goal of this study was to investigate local and surface-averaged temperature fluctuations in boiling for long-term correlations and explore the use of Hurst Exponent, a measure of long-range memory of a time series, as an indicator of a surface's proximity to dry-out. This will allow operation of all surfaces closer to CHF to achieve higher HTCs. This study will also yield insights into conditions prior to dry-out across different surfaces, which have proven difficult to interrogate experimentally so far. Such insights will prove useful in the future to design surfaces which can enhance CHF even further. Additionally, the results of this study will improve understanding of safety

margins in power plants, heat exchangers and cooling of micro-electronics and promote understanding of the role of surface chemistry in delaying dryout.

1.2 Organization of this Work

This thesis is organized as follows:

- Chapter 2 provides a brief introduction to boiling fundamentals followed by the literature study relevant to this study.
- Chapter 3 provides an overview of the experimental facilities used in this work. It also includes details on data reduction of the raw measurements, calibration of the various temperature sensors, and uncertainty analysis.
- Chapters 4 and 5 describe the results from the boiling experiments performed on surfaces with embedded micro-scale RTDs and platinum wires, respectively.
- Chapter 6 extends the analysis outlined in the foregoing chapters to publicly available data of experiments performed in microgravity aboard the International Space Station.
- Chapter 7 summarizes the body of work with the main conclusions highlighted. The avenues that should be explored in future work are also recommended.
- Appendix A outlines the calibration process of a Standard Platinum Resistance Thermometer, the primary standard against which all other temperature sensors were calibrated in this work. It also includes details on data reduction and uncertainty analysis.
- Appendix B outlines the calibration process of type-T thermocouples used in this work, along with details on data reduction and uncertainty analysis.

- Appendix C outlines the steps taken and recipes used for the micro-fabrication of surface-deposited, micro-scale Resistance Temperature Detectors (RTDs) used in this work.

Chapter 2

Background

2.1 Fundamentals of Boiling

2.1.1 Pool Boiling

Pool boiling refers to the situation where a surface immersed in a quiescent pool of liquid is heated to temperatures above the boiling point of the liquid and a majority of the heat transfer from the surface to the liquid occurs due to the continuous nucleation and departure of vapor bubbles (see Figure 2.1). During the formation of such vapor

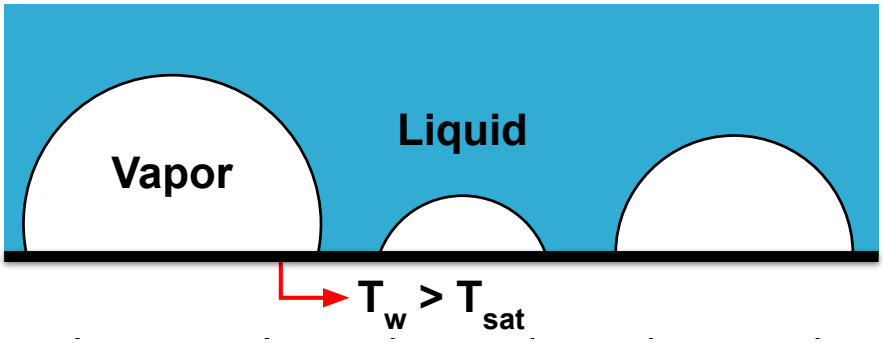

Figure 2.1: Schematic representing pool boiling on a heated surface.

bubbles, large amounts of thermal energy is absorbed by the liquid from the surface in the form of latent heat of vaporization to undergo phase change as the fluid temperature is essentially held constant at the saturation temperature. Owing to the lower density of the vapor being surrounded by higher density liquid, the vapor bubble detaches itself from the heated surface due to buoyancy and departs, making way for fresh liquid to take its place and continue this process of heat transfer and vapor removal. Due to its multi-phase nature, it is a highly efficient heat transfer process where large amounts of heat transfer can be driven by relatively small temperature differences between the surface and the surrounding liquid[1], as is evident in Figure 2.2.

The term *pool* in pool boiling is used to specify the quiescent nature of the liquid which may have finite values of local velocities but the volume-averaged velocity is zero. This is in contrast to *flow* boiling wherein the liquid has a finite volume-averaged velocity. Pool boiling may also be further classified into **saturated** and **sub-cooled** boiling to refer to the average temperature of the liquid. As the names suggest, the average liquid

[1]compared to other methods of heat transfer

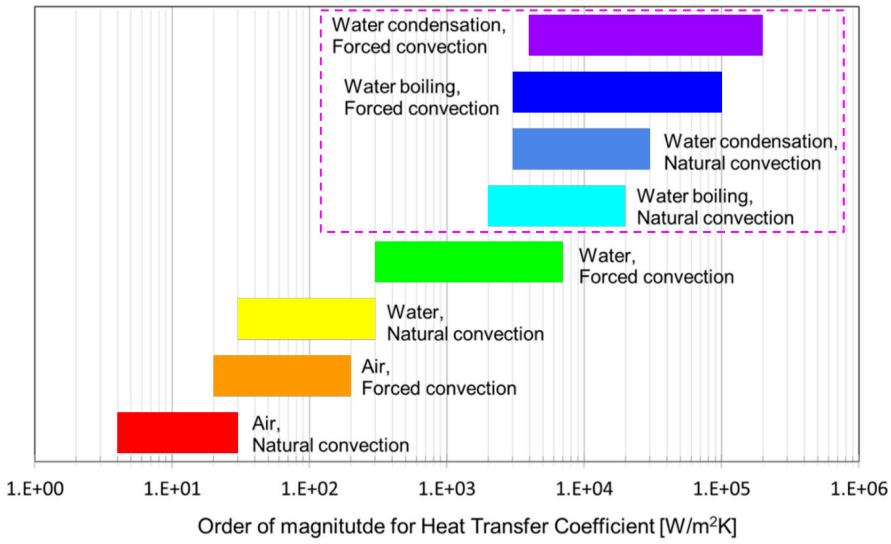

Figure 2.2: Order of magnitude estimates of HTCs associated with different convective techniques, adapted from [14], showing the effectiveness of phase-change heat transfer.

temperature is at (or below) the saturation temperature of the fluid in saturated (or sub-cooled) pool boiling.

2.1.2 The Boiling Curve

Quantitatively, pool boiling is represented on a boiling curve, a graph of the wall heat flux ($q_w^{"}$, heat transfer rate per unit area) vs. the wall superheat, $\Delta T_w = T_w - T_{\text{sat}}$. A representative boiling curve for water on a smooth metallic surface is shown in Figure 2.3. When no heat flux is dissipated by the surface, it is in thermal equilibrium with the surrounding liquid, which may be at or below the saturation temperature. For this discussion however, we will consider saturated pool boiling and hence, the surrounding liquid is at T_{sat}.

As the surface begins to dissipate heat, the surface temperature increases beyond the saturation temperature, that is, $T_w > T_{\text{sat}} \Rightarrow \Delta T_w > 0$. At the lowest values of heat flux dissipation, heat transfer occurs exclusively due to buoyancy-driven natural convection and vapor bubbles are absent. This part of the boiling curve is known as the *free* or *natural convection regime*. The absence of vapor bubbles is because the wall superheat must exceed a threshold, known as **activation superheat** or **bubble incipience temperature**, to provide the surface energy required to form a new liquid-vapor interface for the vapor bubble. This activation superheat is given by

$$\Delta T_w \geq \frac{2\sigma T_{sat}(P_l)}{\rho_v h_{lv} r} \tag{2.1}$$

where P_l is the bulk liquid pressure, σ is the surface tension of the liquid, ρ_v is the vapor density, h_{lv} is the enthalpy of vaporization, and r is the radius of the vapor bubble at nucleation. For water at atmospheric pressure, the activation superheat is typically in the $1 - 5$ K range for values of 6 μm $\leq r \leq$ 30 μm. Such low values of activation superheat are due to the presence of trapped air pockets in surface cavities; however,

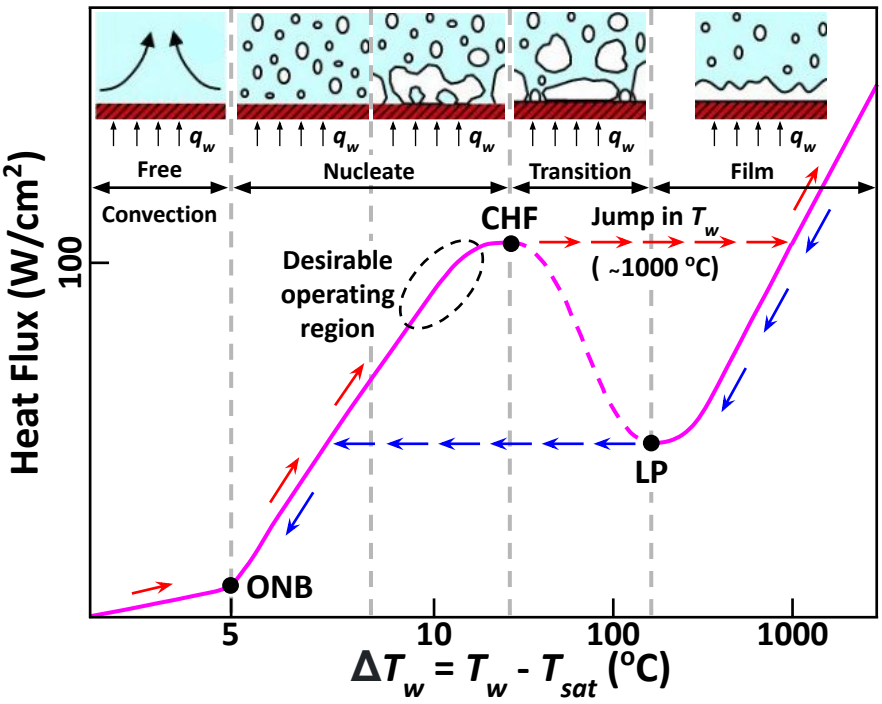

Figure 2.3: A representative pool boiling curve for pure water on a smooth metal surface.

the trapping of air by a cavity depends on many factors, including surface chemistry, roughness, and the local temperature field, all of which affect the contact angle and the shape of the cavity itself. The point on the boiling curve where bubble nucleation starts is known as the Onset of Nucleate Boiling (ONB), and is followed by the *nucleate boiling regime*.

Just beyond ONB, the boiling curve becomes steeper since phase change heat transfer is capable of dissipating increasing amounts of heat flux with smaller increases in the wall superheat. In the nucleate boiling regime, initially, the largest cavities with trapped air or vapor are activated and bubbles nucleate at isolated locations (or nucleation sites) on the surface. But as the heat flux and the wall superheat increase, cavities of smaller mouth radii are also activated. At still higher heat fluxes, nucleation site density increases, and eventually, the bubbles nucleate faster than they can escape from

the surface individually. This results in bubbles coalescing and vapor now escapes the surface in the form of slugs and columns[2].

Eventually, at a certain level of heat flux, known as the *Critical Heat Flux* (CHF), the vapor forming at the surface is considerable and liquid resupply to the dry-spots under the vapor is prevented, causing the dry-spots to grow irreversibly and the surface to be enveloped by a thin vapor film. The sudden drop in the thermal conductivity of the fluid in contact with the surface ($k_v/k_l = 0.036$ for water at $T_{\text{sat}} = 100\,^{\circ}\text{C}$) leads to a sharp and large jump in the wall temperature (of the order of 1000 K). Beyond CHF, heat transfer occurs through the vapor film, and this regime is known as the *film boiling regime*.

Once film boiling is established on a surface, reducing the heat flux below CHF does not result in an immediate transition back to the nucleate boiling regime. Instead the boiling curve exhibits hysteresis and follows the cooling curve marked by the blue arrows in Figure 2.3. Due to the extremely high wall temperatures in the film boiling regime, the vapor film is extremely stable. Any liquid that breaks through the vapor film vaporizes quickly to reestablish the film. With continued decreasing heat flux, this occurs until the *Leidenfrost Point* (labeled LP on the boiling curve) is reached. If the heat flux is reduced below LP, the vapor film breaks down entirely and boiling transitions back to the nucleate boiling regime.

The dashed portion of the boiling curve between CHF and LP is known as the *transition regime*, named due to the transitional nature of the regime that oscillates unpredictably between film and nucleate boiling. This part of the curve is only realized if the wall temperature (and hence, wall superheat), and not the wall heat flux, is controlled.

[2]This regime is also known as the "fully-developed" nucleate boiling regime.

2.1.3 Bubble Ebullition Cycle

The continuous nucleation, growth and departure of vapor bubbles from a boiling surface drives the majority of the heat transfer and forms a very efficient means of mass and thermal energy dissipation resulting in some of the largest heat transfer coefficients (HTCs) in convective heat transfer. Therefore, it is important to understand the lifecycle of a typical vapor bubble on a boiling surface, also known as the bubble ebullition cycle.

Figure 2.4 shows the various stages of a vapor bubble at a cavity of radius r_e acting as an active nucleation site on a surface undergoing saturated pool boiling. The bulk liquid is at P_∞ and $T_\infty = T_{\text{sat}}\big(P_\infty\big)$. The cyclic process starts at $t = 0$ (Figure 2.4a) when an existing vapor bubble departs, entraining with it superheated liquid from the thermal boundary layer that existed near the wall, and is replaced by relatively cooler liquid at T_∞ from the bulk.

This is followed by a period known as the *waiting time*, $t \leq t_w$, during which the superheated thermal boundary layer is restored by heat transfer from the wall (Figure 2.4b). Within this thermal boundary layer, the liquid exists in a superheated metastable state at $T(y) \geq T_{\text{sat}}\big(P_\infty\big) = T_\infty$, with $T(y)$ varying between T_w next to the wall ($y = 0$) and $T_\infty < T_w$ at the edge of the thermal boundary layer ($y = \delta_t$), as shown in Figure 2.4b. The thermal boundary layer thickness is of the order of 10 μm for water undergoing boiling at atmospheric pressure. Due to the no-slip boundary condition at the heated wall, advection within the thermal boundary layer can be neglected. As a result, heat transfer in the thermal boundary layer is modeled as one-dimensional transient conduction and the thermal boundary layer thickness increases with time as $\delta_t \sim \sqrt{\alpha_l t}$, where α_l is the thermal diffusivity of the liquid at T_{sat}. However, convection and turbulence in the bulk fluid away from the wall limits the thickness of the thermal boundary layer.

At the end of the waiting time, $t = t_w$, the residual vapor left behind inside the cavity by the release of the preceding bubble begins to grow. Mikic and Rohsenow (1969) [15]

postulated that for vapor inside the cavity to start growing, the temperature profile within the thermal boundary layer should be such that if a hemispherical vapor bubble of radius r_e was to exist on the cavity with the same mouth radius, the temperature at the top of the hemispherical bubble (at $y = r_e$) should exceed the activation superheat for a vapor bubble of radius r_e given by

$$T\big(y = r_e\big) \geq T_{\text{sat}} + \frac{2\sigma T_{\text{sat}}\big(P_\infty\big)}{\rho_v h_{lv} r_e}$$

Based on this criteria and by using a one-dimensional transient conduction model, they arrived at the following expression for waiting time:

$$t_w = \frac{r_e^2}{4\alpha_l}\left\{\text{erfc}^{-1}\left(\frac{T_{\text{sat}} - T_\infty}{T_w - T_\infty} - \frac{2\sigma T_{\text{sat}}\big(\nu_v - \nu_l\big)}{\big(T_w - T_\infty\big) h_{lv} r_e}\right)\right\}^{-2} \tag{2.2}$$

where ν_l and ν_v are the specific volumes of the liquid and vapor, respectively, and α_l is the thermal conductivity of the liquid. This expression for the waiting time, t_w, yields time scales of the order of 10 ms for water at atmospheric pressure, which is in good agreement with observations by Han and Griffith (1965), Ibrahim and Judd (1985), and Gerardi et al. (2011) [16–18].

In the discussion that follows, the pressure and temperature within the bubble are assumed to be uniform at P_v and T_v, respectively, at all times. When the bubble embryo first begins to grow inside the mouth of the cavity, T_v and P_v are nearly equal to the wall superheat T_w and $P_{\text{sat}}\big(T_w\big)$, respectively. Throughout the rest of the bubble growth process, the capillary pressure difference across the liquid-vapor interface decreases as the bubble radius increases, and P_v drops towards P_∞. Therefore, P_v and T_v always lie

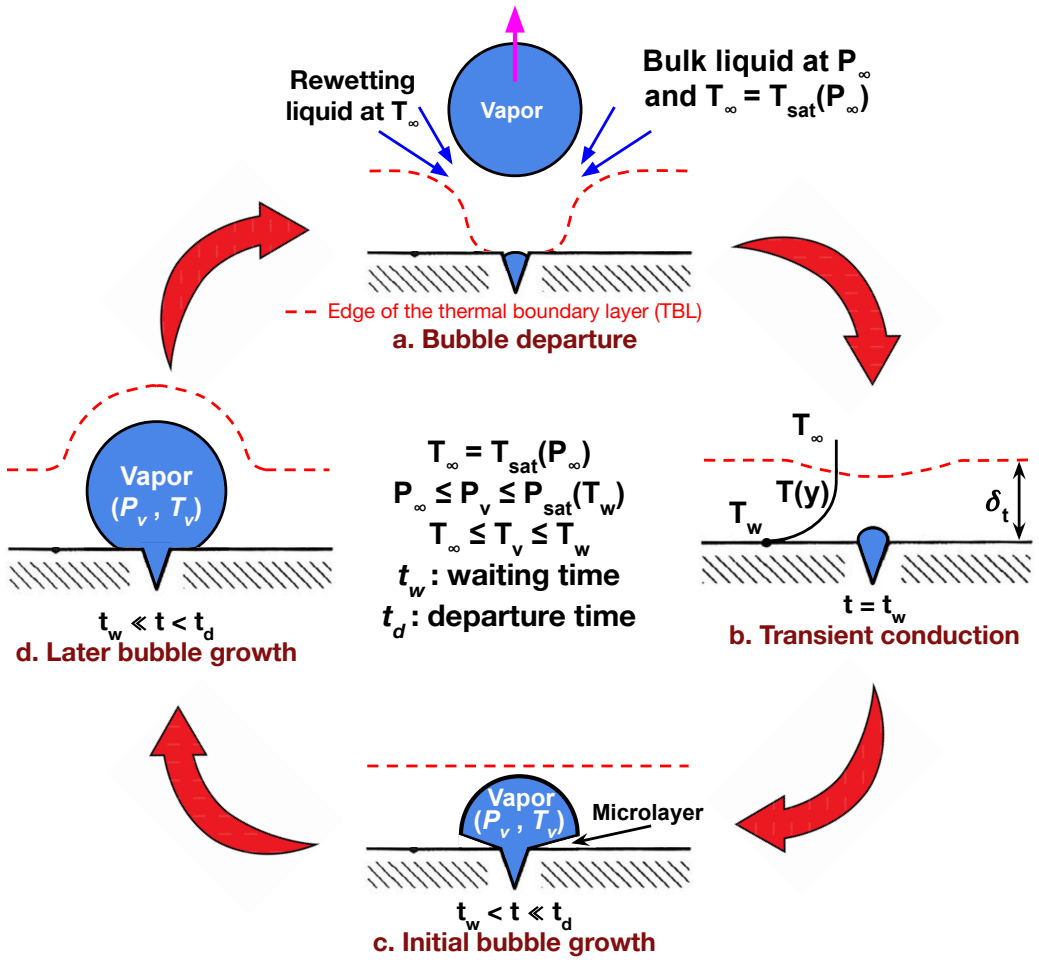

Figure 2.4: Bubble Ebullition Cycle.

in the following ranges:

$$P_\infty \leq P_v \leq P_{\text{sat}}(T_w)$$

$$T_{\text{sat}}(P_\infty) \leq T_v \leq T_\infty$$

As the bubble embryo emerges from the cavity, there is a sudden increase in the radius of curvature of the vapor bubble. At this instant, the capillary pressure difference, $\Delta P = P_v - P_\infty$, which is near the maximum value, triggers a rapid expansion of the bubble

that is resisted primarily by the inertia of the surrounding liquid. During this early stage of bubble growth, also known as the *inertia-controlled* growth stage, the bubble radius grows mostly due to the large capillary pressure difference. This growth stage lasts for a very short time (of the order of 10 μs) and there is an insignificant amount of vapor that is added to the bubble due to evaporation at the liquid-vapor interface. At the end of the initial growth stage, the bubble shape is hemispherical, as shown in Figure 2.4c, and a thin, wedge-shaped layer of liquid (known as the ***microlayer***) gets trapped under the bubble. It varies in thickness from nearly zero near the cavity to a few μm at the edge of the hemispherical bubble [19].

In in the next stage of bubble growth, the vapor temperature (T_v) and pressure (P_v) have reduced significantly and are closer to their lower limits of T_∞ and P_∞, respectively. The bubble now grows mostly from vapor addition to the bubble from two sources: evaporation of liquid at the hemispherical liquid-vapor interface where the thermal energy of the superheated thermal boundary layer is used up as given by the latent heat of vaporization, and evaporation in the microlayer region, which is sustained by heat transfer from wall. This stage is known as the *heat transfer-controlled* or *thermally-controlled* growth stage because the bubble growth is now limited by the rate at which thermal energy can be conducted to the two aforementioned liquid-vapor interfaces.

During the thermally-controlled growth stage, the microlayer may partially or fully evaporate and leave behind a transient dry-spot under the bubble where the local surface temperature becomes elevated. Simultaneously, the thermal energy of the superheated liquid surrounding the hemispherical interface of the bubble is also gradually depleted. The pressure and liquid inertia forces become relatively small compared to the surface tension, which increases with the increasing perimeter (contact line) of the dry-spot. This tends to pull the bubble into a more spherical shape, as shown in Figure 2.4d.

The thermally-controlled growth stage lasts for time of the order of 10 ms, which is

the same as that of the waiting time, t_w. For comparison, the inertia-controlled growth period occupies a very small fraction of the overall growth process and the entire period during which the bubble grows through the two growth stages is known as the departure time, t_d. As a result, the departure frequency of a bubble at a nucleation site is given by $f_d = 1/\big(t_w + t_d\big)$.

Throughout the bubble growth process, the interfacial tension acting along the contact line tends to hold the bubble in place on the surface. Meanwhile, buoyancy forces tend to pull the bubble from the surface in the case of an upward facing horizontal heated surface. The detaching buoyancy force becomes stronger as the bubble becomes larger until eventually it becomes stronger than the retaining surface tension force and causes the bubble to detach from the surface and depart, restarting the cyclic process.

Bubble Growth Radius

As mentioned in the previous section, bubble growth during the thermally-controlled growth stage lasts much longer than the initial inertia-controlled growth stage. During the thermally-controlled growth stage, bubble growth occurs due to evaporation of liquid to vapor at the hemispherical interface and in the microlayer. Mikic and Rohsenow (1969) [15] modeled bubble growth due to evaporation at the hemispherical vapor-liquid interface to derive the following expression of the bubble radius as a function of time, $R(t)$:

$$R(t) = \frac{2\mathrm{Ja}\sqrt{3\pi\alpha_l t}}{\pi}\left\{1 - \frac{T_w - T_\infty}{T_w - T_{\mathrm{sat}}}\left[\left(1 + \frac{t_w}{t}\right)^{1/2} - \left(\frac{t_w}{t}\right)^{1/2}\right]\right\}$$

where t_w is the waiting time given by Equation (2.2), α_l is the thermal conductivity of the liquid and Ja is the Jakob number given by

$$\mathrm{Ja} = \frac{\rho_l c_{p,l}\left(T_w - T_{\mathrm{sat}}\right)}{\rho_v h_{lv}}$$

where $c_{p,l}$ is the specific heat capacity of the liquid.

van Stralen et al. (1975) [20] also derived an expression for the bubble radius as a function of time, $R(t)$, by considering bubble growth exclusively due to evaporation in the microlayer region. Their expression for the bubble growth radius was

$$R(t) = 0.470\,\mathrm{Ja}\,\mathrm{Pr}_l^{-1/6}\sqrt{\alpha_l t}$$

where Pr_l is the Prandtl number of the liquid.

The two equations of bubble radius during the thermally-controlled growth stage given above are mainly analytical and increasingly detailed models of bubble growth have been proposed since ([21–25]). Within the scope of this background, it is merely noted that both the bubble radius expressions are of the form $R(t) \sim \mathrm{Ja}\sqrt{\alpha_l t}$. Experimental data agrees very well with this $R(t) \sim t^{1/2}$ dependence.

Bubble Departure Diameter

The bubble diameter at release, D_d, is primarily determined by the net effect of forces (primarily, surface tension and buoyancy, for pool boiling on an upward facing, horizontal, heated surface) acting on the bubble as it grows on the surface. When the liquid adjacent to the surface has motion due to bubble growth and departure at a neighboring nucleation site for instance, drag and lift forces may also come into effect and act to detach the bubble from the surface. In addition to these forces, wall superheat and contact angle, θ, also affect the departure diameter of the bubble, D_d.

Over the past eighty years, bubble departure has been the subject of numerous studies. The reader is referred to the work of Carey (2020) [26] for an excellent summary of the results, where the expressions of the bubble departure diameter, D_d, are presented in the form of the Bond number, Bo, which is defined as

$$\mathrm{Bo} = \frac{g\big(\rho_l - \rho_v\big)D_d^2}{\sigma}$$

Bubble departure expressions are nominally of the form $\mathrm{Bo}^{1/2} = f\big(\mathrm{Ja}, \theta\big)$ and suggest a singular value of the bubble departure diameter as a function of the wall superheat $(T_w - T_{\mathrm{sat}})$ embedded in Ja.

Bubble Departure Frequency

The bubble departure frequency is dependent on the bubble departure diameter, D_d, since both the rate of bubble growth and size required for release determine the release frequency. Therefore, the size and characteristics of individual nucleation cavities affect bubble growth and wait times resulting in different nucleation sites having different departure frequencies. Carey (2020) [26] provides a summary of all the correlations, but has stated that there is considerable discrepancy between models that are each based on a very limited data set. The correlations summarized in Carey (2020) allow for insight into the relationship of bubble frequency and diameter, but cannot provide predictive capabilities.

2.1.4 Heat Transfer Mechanisms in Pool Boiling

During the life-cycle of the bubble, there are multiple mechanisms by which heat is transferred away from the wall as shown in Figure 2.5. This section briefly describes the different mechanisms.

Natural convection (q_{nc}), as a heat transfer mechanism, constantly transfers heat

from the locations on the heated surface where there are no nucleating bubbles. At active nucleation sites, however, vapor bubbles gives rise to other mechanisms.

When a bubble departs a nucleation site, it leaves behind a dry spot which is rewetted by the surrounding liquid, leading to **transient conduction** (q_{tc}). Due to transient conduction, heat transfer from the surface results in the growth of a superheated liquid layer until a time when a new bubble nucleates ($t = t_w$). During the thermally-controlled bubble growth stage, the thermal energy in superheated liquid layer contributes to evaporation at the hemispherical vapor-liquid interface by providing the energy required for latent heat of vaporization (**superheated liquid evaporation**, q_{sl}). Simultaneously, the bubble also grows due to evaporation in the microlayer region which extracts thermal energy from the surface in the form of **microlayer evaporation** (q_{ml}). During its growth and departure, the bubble also agitates the surrounding fluid which would otherwise be quiescent, except for natural convection currents. This results in enhancement of heat transfer due to fluid motion known as **micro-convection** (q_{mc}).

Within the microlayer, **contact line heat transfer** (q_{cl}) occurs over a very small region close to the three phase contact line. A thin liquid layer is adsorbed onto the surface due to molecular adhesive forces and the thickness of the adsorbed layer increases with the radius from the center of the bubble as shown in Figure 2.5a. Close to the contact line, the liquid layer is thin and evaporation is prevented by molecular adhesive forces. As the thickness of the layer increases, adhesive forces decrease rapidly ($F_a \propto \delta^{-4}$) but conductive resistance begins to increase. There exists an optimum thickness where the

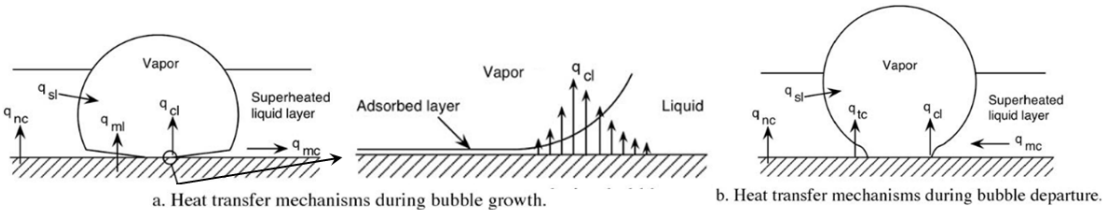

a. Heat transfer mechanisms during bubble growth.

b. Heat transfer mechanisms during bubble departure.

Figure 2.5: Heat Transfer Mechanisms in Pool Boiling. [27]

heat transfer is maximum. Stephan and Hammer (1994) [28] suggested that the radial length over which this heat transfer is greater is less than 1 μm for a bubble of diameter 125 μm.

2.2 Mechanistic Models for CHF on a Plain Surface

Considerable debate exists as to what triggers dry-out. In one of the earliest attempts, Kutateladze (1950) [29] derived a heat flux scale based on dimensional analysis.

He considered the roles of vapor inertia, surface tension and buoyancy to be important at dry-out. In his model, fully developed nucleate boiling at the surface occurs in the form of vapor jets with a velocity perpendicular to the surface, u_g, given by

$$u_v = \frac{q''}{\rho_v h_{lv}}$$

where q'' is the local heat flux, and ρ_v and h_{lv} are the vapor density and enthalpy of vaporization, respectively. Dry-out is triggered when the kinetic energy of the escaping vapor balances the opposing gravitational force acting on the suspended liquid as

$$\rho_v u_v^2 \sim g(\rho_l - \rho_v)\delta^*$$

where ρ_l is the liquid density, g is the acceleration due to gravity, and δ^* is the capillary length given by

$$\delta^* = \left(\frac{\sigma}{g(\rho_l - \rho_v)} \right)^{1/2}$$

in terms of the surface tension, σ. Using the above equations, Kutateladze derived his

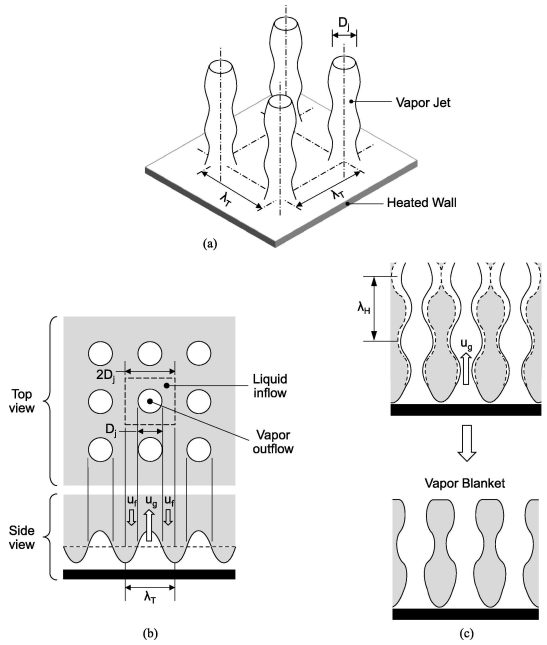

Figure 2.6: Schematic of Zuber's hydrodynamic instability model. (a) Vapor jet formation prior to dry-out. (b) Unit cell containing a single jet and surrounding liquid. (c) Vapor mushroom formation due to Helmholtz instability. [30]

well-known CHF relation as

$$\frac{q''_{CHF}}{\sqrt{\rho_v} h_{lv} [g(\rho_l - \rho_v)]^{1/4}} = K$$

The value of $K = 0.16$ was recommended by Kutateladze for pool boiling on a large horizontal flat surface after fitting experimental data to his CHF relation.

Building on Kutateladze's work, Zuber (1958) [31] postulated that dry-out occurred due to what is commonly known as the hydrodynamic instability theory. According to this model, vapor jets of diameter $D_j = \lambda_T/2$ form on the surface due to the Rayleigh-Taylor instability at distances λ_T apart (Figure 2.6) where λ_T is the Rayleigh-Taylor unstable wavelength. Using continuity, the following relationship between the vapor velocity (u_g)

and liquid resupply velocity (u_f) was established:

$$u_l = \frac{\rho_l}{\rho_v}\left(\frac{\pi}{16-\pi}\right)u_v$$

The velocity difference between the vapor jet and the resupplying liquid sets up the Kelvin-Helmholtz instability at the interface, and growth of this instability causes merging of adjacent vapor jets. This causes formation of the vapor mushroom responsible for preventing liquid from resupplying the heater surface. Zuber's analysis yielded the following expression for CHF:

$$q''_{CHF} = 0.131\sqrt{\rho_v}h_{lv}[\sigma g(\rho_l - \rho_v)]^{1/4} \tag{2.3}$$

This yields the same heat flux scale as Kutateladze, but with a different value of the constant pre-factor. It agrees reasonably well with data over a wide range of system pressure and yields a value of 110 W/cm^2 for water at atmospheric pressure. This model suggests that dry-out is a *far-field* phenomena related to jet break-up away from the surface and placed an upper bound on the value of CHF, commonly known as the CHF hydrodynamic limit.

Haramura and Katto (1983) [32], inspired from Gaertner's (1965) [33] visualization results for vapor structures in pool boiling, considered the drying out of a liquid layer, called macrolayer, underneath a large hovering vapor bubble with many vapor stems emanating across it as shown in Figure 2.7. In this model, dry-out is triggered when the macrolayer dries

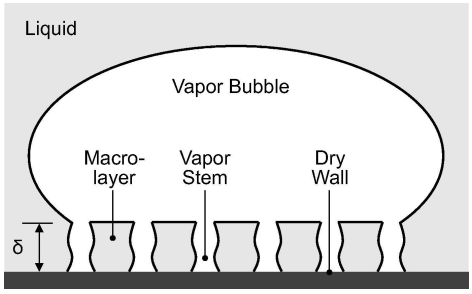

Figure 2.7: Schematic of Haramura and Katto's macrolayer dryout model. [30]

out before the large vapor bubble is able to de-

part. The thickness of the macrolayer is $\delta = \lambda_H/4$ where λ_H is the critical wavelength of the Kelvin-Helmholtz instability. The following expression for CHF was established:

$$q''_{CHF} = 0.721\left[\left(\frac{A_v}{A_w}\right)^2\left(1-\frac{A_v}{A_w}\right)\frac{\frac{\rho_l}{\rho_v}+1}{\left(\frac{11}{16}\frac{\rho_l}{\rho_v}+1\right)^{3/5}}\right]^{5/16}\sqrt{\rho_v}h_{lv}[g(\rho_l-\rho_v)]^{1/4}$$

where A_v is the heater surface area occupied by vapor jets and A_w is the total heater surface area. This heat flux scale is the same as those of Zuber and Kutateladze.

Nikolayev and Beysens (1999) [34] identified the vapor recoil force due to the evaporation of liquid molecules at the liquid-vapor bubble interface as contributing to the spread of the dry-spot under a vapor bubble. As liquid changes into vapor at the liquid-vapor interface, the interface gets pushed away from the center of the bubble to accommodate the increased volume of the vapor. This recoil force per unit area, P_r, is given by

$$P_r = \eta^2\left(\rho_v^{-1} - \rho_l^{-1}\right)$$

where η is the evaporated mass flux (evaporated mass per unit time per unit area). The authors showed through simulations and experiments [35, 36] that the vapor recoil force is especially strong in the microlayer where the evaporated mass flux is significant, due to microlayer evaporation, which is related to the local heat transfer, q, as

$$q = \eta h_{lv}$$

Concurrently, Kandlikar (2001) [37] considered the effect of contact angle by equating the force exerted by the vapor recoil to the retaining surface tension force acting at an angle to the surface that anchors the base of the bubble to the surface (Figure 2.8a). He postulated that, at CHF, the vapor recoil force just exceeds the surface tension force

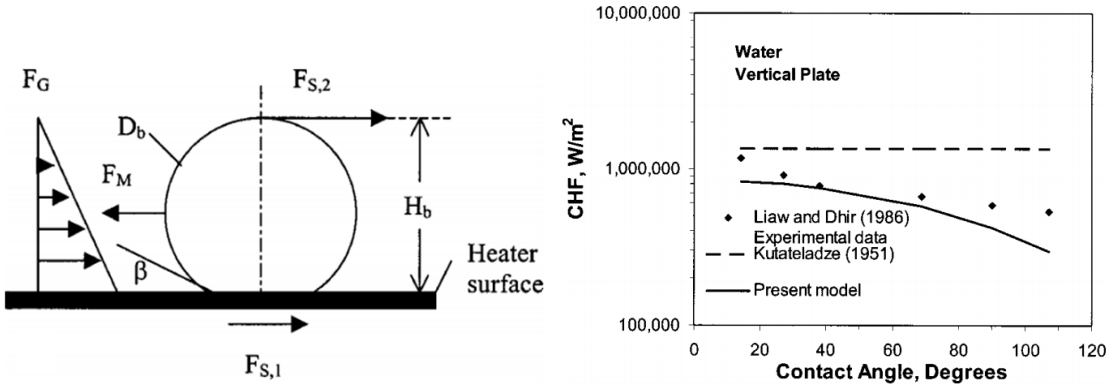

(a) (b)

Figure 2.8: (a) Forces due to surface tension, gravity and momentum acting on a bubble parallel to the heater surface and (b) Effect of contact angle on CHF for water boiling on a vertical plate; comparison of the static force balance model and Kutateladze's correlation with experimental data. [37]

and causes the bubble to stretch and cover the entire surface as a thin vapor film. He derived the following relation for CHF:

$$q''_{CHF} = \left(\frac{1+\cos\beta}{16}\right)\left[\frac{2}{\pi}+\frac{\pi}{4}(1+cos\beta)\cos\phi\right]^{1/2}\sqrt{\rho_v}h_{lv}[g(\rho_l-\rho_v)]^{1/4}$$

where β is the contact angle and ϕ is the angle that the heater surface makes with the horizontal. Although Kandlikar's formulation involved a force balance without considering the hydrodynamics of the vapor jets and resupplying liquid, he arrived at a similar expression to Zuber's hydrodynamic model with a different pre-factor constant which included the effect of the contact angle and heater orientation, and was able to explain the lower CHF values exhibited by smooth surfaces with higher static contact angles (Figure 2.8b). Note that for perfectly wetting surfaces ($\beta = 0$), the static force model simplifies to Zuber's hydrodynamic model.

Theofanous et al. (2002) [38] showed that CHF values can be made to vary from

well below the CHF hydrodynamic limit to significantly higher values by changing the surface nanomorphology. They conducted pool boiling experiments on smooth titanium films[3] deposited on borosilicate glass slides through nanofabrication techniques. They progressively "aged" titanium films by heating them to 300-400 °C over 2 seconds, which resulted in sub-micrometer scale islands of oxides forming on the films to varying degrees, as revealed by Scanning Electron Microscope images. The "aged" heaters exhibited higher CHF values, lower activation superheats, and higher nucleation site densities than less-"aged" (or fresh) heaters.

Using infrared thermometry to measure the temperature field on the heater surface, they also documented a non-uniform temperature distribution on the surface with *hot-spots* where large temperature gradients exist. They conjectured that these *reversible hot-spots* correspond to dry patches of the surface that were re-wetted and cooled by the liquid film, and that dry-out was triggered by irreversible growth of these hot spots. They argued that dry-out is governed by near-surface dynamics close to the moving three phase contact line. This explained satisfactorily why surface characteristics play a role in altering CHF. Theofanous and Dinh (2006) [39], in a follow-up study, proposed that CHF occurs when the vapor recoil force due to the evaporating liquid in the microlayer, which pushes the contact line away from the center of the hot spot, exceeds the surface tension force responsible for resupplying liquid to the microlayer. They arrived at an expression for CHF given by:

$$q''_{CHF} = \kappa^{-1/2}\sqrt{\rho_v}h_{lv}[g(\rho_l - \rho_v)]^{1/4}$$

where κ is a surface dependent parameter that decreases with increasing surface wettability. The authors did not comment on how to compute κ however. Additionally, despite evidence to the contrary, this model, like other hydrodynamic models, also assumed a uniform wall heat flux and surface temperature.

[3]Surface roughness root mean square values of ±4 nm measured using Atomic Force Microscopy.

2.3 Roughness Effects on Pool Boiling CHF

The seminal work of Theofanous et al. (2002) [38] showed that CHF could surpass Zuber's hydrodynamic limit if surfaces could be engineered to enhance liquid resupply to a drying spot under a growing bubble. In the two decades since, this has been demostrated in a variety of ways through surface structuring (See Figure 2.9).

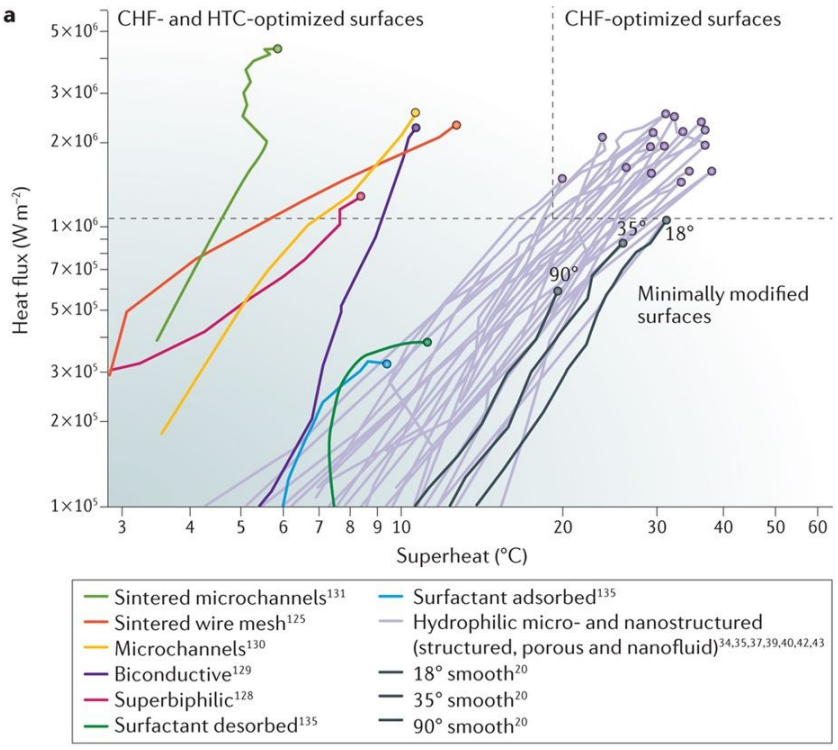

Figure 2.9: Enhancements in pool boiling performances. Reproduced from Cho et al. (2017) [40].

Many studies have documented enhancement of HTC and CHF values as a result of micro- and nano-texturing [41–44], micro-porous surfaces [45, 46], nanofluids [47–49], and micro-channels [50, 51].[4] These enhancements in CHF and HTC of up to 200 % with such surfaces have been attributed to higher nucleation site density and increased

[4]See Mori and Utaka [52] for a comprehensive review.

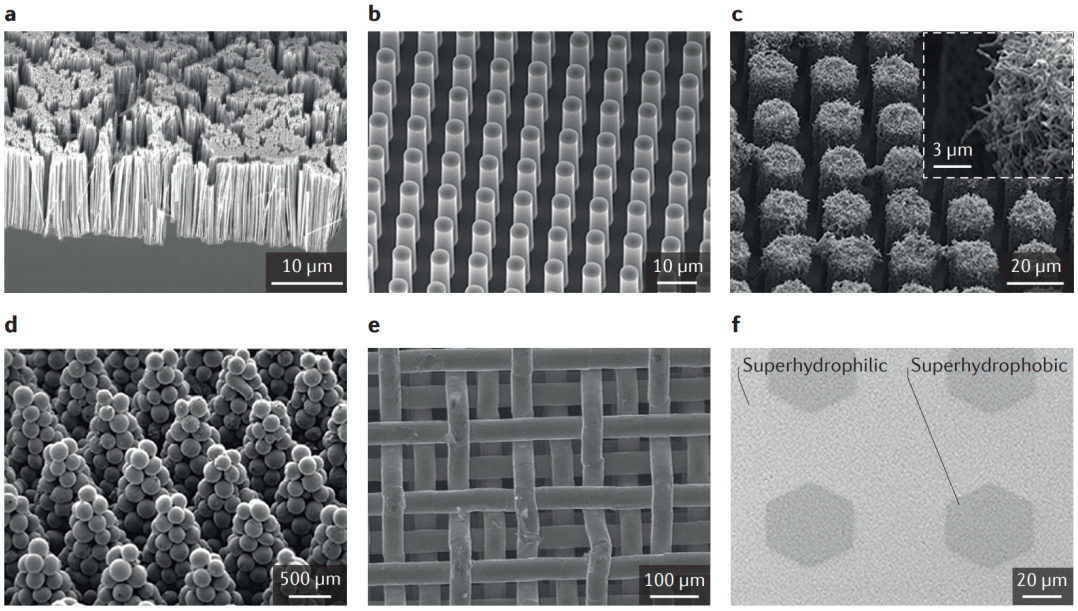

Figure 2.10: SEM images of representative textured surfaces for CHF enhancement. a) Nanowires. b) Micropillars. c) Hierarchical structures. d) Sintered copper particles. e) Wire meshes. f) Biphilic surfaces. Reproduced from Cho et al. (2017) [40].

surface tension driven flow due to small length scales on the surface. In particular, the enhancement of CHF due to microporous surfaces has been shown to be the result of liquid wicking towards a dry spot [53, 54] and surfaces that maximize wicking are known to exhibit enhanced CHF [55]. Plawsky et al. (2008) [56] provided an excellent review of how nano- and micro-scale roughness can affect transport phenomena near the contact line (thin film region) independent of surface tension. More recently, Dhillon et al. (2015) [44] were able to relate timescales associated with the heating of the center of a dry-spot up to a critical temperature with the time associated with the motion of the rewetting liquid front advancing over the distance of a bubble diameter. They observed that for micro-pillar surfaces with varying pillar-to-pillar spacing, dry-out occurred when the ratio of the heating timescale to the rewetting timescale approached or fell below unity. Except for the case of arrays of equally-spaced micro-pillars, no theoretical models exist for predicting CHF on textured surfaces. Nevertheless, this

evidence encourages that from a fluid dynamics standpoint, a certain set of universal conditions can be expected to be satisfied for any surface undergoing dry-out.

2.4 Non-Hydrodynamic and Non-Linear Features of Pool Boiling

Surfaces that exhibit CHFs well beyond the hydrodynamic limit (Equation (2.3)) reveal that CHF models only partially capture the physics governing dry-out. Tachibana et al. (1967) [57] demonstrated that in certain cases, non-hydrodynamics aspects like surface material and thickness of the heater also affect CHF. They also observed that surfaces with affinity for water have comparatively higher CHFs and attribute this effect to the interfacial properties of the heater surface. The authors, and, later, Unal et al. (1992), investigated numerically the hypothesis that dry-out occurs when the temperature at the center of a dry-spot exceeds the Leidenfrost temperature such that the liquid is unable to contact the surface again and the dry-spot grew irreversibly. More recently, Arik and Bar-Cohen (2003) [58] proposed correlations for CHF which show dependence on the thermal activity parameter, $S = \delta\sqrt{\rho_h c_h k_k}$, where δ is the heater thickness, ρ_h is the surface density, c_h is the surface specific heat capacity and k_h is the surface thermal conductivity. These studies demonstrated that interfacial and bulk surface properties also contribute to the dynamics at dry-out.

Non-Uniform Surface Temperature Distribution

Hydrodynamic models implicitly assume that surface temperatures and wall heat fluxes are uniform and are based on linear models of nucleation site activation wherein the density of active nucleation sites can be obtained from a specified cavity size distribution of the surface and an activation-superheat relationship (Equation (2.1)). In reality, studies using infrared thermometry ([38, 59]) have revealed highly non-uniform temperature and heat flux distributions on heated surfaces with temperature gradients as

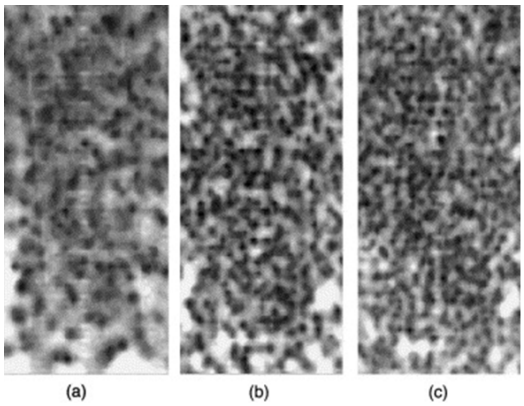

(a) IR thermometry images of an oxidized titanium film deposited on a glass substrate in DI water at (a) 34.8 W/cm^2, (b) 105 W/cm^2 and (c) 151.7 W/cm^2. Dark and light spots correspond to cold and hot temperatures respectively. [38]

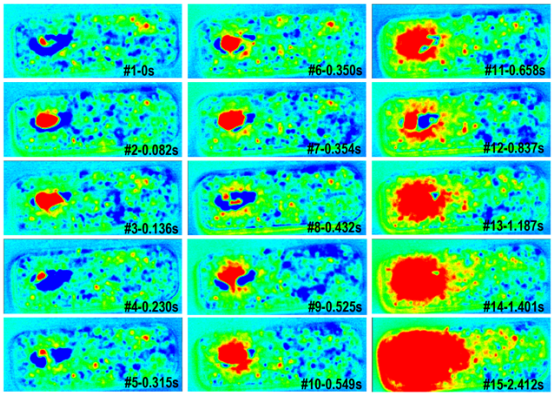

(b) IR thermometry images of an indium tin oxide film heater deposited on sapphire substrate in ethanol at 48 W/cm^2. The images show evolution of temperature gradients over time. Red and blue spots roughly correspond to 150 °C and 100 °C, respectively. [59]

Figure 2.11: IR thermometry images showing temperature gradients on heater surfaces.

large as 50 K over 3 mm (Figure 2.11). Such large gradients may drastically alter the local surface chemistry due to dependence of surface tension and contact angle on temperature, while the apparent contact angle is also known to increase due to evaporation at the contact line [56]. Non-uniform surface temperatures also cause non-uniform wall heat fluxes since local hot spots act as instantaneous dry spots where heat transfer is inhibited.

Intermittency of Nucleation Sites

Hydrodynamic models also assume that individual nucleation sites make equal contributions to the heat flux. In stark contrast, numerous experiments have documented observations of hysteresis, intermittent activity, and deactivation of nucleation sites under the cooling influence of neighboring active sites ([60–62]). Studies point to non-linear interactions between bubbles and the solid wall, and between neighboring bubbles through hydrodynamic interactions as well as through wall conduction. Judd and Chopra (1993)

[60] examined these interactions and reported that bubbles growing at nucleation site are able to promote or hinder the formation of neighboring bubbles at adjacent nucleation sites by depositing or displacing the neighboring vapor nuclei. They also showed that coalescence resulted in a decrease in bubble frequency. Bonjour et al. (2000) [63] pointed out that interactions between adjacent bubbles during coalescence reduced the local wall temperature and in the case of a large number of such simultaneous interactions, heat transfer was impaired or dry-out was triggered. Shoji (2002) [64] studied bubble formation and departure frequency using a submerged orifice and observed that the bubble departure frequency underwent a period doubling bifurcation as the air flow rate was increased. The author remarked that in the relatively more complex systems of boiling, bubble formation and departure would be more non-linear and complicated.

Broadband Distributions of Bubble Departure Diameters and Frequencies

Shoji and co-workers (2001-2004) [65–67] have documented the change in mean departure diameter at a particular nucleation site as a function of the distance to the nearest active nucleation site, and suggested classification of these interactions into liquid-liquid, liquid-solid and solid-solid interactions. Judd and Chopra (1993) [60] examined these interactions and demonstrated that broad distributions in departure diameter and departure time can occur, approximated by Poisson and Gamma distributions, respectively. These are a result of vapor seeding, trapping or absorption due to advancing/receding contact lines and/or thermal de-activation of nearby nucleation sites. Simulations of such mechanisms by Mallozzi et al. (2000) [68], and experimental observations of McSharry et al. (2002) [69] yield broad distributions of departure diameters. Recently, Jukanti and Srinivasan (2024) [70] have considered the role of bubble-bubble interactions in the bubble growth process and have shown that assumptions of a fluctuating pressure field and accompanying unsteady evaporation into a growing bubble can result in stochastic behavior in bubble departure events. Their calculations yielded a range of bubble departure diameters at a single nucleation site that followed a Poisson

distribution, similar to observations from earlier experiments.

Scale-free Behavior in Boiling

The broad range of bubble departure diameters and departure times arising from interactions also result in highly unsteady temperature fields at nucleation sites, which strongly depend on the temperature history at those sites as well as those at neighboring locations [71]. However, the statistics of these fluctuations have not received much attention until recently. This unsteady aperiodic temperature field has been shown to result in highly nonlinear behavior by several researchers. Several researchers have documented scale-free, power-law behavior in the power spectra of temperature fluctuations (Skokov et al. (2010) [72]) and acoustic emissions (Lloveras et al. (2012) [73]), and dry spot area distribution on the heater surface (Charignon et al. (2015) [74], and Sathyamurthi and co-workers (2008-2009) [7, 8]). These studies all suggest the lack of a single departure frequency or bubble diameter.

More recently, Zhang et al. (2022) [75] performed a Direct Numerical Simulation (DNS) study that modeled nucleation site interactions stochastically using Rayleigh and Poisson distributions and argued that dry-out occurs when the probability of interaction between neighboring nucleation sites exceeded 98%. In a different study, Zhang et al. (2023) [76] conjectured that the progression of the boiling system along the boiling curve can be ascertained by considering the development of dry spots and modeling this process using invasive percolation theory. Both of these independent studies model nucleation site interactions as stochastic processes.

2.5 On the Study of Long-Term Correlations in Boiling

Sadasivan et al. (1995) [77] first noted that for a complete and accurate picture of boiling, modeling efforts should include elements that characterize the heater surface, the fluid, and the heater-fluid interface, and the interactions between them, as shown

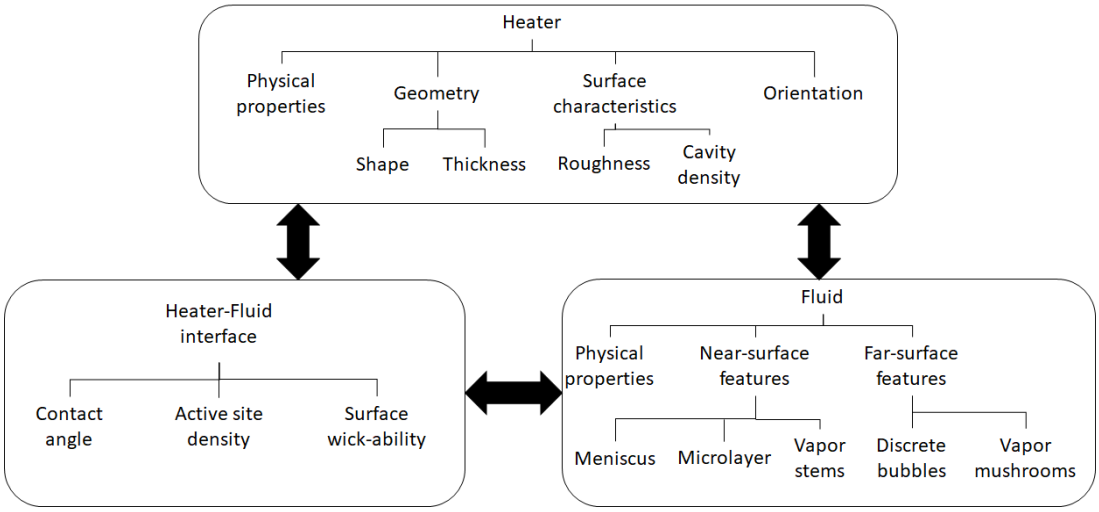

Figure 2.12: Conjugate problem in pool boiling. [77]

in Figure 2.12. Hydrodynamic models are based on the idea that some adverse event occurs on the liquid side to eliminate the liquid supply and these models rely on a static picture of the flow and extrapolate conditions at a single length scale (vapor column, mushroom vapor stem, bubble diameter, microlayer, etc.) to the entire system. However, there is overwhelming evidence to the contrary. Non-linear phenomena like non-uniform surface temperature, intermittent nucleation site activity and interactions with neighboring nucleation sites, and meniscus behavior renders the boiling process a complex dynamical system that is extremely difficult to model accurately.

An alternative approach to studying complex systems is to study the statistics of data series generated by such systems. Data series generated by complex systems are known to exhibit fluctuations on a wide range of time scales and/or broad distributions of the values. In both equilibrium and non-equilibrium situations, the natural fluctuations are often found to follow scaling relations over several orders of magnitude. Such scaling laws allow for a characterization of the data and the generating complex system by scaling exponents, which can serve as characteristic fingerprints of the systems in comparisons with other systems and with models.

One characteristic of data series which exhibit fluctuations over a wide spectrum is that the data series appear self-affine. In a general sense, self-affinity in a data series implies that the data series appear similar at different scales of magnifications (or observations). Mathematically, however, self-affinity of a data series requires that, given a series, $x(t)$ where $0 < t < t_0$, with known statistical moments, the time series $x(at)$ where $0 < t < t_0/a$ has the same statistics as $a^H x(t)$ for all values of a and some value of the scaling exponent, H.[5] Self-affine time series and time series becoming self-affine upon integration are commonly denoted as "fractals", even though they are not fractal in the strict sense. Here, the term "fractal" will be used in the more general sense which include all data, where some scaling exponent, like H in the example above, can be reasonably defined.

In the last 20 years, self-affine or fractal scaling behavior has been reported in many natural time series generated by complex systems, including geophysical, medical, physiological, astrophysical, and financial systems [10–13]. Phase transitions in complex systems are often associated with changes in the dynamics of their self-affinity, allowing for a detection of such transitions (or corresponding states) by fractal analysis. One example for a successful application of this approach is the human cardiovascular system, where the fractality of heartbeat interval time series was shown to reflect certain cardiac impairments as well as sleep stages [78, 79]. While the fractal nature of boiling has been demonstrated by investigators like Shoji (1995) [6] and Sathyamurthi (2008) [7], the use of this property in estimating the system's proximity to CHF remains unexplored.

Particularly, self-affine data exhibit long-range correlations in the sense that the autocorrelation function of self-affine data series decline as a power-law. The Hurst exponent, H, is a statistical measure that captures this decline. Previously, calculation of H has been used to predict and prevent the order/disorder transition in engineering systems. For example, in gas turbine combustors, at certain Reynolds numbers, the broadband

[5] Self-similarity is the particular case of self-affinity where $a = 1$.

noise of turbulent combustion may lock-in to the natural frequency of the duct, producing thermo-acoustic instabilities (at few distinct frequencies). This is detrimental to the operation of the combustor and results in frequent replacement of parts. At Reynolds numbers where the system is stable but is not far from this lock-in frequency, an intermittent pressure signal is produced. Using the Hurst exponent of pressure fluctuations as a precursor, Nair and Sujith [80] were able to detect and turn off an impending instability. The present study is an adaptation of that analysis to temperature fluctuations in pool boiling.

In Saini and Srinivasan (2021) [81] (see details in Chapter 6), it was demonstrated that local fluctuations of heat flux of discrete heaters in the Multi-heater Array Boiling Experiment (MABE, [82]) showed long-term correlations which could be described using the Hurst exponent. For each fixed wall temperature along the boiling curve, Hurst exponents were calculated for the measured temporally intermittent heat flux fluctuations, and it was shown that the behavior of the Hurst exponent was universal along the boiling curve, independent of system pressure or subcooling. This universal behavior resulted in values of H that were close to 1.0 at the onset of nucleation, decreasing along the boiling curve towards a value close to 0.5 at dry-out, before increasing again to larger values in the film boiling regime. More recently, analysis of the intermittent time series of bubble departures in Jukanti and Srinivasan (2024) [70] suggested that as the wall superheat is increased, bubble departure frequencies go from periodic to a more chaotic, nearly random, behavior. This is expected to have implications for the rise and fall of temperatures under the bubble, which may exhibit similar behavior of transition to more chaotic fluctuations as nucleation site density and accompanying bubble interactions increase.

Chapter 3

Experimental Facilities

3.1 Facility for Surface Pool Boiling Experiments

Figure 3.1 shows a schematic of the experimental facility used for surface pool boiling experiments. The boiling chamber was a hollow cuboid vessel made of polycarbonate and had a capacity of 350 mL. To heat and maintain the boiling fluid at its saturation temperature, three flexible film heaters were attached to the inside walls of the chamber. These heaters were 1-inch square film heaters which had nominal resistances of 78.4 Ω and were rated for a maximum DC voltage of 28 V. The three chamber heaters were connected in parallel and supplied by a DC Power Supply rated to supply a maximum voltage and current of 35 V and 1.4 A, respectively. When operating at its limit, the DC power supply was capable of dissipating 47 W through the flexible film heaters, which was sufficient to maintain the boiling liquids used in experiments at their saturation temperatures in the chamber. In addition to this, a reflux condenser was used to condense the vapors generated from the boiling liquid and form a closed flow loop. The condenser was supplied with water at 4 °C by an isothermal bath. A type-T thermocouple (designated "pool thermocouple" hereunto) was used to monitor

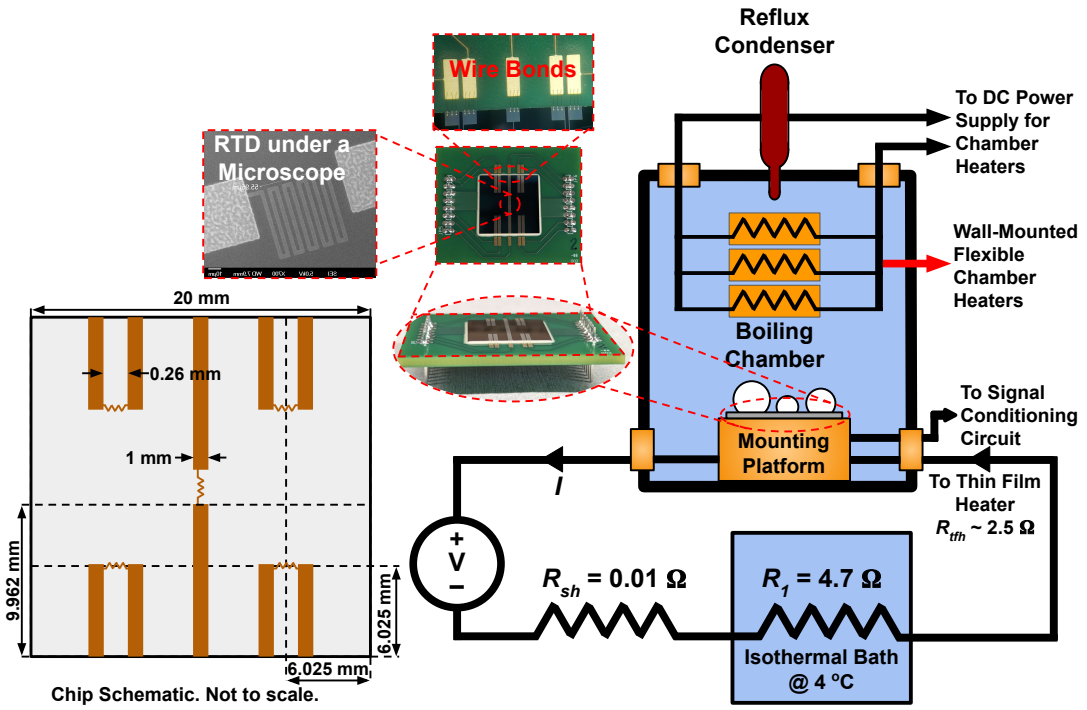

Figure 3.1: (Right) Schematic of the Surface Pool Boiling Experiment Facility. The insets show the boiling surface chip mounted on a PCB, wire bonds to make connections from the PCB to the chip, and an image of a central RTD (serpentine coil) under a Scanning Electron Microscope. (Left) The chip schematic (not to scale) shows the locations of the corner RTDs on the chip, the dimension of the chip, and the lengths and widths of the leads.

and measure the temperature of liquid in the chamber.

The boiling surfaces were fabricated using nano-fabrication processes in a clean-room using a 600 μm-thick sapphire wafer as the substrate (for details of the process, refer to Appendix C). Each surface was a square chip with a side of 2 cm diced out of a sapphire wafer at the end of the fabrication process. Platinum was deposited on the top side of the wafer in the form of serpentine coils to form thin-film Resistance Temperature Detectors (RTDs). One such RTD is shown in the leftmost inset of Figure 3.1. Five RTDs were deposited on every surface, one at the center and four at a distance of 6.025 mm from the corners, as shown in the chip schematic. The deposited platinum was

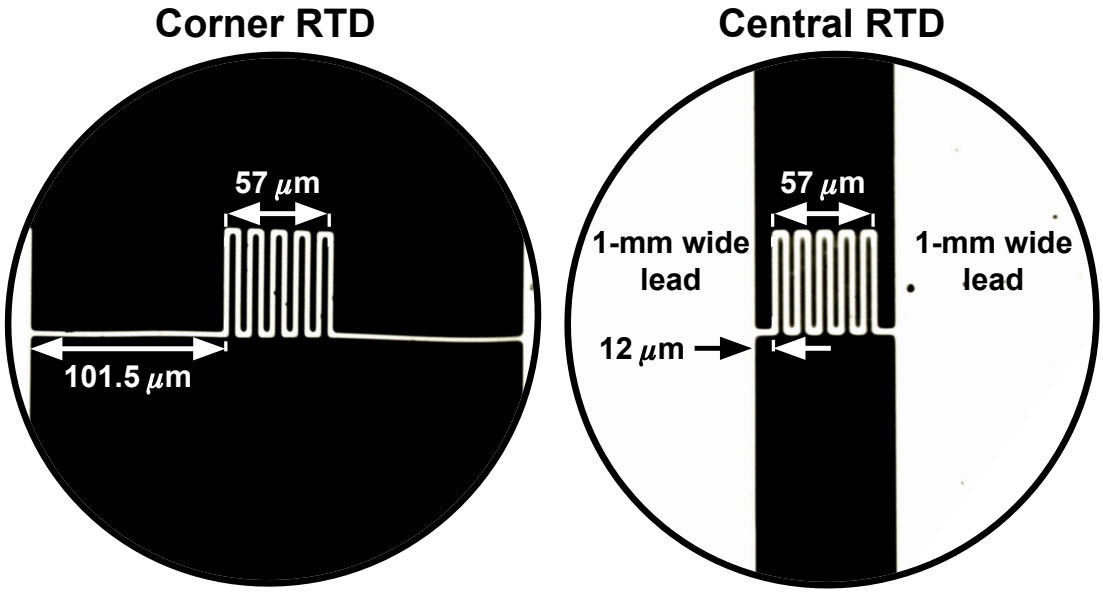

Figure 3.2: Corner and Central RTD under a microscope. The length of the trace between the serpentine coil and the 1-mm wide leads were larger for corner RTDs due to design constraints of the PCB.

75-nm thick. The serpentine coils of the RTD were 3 μm-wide and were spread over a square area of side 57 μm. The leads from the edge of the chip to the RTDs were 1 mm-wide to ensure that the leads contributed only a small fraction to the total resistance of the RTDs. As a result, the leads contributed 4.3% and 8.8% to the total resistance for the corner and central RTDs, respectively.

Figure 3.2 shows dark-field images of a corner and a central RTD under a microscope. Due to the two leads of corner RTDs running parallel to each other, they had to be placed farther apart due to constraints in the PCB design. This was not an issue with the central RTD as the leads terminated at opposite edges of the square chips. Therefore, the corner RTDs had longer traces connecting the serpentine coils to the leads. This resulted in the nominal resistances of the corner and central RTDs being 1.4 kΩ and 1.0 kΩ, respectively, despite the overall lead resistance being higher for the central RTDs.

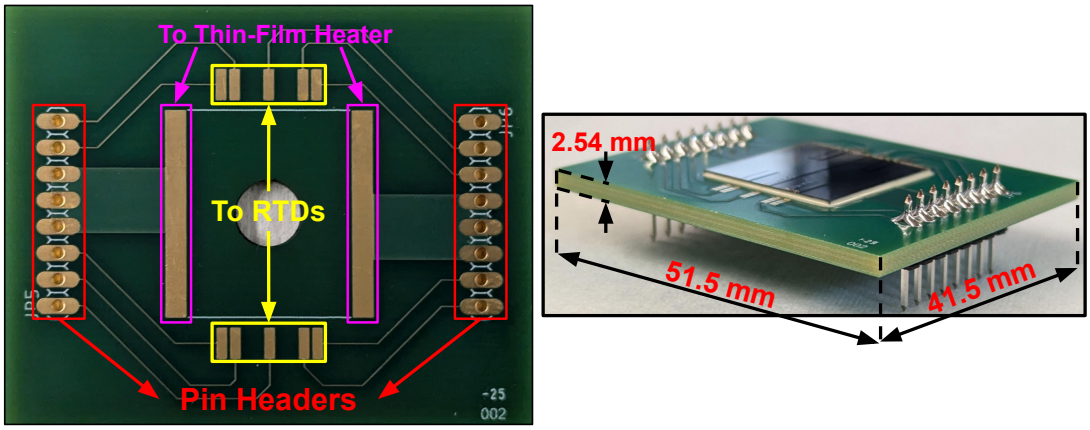

Figure 3.3: (Left) Printed Circuit Board (PCB) on which the chips were assembled. The two rows of bond pads were connected to the RTD leads using wire bonds. The long vertical bond pads were connected to the backside thin-film heater on the chip using an electrically conductive silver-filled epoxy. (Right) A chip assembled on a PCB along with pin headers to mount onto the boiling platform.

The square chips were assembled on Printed Circuit Boards (PCBs)[1] shown in Figure 3.3. The two rows of bond pads on the PCB (highlighted in yellow) were connected to the RTDs on the topside of the chip using wire bonds. A 75 nm thick platinum film was deposited on the backside of the chip to use as a resistance heater (hereafter referred to as the "thin-film heater"). The pair of long vertical bond pads (highlighted in pink) on the PCB were connected to the aforementioned thin-film heater using an electrically conductive silver-filled epoxy. Pin headers were soldered to the two vertical rows of connectors (highlighted in red) by means of which the electrical connections to the thin-film heater (to supply power for boiling) and the RTDs (to measure fluctuations) were made. The hole in the center of the PCB was provided to attach a thermocouple to the backside of the chip (hereafter designated the "backside thermocouple") using a thermally conductive epoxy[2]. After assembling the chip on PCB, an epoxy was used for "edge beading" along the periphery of chip on the top of the PCB, and along the

[1]The PCBs were made from a composite material of woven fibreglass and epoxy resin. The commercial name of the material is FR-4 and has a reported thermal conductivity of 0.29 - 0.35 W/m-K.

[2]The thermocouple was attached to the backside before every experiment, and not at the time of the chip assembly on PCB.

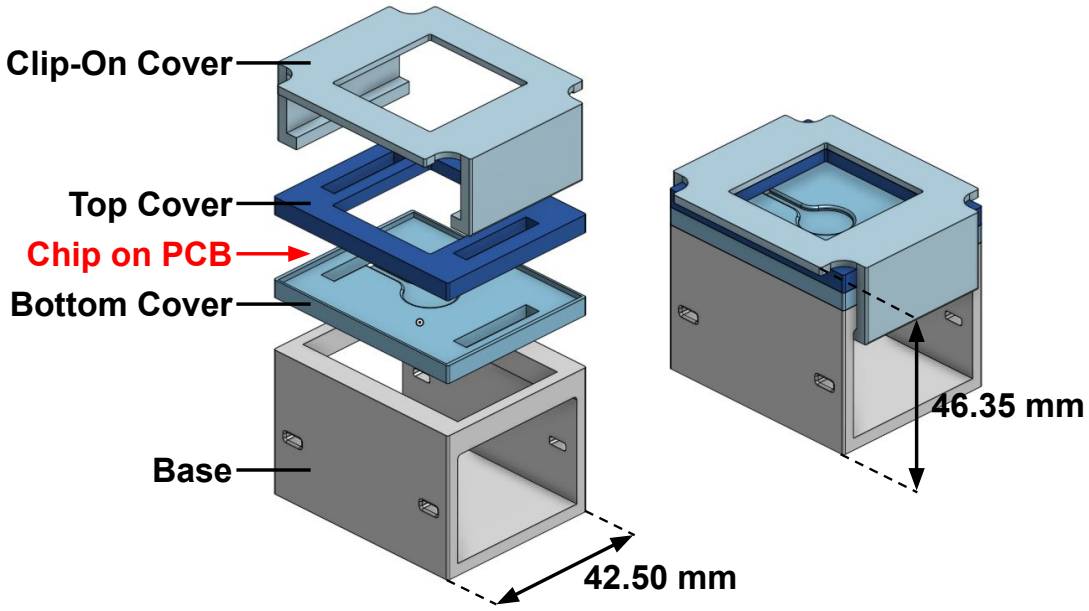

Figure 3.4: (Left) Blow-Up of the Boiling Platform. Space for the chip on PCB is shown in red. (Right) Assembled Boiling Platform without the chip on PCB.

periphery of the hole on the bottom of the PCB. This was done to ensure that during experiments, liquid did not seep into, and consequently boil in, the space between the bottom of the chip and the PCB.

CAD rendering of the mounting platform is shown in Figure 3.4. All parts of the platform were 3-D printed using Acrylonitrile Butadiene Styrene (ABS), a thermoplastic that has a maximum operating temperature of 105 °C and a thermal conductivity of 0.1 W/m-K. The chip on PCB was placed between the bottom and top covers, which had openings for the pin headers. The bottom cover had an indentation for the backside thermocouple to fit so that the bottom of the sample could sit flush on it. The space provided in the base was used to make electrical connections to the pin headers, and also hold counterweights made of stainless steel to ensure that platform did not float in the boiling fluid. The clip-on cover was used to hold all the parts of the boiling platform together.

3.1.1 Estimating Heat Losses from Boiling Platform

It was important that the power supplied to the thin-film heater was dissipated mostly through boiling on the top chip surface and heat loss due to conduction through the PCB or the boiling platform had to be minimized. Figure 3.4 (top) shows a schematic representation of the chip on PCB mounted on the boiling platform along with nominal thicknesses (not to scale) of the different materials. The heat generated at the bottom of the chip by the thin-film resistance (not shown) has two pathways. It is either conducted through the chip to the top surface and then dissipated to the fluid by boiling, or it may be conducted into the PCB through the thermal epoxy, from where it can be further dissipated through the PCB or parts of the boiling platform before eventually being dissipated into the fluid due to natural convection.

To estimate the power that is carried out through the second aforementioned path, a thermal resistance network (shown in Figure 3.5 (bottom)) may be used. The thermal resistance network represents the two pathways of heat transfer from the bottom of the chip at temperature T_1 to the fluid at temperature, T_∞. An implicit assumption of using a thermal resistance network is that conduction within the solids occurs in one direction only, which in the present case is assumed to be perpendicular to the chip surface. Although conduction within the chip, PCB, and the boiling platform is going to be three-dimensional, a one-dimensional model such as the thermal resistance network will over-estimate the heat transfer due to conduction, which is preferred for the purpose of heat loss calculations.

The thermal resistance associated with 1-D conduction through the various parts of the mounting platform was calculated as

$$R_{\text{cond}} = \frac{L}{kA}$$

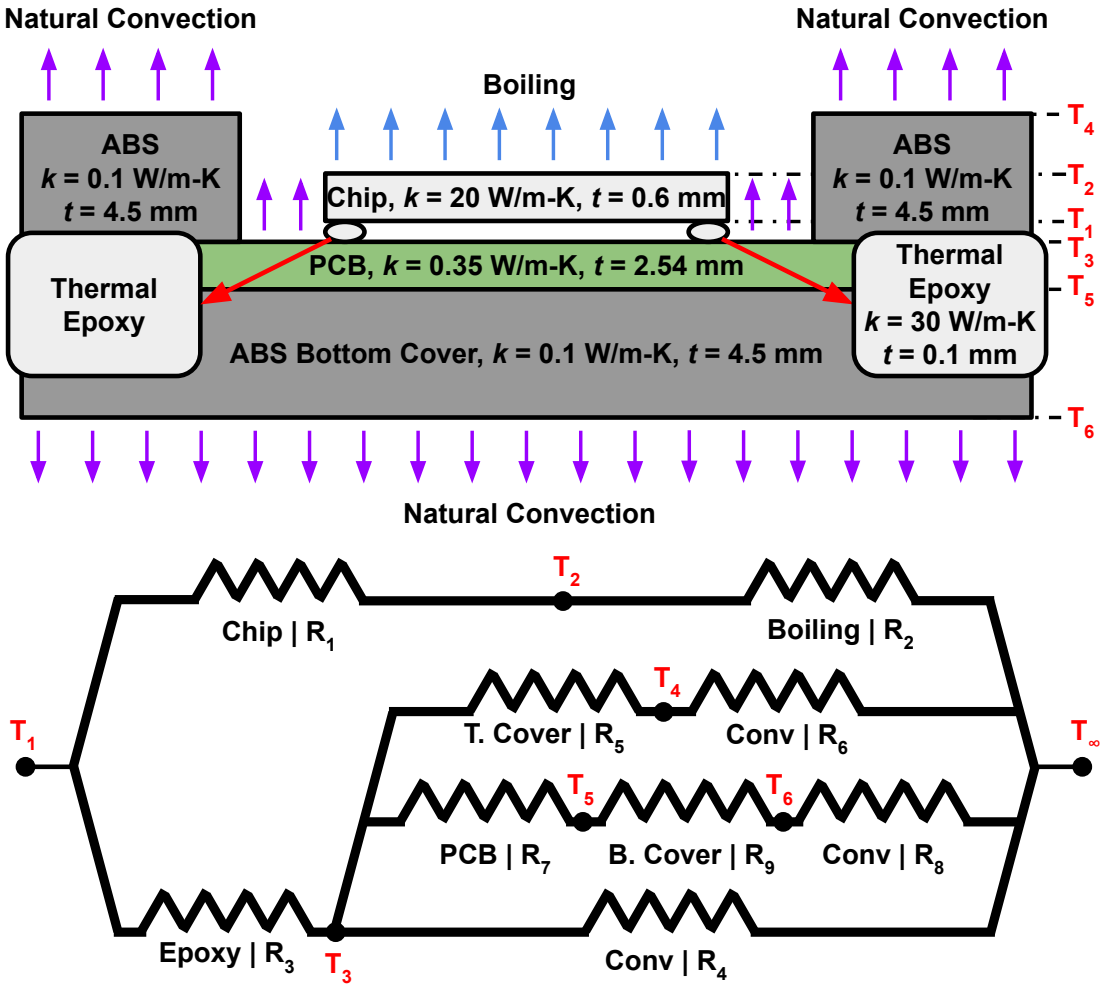

Figure 3.5: (Top) 1-D view of the Boiling Platform. (Bottom) Thermal Resistance Network used to estimate heat losses.

where L is the thickness of solid, k the thermal conductivity of the material, and A is the surface area perpendicular to the direction of heat transfer. Table 3.1 lists the values of L, k, and A used for the different parts of the mounting platform and the corresponding thermal resistance values.

In addition to the conductive thermal resistances, the thermal resistance associated with convection to the boiling liquid through the various parts of the mounting platform was

Part Description	Variable	Thickness (mm)	Thermal Conductivity (W/m-K)	Surface Area (m^2)	Thermal Resistance (K/W)
Chip	R_1	0.6	25	4×10^{-4}	0.06
Epoxy	R_3	0.1	30	8×10^{-5}	0.042
Top Cover	R_5	4.5	0.1	1.4×10^{-3}	32.92
PCB	R_7	2.54	0.35	1.2×10^{-3}	5.87
Bottom Cover	R_9	4.5	0.1	2.3×10^{-3}	19.85

Table 3.1: Conductive Thermal Resistance Calculations

calculated as

$$R_{\text{conv}} = \frac{1}{hA}$$

where h is the convective heat transfer coefficient. In addition to the boiling from the chip surface, there are three surfaces from which convective heat transfer occurs. The first surface is on the PCB along the perimeter of the chip (between the edge of the chip and the ABS top cover), the second surface is the ABS top cover, and the third surface is the ABS bottom cover. For all three surfaces, the convective heat transfer coefficient was determined using an appropriate Nusselt number correlation for natural convection from horizontal plates. The empirical correlation applied to the first two surfaces on the topside was for the upper surface of a hot plate from [83]:

$$\overline{\text{Nu}}_{L_c} = 0.54\text{Ra}_{L_c}^{1/4} \quad (10^4 \leq \text{Ra}_{L_c} \leq 10^7,\ \text{Pr} \geq 0.7)$$
$$\overline{\text{Nu}}_{L_c} = 0.15\,\text{Ra}_{L_c}^{1/3} \quad (10^7 \leq \text{Ra}_{L_c} \leq 10^{11},\ \text{all Pr})$$

For the final surface, the empirical correlation used was for lower surface of a hot plate from [84]:

$$\overline{\text{Nu}}_{L_c} = 0.52\ \text{Ra}_{L_c}^{1/5} \quad (10^4 \leq \text{Ra}_{L_c} \leq 10^9,\ \text{Pr} \geq 0.7)$$

In the correlations above, Ra_{L_c} is the Rayleigh number and was calculated as

$$\mathrm{Ra}_{L_c} = \frac{g\beta\big(T_s - T_\infty\big)L_c^3}{\alpha\nu}$$

where $g = 9.81$ m/s^2, is the acceleration due to gravity, L_c is the characteristic length scale, $\big(T_s - T_\infty\big)$ is the temperature difference between the surface and the surrounding fluid, and β, α and ν are the volumetric thermal expansion coefficient, thermal diffusivity and kinematic viscosity of the boiling fluid, respectively. A value of $\big(T_s - T_\infty\big) = 30$ K was used based on observations of maximum temperature difference from experiments carried out. L_c, the characteristic length scale for horizontal surfaces was calculated as $L_c = A_s/P$, where A_s and P were the surface area (one side) and perimeter of the surface, respectively. Note that the two topside surfaces did not have a central region. Therefore, the inner edge was also considered in the perimeter of the surfaces.

Table 3.2 lists the values of A_s, L_c, $\overline{\mathrm{Nu}}_{L_c}$ and h calculated for the three surfaces, and the corresponding thermal resistance values using thermo-physical properties of Novec 7000 [85]. Also listed in Table 3.2 is the heat transfer coefficient and the corresponding thermal resistance associated with boiling from the chip surface. These values were calculated using data from boiling experiments carried out in one of the boiling fluids, Novec 7000 [85].

Variable	Surface Area (m^2)	Characteristic Length (mm)	Nusselt Number	Heat Transfer Coefficient (W/m^2K)	Thermal Resistance (K/W)
R_2	–	–	–	4200	0.60
R_4	5.0×10^{-4}	2.5	15.96	478.91	4.18
R_6	13.7×10^{-4}	4.4	24.33	416.13	1.76
R_8	22.7×10^{-4}	118	19.84	125.82	3.51

Table 3.2: Convective Thermal Resistance Calculations. Refer to Figure 3.5 for context.

Having calculated the thermal resistances, the percentage of heat loss can be calculated by simplifying the thermal resistance circuit. The thermal resistance to heat transfer by boiling was calculated as $R_{\text{boil}} = R_1 + R_2$ while the thermal resistance to heat loss pathways was calculated as $R_{\text{loss}} = R_3 + \left\{1/R_4 + 1/(R_5 + R_6) + 1/(R_7 + R_8 + R_9)\right\}^{-1}$. Finally, the percentage of heat loss can be estimated as

$$\frac{q_{\text{loss}}}{q_{\text{tot}}} = \frac{R_{\text{tot}}}{R_{\text{loss}}} = \frac{\left\{1/R_{\text{boil}} + 1/R_{\text{loss}}\right\}^{-1}}{R_{\text{loss}}} = 0.164 \text{ or } 16.4\%$$

The majority of the heat loss occured due to convection from the PCB surface that was left uncovered by the ABS top cover. This was done to accommodate the wire bonds from the PCB to the chip and also allow for liquid resupply from beyond the edges of the chip since the chip surface was below the level of the top surface of the top cover. Nevertheless, it is worth mentioning again that these losses are estimated using a 1-D conduction model, which assumed one-dimensional temperature gradients and underestimated the thermal resistances to heat loss pathways, and thereby, overestimating the heat losses.

3.1.2 Electrical Circuit

As shown in Figure 3.1, the platinum thin-film heaters on the backside of the chips (R_{tfh}) were connected in series with a shunt resistor (R_{sh}) and an additional resistor (R_1). The thin-film heaters had a nominal resistance of 2 Ω at room temperature and were powered by a DC power supply that operated in constant voltage mode. The resistance of the thin-film heater fluctuated when boiling occurred on the surface as a result of temperature fluctuations across the surface. Adding the additional resistor (R_1) ensured that these resistance fluctuations (dR_{tfh}) were only a small percentage of the total load resistance ($R_{\text{load}} = R_1 + R_{\text{tfh}} + R_{\text{sh}}$) to the DC power supply. As a result of this, the fluctuations in the current, I, through the circuit, due to the DC power

supply operating in constant voltage mode and compensating for the fluctuations in the thin-film resistance, dR_{tfh}, were also smaller, and were given by

$$\frac{dI}{I} = -\frac{dR_{\text{tfh}}}{R_{\text{load}}}$$

These current fluctuations were measured to be less than 0.01% during the experiments.

The 4.7 Ω resistor was a power resistor packaged in a finned aluminum housing and capable of dissipating 300 W. It was immersed in a beaker filled with silicone oil, that was cooled by being placed in the isothermal bath circulating chilled water (at 4 °C) to the reflux condenser. The resistance of the additional resistor was monitored during the experiments and the change was less than 0.3% over the course of the experiments, indicating that the resistance was constant despite self-heating.

The shunt resistor was used to measure the current flowing through the circuit. It came packaged with an in-built fan and was rated for a maximum current of 20 A. It had a resistance of 9.979 $\times 10^{-3}$ Ω ± 0.087%.[3] At maximum currents measured during the experiment ($\sim$ 5.7 A), the self-heating of the shunt resistor was insignificant ($I^2 R_{\text{sh}} \sim 10^{-1}$ W) and therefore the resistance of the shunt resistor was assumed to stay constant.

The power supplied to the thin-film heater was given by $P = I^2 R_{\text{tfh}}$. Due to the fluctuations in both the resistance of the thin-film resistance and the current through the circuit, the fluctuations in the power dissipated by the thin-film heater could be estimated as

$$\begin{aligned} dP &= \frac{\partial P}{\partial I}\, dI + \frac{\partial P}{\partial R_{\text{tfh}}}\, dR_{\text{tfh}} \\ \Rightarrow dP &= 2 I R_{\text{tfh}}\, dI + I^2\, dR_{\text{tfh}} \end{aligned}$$

[3] uncertainty with a 95% confidence interval.

Plugging in $dI = -I(dR_{\text{tfh}}/R_{\text{load}})$, the equation above simplified to

$$\frac{dP}{P} = \left(1 - 2\frac{R_{\text{tfh}}}{R_{\text{load}}}\right)\frac{dR_{\text{tfh}}}{R_{\text{tfh}}}$$

Without the power resistor, $R_{\text{load}} \approx R_{\text{tfh}}$ and $dP/P \approx -dR_{\text{tfh}}/R_{\text{tfh}}$. Therefore, the addition of the power resistor also dampened the power fluctuations. The maximum power fluctuations were measured to be less than 0.3% during the experiments (see Section 3.1.5.1 for details of this calculation).

3.1.3 Signal Conditioning of RTD Signals

To estimate the resistance of RTDs, a test current was passed through them and the corresponding potential drop was measured at desired sampling speeds. The resistance could then be calculated using Ohm's law as $R_{\text{RTD}} = \Delta V_{\text{RTD}}/I_s$, where I_s is the test current. A test current of 100 μA generated by Texas Instruments REF200AU current source [86] was used for this purpose. This value of test current was chosen to ensure that self-heating of the RTDs was insignificant. For example, the nominal resistance of the RTDs was $\sim$ 1.5 kΩ. Therefore, a 100 μA test current resulted in generation of $I_s^2 R_{\text{RTD}} = 15$ μW of self-heating power, corresponding to a local heat flux of less than 0.5 W/cm^2. This heat flux was only 4.3% of the lowest observed CHF values of 11.69 W/cm^2. While a low value of the self-heating heat flux ensured that the test current did not contribute significantly to increasing the local surface temperature, it also ensured that the additional heat flux dissipation relative to surrounding locations during boiling resulted in nucleation at the location of the RTDs, as was observed visually boiling during experiments.

Figure 3.6 shows a 1-second segment of voltage fluctuations (sampled at 1 kHz for 60 seconds and rescaled to have unit power) taken from an RTD on a surface undergoing boiling, and the corresponding Power Spectral Density (PSD). As is evident, there were

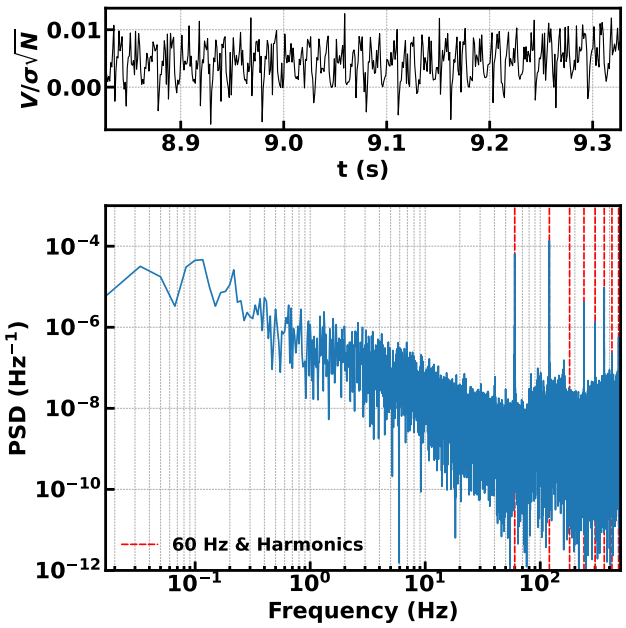

Figure 3.6: (Top) $\frac{1}{2}$-s segment of a rescaled RTD Signal from a surface undergoing boiling. (Bottom) Power Spectral Density (PSD) of the RTD Signal showing peaks at line noise and harmonics.

peaks that lined up exactly with 60 Hz and its harmonics (vertical lines shown in red) that suggested the presence of significant line noise and its harmonics. This noise was present despite care taken to reduce electromagnetic interference by shielding all wires, and using appropriate bypass capacitors for all DC power sources involved.

To filter out the noise, the voltage signal from the RTDs was fed into instrumentation amplifiers (in-amp). In-amps are differential amplifiers capable of rejecting common-mode signals that appear simultaneously and in-phase on differential signals. Ideally, a differential signal, such as a voltage drop across an RTD in the present case, that is measured is simply $\Delta V = V_+ - V_-$, where V_+ and V_- are the high and low potentials across the RTD. However, the actual differential signal measured by instruments is $\Delta V = A_\mathrm{d}\big(V_+ - V_-\big) + \frac{1}{2}A_\mathrm{cm}\big(V_+ + V_-\big)$, where A_d and A_cm are differential gain and common-mode gain, respectively. This implies that common mode signals are not

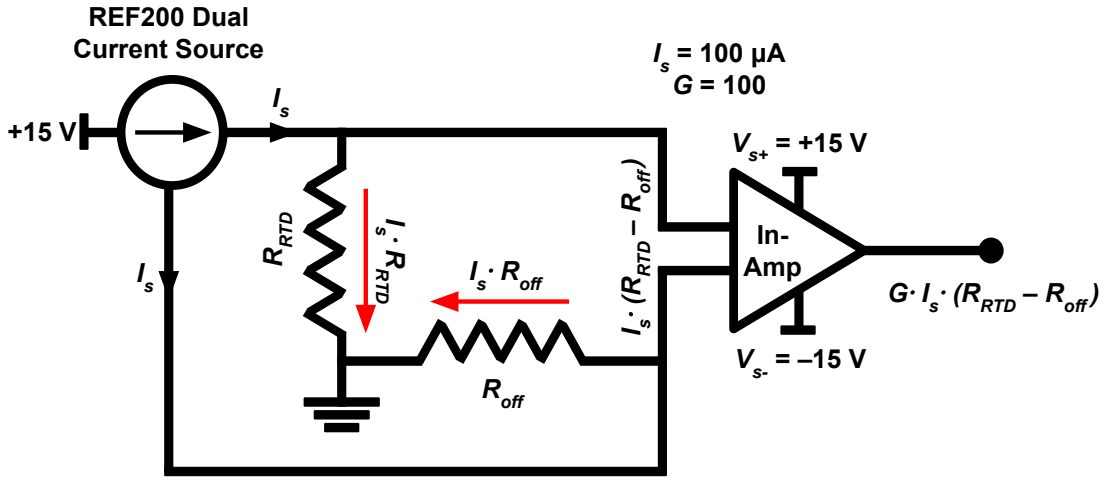

Figure 3.7: Using offset resistors to avoid saturating the instrumentation amplifier.

entirely rejected, and the requirement is that A_{d} is sufficiently larger than A_{cm}.

The ability of a device to reject common-mode noise is quantified by Common-Mode Rejection Ratio (CMRR), which is defined as CMRR (in dB) $= 20 \log_{10} \left(\left| A_{\mathrm{d}} / A_{\mathrm{cm}} \right| \right)$. The in-amp used was AD8221 by Analog Devices, a gain ($G = V_{\mathrm{out}}/V_{\mathrm{in}}$) programmable in-amp whose CMRR depended on the set value of G. It had a CMRR of 120 dB and 80 dB at G=100 and G=1, respectively. Therefore, the gain was set to 100 to achieve the higher CMRR.

A $G = 100$ meant that care had to be taken to ensure that the output from the amplifier did not saturate since the maximum/minimum output of the amplifier was limited by the voltage ($\pm V_s$) supplied to the power supply pins. For instance, for $V_s = \pm 15$ V that the in-amp was operated at, the output was limited to $-15 \text{ V} \leq V_{\mathrm{out}} \leq 15$ V, and therefore, the input to the in-amp was limited to $-0.15 \text{ V} \leq V_{\mathrm{in}} \left(= V_{\mathrm{out}}/G \right) \leq 0.15$ V.

Since the nominal resistances of the corner and central RTDs at room temperature were 1.4 and 1.0 kΩ, respectively, and the test current used was 100 µA, the nominal potential drops across the RTDs were 0.14 V and 0.10 V, respectively. These were

too close to the upper limit of 0.15 V on V_{in}. Therefore, offset resistors were used as shown in Figure 3.7 to reduce the potential drops across the RTDs before being fed to the input of the in-amps. The resistance of the offset resistors[4] was assumed to stay constant because the powers dissipated were of the order of 10 μW and self-heating was negligible. A single REF200, a dual-current source, was used to provide both test currents for a single RTD-offset resistor pair. As a result of this arrangement, V_{in} and V_{out} were given by

$$V_{\text{in}} = I_s\big(R_{\text{RTD}} - R_{\text{off}}\big) \tag{3.1}$$

$$V_{\text{out}} = G\, I_s\big(R_{\text{RTD}} - R_{\text{off}}\big) \tag{3.2}$$

where $G = 100$, $I_s = 100$ μA, and R_{RTD} and R_{off} were the resistances of the RTDs and offset resistors, respectively. At room temperature, the input to and the output from the in-amps was close to 0 V and as a result, the in-amps never saturated even when the resistance of the RTDs increased during the experiments.

Figure 3.8 demonstrates the effect of using the in-amp. The voltage fluctuations from an RTD on a surface undergoing similar boiling conditions to that of Figure 3.6 was fed to the in-amp. As is evident from the PSD, the peaks corresponding to line harmonics were significantly attenuated, by about two orders-of-magnitude, resulting in the fluctuations which started to resemble a sawtooth wave.

3.1.4 Calibration of the RTDs

Before being used in an experiment, the RTDs on every surface were calibrated in an isothermal bath filled with De-Ionised (DI) water. Starting from room temperature ($\sim$ 22 °C), the isothermal bath was set to successively higher reference temperatures of 30, 38, 46, 54, 60, and 68 °C and the corresponding potential drop across the RTDs

[4]The offset resistors used had resistance values of 1.4 kΩ and 1.0 kΩ for the corner and central RTDs, respectively.

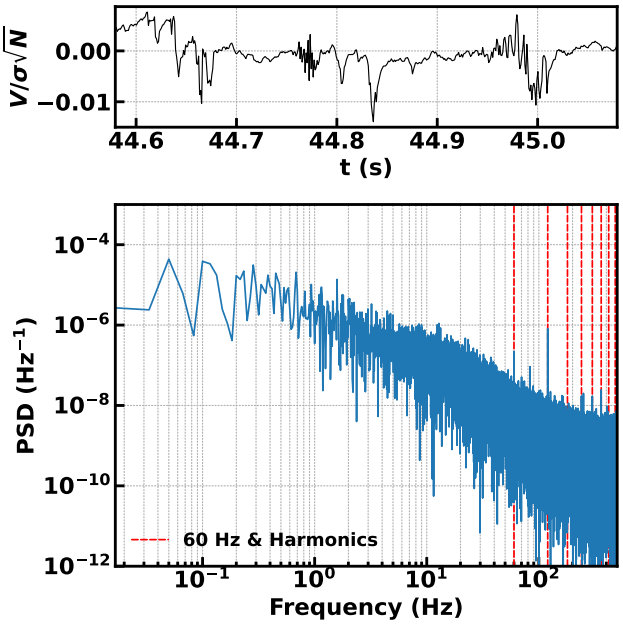

Figure 3.8: An RTD Signal from a surface undergoing boiling was fed into an In-Amp. (Top) A $\frac{1}{2}$-s segment of an RTD Signal rescaled to have unit power, and (Bottom) PSD showing that the peaks corresponding to line noise and harmonics were attenuated by about two orders of magnitude.

measured. This way, a total of 7 data points were obtained to get a calibration curve.

At every set temperature, sufficient time was given for the isothermal bath and RTDs to reach steady state before measurements were taken. A type-T thermocouple was placed in the isothermal bath to measure the pool temperatures where were used as the reference temperatures. Once steady state was reached, voltage measurements from the two (pool and backside) thermocouples and every working RTD were taken sequentially. This sequential measurement was repeated 100 times, for a maximum number of 700 measurements when all 5 RTDs on a surface were working at each reference temperature, and was done over a period of roughly 3 minutes. Additionally, the measurements were taken at the highest accuracy configuration of the digital multimeter (which included the

maximum permissible integration time[5] and the maximum settling time[6] when switching measurement channels) for every measurement.

3.1.4.1 Data Reduction and Uncertainty Analysis

The sample size of measurements from every sensor taken during calibration was $N = 100$. The sample mean was used to represent the true value of the measurement from the sensor and the sample standard deviation was used to calculate the measurement uncertainty with 95% confidence as

$$U_{95\%} = t_{95\%,N-1}\frac{s}{\sqrt{N}} \tag{3.3}$$

where s was the sample standard deviation, $N = 100$ was the sample size, and $t_{95\%,N-1} = 1.984$ was the two-sided value for student's t distribution for 95% confident with $N-1 = 99$ degrees of freedom.

The sample means and standard deviations of the measured EMFs from the pool and backside thermocouples were converted into temperature values and their corresponding uncertainty using the type-T thermocouple calibration curve (see Appendix B for details). The pool thermocouple measurements were taken as a sanity check to ensure that the backside thermocouple measured close to the same temperature as the pool thermocouple, and the differences in the temperatures were checked for statistical significance. Only measurements from the backside thermocouple were taken as the reference temperatures for the RTD calibration curves.

The voltage measurements from the RTDs were first converted into the corresponding

[5]The maximum integration time setting available on the digital multimeter was $\frac{1}{12}$ s or averaging over 5 power line cycles.

[6]The settling time was how long the digital multimeter waited to start taking a measurement after a new channel was connected to.

resistances using Equation (3.2) as

$$R_{\text{RTD}} = \frac{V_{\text{out}}}{G\, I_s} + R_{\text{off}} \tag{3.4}$$

where the sample mean of the voltage measurements was taken as V_{out}, $G = 100$, $I_s = 100$ μA, and R_{off} was the value of the offset resistor used. The offset resistances were measured beforehand and the corresponding uncertainty with 95% confidence estimated using Equation (3.3). The uncertainty in the values of the offset resistors and the potential drop across RTDs were propagated using Equation (3.4) to estimate the uncertainty in the RTD resistance as

$$U_{R_{\text{RTD}}} = \sqrt{\left(\frac{U_{V_{\text{out}}}}{G\, I_s}\right)^2 + \left(U_{R_{\text{off}}}\right)^2} \tag{3.5}$$

The uncertainty in the RTD resistances (R_{RTD}) calculated this way were of the order of 0.1%, and hence considered negligible.

Figure 3.9a shows the resistance values as a function of temperature from a representative calibration run[7] for all 5 RTDs. As is evident, the resistance values for all RTDs varied significantly at room temperature. This was due to the non-uniform deposition of platinum across the surface during the micro-fabrication process of the RTDs (see Appendix C for details). However, the values increased linearly with temperature as expected.

Since the RTDs had different resistance values, the RTDs were designated colors (as names) to distinguish them from each other. The 4 corner RTDs were designated the colors yellow, blue, grey and red while the central RTD was designated green. In

[7]These calibration curves are for a Parylene-C coated chip used in a boiling experiment with Novec-7100.

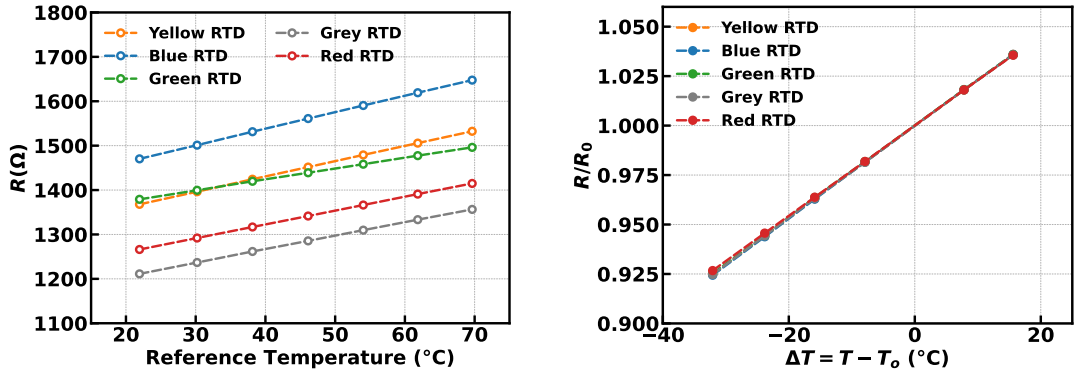

(a) Resistance as a function of temperature for RTDs.

(b) Non-dimensional resistance as a function of temperature change.

Figure 3.9: Representative calibration curves. (a) Resistance as a function of temperature for RTDs. (b) Calibration curve replotted using Equation (3.6) with $T_0 = 54$ °C. The slope of the curve represents the linear temperature coefficient of resistivity (TCR) of platinum.

all figures that follow, curves for the different RTDs will be plotted using the color designated to them, wherever applicable.

In Figure 3.9a, note that the slope of the green central RTD is visibly different from the slope of the other RTDs. This is due to the different traces of the serpentine coil and the leads as was shown in Figure 3.2. Since the RTDs are made of platinum, the calibration curves were made to collapse on one another by first writing the resistance of a platinum resistor using the linearized form of Callendar-Van Dusen equation as[8]

$$R_{\text{RTD}} = R_0\Big(1 + \alpha \cdot \big(T - T_0\big)\Big)$$

where α is the linear temperature coefficient of resistivity (TCR) and R_0 is a reference value of the RTD at some reference temperature, T_0. The above equation was then

[8]The Callendar-Van Duses equation for $0°\text{C} \leq T \leq 661°\text{C}$ is $R = R_0\Big(1 + \alpha\big(T - T_0\big) + \beta\big(T - T_0\big)^2\Big)$. For small temperature ranges however, $\beta = 0$ may be assumed.

rearranged to non-dimensionalize the resistance as

$$\frac{R_{\mathrm{RTD}}}{R_0} = 1 + \alpha \cdot \left(T - T_0\right) \tag{3.6}$$

Since α is a material property of platinum, all calibration curves collapsed onto a single curve as shown in Figure 3.9b, which was plotted by using the resistance values of the RTDs at $T_0 = 54$ °C as R_0.

The uncertainty in the non-dimensional resistances were calculated by propagating the uncertainty in the offset resistors and the RTD resistance used as the reference value using Equation (3.6) as

$$U_{\left(R_{\mathrm{RTD}}/R_0\right)} = \sqrt{\left(\frac{U_{R_{\mathrm{RTD}}}}{R_0}\right)^2 + \left(\frac{R_{\mathrm{RTD}}}{R_0^2}\, U_{R_0}\right)^2} \tag{3.7}$$

where R_0 and U_{R_0} were the RTD resistance at the chosen reference temperature T_0 and the corresponding uncertainty, respectively. The uncertainties in the non-dimensional resistances (R_{RTD}/R_0) calculated this way were of the order of 0.1%, and hence considered negligible.

Equation (3.6) was used to estimate the value of TCR by performing a linear regression on the transformed calibration data points (Figure 3.9b). Note that using one of the calibration data points as the reference values (T_0 and R_0) meant the loss of one calibration data point since the linear fits had to pass through the transformed data point ($\Delta T = 0$ °C and $R_{\mathrm{RTD}}/R_0 = 1$). Therefore, the value of TCR was estimated as the slope of the best linear fit with a y-intercept of 1 and passing through the remaining calibration data points using the method of least squares.

Figure 3.10 shows representative TCR values of RTDs from calibration of three different

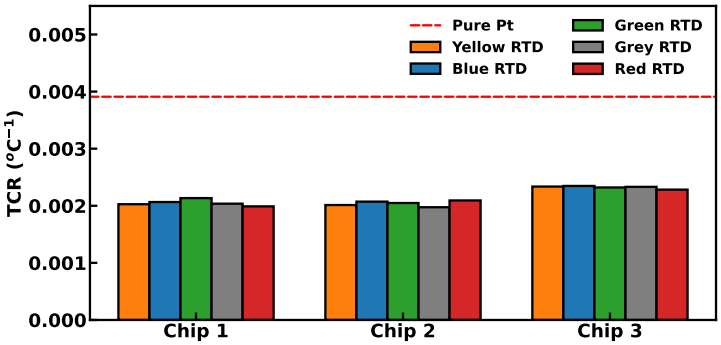

Figure 3.10: Variation of TCR values across RTDs and chips.

chips and the reported TCR value of pure platinum, $\alpha = 3.92 \times 10^{-3}$ °C^{-1}. The large deviation from the reported TCR of pure platinum can be attributed to two factors. First, the reported TCR was defined using the resistance values at 0 °C and 100 °C, in contrast to the present study in which TCR was calculated with $T_0 = 54$ °C and by using a linear fit to 6 data points using the method of least squares. Second, the thickness of the deposited platinum film (75 nm) and the annealing time during the micro-fabrication surface (see details in Appendix C) also contributed to the value of TCR. TCR values as low as 2.8×10^{-3} °C^{-1} for 100 nm-thick platinum RTDs have been reported [87].

It should also be noted that the variation in TCR values across the RTDs on the same chip was small, while the variation was larger across RTDs on different chips. This was attributed to the variation in the platinum deposition thickness across different wafers. As will be noted in Appendix C, chips were diced from sapphire wafers. RTDs on chips from different wafers were likely to have larger variation in the deposition thickness of the platinum film (and hence TCR values) than RTDs from the same chip. The three chips represented in Figure 3.10 were in fact diced from three separate wafers.

To calculate the uncertainty in the estimated value of TCR, the standard error of the

slope, s_m, derived from the method of least squares, was used as

$$U_{\alpha,95\%} = t_{95\%,\nu-2}\, s_m$$

where $\nu = 7$ was the number of calibration data points, and $t_{95\%,\nu-2} = 2.571$ was the two-sided value for student's t distribution for 95% confident with $\nu - 2 = 5$ degrees of freedom. The loss of two degrees of freedom was due to using one of the calibration data points for the reference values, and using the remaining points to estimate the slope. The uncertainties in the estimate of TCR values calculated this way were of the order of 1%.

Once the values of R_0, T_0, and α were known after calibration, future voltage measurements from the RTDs were converted into temperatures as

$$\begin{aligned} R_{\text{RTD}} &= \frac{V_{\text{out}}}{G\, I_s} + R_{\text{off}} \\ T &= T_0 + \frac{1}{\alpha}\left(\frac{R_{\text{RTD}}}{R_0} - 1\right) \end{aligned} \tag{3.8}$$

And the associated uncertainty in the values of T_0, R_0, R_{RTD}, and α were propagated using Equation (3.8) to estimate the uncertainty in temperature as

$$U_T = \sqrt{\left(U_{T_0}\right)^2 + \left\{\frac{1}{\alpha^2}\left(\frac{R_{\text{RTD}}}{R_0} - 1\right)U_\alpha\right\}^2 + \left(\frac{R_{\text{RTD}}}{\alpha R_0^2}U_{R_0}\right)^2 + \left(\frac{1}{\alpha R_0}U_{R_{\text{RTD}}}\right)^2} \tag{3.9}$$

3.1.5 Experimental Procedure

After calibrating the RTDs on a chip in the isothermal bath filled with DI water, the chips were cleaned in a two-step process to remove any surface contaminants that might have been picked up during the calibration process. First, the chips were washed with

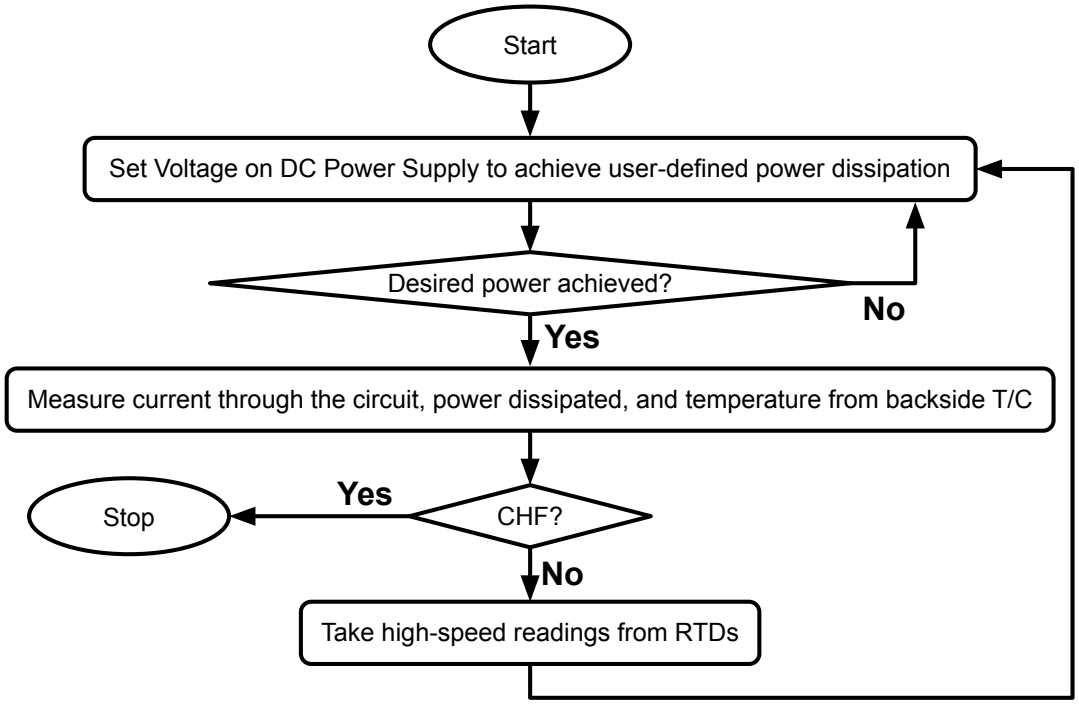

Figure 3.11: Process Flow of Surface Boiling Experiments.

acetone, isopropyl alcohol, and DI water (in that order) and blow-dried using nitrogen. Then, the chips were further cleaned using oxygen plasma in a chamber for 30 minutes. Finally, they were mounted on the boiling platform in the chamber for the boiling experiment, and the chamber was filled with the boiling fluid.

To bring the boiling fluid up to saturation temperature and degas the chamber, the chamber heaters were turned on for two hours. During this time, power was also supplied to the thin film heater on the backside of the chip to dissipate 0.5 W/cm^2 of heat flux and degas the boiling surface, removing any trapped air.

After degassing the chamber for two hours, experiments were started. Figure 3.11 outlines the process flow of the experiment. The power dissipated by the chip surface was increased in steps by increasing the voltage output from the DC Power Supply

powering the thin-film heater. The voltage output was varied until the desired power was achieved (See Section 3.1.5.2 for details). Once the desired power was achieved, high-accuracy, slow-speed measurements (at a sampling rate of 12 Hz) were taken to calculate the current through the circuit, the power dissipated by the chip and the temperature measured by the backside thermocouple. If CHF was detected from any of the measurements, the experiment was stopped[9]. Otherwise, high-speed measurements were taken from working RTDs next. 60,000 readings were taken (at a sampling rate of 1 kHz for 1 minute) from each RTD before moving onto the next. After measurements were taken from all working RTDs, the power to the thin-film heater was increased again, and the entire process repeated until CHF occurred.

3.1.5.1 Calculating Power Dissipation

To calculate the power dissipated by the thin-film heater, voltage drop measurements were taken as shown in Figure 3.12. In addition to these three potential drop measurements, the EMFs from the pool and backside thermocouple were also recorded. These measurements were repeated sequentially 100 times for a total of 500 measurements at the highest accuracy setting of the digital multimeter. Therefore, the sample size of measurements was $N = 100$, and the sample mean was assumed to be the true value of measurement. The sample standard deviation was used to calculated the associated uncertainty using Equation (3.3).

The sample means and standard deviations of the measured EMFs from the pool and backside thermocouples were converted into temperature values and their corresponding uncertainty using the type-T thermocouple calibration curve (see Appendix B for details). The pool thermocouple measurements were used to confirm that the boiling fluid was maintained at saturation temperature, T_{sat}. The temperature measured by

[9]Most of the times, this was detected when the current dropped to zero as the chip surface cracked when CHF occurred. Rarely, the chip surface did not crack and the temperature measured by the backside thermocouple increased drastically.

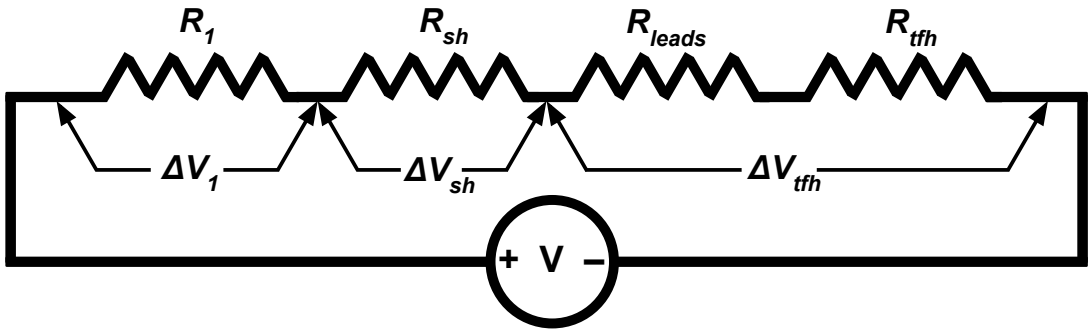

Figure 3.12: Potential drop measurements taken to measure the power dissipated by the thin-film heater. R_{leads} was the resistance of the leads used to connect the thin-film heaters on the backside of the chips to the rest of the circuit. R_1 and R_{sh} were the additional and shunt resistors, respectively.

the backside thermocouple was only used as a marker to detect CHF, and was not used as an accurate measurement of the surface temperature, T_{w}. Instead, the surface temperature was estimated from the average of the RTD measurements converted into temperatures (see Section 3.1.5.3 for details). Then, the excess temperature of the surface was calculated as

$$\Delta T_{\text{w}} = T_{\text{w}} - T_{\text{sat}}$$

The current flowing through the circuit was measured using the potential drop across the shunt resistor as

$$I = \frac{\Delta V_{\text{sh}}}{R_{\text{sh}}}$$

where $R_{\text{sh}} = 9.979 \times 10^{-3}\ \Omega \pm 0.087\%$ within a 95% confidence interval. The uncertainty in the current was estimated by propagating the uncertainty in the voltage measurement

and the shunt resistance as

$$U_I = \sqrt{\left(\frac{U_{\Delta V_{\mathrm{sh}}}}{R_{\mathrm{sh}}}\right)^2 + \left(\frac{\Delta V_{\mathrm{sh}}}{R_{\mathrm{sh}}^2} U_{R_{\mathrm{sh}}}\right)^2}$$

The uncertainty in the current measurement was also taken as a measure of the fluctuations in the current through the circuit and was of the order of 0.01% as noted earlier. The thin-film heater resistance was then calculated as

$$R_{\mathrm{tfh}} = \frac{\Delta V_{\mathrm{tfh}}}{I} - R_{\mathrm{leads}}$$

where R_{leads} was the resistance of the leads used to connect the thin-film heaters to the rest of the circuit. It was important to consider R_{leads} because only the potential drop across $R_{\mathrm{leads}} + R_{\mathrm{tfh}}$ could be measured due to the construction of the setup, and R_{leads} was measured to be 0.202 $\Omega \pm 0.16\%$, which was $\sim 10\%$ of the nominal value of $R_{\mathrm{tfh}} = 2\ \Omega$ at room temperature. The associated uncertainty in R_{tfh} was calculated by propagating the uncertainty in ΔV_{tfh}, I, and R_{leads} as

$$U_{R_{\mathrm{tfh}}} = \sqrt{\left(\frac{U_{\Delta V_{\mathrm{tfh}}}}{I}\right)^2 + \left(\frac{\Delta V_{\mathrm{tfh}}}{I^2} U_I\right)^2 + \left(U_{R_{\mathrm{leads}}}\right)^2}$$

The power dissipated by the chip was calculated as

$$P_{\mathrm{tfh}} = I^2\, R_{\mathrm{tfh}}$$

6And the associated uncertainty was calculated by propagating the uncertainty in the current and the thin-film heater ressitance as

$$U_{P_{\mathrm{tfh}}} = \sqrt{\left(2 I R_{\mathrm{tfh}} U_I\right)^2 + \left(I^2\, U_{R_{\mathrm{tfh}}}\right)^2}$$

The uncertainty in the power was also taken as a measure of the fluctuations in the power dissipated by the wire and was less than 0.3% as noted earlier. Finally, the heat flux was calculated as $q'' = P_{\text{tfh}}/A$ and the associated uncertainty was

$$U_{q''} = \frac{U_{P_{\text{tfh}}}}{A}$$

where $A = 4$ cm^2 was the surface area of the chip.

The potential drop across the additional resistor was also measured and used to monitor the resistance of the additional resistor as $R_1 = \Delta V_1/I$. As noted in Section 3.1.2, R_1 was a power resistor packaged in a finned aluminum housing and was immersed in a beaker filled with silicone oil. The beaker was cooled by being placed in a isothermal bath that maintained water at 4 °C. As a result, the change in R_1 was found to be of the order of 0.1 % from the start to the end of experiments.

3.1.5.2 Stepping up power

The power for the thin film heater was sourced from a DC power supply that was operated to provide a constant (user-defined) set voltage. However, it was desired to achieve set values of power (or heat flux) dissipation. Therefore, the set voltage had to be calculated from the desired power. Since the thin-film heater was connected in series with the additional resistor (R_1) and the shunt resistor (R_{sh}) as shown in Figure 3.12, the relationship between the set voltage (V_{set}) and the required potential drop ($\Delta V_{\text{tfh,set}}$) across the thin-film heater to achieve the required power dissipation (P_{set}) was calculated as

$$\Delta V_{\text{tfh,set}} = \sqrt{P_{\text{set}}\, R_{\text{tfh}}} \tag{3.10}$$

$$V_{\text{set}} = \Delta V_{\text{tfh,set}}\, \frac{R_{\text{tot}}}{R_{\text{tfh}}} \tag{3.11}$$

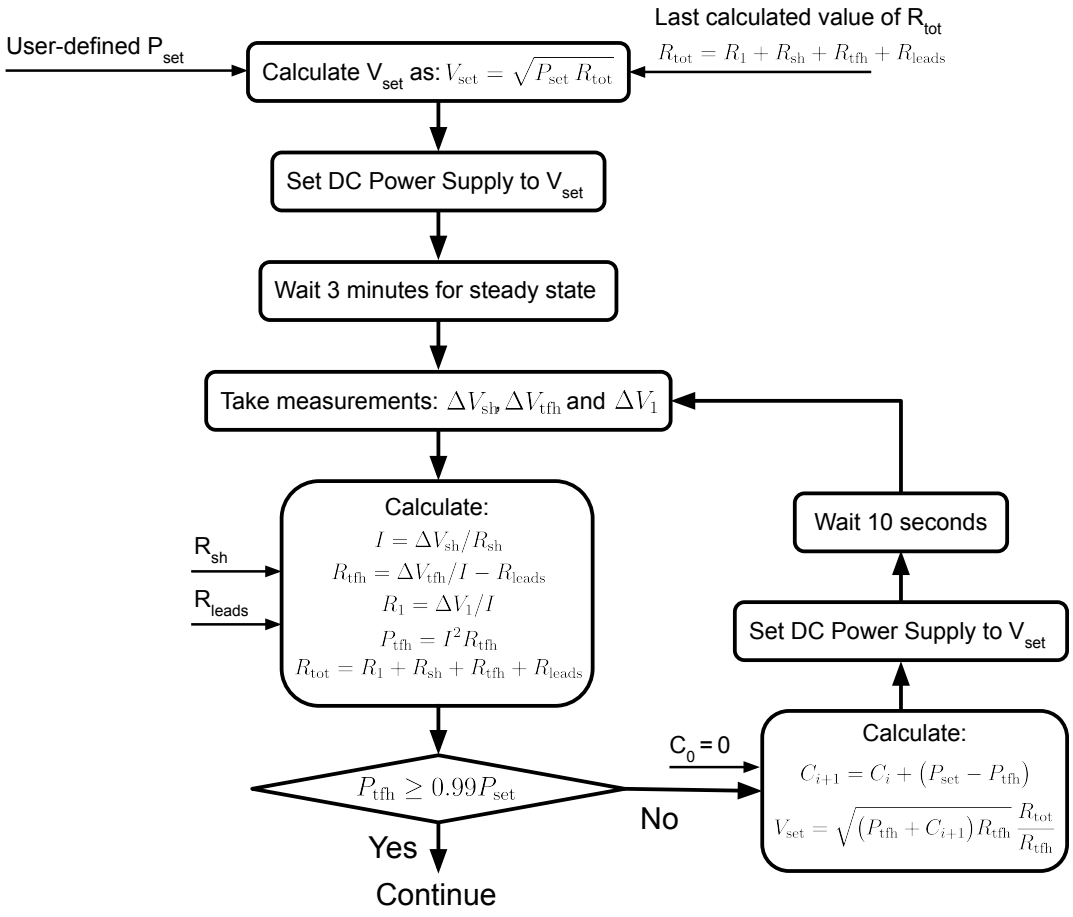

Figure 3.13: Process flow to change $V_{\rm set}$ until desired power was achieved.

where $R_{\rm tot} = R_1 + R_{\rm sh} + R_{\rm leads} + R_{\rm tfh}$ was the total resistance to the DC power supply.

Since the thin-film heater was made of platinum, its resistance increased as the chip surface heated up. This increasing resistance of the thin-film heater had to be compensated for when calculating $V_{\rm set}$. Figure 3.13 shows the process followed to step up the power supplied to the chip surface and compensate for the increasing resistance of the thin-film heater. After setting the first calculated voltage $V_{\rm set}$ on the power supply, the system idled for 3 minutes to allow the chip surface to reach steady state. During this waiting time however, voltage measurements from the RTDs that were taken at the previous

voltage setting were transferred from the memory buffer of the digital multimeter to the computer. This data transfer took about 1.5 minutes when all RTDs were working and 300,000 readings (= 60,000 readings/RTD × 5 RTDs) had to be transferred.

After the waiting time, measurements of ΔV_1, ΔV_{sh}, ΔV_{tfh} and the backside thermocouple EMF were taken sequentially and repeated 40 times for a total of 160 measurements over a period of 20 seconds. The sample means were taken as the true value of the measurements. The current through the circuit and the power dissipated by the chip surface were calculated as explained in Section 3.1.5.1. Measurements from the backside thermocouple were taken to detect a drastic increase in temperature due to CHF, in which case the experiment was ended. The experiment was also ended if the calculated current through the circuit dropped to 0 Amps, indicating a cracked chip surface.

If however, the calculated power dissipation was greater than 99% of the desired power, P_{set}, the experiment proceeded to the next step. Otherwise, a correction factor, C_i was calculated based on the calculated and desired power as

$$C_{i+1} = C_i + \left(P_{\mathrm{set}} - P_{\mathrm{tfh}}\right) \quad \text{where } C_0 = 0$$

Then, the next value of V_{set} was calculated as

$$V_{\mathrm{set}} = \sqrt{\left(P_{\mathrm{tfh}} + C_{i+1}\right) R_{\mathrm{tfh}}}\, \frac{R_{\mathrm{tot}}}{R_{\mathrm{tfh}}}$$

Since the thin-film heater resistance monotonically increased with the power dissipated, the first calculated value of V_{set} always resulted in a $P_{\mathrm{tfh}} < P_{\mathrm{set}}$, and subsequent corrections to V_{set} resulted in P_{tfh} approaching P_{set} from lower values. Once the desired power was achieved, the correction factor was reset to 0 and the experiment proceeded to high-speed measurements of RTDs.

3.1.5.3 High Speed Measurements

High-speed measurements from the RTDs were taken at 1 kHz for 1 minute one RTD at a time, i.e. 60,000 measurements were taken from a single RTD before moving onto the next one. Sequentially repeating a single measurement from every RTD 60,000 times was not possible because the minimum settling time associated with switching measurement channels during multiplexing was too high to achieve a sampling rate of 1 kHz.

The high-speed measurements were temporarily stored in the buffer memory of the digital multimeter. The buffer memory had a capacity for 450,000 measurements, with additional measurements overwriting the stored measurements. Therefore, at every power level, the measurements were transferred to permanent memory after measurements from all working RTDs were taken and the DC power supply was set to the first voltage setting for the next desired power. This was done during the 3 minutes long waiting time allowed for the thin-film heater to reach steady state. On average, 300,000 readings took about 1.5 minutes to be transferred from the buffer memory.

3.1.6 Digital Filtering and Post-Processing

As noted in Section 3.1.3, the power spectral density of the voltage measurements showed that line noise and its harmonics were attenuated by up to two orders of magnitude due to using the in-amps to reject common mode noise. Despite this, the peaks corresponding to line noise and its harmonics still existed. These were entirely removed in post-processing by a digital filtering process outlined below.

In the digital filtering process, 1 Hz windows about 60 Hz and harmonics were scanned for a local peak in the power spectra. Two such windows around 60 Hz and 120 Hz are shown in Figure 3.14 for the RTD Signal used in Figure 3.8. A Gaussian fit $\left(c \cdot e^{-ax^2} + b\right)$ was then applied to the power spectra (orange dashed line) using the method of least

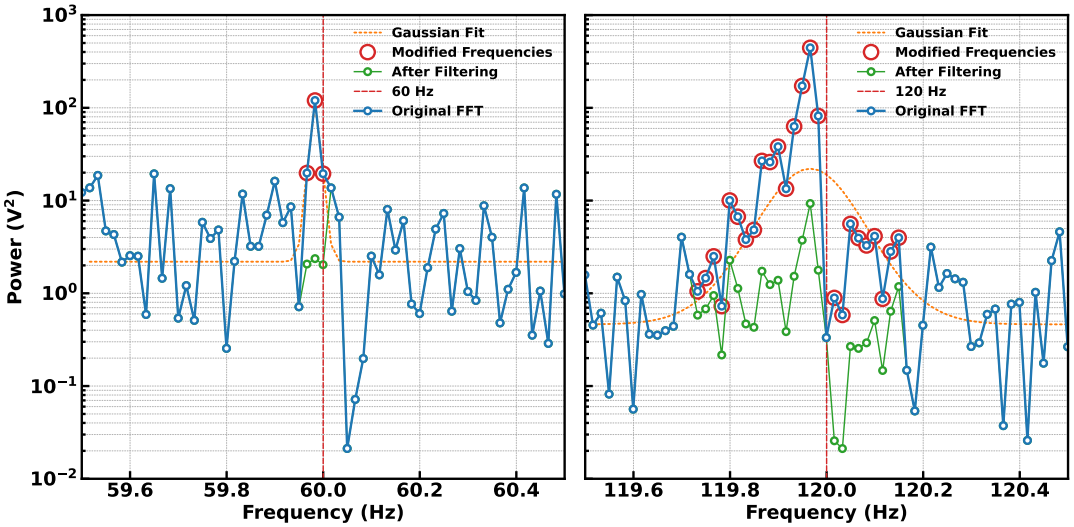

Figure 3.14: Digital filtering process: Power Spectra showing 1 Hz windows around line noise (60 Hz) and harmonics (only 120 Hz shown here) were scanned for peaks and Gaussian fits $\left(c \cdot e^{-ax^2} + b\right)$ were applied using method of least squares (dashed orange line). Only frequencies where the amplitudes exceeded a threshold of $b + 10^{1/4}$ V^2 were modified. The amplitudes of frequencies that were modified before and after attenuation are shown in red and green, respectively.

squares. To minimize altering the original signal, only the amplitudes at frequencies where the Gaussian fit exceeded a threshold of $b+10^{1/4}$ were attenuated. In Figure 3.14, the amplitudes of frequencies that were modified before and after attenuation are shown in red and green, respectively. The Fourier transform with the modified amplitudes was inverted to recover the filtered signal in the time domain. Figure 3.15 shows 1-s segments of the original and filtered time series and the PSDs before and after the digital filtering process. As is evident from the PSD on the right, the peaks corresponding to line noise and its harmonics were entirely removed. Additionally, the 1-s segment shows the filtered signal almost entirely overlapping the original signal, confirming that the digital filtering process made minimal changes to the original signal.

The digitally filtered voltage fluctuations from the RTDs were converted to temperatures

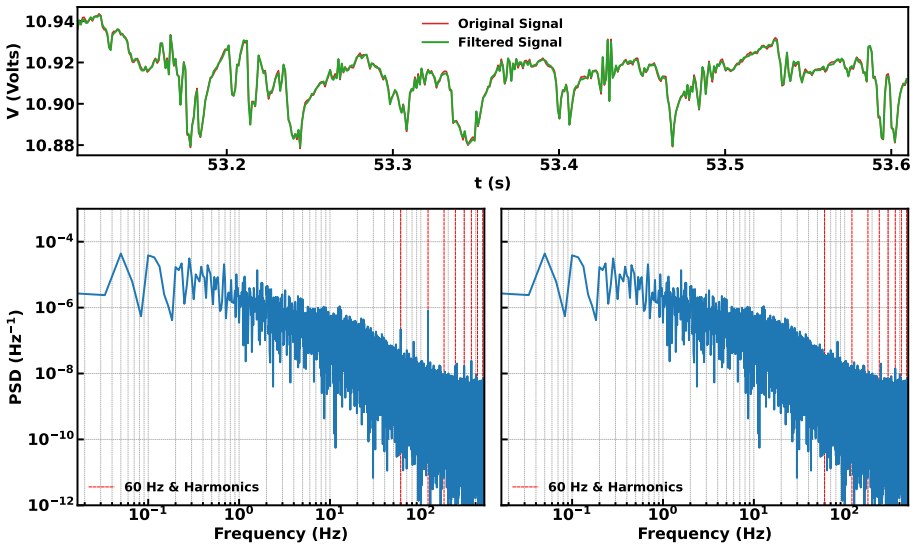

Figure 3.15: Effect of digital filtering on an RTD Signal from a surface undergoing boiling. (Top) A $\frac{1}{2}$-s interval of an RTD signal before (red) and after (green) digital filtering. (Bottom) PSDs of the RTD signals before (left) and after (right) digital filtering demonstrating that effect of the digital filtering process in removing the peaks corresponding to line noise and harmonics.

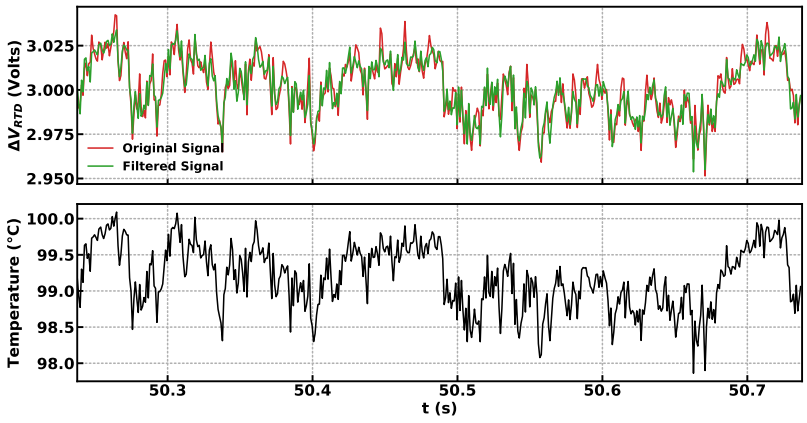

Figure 3.16: Post-processing steps of an RTD Signal. (Top) $\frac{1}{2}$-s segment of voltage fluctuations (red) from an RTD on a surface undergoing boiling, and the corresponding digitally filtered output (green). (Bottom) Digitally filtered RTD signal converted into temperature fluctuations using Equation (3.8).

using Equation (3.8), restated here for convenience:

$$R_{\text{RTD}} = \frac{V_{\text{out}}}{G\,I_s} + R_{\text{off}}$$

$$T = T_0 + \frac{1}{\alpha}\left(\frac{R_{\text{RTD}}}{R_0} - 1\right)$$

Figure 3.16 shows a representative $\frac{1}{2}$-s segment of voltage fluctuations from an RTD that was digitally filtered and then converted to its corresponding temperature fluctuations using Equation (3.8) and the RTD's calibration curve. The associated uncertainty in the temperature conversion was calculated using Equation (3.5) and Equation (3.9), restated here for convenience:

$$U_{R_{\text{RTD}}} = \sqrt{\left(\frac{U_{V_{\text{out}}}}{G\,I_s}\right)^2 + \left(U_{R_{\text{off}}}\right)^2}$$

$$U_T = \sqrt{\left(U_{T_0}\right)^2 + \left\{\frac{1}{\alpha^2}\left(\frac{R_{\text{RTD}}}{R_0} - 1\right)U_\alpha\right\}^2 + \left(\frac{R_{\text{RTD}}}{\alpha R_0^2}U_{R_0}\right)^2 + \left(\frac{1}{\alpha R_0}U_{R_{\text{RTD}}}\right)^2}$$

where $U_{V_{\text{RTD}}} = 0.5$ mV or 5×10^{-4} V, half the measurement resolution[10]. This was because every voltage reading represented an instantaneous resistance of the RTD as a result of boiling around the RTD, and as is the case for single measurements, the associated uncertainty is half the resolution of measurement. With the uncertainty in the values of the offset resistances ($U_{R_{\text{off}}}$) being of the order of 10^{-3} Ω, $G = 100$, and $I_s = 10^{-4}$ Amps, the uncertainty in the RTD resistance ($U_{R_{\text{RTD}}}$) was ~ 0.5 Ω. This uncertainty was propagated to calculate the uncertainty in temperature conversion (U_T), which was of the order of 0.1 °C.

[10]For a sampling rate of 1 kHz, the stated resolution of the DMM was $4\frac{1}{2}$ digits, which corresponded to a resolution of 1 mV for the 10 V range used to measure the voltages

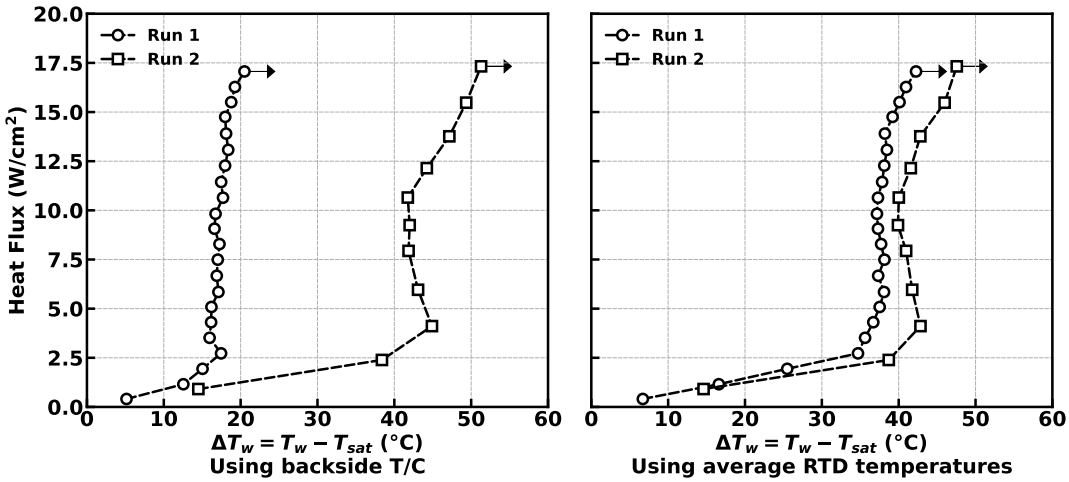

Figure 3.17: Comparing average surface temperature estimates using (left) the backside thermocouple measurements and (right) the high-speed RTD measurements by plotting boiling curves from two experiments with the same surfaces and boiling fluid.

As mentioned in Section 3.1.5.1, the surface temperature was taken as the average of all RTD measurements. When all RTDs worked, the measurements were taken over a period of 5 minutes from RTDs spread across the boiling surface. Therefore, it was a better estimate of the surface temperature (averaged in time and space) than the temperature measured by the backside thermocouple. Figure 3.17 shows separate boiling curves plotted using the backside thermocouple measurements and the average of RTD temperatures for two boiling experiments with the same surface and boiling fluid[11]. The closer resemblance of the boiling curves when using the average RTD temperatures suggested that the RTD measurements were a more reliable estimate of the average surface temperature. Despite care taken when attaching the backside thermocouple to the backside of the chip on PCB using a thermally conductive epoxy, there was the possibility that during curing of the epoxy, it would flow between the thermocouple bead and the backside surface of the chip causing the thermocouple bead to lose contact

[11]These two runs were for Parylene-C coated surfaces in Novec 7100 as the boiling fluid. See Chapter 4 for details.

with the surface and as a result, give temperature readings between the chip surface temperature and the boiling fluid at its saturation temperature. Regardless, the RTDs could still be calibrated using the backside thermocouple because during calibrations, the chip was allowed to reach a steady state and be in thermal equilibrium with the surrounding fluid, resulting in uniform temperatures.

Therefore, the average surface temperature was estimated as the average of all the high-speed RTD measurements. The associated uncertainty was estimated as

$$\frac{1}{N}\sqrt{\sum_{i=1}^{N}\left(U_{T,i}\right)^2}$$

where N was the number of RTD measurements and $U_{T,i}$ was the uncertainty associated with the RTD temperature as calculated by Equation (3.9). Due to the extremely large number of RTD measurements (N = 300,000 when all RTDs worked), the associated uncertainty was of the order of 1 mK.

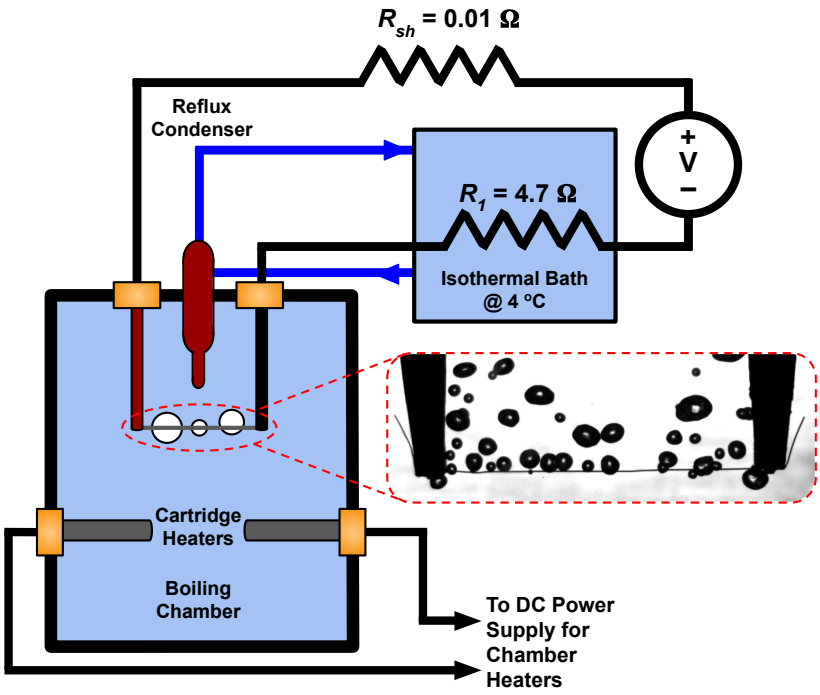

Figure 3.18: Schematic of the Wire Pool Boiling Experiment Facility. The inset shows an image taken by a high-speed camera while boiling occurred on a wire connected between electrodes.

3.2 Facility for Wire Pool Boiling Experiments

Figure 3.18 shows a schematic of the experimental facility used for wire pool boiling experiments. The boiling chamber was the same as before, a hollow cuboid vessel made of polycarbonate with a volumetric capacity of 350 mL. To heat and maintain the boiling fluid at its saturation temperature however, two $\frac{1}{4}$-inch diameter cartridge heaters were used instead of the wall-mounted flexible film heaters as before. These heaters were 2 inches long and had nominal resistances of 57.6 Ω. The two cartridge heaters were connected in parallel and powered by a DC Power Supply rated to supply a maximum voltage and current of 35 V and 1.4 A, respectively. When operating at its limit, the DC power supply was capable of dissipating 42.5 W through the two cartridge heaters, which was sufficient to maintain the boiling liquids used in experiments at their

saturation temperatures in the chamber. In addition to this, a reflux condenser was used to condense the vapors generated from the boiling liquid and form a closed flow loop. The condenser was supplied with water at 4 °C by an isothermal bath. A type-T thermocouple (designated "pool thermocouple") was used to monitor and measure the temperature of liquid in the chamber.

Boiling occurred on a 0.1-mm diameter platinum wire that was powered by a DC power supply and connected in series with a 0.01 Ω shunt resistor (R_{sh}) and an additional 4.7 Ω resistor (R_1). The platinum wire was held between two grabber test clips that acted as terminals and extended through the removable top cover of the boiling chamber. The distance between the two terminals and hence the length of the wire (L_{wire}) was 23 ± 0.5 mm. The wire was replaced for each experiment and had a nominal resistance of ~ 0.33 Ω at room temperature. Adding the additional 4.7 Ω resistor (R_1) ensured that these resistance fluctuations (dR_{pt}) were only a small percentage of the total load resistance ($R_{\mathrm{load}} = R_1 + R_{\mathrm{pt}} + R_{\mathrm{sh}}$) to the DC power supply. As a result of this, the fluctuations in the current, I, through the circuit, due to the DC power supply operating in constant voltage mode and compensating for the fluctuations in the thin-film resistance, dR_{pt}, were also smaller, and were given by

$$\frac{dI}{I} = -\frac{dR_{\mathrm{pt}}}{R_{\mathrm{load}}}$$

These current fluctuations were measured to be less than 0.1% during the experiments (see Section 3.2.2.1 for details of this calculation).

The 4.7 Ω resistor (R_1) was a power resistor packaged in a finned aluminum housing and capable of dissipating 300 W. It was immersed in a beaker filled with silicone oil, that was cooled by being placed in the isothermal bath circulating chilled water (at 4 °C) to the reflux condenser.

The shunt resistor ($R_{\rm sh}$) was used to measure the current flowing through the circuit. It came packaged with an in-built fan and was rated for a maximum current of 20 A. It had a resistance of 9.979 $\times 10^{-3}$ $\Omega \pm 0.087\%$.[12] At maximum currents measured during the experiment (~ 4.5 A), the self-heating of the shunt resistor was insignificant ($I^2 R_{\rm sh} \sim 10^{-1}$ W) and therefore the resistance of the shunt resistor was assumed to stay constant.

The power supplied to the platinum wire was given by $P_{\rm pt} = I^2 R_{\rm pt}$. Due to the fluctuations in both the resistance of the wire and the current through the circuit, the fluctuations in the power dissipated through the wire could be estimated as

$$dP_{\rm pt} = \frac{\partial P_{\rm pt}}{\partial I} dI + \frac{\partial P_{\rm pt}}{\partial R_{\rm pt}} dR_{\rm pt}$$
$$\Rightarrow dP_{\rm pt} = 2 I R_{\rm pt}\, dI + I^2\, dR_{\rm pt}$$

Plugging in $dI = -I(dR_{\rm pt}/R_{\rm load})$, the equation above simplified to

$$\frac{dP_{\rm pt}}{P_{\rm pt}} = \left(1 - 2\frac{R_{\rm pt}}{R_{\rm load}}\right) \frac{dR_{\rm pt}}{R_{\rm pt}}$$

Without the power resistor, $R_{\rm load} \approx R_{\rm pt}$ and $dP_{\rm pt}/P_{\rm pt} \approx -dR_{\rm pt}/R_{\rm pt}$. Therefore, the addition of the power resistor also dampened the power fluctuations. The maximum power fluctuations were measured to be less than 0.3% during the experiments (see Section 3.2.2.1 for details of this calculation).

3.2.1 Calibration of Wires

The platinum wires for the experiments were taken from a single 300-gm spool. To characterize the entire spool, 10 lengths of wire were calibrated in an isothermal bath

[12] uncertainty with a 95% confidence interval.

filled with DI water. Starting from room temperature ($\sim$ 22 °C), the isothermal bath was set to successively higher reference temperatures of 30, 38, 46, 54, 60, and 68 °C and the resistances of the wires were measured using the four-wire resistance measurement method for a total of 7 calibration data points. Due to the small resistance values of the lengths of platinum wires, which were comparable to the resistance of lead wires, it was important to use the four-wire resistance measurement method rather than the standard two-wire resistance measurement method for accurate measurement of the wire resistances.

At every set temperature, sufficient time was given for the isothermal bath and the platinum wires to reach steady state before measurements were taken. A type-T thermocouple was placed in the isothermal bath to measure the pool temperatures, which were used as reference temperatures. Once steady state was reached, voltage measurements from the thermocouple and four-wire resistance measurements of the platinum wire were taken sequentially. The sequential measurements were repeated 100 times at each reference temperature and were taken at the highest accuracy configuration of the digital multimeter (which included the maximum permissible integration time[13] and the maximum settling time[14] when switching measurement channels).

3.2.1.1 Data Reduction and Analysis

The sample size of measurements from the thermocouple and platinum wire during calibration was $N = 100$. The sample mean was used to represent the true value of the measurements and the sample standard deviation was used to calculate the measurement

[13]The maximum integration time setting available on the digital multimeter was $\frac{1}{12}$ s or averaging over 5 power line cycles.

[14]The settling time was how long the digital multimeter waited to start taking a measurement after a new channel was connected to.

uncertainty with 95% confidence using Equation (3.3), restated here for convenience:

$$U_{95\%} = t_{95\%,N-1}\frac{s}{\sqrt{N}}$$

where s was the sample standard deviation, $N = 100$ was the sample size, and $t_{95\%,N-1} = 1.984$ was the two-sided value for student's t distribution for 95% confident with $N-1 = 99$ degrees of freedom.

The sample means and standard deviations of the thermocouple EMFs from the pool were converted into temperature values and their corresponding uncertainty using the type-T thermocouple calibration curve (see Appendix B for details). The pool thermocouple measurements were taken as the reference temperatures for the calibration curves.

Figure 3.19a shows the wire resistance as a function of the reference temperature from one of the calibration runs. The resistance of a platinum wire can be related to the temperature of the wire using the Callendar-Van Duses equation as

$$R = R_0\Big(1 + \alpha\big(T - T_0\big) + \beta\big(T - T_0\big)^2\Big)$$

where R_0 is a reference value of the wire at some reference temperature, T_0, α is the linear temperature coefficient of resistivity (TCR). Over small temperature ranges however, it may be assumed that $\beta = 0$ and the linearized form of the Callendar-Van Duses equation can be written as

$$R_{\text{pt}} = R_0\Big(1 + \alpha \cdot \big(T - T_0\big)\Big)$$

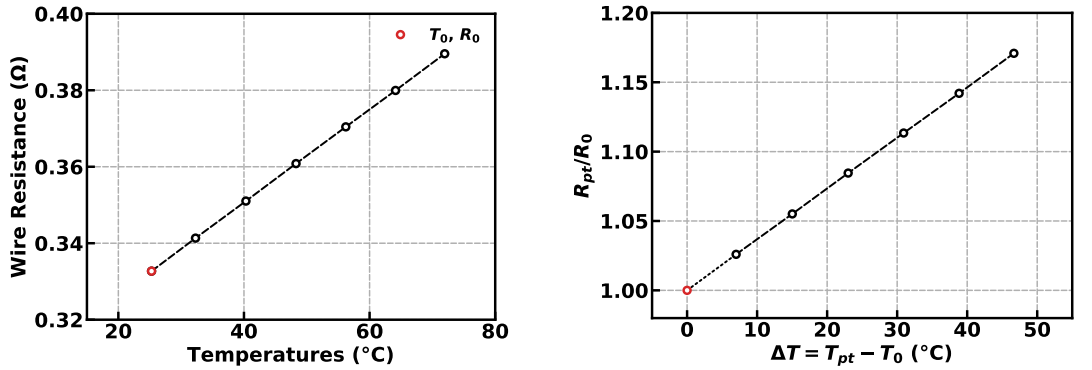

(a) Resistance as a function of temperature. The data point in red was used for reference values (T_0 and R_0).

(b) Non-dimensional resistance as a function of temperature change using one of the calibration data points as T_0 and R_0.

Figure 3.19: A representative calibration curve. (a) Resistance as a function of temperature for a platinum wire from one of the calibration runs. (b) Calibration curve replotted using with $T_0 = 25.29$ °C. The slope of the curve represents the linear temperature coefficient of resistivity (TCR) of the platinum wire.

The above equation can then be rearranged to non-dimensionalize the resistance as

$$\frac{R_{\text{pt}}}{R_0} = 1 + \alpha \cdot \big(T - T_0\big)$$

Figure 3.19b shows the transformed calibration curve where the first calibration data point (in red) was used as T_0 and R_0. The TCR was then estimated by calculating the slope using linear regression. Note that using one of the calibration data points as the reference values meant that any linear fit had to pass through ($\Delta T = 0$ °C and $R_{\text{pt}}/R_0 = 1$) by definition. Thus, that calibration data point could not be used in linear regression and this resulted in the loss of one degree of freedom. The value of TCR had to be estimated as the slope of the best linear fit with a y-intercept of 1 and passing through the remaining calibration data points. This was done using the method of least squares and the standard error of slope (s_m) obtained from the method was used to

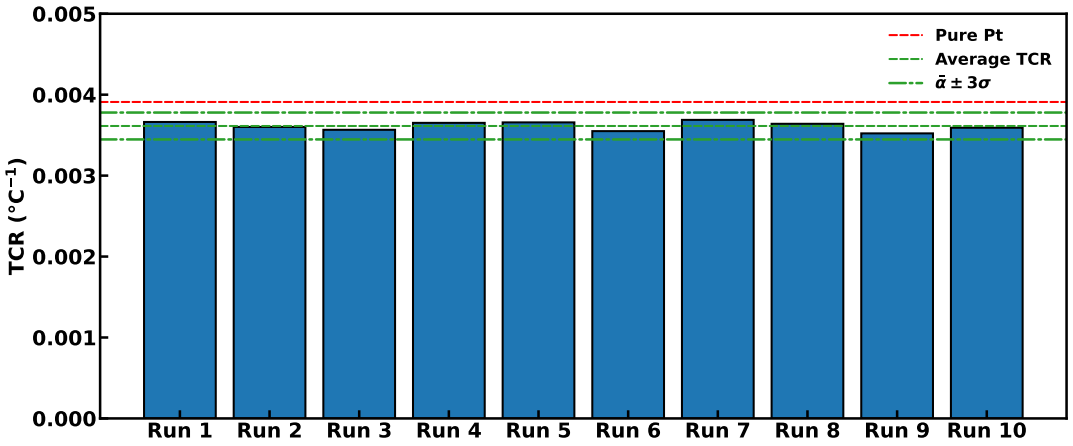

Figure 3.20: TCR values estimated from 10 calibration runs.

calculate the uncertainty in the estimate of TCR as

$$U_{\alpha,95\%} = t_{95\%,\nu-2}\, s_m$$

where $\nu = 7$ was the number of calibration data points, and $t_{95\%,\nu-2} = 2.571$ was the two-sided value for student's t distribution for 95% confident with $\nu - 2 = 5$ degrees of freedom. The loss of an additional degrees of freedom resulted from estimating slope from the remaining data points. The uncertainty in the estimate of TCR values calculated this way were of the order of 1%.

Figure 3.20 shows the estimated values of TCR from the 10 calibration runs and the reported TCR value of pure platinum ($\alpha = 3.92 \times 10^{-3}$ °C^{-1}). The deviation in the estimated TCR values was attributed to the use of resistance values at $T = 0$ °C and 100 °C to calculate the reported TCR. This contrasts to the present study in which the TCR was calculated with $T_0 \sim 24$ °C and by performing a linear fit to 6 data points using the method of least squares.

The mean value of TCR and the associated uncertainty with 95% confidence interval

from the 10 calibration runs was 3.613×10^{-3} °C^{-1} $\pm 4.59\%$. These values were assumed to represent the true value of the TCR for any length of wire taken from the original spool. As mentioned earlier, a new length of platinum wire was used for every experiment. At the start of all experiments, the resistance of the wire and the corresponding temperature was measured to be used as the reference values (T_0 and R_0) so that all wire resistances from that experiment could be converted to wire temperatures using

$$T_{\text{pt}} = T_0 + \frac{1}{\alpha}\left(\frac{R_{\text{pt}}}{R_0} - 1\right) \tag{3.12}$$

And the associated uncertainty in the wire temperature was calculated as

$$U_{T_{\text{pt}}} = \sqrt{\left(U_{T_0}\right)^2 + \left\{\frac{1}{\alpha^2}\left(\frac{R_{\text{pt}}}{R_0} - 1\right)U_\alpha\right\}^2 + \left(\frac{R_{\text{pt}}}{\alpha R_0^2}U_{R_0}\right)^2 + \left(\frac{1}{\alpha R_0}U_{R_{\text{pt}}}\right)^2} \tag{3.13}$$

3.2.2 Experimental Procedure

Before running the experiments, the boiling fluid inside the chamber was brought up to saturation temperature and the chamber degassed for two hours using the chamber heaters. During this time, power was also supplied to the platinum wire to dissipate 0.5 W/cm^2 of heat flux and degas the surface, removing any trapped air. A type-T thermocouple (designated "pool thermocouple" hereunto) was used to monitor the temperature of the boiling fluid.

After degassing the chamber for two hours, experiments were started. Figure 3.21 outlines the process flow of the experiment. The first task was to measure the wire resistance at the saturation temperature of the boiling fluid to use as reference resistance and temperature (R_0 and T_0), which would then allow for converting wire resistance measurements using Equation (3.12). A small test current of ~ 0.1 Amps was made to pass through the wire using the DC power supply. The heat flux dissipated for the

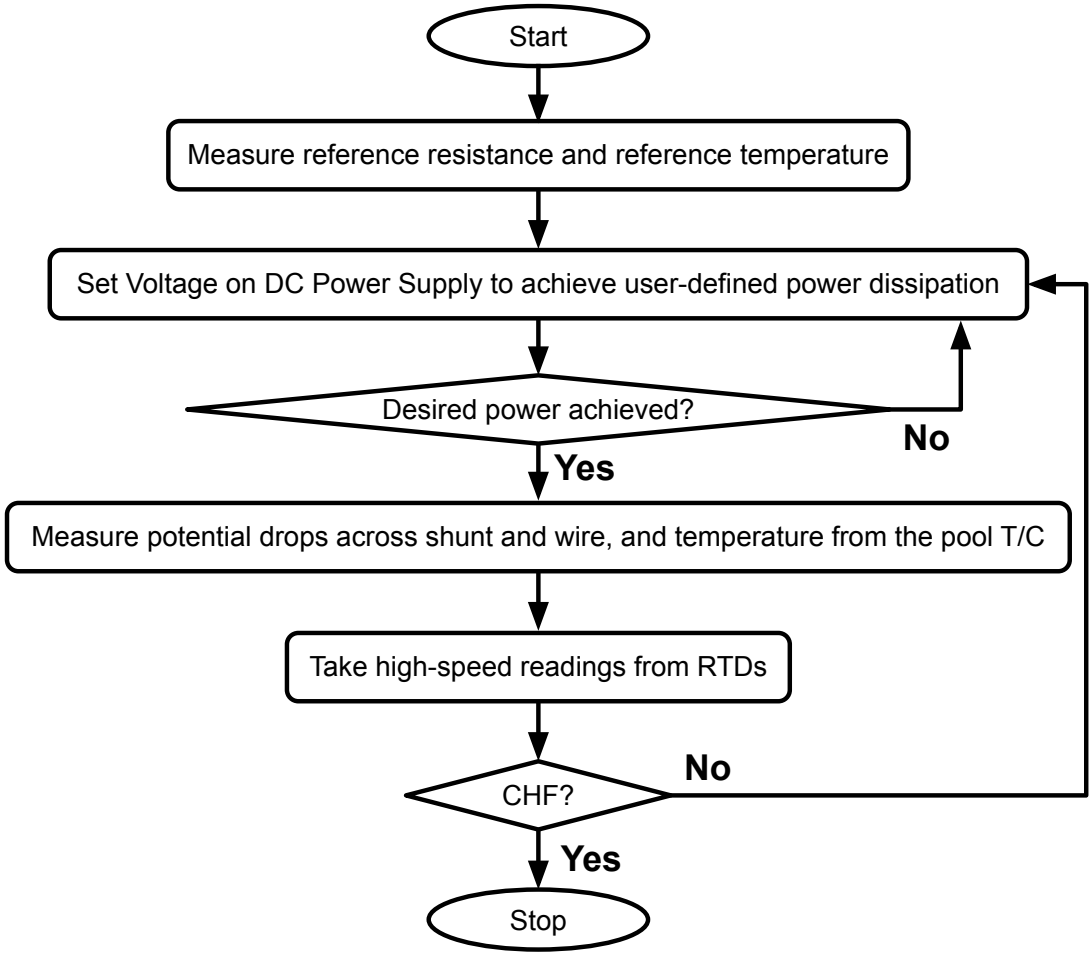

Figure 3.21: Process Flow of Wire Boiling Experiments.

test current was ~ 0.05 W/cm^2 and hence, self-heating of the wire was minimal and it was assumed that the temperature of the wire was the same as the temperature of the boiling fluid at its saturation temperature. The potential drops across the shunt and the wire, and the pool thermocouple EMF was then measured sequentially, and the three measurements repeated 40 times for a total of 120 measurements. These measurements were made with the digital multimeter configured for highest accuracy measurements and the sample means of the measurements were assumed to represent the true values with the associated uncertainties calculated using Equation (3.3).

The sample mean and standard deviation of the pool thermocouple EMFs were converted into a temperature value and its associated uncertainty using the type-T thermocouple calibration curve (see Appendix B for details). These values were taken as the reference temperature, T_0, and the uncertainty in the reference temperature, U_{T_0}, for the wire.

The test current, I_s through the wire and its associated uncertainty were first estimated using the potential drop across the shunt resistor (ΔV_{sh}) and its associated uncertainty as

$$I_s = \frac{\Delta V_{\text{sh}}}{R_{\text{sh}}}$$

$$U_I = \sqrt{\left(\frac{U_{\Delta V_{\text{sh}}}}{R_{\text{sh}}}\right)^2 + \left(\frac{\Delta V_{\text{sh}}}{R_{\text{sh}}^2} U_{R_{\text{sh}}}\right)^2}$$

where R_{sh} and $U_{R_{\text{sh}}}$ are the shunt resistance and its associated uncertainty.

The wire resistance, which was assumed to be the reference resistance, R_0, for the wire, was finally calculated as

$$R_{\text{pt}}\big(= R_0\big) = \frac{\Delta V_{\text{pt}}}{I} - R_{\text{leads}}$$

where R_{leads} was the resistance of the leads used to connect the wire to the rest of the circuit (see Figure 3.22). It was important to consider R_{leads} because only the potential drop across $R_{\text{leads}} + R_{\text{pt}}$ could be measured due to the construction of the setup, and R_{leads} was measured to be $2.48 \times 10^{-2}\ \Omega \pm 2.37\%$, which was $\sim 7.5\%$ of the nominal value of R_{pt} ($= 0.33\ \Omega$) at room temperature. The associated uncertainty in R_{pt} was

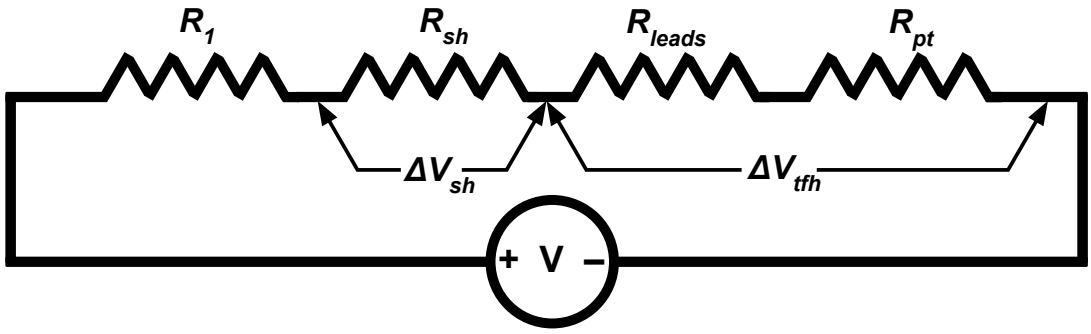

Figure 3.22: Potential drop measurements taken to measure the power dissipated by the platinum wire. R_{leads} was the resistance of the leads used to connect the platinum wire to the rest of the circuit. R_1 and R_{sh} were the additional and shunt resistors, respectively.

calculated by propagating the uncertainty in ΔV_{pt}, I, and R_{leads} as

$$U_{R_{\text{pt}}} = \sqrt{\left(\frac{U_{\Delta V_{\text{pt}}}}{I}\right)^2 + \left(\frac{\Delta V_{\text{pt}}}{I^2} U_I\right)^2 + \left(U_{R_{\text{leads}}}\right)^2}$$

With the reference temperature and resistance calculated, the power dissipated by the wire was increased by increasing the voltage output from the DC Power Supply powering the platinum wire. High-accuracy, slow-speed measurements (at a sampling rate of 12 Hz) of the potential drop across the shunt, potential drop across the wire and the pool thermocouple EMF were recorded to calculate the average heat flux dissipated by the wire (see Section 3.2.2.1 for details). The voltage output from the DC Power Supply was varied until a (user-defined) desired power was achieved (see Section 3.2.2.2 for details), followed by 60,000 measurements (at a sampling rate of 1 kHz for 1 minute) of the potential drop across the platinum wire. Then, the power to the wire was increased to the next desired power, and the entire process was repeated until CHF occurred.

3.2.2.1 Calculating Power Dissipation

To calculate the power dissipated by the wire, voltage drop measurements were taken as shown in Figure 3.22. In addition to the potential drops across the shunt (ΔV_{sh}) and the wire (ΔV_{pt}), the EMFs from the pool thermocouple were also recorded. These measurements were repeated sequentially 40 times for a total of 120 measurements at the highest accuracy setting of the digital multimeter. Therefore, the sample size of measurements was $N = 40$, and the sample mean was assumed to be the true value of measurement. The sample standard deviation was used to calculate the associated uncertainty using Equation (3.3).

The sample means and standard deviations of the measured EMFs from the pool thermocouples were converted into temperature values and their corresponding uncertainty using the type-T thermocouple calibration curve (see Appendix B for details). The pool thermocouple measurements were used to confirm that the boiling fluid was maintained at saturation temperature, T_{sat}.

The current flowing through the circuit was measured using the potential drop across the shunt resistor as

$$I = \frac{\Delta V_{\mathrm{sh}}}{R_{\mathrm{sh}}} \tag{3.14}$$

where $R_{\mathrm{sh}} = 9.979{\times}10^{-3}\ \Omega \pm 0.087\%$ within a 95% confidence interval. The uncertainty in the current was estimated by propagating the uncertainty in the voltage measurement and the shunt resistance as

$$U_I = \sqrt{\left(\frac{U_{\Delta V_{\mathrm{sh}}}}{R_{\mathrm{sh}}}\right)^2 + \left(\frac{\Delta V_{\mathrm{sh}}}{R_{\mathrm{sh}}^2} U_{R_{\mathrm{sh}}}\right)^2}$$

The uncertainty in the current measurement was also taken as a measure of the fluctuations in the current through the circuit and was of the order of 0.1% as noted earlier. The wire resistance was then calculated as

$$R_{\mathrm{pt}} = \frac{\Delta V_{\mathrm{pt}}}{I} - R_{\mathrm{leads}} \tag{3.15}$$

where R_{leads} was the resistance of the leads used to connect the wire to the rest of the circuit. The associated uncertainty in R_{pt} was calculated by propagating the uncertainty in ΔV_{pt}, I, and R_{leads} as

$$U_{R_{\mathrm{pt}}} = \sqrt{\left(\frac{U_{\Delta V_{\mathrm{pt}}}}{I}\right)^2 + \left(\frac{\Delta V_{\mathrm{pt}}}{I^2} U_I\right)^2 + \left(U_{R_{\mathrm{leads}}}\right)^2}$$

The power dissipated by the chip was calculated as

$$P_{\mathrm{pt}} = I^2 R_{\mathrm{pt}}$$

The power calculated thus was used for power adjustment purposes (see Section 3.2.2.2 to achieve user-defined power dissipation. These measurements were not used to calculate the average temperature of the wire, or the power dissipated by the wire for the boiling curve. Instead, the high-speed measurements of voltage fluctuations across the wire were used for this purpose (see Section 3.2.3).

The uncertainty associated with the power dissipated was calculated by propagating the uncertainty in the current and the wire resistance as

$$U_{P_{\mathrm{pt}}} = \sqrt{\left(2 I R_{\mathrm{pt}} U_I\right)^2 + \left(I^2 U_{R_{\mathrm{pt}}}\right)^2}$$

The uncertainty in the power was also taken as a measure of the fluctuations in the power dissipated by the wire and was less than 0.3% as noted earlier.

Finally, the heat flux was calculated as $q'' = P_{\text{pt}}/A_{\text{wire}}$. The surface area of the wire A_{wire} and its associated uncertainty were calculated as

$$A_{\text{wire}} = \pi D_{\text{wire}} L_{\text{wire}}$$
$$U_{A_{\text{wire}}} = \pi D_{\text{wire}} U_{L_{\text{wire}}}$$

where D_{wire} (= 0.01 cm) was the diameter of the wire, and L_{wire} (= 2.3 cm) and $U_{L_{\text{wire}}}$ (= 0.05 cm) were the length of the wire and the associated uncertainty with a 95% confidence interval, respectively. Finally, the uncertainty in the heat flux was calculated as

$$U_{q''} = \sqrt{\left(\frac{U_{P_{\text{pt}}}}{A_{\text{wire}}}\right)^2 + \left(\frac{P_{\text{pt}}}{A_{\text{wire}}^2} U_{A_{\text{wire}}}\right)^2}$$

3.2.2.2 Stepping up power

The power for the platinum wire was sourced from a DC power supply that was operated to provide a constant (user-defined) set voltage. However, it was desired to achieve set values of power (or heat flux) dissipation from the wire. Therefore, the set voltage had to be calculated from the desired power. Since the wire was connected in series with the additional resistor (R_1) and the shunt resistor (R_{sh}) as shown in Figure 3.22, the relationship between the set voltage (V_{set}) and the required potential drop ($\Delta V_{\text{pt,set}}$) across the wire to achieve the required power dissipation (P_{set}) was calculated as

$$\Delta V_{\text{pt,set}} = \sqrt{P_{\text{set}} R_{\text{pt}}} \tag{3.16}$$

$$V_{\text{set}} = \Delta V_{\text{pt,set}} \frac{R_{\text{tot}}}{R_{\text{pt}}} \tag{3.17}$$

where $R_{\text{tot}} = R_1 + R_{\text{sh}} + R_{\text{leads}} + R_{\text{pt}}$ was the total resistance to the DC power supply.

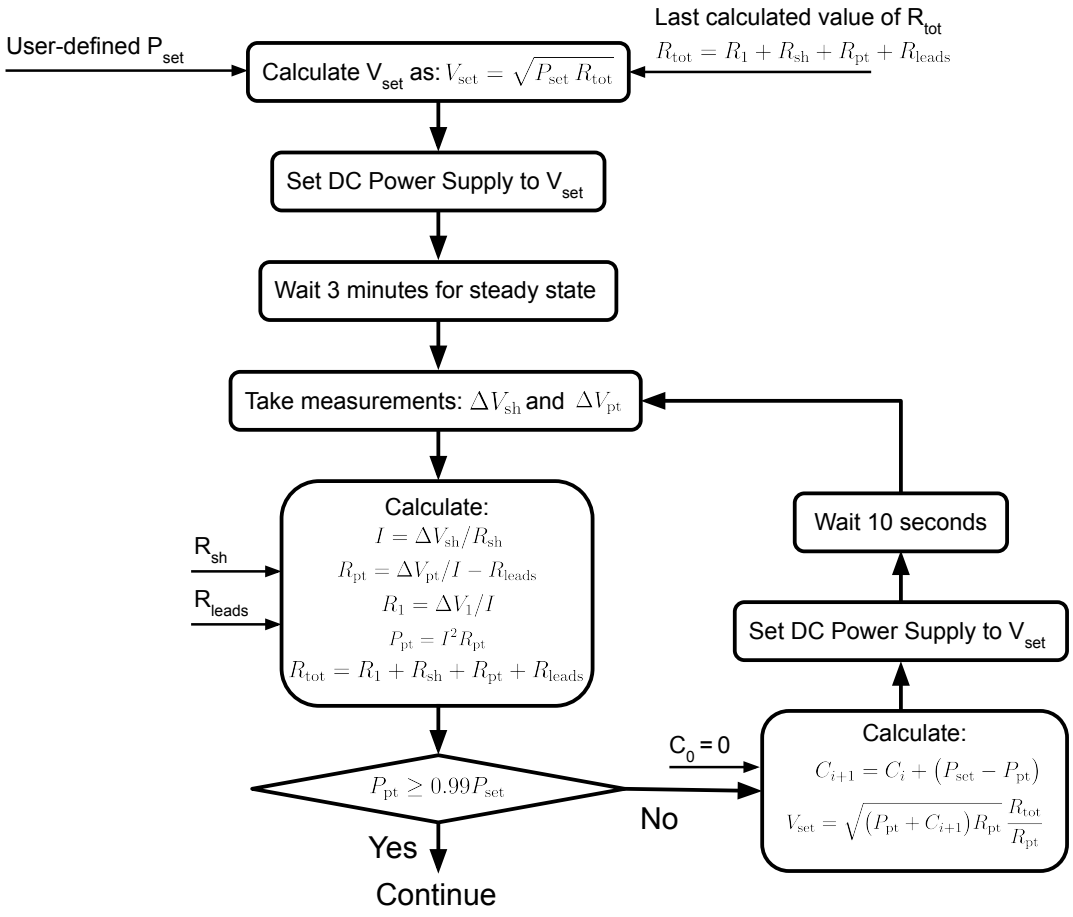

Figure 3.23: Process flow to change $V_{\rm set}$ until desired power was achieved.

Since the wire was made of platinum, its resistance increased with the power dissipation as the wire heated up. This increasing resistance of the wire had to be compensated for when calculating $V_{\rm set}$. Figure 3.23 shows the process followed to step up the power supplied to the wire and compensate for its increasing resistance. After setting the first calculated voltage $V_{\rm set}$ on the power supply, the system idled for 3 minutes to allow the wire to reach steady state. Then, measurements of ΔV_1, $\Delta V_{\rm sh}$, and $\Delta V_{\rm pt}$ were taken sequentially and repeated 40 times for a total of 120 measurements over a period of 15 seconds. The sample means were taken as the true value of the measurements. The

current through the circuit and the power dissipated by the wire were calculated as outlined in Section 3.2.2.1. If the power dissipated was greater than 99% of the desired power, P_{set}, the experiment proceeded to the next step. Otherwise, a correction factor, C_i was calculated based on the calculated and desired power as

$$C_{i+1} = C_i + \left(P_{\text{set}} - P_{\text{pt}}\right) \quad \text{where } C_0 = 0$$

Then, the next value of V_{set} was calculated as

$$V_{\text{set}} = \sqrt{\left(P_{\text{pt}} + C_{i+1}\right) R_{\text{pt}}}\, \frac{R_{\text{tot}}}{R_{\text{pt}}}$$

Since the wire resistance monotonically increased with the power dissipated, the first calculated value of V_{set} always resulted in a $P_{\text{pt}} < P_{\text{set}}$, and subsequent corrections to V_{set} resulted in P_{pt} approaching P_{set} from lower values. Once the desired power was achieved, the correction factor was reset to 0 and the experiment proceeded to high-speed measurements of the potential drop across the wire.

3.2.2.3 High Speed Measurements

High-speed measurements of the voltage fluctuations across the wire were taken at 1 kHz for 1 minute for a total of 60,000 readings at every power level. After the measurements were complete, the transfer of readings from the digital multimeter to a computer took about 20 seconds, following which the power level was increased to the next desired power.

The digital multimeter was capable of $4\frac{1}{2}$ digits accuracy at 1 kHz. Since the range of measurements was 10 V, this meant that the least significant digit or the resolution of the measurements was 1 mV.

Each of the 60,000 readings represented the potential drop across the wire that had

a space-averaged instantaneous resistance as a result of boiling affecting the temperatures along the entire length. Since the uncertainty for a single measurement is half the resolution of measurement, the uncertainty associated with the high-speed voltage measurements ($U_{\Delta V_{\mathrm{pt}}}$) was 0.5 mV or 5×10^{-4} V.

3.2.3 Post-Processing

The high-speed voltage fluctuations from the wire (ΔV_{pt}) were converted to corresponding temperatures using Equation (3.14), Equation (3.15), and Equation (3.12), summarized here for convenience:

$$I = \frac{\Delta V_{\mathrm{sh}}}{R_{\mathrm{sh}}}$$

$$R_{\mathrm{pt}} = \frac{\Delta V_{\mathrm{pt}}}{I} - R_{\mathrm{leads}}$$

$$T_{\mathrm{pt}} = T_0 + \frac{1}{\alpha}\left(\frac{R_{\mathrm{pt}}}{R_0} - 1\right)$$

where $\alpha = 3.613 \times 10^{-3}$ °C^{-1} from the calibration runs (see Section 3.2.1 for details), and T_0 and R_0 were measured at the start of each experiment. For the calculation of the current, the sample mean of high accuracy measurements of ΔV_{sh} recorded before high-speed voltage fluctuation measurements was used assuming that the current through the circuit remained constant at every power level. This assumption was valid since it was observed (as detailed in Section 3.2.2.1) that current fluctuations were less than 0.1%.

Figure 3.24a shows 1-s segments of voltage fluctuations across a wire undergoing boiling in 0.1% silica-nanofluid solution at a low and a high heat flux, and the corresponding wire resistance and temperature fluctuations calculated using the equations above. Figure 3.24b shows the PSDs of the temperature fluctuations that are broadband and unlike fluctuations from the surface experiments, do not exhibit peaks corresponding to

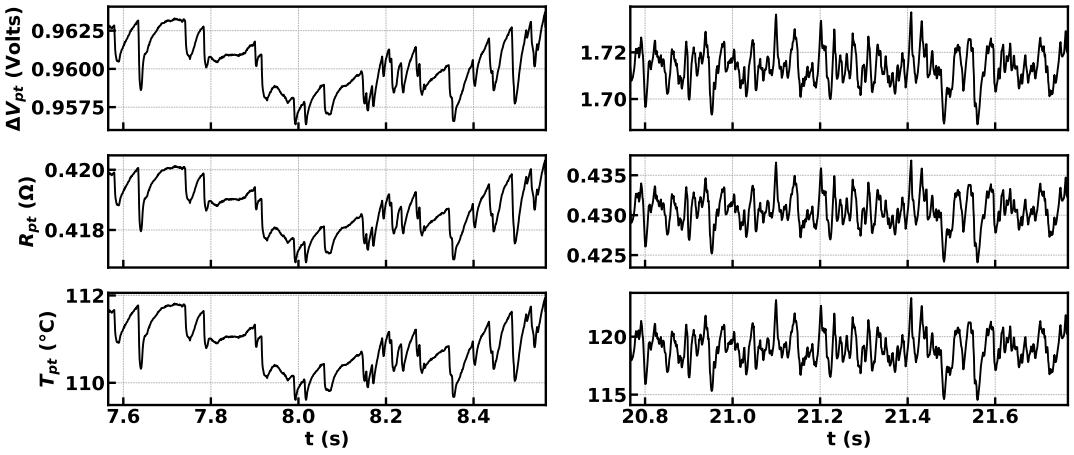

(a) 1-s segments of voltage fluctuations across a wire (top) and corresponding wire resistance (middle) and temperature fluctuations (bottom) recorded at a (left) low heat flux and a (right) high heat flux from a wire boiling experiment in 0.1% silica-nanofluid solution.

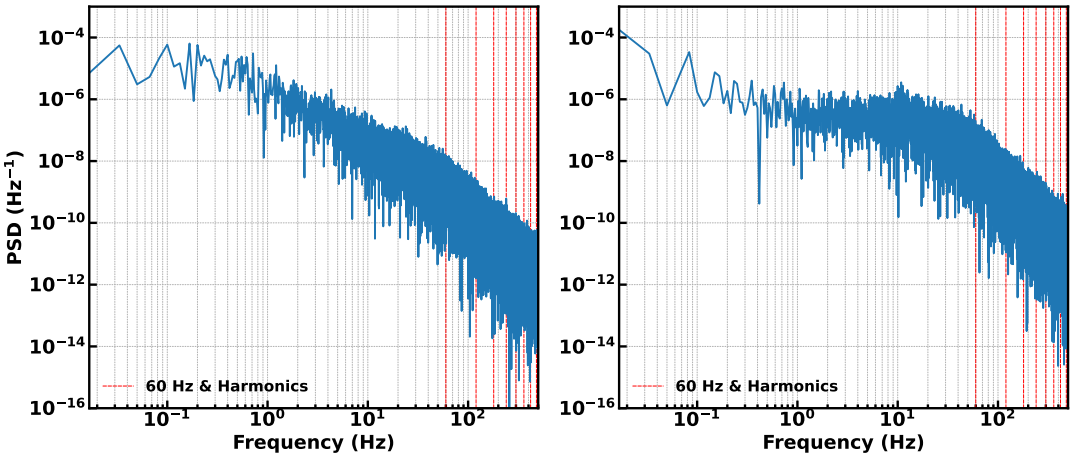

(b) PSDs of the time series.

Figure 3.24: (Top) Converting voltage fluctuations into temperatures, and (bottom) PSDs of the temperature fluctuations.

line noise and harmonics.

The uncertainty in estimation of the wire temperatures was calculated by propagating the uncertainties in the shunt voltage measurement ($U_{\Delta V_{\mathrm{sh}}} \sim 0.01$ V), shunt resistance value ($U_{R_{\mathrm{sh}}} = 8.68 \times 10^{-6}$ Ω), leads resistance value ($U_{R_{\mathrm{leads}}} = 5.88 \times 10^{-4}$ Ω), reference

temperature and resistance ($U_{T_0} \sim 10^{-3}$ °C and $U_{R_0} \sim 10^{-4}$ Ω), and TCR ($U_\alpha = 3.96 \times 10^{-5}$ °C^{-1}) as

$$\begin{aligned} U_I &= \sqrt{\left(\frac{U_{\Delta V_{\rm sh}}}{R_{\rm sh}}\right)^2 + \left(\frac{\Delta V_{\rm sh}}{R_{\rm sh}^2} U_{R_{\rm sh}}\right)^2} \\ U_{R_{\rm pt}} &= \sqrt{\left(\frac{U_{\Delta V_{\rm pt}}}{I}\right)^2 + \left(\frac{\Delta V_{\rm pt}}{I^2} U_I\right)^2 + \left(U_{R_{\rm leads}}\right)^2} \\ U_{T_{\rm pt}} &= \sqrt{\left(U_{T_0}\right)^2 + \left\{\frac{1}{\alpha^2}\left(\frac{R_{\rm pt}}{R_0} - 1\right) U_\alpha\right\}^2 + \left(\frac{R_{\rm pt}}{\alpha R_0^2} U_{R_0}\right)^2 + \left(\frac{1}{\alpha R_0} U_{R_{\rm pt}}\right)^2} \end{aligned} \tag{3.18}$$

As was noted in Section 3.2.2.3, the uncertainty in a single measurement of the potential drop across the wire ($U_{\Delta V_{\rm pt}}$) was 5×10^{-4} V, half the measurement resolution. The maximum uncertainty in temperature conversion ($U_{T_{\rm pt}}$) calculated was ~ 1 °C.

To plot the boiling curve, the wire temperature fluctuations were averaged to represent the time-averaged wire temperature ($\overline{T_{\rm pt}}$) at every power level. The associated uncertainty was estimated as

$$U_{\overline{T_{\rm pt}}} = \frac{1}{N} \sqrt{\sum_{i=1}^{N} \left(U_{T_{{\rm pt},i}}\right)^2}$$

where N was the number of measurements and $U_{T_{{\rm pt},i}}$ was the uncertainty associated with the wire temperatures as calculated by Equation (3.18). Due to the extremely large number of temperature measurements (N = 60,000), the associated uncertainty was of the order of 1 mK.

The excess temperatures and the associated uncertainty were calculated as

$$\Delta T = \overline{T_{\mathrm{pt}}} - T_{\mathrm{sat}}$$
$$U_{\Delta T_{\mathrm{pt}}} = \sqrt{\left(U_{\overline{T_{\mathrm{pt}}}}\right)^2 + \left(U_{T_{\mathrm{sat}}}\right)^2}$$

where T_{sat} and $U_{T_{\mathrm{sat}}}$ were the saturation temperature of the fluid and the associated uncertainty, respectively. These were estimated by the temperature measurements from the pool thermocouple since the boiling fluid was maintained at saturation temperature.

Similarly, the wire resistance fluctuations were averaged to represent the time-averaged wire resistance ($\overline{R_{\mathrm{pt}}}$) and used to calculate the average power dissipated and heat flux as $\overline{P_{\mathrm{pt}}} = I^2\overline{R_{\mathrm{pt}}}$ and $\overline{q''} = \overline{P_{\mathrm{pt}}}/A_{\mathrm{wire}}$, respectively. The uncertainty in the average wire resistance was calculated as

$$U_{\overline{R_{\mathrm{pt}}}} = \frac{1}{N}\sqrt{\sum_{i=1}^{N}\left(U_{R_{\mathrm{pt},i}}\right)^2}$$

where N was the number of measurements and $U_{R_{\mathrm{pt},i}}$ was the uncertainty associated with the wire resistance fluctuations as calculated by Equation (3.18). The uncertainty in the average wire resistance was propagated using the following set of equations:

$$U_{\overline{P_{\mathrm{pt}}}} = \sqrt{\left(2I\overline{R_{\mathrm{pt}}}U_I\right)^2 + \left(I^2\,U_{\overline{R_{\mathrm{pt}}}}\right)^2}$$
$$U_{\overline{q''}} = \sqrt{\left(\frac{U_{\overline{P_{\mathrm{pt}}}}}{A_{\mathrm{wire}}}\right)^2 + \left(\frac{\overline{P_{\mathrm{pt}}}}{A_{\mathrm{wire}}^2}U_{A_{\mathrm{wire}}}\right)^2}$$

where U_I was the uncertainty in current, and $A_{\mathrm{wire}} = \pi D_{\mathrm{wire}}\,L_{\mathrm{wire}}$ and $U_{A_{\mathrm{wire}}} = \pi D_{\mathrm{wire}}\,U_{L_{\mathrm{wire}}}$ were the surface area of the wire and the associated uncertainty. The uncertainty in the average heat flux was calculated to be of the order 1%. Figure 3.25 shows repeatability in the boiling curves from wire experiments performed in 0.1% silica-nanofluid solution plotted using the equations outlined above.

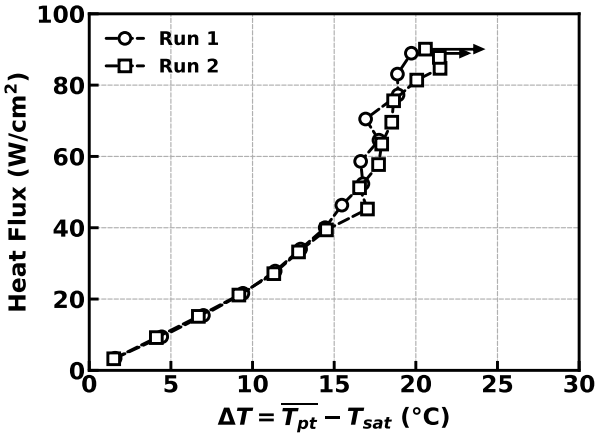

Figure 3.25: Boiling curves for two wire experiments performed in 0.1% silica-nanofluid solution.

Chapter 4

Results: Surface Pool Boiling Experiments

4.1 Experimental Runs

Table 4.1 lists the set of experiments performed using different surface-fluid combinations along with the observed values of CHF. Although sapphire subtrates were used to microfabricate all surfaces, the name designated to any surface refers to the final layer deposited during the microfabrication process as outlined in Appendix C. The choice of the final layers on the surfaces (SiO_2, Amorphous Silicon or A-Si, Nickle or Ni, and Parylene-C) was based on the reported contact angle of water on the chosen layers, which spanned $\sim 0^\circ$ for SiO_2 and $\sim 90^\circ$ for Parylene-C. This variation in contact angle was expected to produce CHF values that spanned one order of magnitude. However, the higher power dissipation requirements to achieve dry-out in DI water and the higher temperatures involved made it unfeasible to carry out experiments in DI water for even the lowest expected CHF values of ~ 40 W/cm^2 in Parylene-C. Therefore, Novec 7000

S.No.	Boiling Fluid	Surface	Identifier	T_{sat} at 1 atm (°C)	Observed CHF (W/cm^2)
1	Novec 7000	SiO_2	SiO_2-N70-1	34	14.14
2		SiO_2	SiO_2-N70-2		12.90
3		A-Si	A-Si-N70		13.82
4		Ni	Ni-N70		15.16
5	Novec 7100	SiO_2	SiO_2-N71	61	12.97
6		A-Si	A-Si-N71		11.69
7		Ni	Ni-N71		13.57
8		Parylene-C	P-N71-1		17.06
9		Parylene-C	P-N71-2		17.32

Table 4.1: List of surface pool boiling experiments performed. The identifier is for referencing the experimental run in the results that follow.

and Novec 7100[1] were chosen as alternative boiling fluids. These fluids were dielectric, nonpolar hydrofluoroethers with zero ozone depletion potential that were designed to replace fluorinated hydrocarbons as refrigerants. Due to the volatile nature of the fluids, contact angle measurements using the sessile drop technique was made difficult because the drops evaporated far too quickly to yield any measurements. Therefore, contact angle measurements were not performed for these fluids.

Figure 4.1 shows the values of CHFs observed in the experiments. Some surface-fluid combinations were tested for repeatability. It is noted that the largest variation[2] was observed for SiO_2 in Novec 7100 at 9.2%. Such large variations in boiling heat transfer experiments are commonplace. The highest values of CHF ($\sim$ 17 W/cm^2) was observed for Parylene-C in Novec 7100.

Figure 4.2 compares the CHF values for similar surfaces across the two boiling fluids. For SiO_2, A-Si, and Ni surfaces, the CHF value was slightly reduced in Novec 7100. This is in accordance with Zuber's expression for CHF (Equation (2.3)) for Novec 7000 and Novec 7100, which estimates the CHF values at 18.82 W/cm^2 and 16.35 W/cm^2

[1]Purchased from 3M.

[2]The variation was the difference in the observed CHF values as a percentage of the average value.

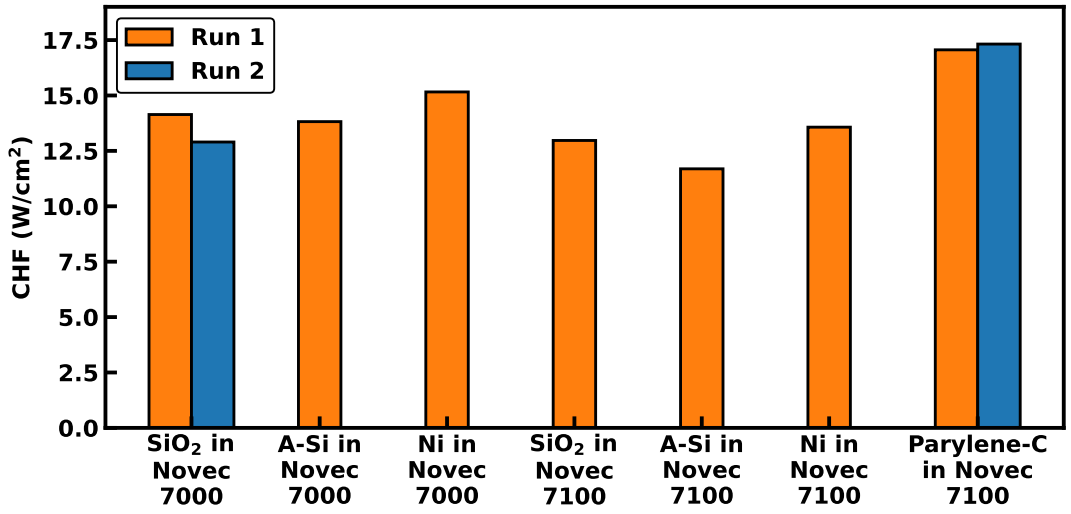

Figure 4.1: Observed CHF values for surface pool boiling experiments.

for the two fluids, respectively.

Figure 4.3 shows the boiling curves for experiments carried out in Novec 7000 (left)

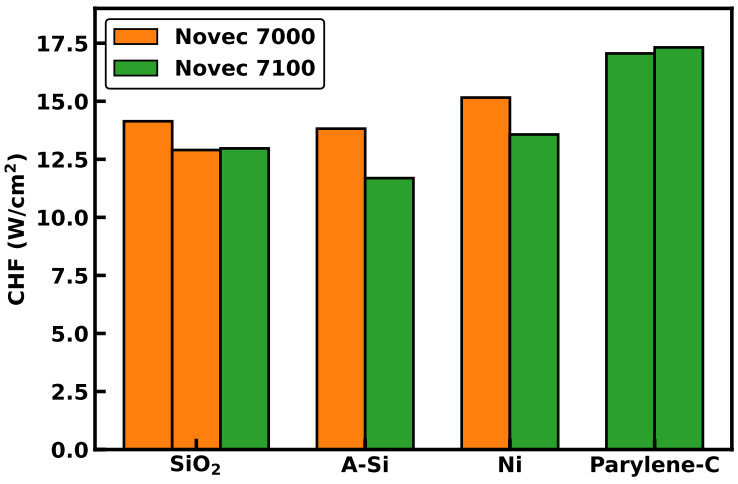

Figure 4.2: Comparison of CHF values for surfaces across the two boiling fluids. Experiments of SiO_2 in Novec 7000, A-Si in Novec 7100, and Parylene-C in Novec 7100 were tested for repeatability.

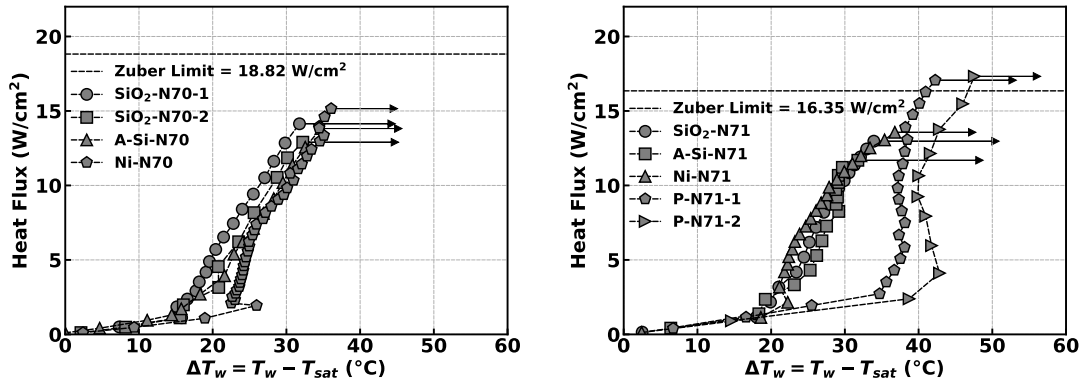

Figure 4.3: Boiling curves for surface experiments performed in Novec 7000 (left) and Novec 7100 (right). Also shown are the CHF values for the two fluids calculated using Zuber's expression (Equation (2.3)). The arrows represent the last data point before dry-out when heat flux is increased.

and Novec 7100 (right). While the boiling curves for SiO_2, A-Si, and Ni do not appear significantly different, the boiling curves for the Parylene-C surfaces in Novec 7100 exhibit a delayed onset of nucleate boiling along with markedly higher wall superheats (ΔT_w) in the nucleate boiling regime.

In reporting the experimental data in the foregoing sections, the heat flux along the boiling curve from an experiment is non-dimensionalized as

$$q^* = \frac{q}{q_{\text{CHF}}}$$

where q_{CHF} was the last heat flux before dry-out occurred in the experiment.

4.2 Statistical Distributions

The statistics of temperature fluctuations are first analyzed to determine whether the time series are stationary or non-stationary. In the most general sense, a time series is said to be stationary if the statistical moments (such as the mean, standard deviation,

etc.) of the time series stay constant regardless of the moment in time when the time series is sampled. Since the statistical moments also define the distribution density of values of the time series, stationarity implies that the distribution density stays constant too.

In practice, since there is often only one realization of a time series, stationarity requires that shorter segments of the time series also exhibit the same statistics as the parent time series. However, there exists a minimum segment size below which the definition of stationarity may be violated. For instance, if a time series captures some periodic

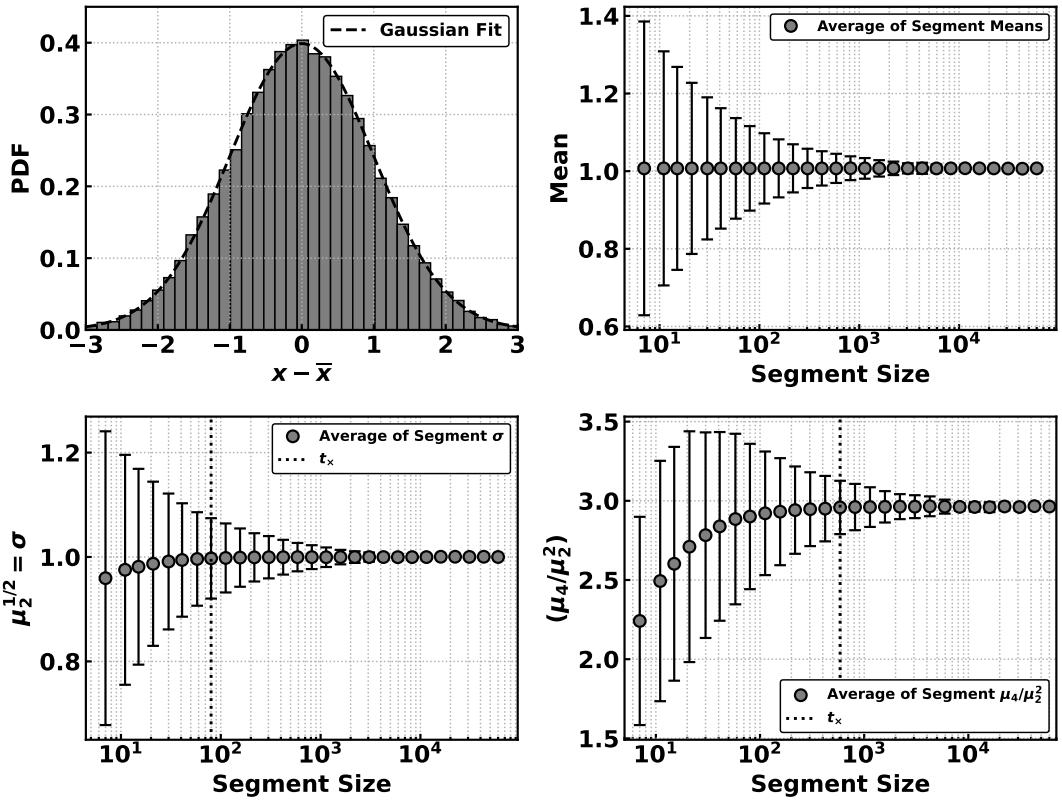

Figure 4.4: (Top-left) Probability density distribution of the white noise series with a Gaussian PDF overlaid. Variation in the mean (top-right), standard deviation (bottom-left) and kurtosis (bottom-right) as a function of segment size.

process with time period T over a long period $t \gg T$, segments of the time series spanning periods less than T will not exhibit the same statistics. Therefore, when testing for stationarity, care should be taken that the smallest segments of the time series considered span time scales larger than the largest time scale of the system. This idea is illustrated in Figure 4.4 which shows the probability density distribution of a synthetically generated white noise[3] time series, and the variation in the means, standard deviations ($\sigma = \mu_2^{1/2}$) and kurtosises (μ_4/μ_2^2) as a function of segment size. The white noise series of size $N = 60{,}000$ was synthetically generated by randomly sampling a Gaussian distribution with population mean and standard deviation values of unity. For any given segment size w, the time series was split into $N_w = \text{int}(N/w)$ number of non-overlapping segments of size w starting from the beginning and another N_w non-overlapping segments of size w starting from the end of the time series, for a total of $2N_w$ segments[4]. For each segment, the statistical moments (mean, standard deviation and kurtosis) were calculated such that for any moment, there were $2N_w$ values from the $2N_w$ segments. Finally, the average values of the moments were then plotted for the segment size w being considered, along with the root-mean-square error (RMSE) in the calculation of the average moment from the moments of the individual segments as error bars.

It is evident that the mean, standard deviation ($\mu_2^{1/2}$ or σ), and kurtosis (μ_4/μ_2^2) of the white noise time series all converge to the values expected for a Gaussian distribution[5], The rate of convergence, however, is slower for higher order moments. The average mean value for even the smallest segment size ($w = 8$) is 1.0 even though the RMSE in the estimation from segment means is very large. The average standard deviation and average kurtosis of the segments start at low values for the smallest segment sizes but increase and converge to their respective values by segment sizes of 80 points and 600

[3]White noise is stationary.

[4]This way neither data at the end or the beginning were neglected.

[5]The white noise was sampled from a Gaussian distribution of population mean and standard deviation values of unity. Additionally, the kurtosis of a Gaussian distribution is 3.

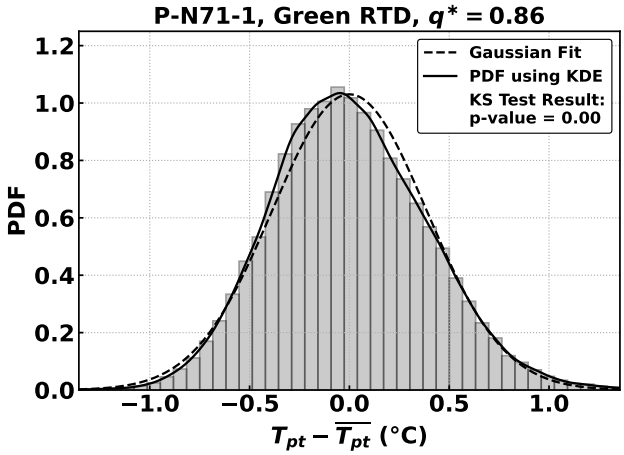

Figure 4.5: A continuous Probability Density Function (PDF) was estimated using Kernel Density Estimation.

points, respectively (vertical line labeled $t_\times$ in Figure 4.4). This is also expected as larger deviations $(x - \overline{x})$ contribute more to higher-order central moments ($\mu_m \sim (x - \overline{x})^m$), and since their probability of occurrence is low, larger segment sizes are required to ensure an appropriate number of the large deviations required for convergence.

4.2.1 PDFs of RTD Temperature Fluctuations

To obtain an estimate of the Probability Density Function of temperature fluctuations from an RTD, a discrete probability density distribution was first constructed, as shown in Figure 4.5. Then, the PDF was estimated using Kernel Density Estimation (KDE) [88], which uses weighted Gaussian kernels to estimate a continuous PDF for the given discrete distribution density. In Figure 4.5, the solid line is the estimated PDF from KDE and fits very well with the discrete distribution density. Also plotted is the a Gaussian distribution (dashed line) with the same population mean and standard deviation as with the temperature fluctuations.

Since the underlying distribution density and the estimated PDF appear Gaussian, the

S.No	Exp. Identifier	RTD	$q^* = q/q_{\text{CHF}}$
1	Ni-N71	Green	0.42
2	SiO_2-N71	Red	0.67
3	SiO_2-N71	Red	0.71
4	P-N71-1	Grey	0.11

Table 4.2: List of time series for which the KS test returned a p-value > 0.05 implying that the PDF was the same as the Gaussian distribution.

time series was tested for the likelihood of being drawn from a Gaussian distribution using the implementation of the Kolmogorov-Smirnov (KS) test [89] in the programming language Python. The KS test compares the continuous density function of the underlying data to that of a Gaussian distribution with the null hypothesis that the data is distributed according to a Gaussian distribution. If the p-value output by the test is less than 0.05[6], the null hypothesis is rejected, i.e. the data was not sampled from the Gaussian distribution. For the time series shown in Figure 4.5, a p-value of near zero implied that the underlying distribution density is not Gaussian despite appearing so.

The KS test was applied to all 642 time series that were acquired from the experiments. Only 4 time series (0.62% of the total number of time series acquired) returned a p-value greater than 0.05 and are listed in Table 4.2.

Figure 4.6 shows the PDFs of temperature fluctuations from a randomly chosen RTD for all experiments spanning a range of non-dimensional heat flux values ($q^* = q/q_{\text{CHF}}$) from ~ 0.25 to 1.0. The general observation is that at lower heat fluxes ($q^* < 0.7$), the fluctuations have a relatively narrow amplitude. As q^* increases, however, the PDFs spread out and tend to become positively skewed (see red lines corresponding to $q^* = 1.0$), implying that larger excursions from the mean towards higher temperatures are observed as the system approaches CHF. This likely reflects the longer periods of time the surface stays dry and hence, at higher temperatures. This pattern, however, is not

[6]A p-value of 0.05 corresponds to a confidence level of 95%.

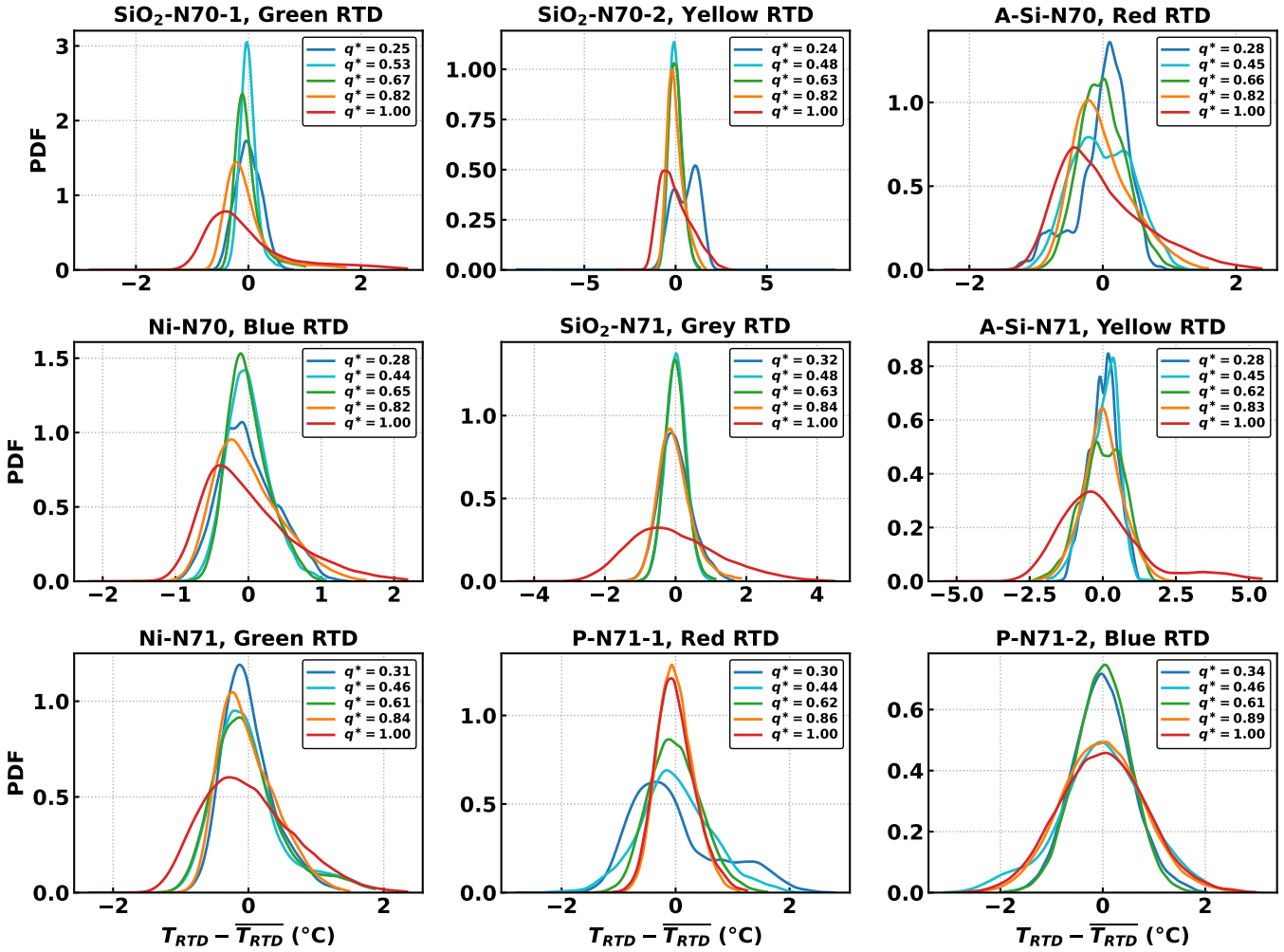

Figure 4.6: PDFs of temperature fluctuations from a arbitrarily chosen RTD for each experiment at non-dimensional heat flux values ($q^* = q/q_{\mathrm{CHF}}$) ranging from ~ 0.25 to 1.0.

followed by the temperature fluctuations of the Red RTD from the boiling experiment of Parylene-C in Novec 7100 (red line in the bottom-center plot labeled **P-N71-1**), which shows the reverse trend of spread out PDFs at low q^* becoming narrower and higher at high q^*. Also, the PDFs of the Blue RTD from the repeat run of Parylene-C in Novec 7100 (bottom-center plot labeled **P-N71-2**) spread out as q^* increases but stay symmetric and do not positively skew.

Figure 4.7 shows the PDFs of all working RTDs from the first experiment of Parylene-C in Novec 7100 (P-N71-1). For all RTDs, the PDFs become narrowest and highest at $q^* \sim 0.86$. The PDFs of Yellow, Green and Grey RTDs at higher q^* also seem more

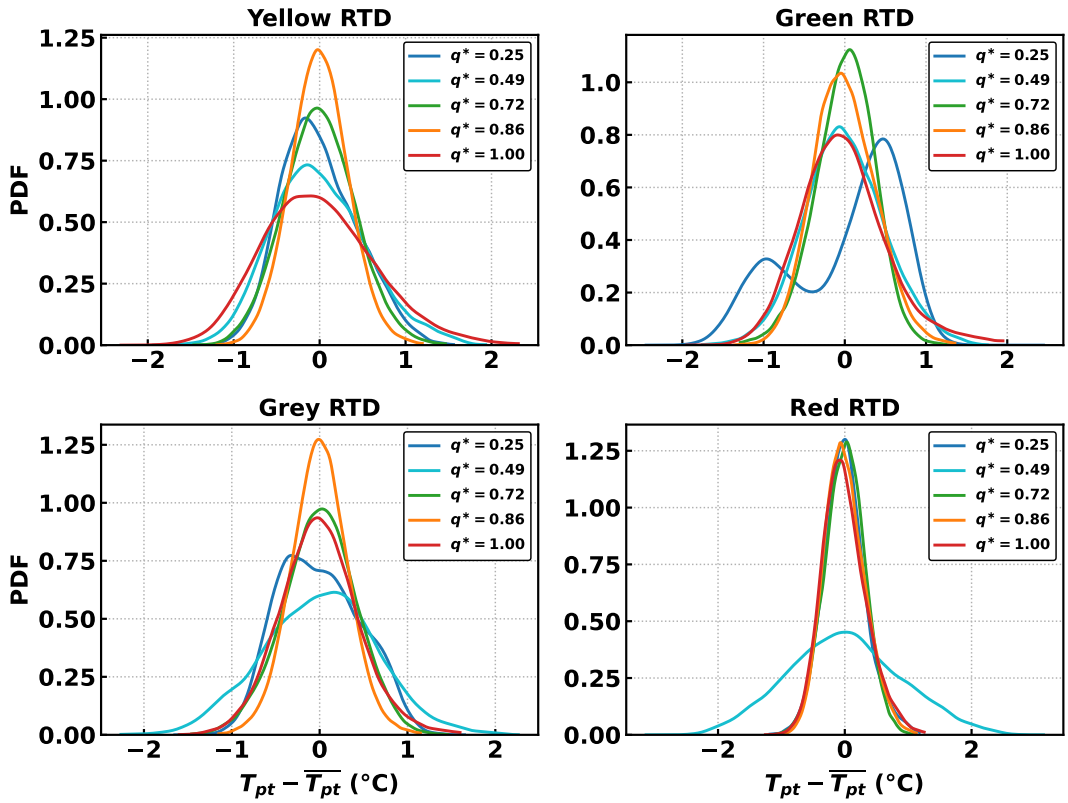

Figure 4.7: PDFs from all working RTDs from the boiling experiment of Parylene-C in Novec 7100 - Run 1.

symmetric than the PDFs at lower q^*. It should be noted that the boiling curve for the Parylene-C experiments in Novec 7100 presented the highest observable CHFs and the highest average wall superheat in the nucleate boiling regime (see Figure 4.3).

4.2.2 Variation of Statistical Moments with Segment Size

Figures 4.8 and 4.9 show the variation in mean, standard deviation ($\mu_2^{1/2} = \sigma$), and kurtosis (μ_4/μ_2^2) with segment size for non-dimensional heat flux values of ~ 0.5, 0.75, and 1.0. The choice of which experimental runs and RTDs are to be analyzed was arbitrary in both figures. Note that segment size refers to the duration (in s) that a segment spanned. Since the RTDs were sampled at 1000 Hz, a segment of 1000 data points, for instance, spanned 1 s.

As can be seen, the average of the segment means did not vary from the mean of the entire time series for even the smallest span of 8 ms considered for any q^*. The standard deviation and kurtosis, however, eventually converge, taking shorter segment sizes as q^* increases. This was a general trend that was observed approximately across all experiments and could be explained by an increase in bubble frequencies at higher heat fluxes. As bubble frequencies increase, increasingly shorter segment sizes are required to capture enough fluctuations to mimic the statistics of the entire time series.

Also note the overshoot in the kurtosis for $q^* \sim 0.5$ around segment sizes of $0.1 - 1.0$ s in both Figures 4.8 and 4.9 that was absent in the statistics of white noise (Figure 4.4). The initial increase in the kurtosis with the segment size is similar to that of white noise and is a result of more appropriately sized segments (which reflect the time series better) being considered. Once the highest average value is achieved at the mid-range segment sizes of $0.1 - 1.0$ s, however, the large excursions from the mean ($x - \overline{x}$), which contribute more to higher order moments ($\mu_m \sim (x - \overline{x})^m$), do not scale with span to maintain the higher average values. This occurs because at the relative low heat flux of $q^* = 0.5$, large excursions from the mean are not as common as those at higher heat

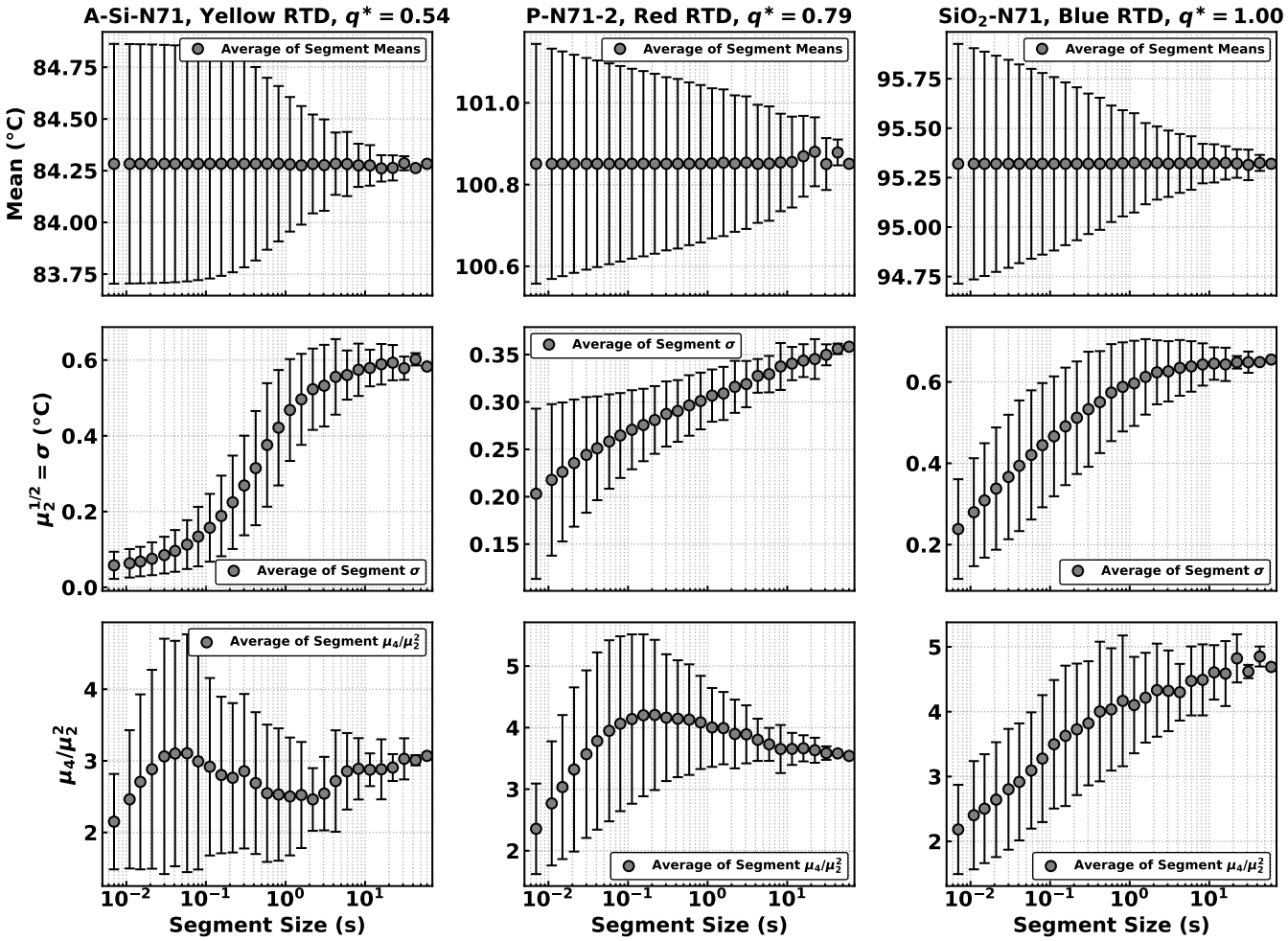

Figure 4.8: Variation in mean (top row), standard deviation (middle row) and kurtosis (bottom row) of temperature fluctuations with segment size at $q^* \simeq 0.50$, 0.75, and 1.0. Each column corresponds to temperature fluctuations from an arbitrarily chosen chosen experimental run and RTD.

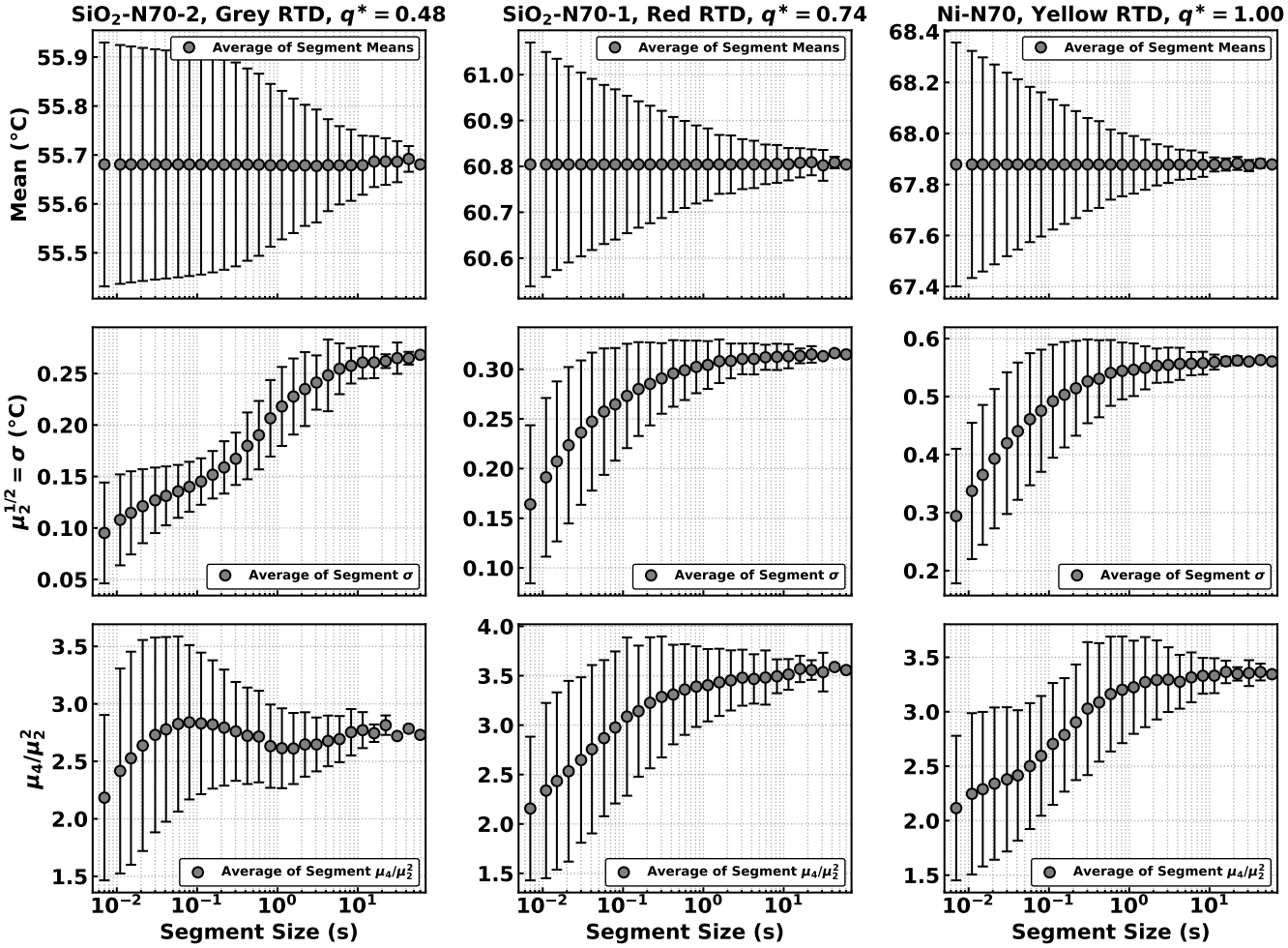

Figure 4.9: Variation in mean (top row), standard deviation (middle row) and kurtosis (bottom row) of temperature fluctuations with segment size at $q^* \simeq 0.50$, 0.75, and 1.0. Each column corresponds to temperature fluctuations from an arbitrarily chosen chosen experimental run and RTD.

fluxes.

It should also be noted that the increase in convergence time with the order of the moment (for the same time series) is not universal. In the statistics of white noise, the convergence time (dashed lines labelled $t_\times$ in Figure 4.4) for standard deviation was an order of magnitude faster than the same for kurtosis. In all of the RTD temperature fluctuations shown in Figures 4.8 and 4.9 however, the convergence time for kurtosis is comparable to convergence time for standard deviation.

4.2.3 Variation of Statistical Moments with q^*

Figure 4.10 shows the evolution of the standard deviation ($\mu_2^{1/2} = \sigma$), skewness ($\mu_3/\mu_2^{3/2}$), and kurtosis (μ_4/μ_2^2) with the non-dimensional heat flux ($q^* = q/q_{\text{CHF}}$). To avoid clutter, two measures are taken. Firstly, the experiments carried out in Novec 7000 and Novec 7100 are presented separately in the left and the right columns of the figure, respectively. Secondly, for each experiment at a given q^*, the mean of the statistical moments from all working RTDs is presented.

The standard deviations for all experiments collapse remarkably well for the experiments carried out in Novec 7000 while there is considerable spread for the experiments in Novec 7100. At low q^* values, the experiments with Parylene-C surfaces, which were also noted for the higher wall superheats cases and symmetric PDF cases earlier, stand out from the rest. At higher q^* values, the curve for A-Si in Novec 7100 (A-Si-N71) also diverges from the other curve with higher values of standard deviation. As will be explained through Power Spectral Density (PSD) figures in the next section, this could be attributed to noise in the fluctuations which were conspicuously absent at lower q^* values for the same experiment.

The skewness, which represents the asymmetry for Gaussian-like distrbutions was noted to be positive at higher q^* values when discussing PDFs. That fact is borne out in the

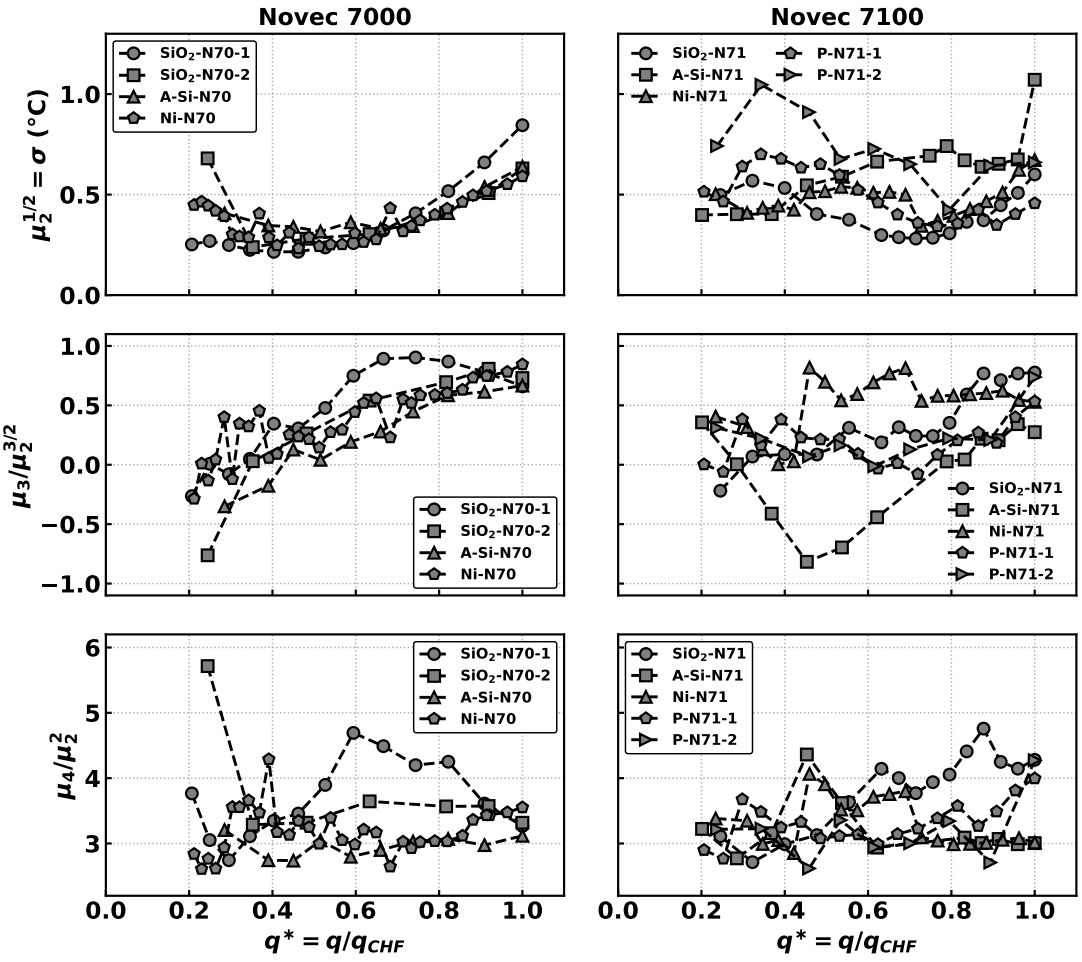

Figure 4.10: Evolution of statistical central moments of orders 2, 3 and 4 (standard deviation, skewness, and kurtosis, respectively) along the boiling curve. To avoid clutter, the mean of the statistical moments from all working RTDs is presented for each experiment at any given q^*.

values of skewness which are larger than 0 at higher q^* values. The postive skewness at higher q^* values is attributed to large, positive excursions from the mean, which were more frequent at high heat fluxes as the surface conditions proceed towards dry-out. Again, the only significant outlier is the experiment of A-Si in Novec 7100 (A-Si-N71), which drops to a minimum skewness of ~ -0.8 before reversing course and becoming

positively skewed like the other curves.

Finally, the kurtoses, which represents distributions with heavy-tails relative to those of the Gaussian distribution, behave erratically with no clear trend. A value larger (or smaller) than 3.0 implies that the tail of the distribution is heavier (or lighter) than that of the Gaussian distribution. This means that the likelihood of large excursions (positive or negative) from the mean is more likely for the distribution under consideration than expected from a Gaussian distribution. It is interesting to note that experiments with SiO_2 in either fluid exhibited kurtosis values that are significantly larger than 3.0 but it is uncertain why this occurred.

4.3 Frequency Spectrum Analysis

Figure 4.11 shows representative 2-s segments of RTD fluctuations and their corresponding Power Spectral Densities (PSDs) at moderate and high q^* values of ~ 0.5 and ~ 0.85. For $q^* = 0.48$, the 2-s segment shows multiple cycles of the typical, sawtooth-like rise and fall of temperatures under a nucleating bubble, as has been reported in studies like Kenning (1996) [62]. It should be noted, however, that the rise and fall are aperiodic and intermittent, which is reflected in the corresponding PSD by the absence of a dominant frequency. The 2-s segment for $q^* = 0.84$ also shows the sawtooth-like waves, but with a more noise-like behavior along the entire segment. This is reflected in values of the PSDs at $f > 60$ Hz, which are higher for $q^* = 0.84$, and the slope of drop-off of the PSD is also more gradual (PSD $\sim f^{-1.10}$) than for the case of $q^* = 0.48$ (PSD $\sim f^{-1.23}$).

Figure 4.12 shows another instance of 2-s segments of RTD fluctuations and their corresponding PSDs at moderate and high q^* values of ~ 0.5 and ~ 0.8. For $q^* = 0.48$, note that the PSD flattens, relatively speaking[7], for frequencies greater than 60 Hz. This

[7]For $q^* = 0.48$ at $f > 60$ Hz, the PSD is shown to scale first as $f^{-0.53}$ and then as $f^{0.69}$. This is because the slopes were determined using a algorithm which detected changes in slope, and as the PSD

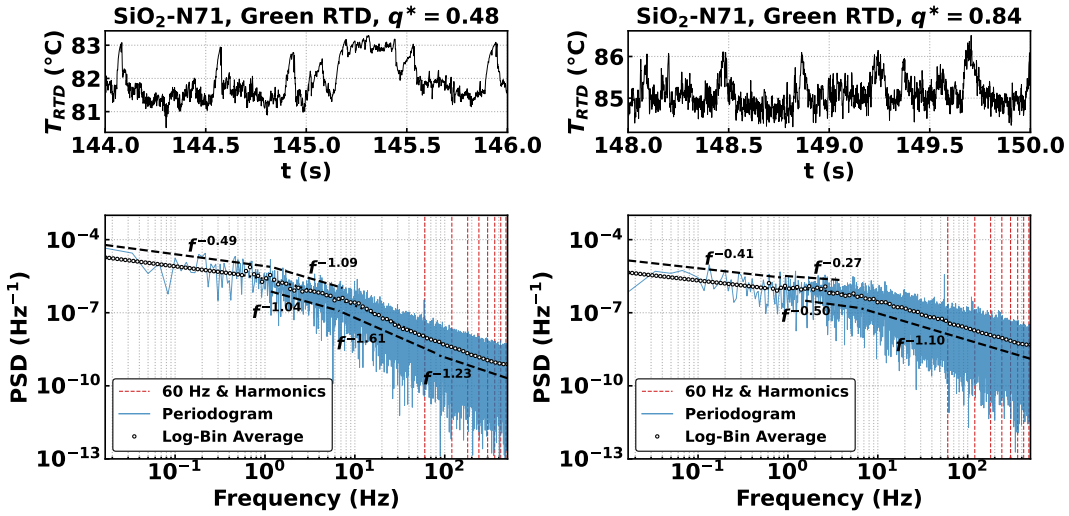

Figure 4.11: Representative Power Spectral Densities. The temperature fluctuations were taken from the Green RTD in a boiling experiment of SiO_2 surface in Novec 7100.

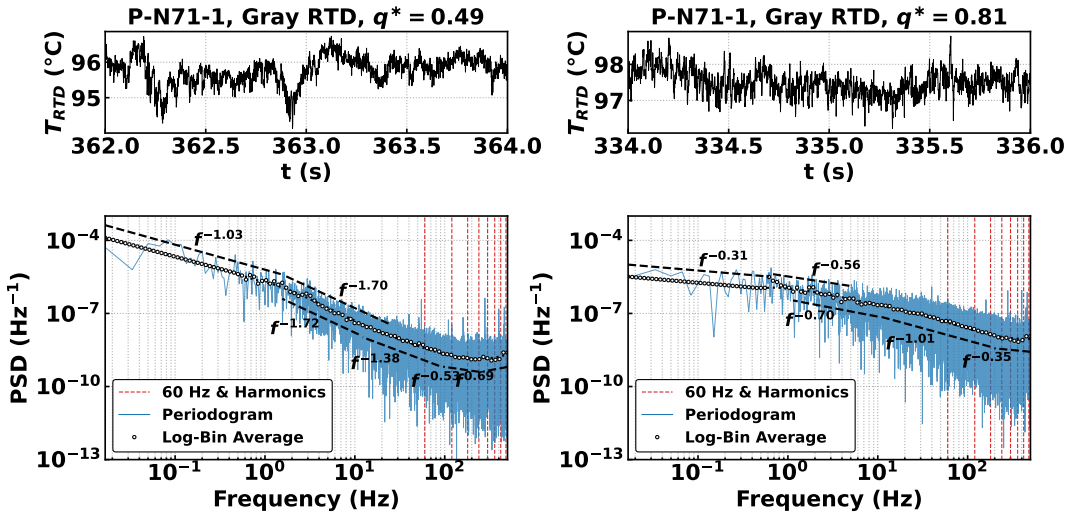

Figure 4.12: A separate set of PSDs showing PSD curve flattening out at the highest frequencies. The temperature fluctuations were taken from the Gray RTD in first boiling experiment of the Parylene-C surface in Novec 7100.

flattened, it detected two different slopes. As is visually evident, however, the slope is near zero (the average of the two slopes detected by the algorithm).

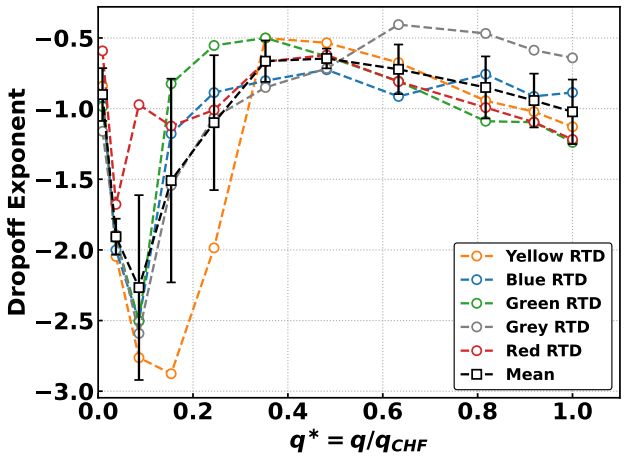

Figure 4.13: The evolution of the scaling exponent of PSD vs. frequency (PSD $\sim f^m$) in the range 6 Hz $\leq f \leq$ 60 Hz. The evolution curve is for the repeat boiling experiment of SiO_2 surface in Novec 7000 (SiO_2-N70-2).

effect is especially pronounced in the PSD for $q^* = 0.49$.

The scale-free nature of the temperature fluctuations is evident from the PSDs presented above. Scale-free behavior in quanties measured during boiling has also been observed by Skokov et al. (2010) [72] and Lloveras et al. (2012) [73]. In the absence of characteristic scales, the dynamics of the system may be characterized by the drops in the PSDs instead. Figure 4.13 shows the drop of the power law exponent for the repeat boiling experiment of SiO_2 in Novec 7000 (SiO_2-N70-2) for all the RTDs. The drop-off exponent was estimated by considering only the PSD in the range of 6 Hz $\leq f \leq$ 60 Hz (spanning a decade). This was because in some experiments (see Figure 4.12), the PSD flattened (or started to) at $f \geq 60$ Hz. This also had the desired effect of neglecting line noise and harmonics, which affected only the frequencies at 60 Hz or higher, if and when present. Also plotted in Figure 4.13 is an average curve corresponding to the average values of the exponents from the working RTDs at each q^*.

Figure 4.14 compares the average curves from all experiments, with the curves for

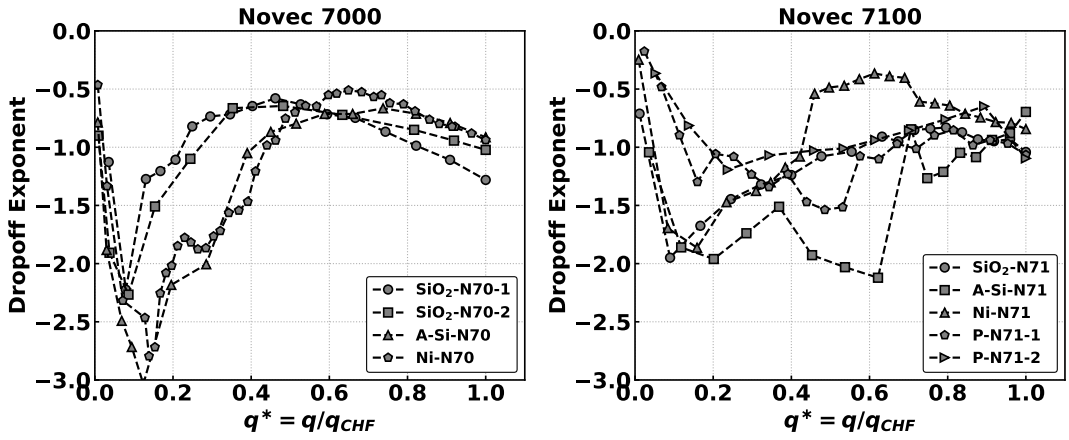

Figure 4.14: The evolution of the scaling exponent of PSD vs frequency (PSD $\sim f^m$) in the range 6 Hz $\leq f \leq$ 60 Hz for all surface experiments. For each experiment, the curve represent the average values of the exponents from all working RTDs.

experiments in Novec 7000 and Novec 7100 plotted separately to avoid clutter. The average curves for experiments in Novec 7000 first drop to values below -2.0 after which they start increasing. Note that the first few points in all experiments corresponded to the natural convection regime with no bubble nucleation. After the Onset of Nucleate Boiling (ONB, at $q^* \sim 0.1$), the drop-off exponents increase until a maximum value is achieved at moderate $q^*(\sim 0.5)$. Beyond this point, the drop-off exponents decrease again and converge to a value of $\sim$ -1.0 at dry-out. The curves for Novec 7000 also appear to collapse.

The average curves for experiments in Novec 7100 are more spread out and do not collapse so well as they do for experiments in Novec 7000. Also, the dropoff exponents appear to follow a general trend of monotonic increase from ONB to dry-out. However, there are two similarities in the average curves across the fluids. Firstly, the dropoff exponents initially decrease to lower values before the ONB at $q^* \sim 0.1$. Secondly, the dropoff exponents all converge to a value of -1.0 at dry-out.

Finally, Figure 4.15 shows 2-s segments of RTD fluctuations and their corresponding

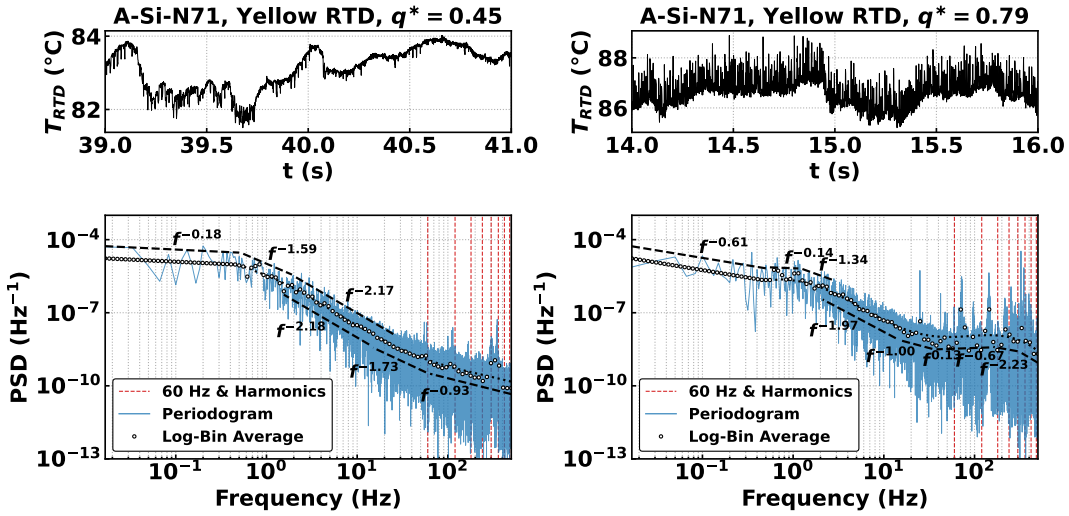

Figure 4.15: The PSDs show the presence of noise in temperature fluctuations at high $q^* = 0.79$ relative to a moderate $q^* = 0.45$ for the boiling experiment of A-Si in Novec 7100 (A-Si-N71).

PSDs at moderate and high q^* values of ~ 0.5 and ~ 0.8 for the boiling experiment of A-Si in Novec 7100 (A-Si-N71). As was noted in Section 4.2.3, the variation in the statistical moments with q^* for A-Si-N71 were outliers. The 2-segment segment and the corresponding PSD at $q^* = 0.45$ show a low level of noise present (small peaks in the PSD for $f \geq 60$ Hz). At $q_* = 0.79$, however, the PSD for $f \geq 60$ Hz shows a significantly increased level of noise, and this is also reflected in the 2-s segment. The likelihood of these peaks corresponding to a boiling phenomena are low since they were not observed in any of the other experiments. Since these peaks presented themselves at frequencies other than 60 Hz or its harmonics, it was not filtered out during the digital filtering process.

4.4 Autocorrelation Function Analysis

For further insight into the statistics of fluctuations, and to check for the presence of long-term temporal correlations, the Auto-Correlation Function (ACF) is analyzed. The auto-correlation function, ACF(k) for a given lag $k \geq 0$, is defined as

$$\mathrm{ACF}(k) = \frac{1}{\sigma^2}\left(\frac{1}{N-k}\sum_{i=1}^{N-k}(x_i - \bar{x})\,(x_{i+k} - \bar{x})\right)$$

where (x_i, $i = 1, ..., N$) is the i-th observation in a time series of N equidisitant measurements, $\bar{x}$ is the mean of the time series, and σ is the standard deviation of the time series.

ACF(k) is a measure of how well a time series is correlated with a delayed copy of itself with lag k. The range of ACF(k) is $-1 \leq \mathrm{ACF}(k) \leq 1$. Since a time series is perfectly correlated with itself, ACF($k = 0$) $= 1$ is trivial.

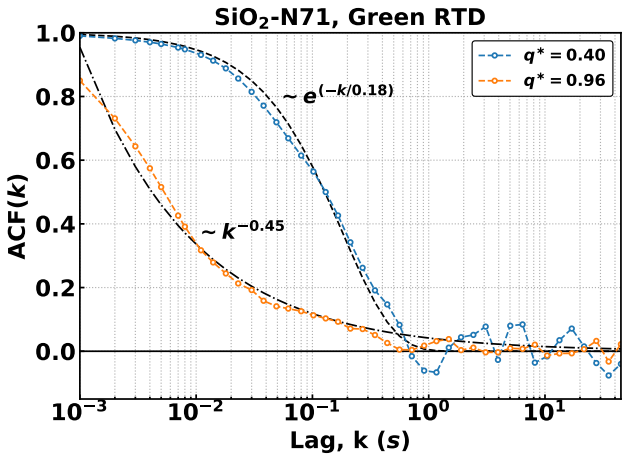

Figure 4.16: Decay of ACF(k) for RTD temperature fluctuations at moderate and high q^* values. The temperature fluctuations were taken from the Green RTD in the boiling experiment of SiO_2 in Novec 7100 (SiO_2-N71).

The decay of ACF(k) with k characterizes whether a time series has any long- or short-range correlations. In a white noise time series, where any observation is entirely uncorrelated with all future observations, even in its immediate vicinity, ACF(k) $\simeq 0$ for all $k > 0$. For time series with short-term correlations, either ACF(k) drops to zero after a certain lag, or it eventually has an exponential decay (ACF(k) $\sim \exp(-k)$). This occurs because the correlation between a pair of values in the time series at separation of k apart decreases rapidly as k increases. For a time series with long-term correlations, however, the correlations persist even as k increases and, therefore, ACF(k) declines as a power-law (ACF(k) $\sim k^{-\gamma}$, $0 < \gamma < 1$), which is a slower decay than an exponential decay.

Figure 4.16 illustrates the representative decay of ACF(k) for RTD temperature fluctuations at a moderate and a high q^*. It is evident that temperature fluctuations for $q^* = 0.40$ and 0.96 decay exponentially ($\sim \exp(-k)$) and as a power-law ($\sim k^{-\gamma}$), respectively.

Figure 4.17 shows the change in the nature of ACF(k) decay across five values of $q^* \simeq$ 0.25, 0.4, 0.7, 0.85, and 1.0 for all experiments. The choice of which RTD to consider for any experiment was arbitrary. The general trend across all experiments is that at low q^* values of 0.25 and 0.4, ACF(k) decays exponentially, indicating that the temperature fluctuations are short-term correlated. At moderate and high values of q^*, ACF(k) decays as a power-law, indicating long-term correlations in the time series.

Note the scatter in the curves for $q^* = 0.83$ and 1.0 for A-Si-N71, $q^* = 0.69$ for Ni-N71, and $q^* = 0.89$ for P-N71-2. By examining the PSDs of those particular time series (Figure 4.18), the scatter in the ACFs is attributed to noise at frequencies other than 60 Hz, and its harmonics. It is unlikely that the peaks in the PSDs correspond to some cylic process during boiling because of its intermittent presence in a few temperature fluctuations only. Despite multiple measures taken to reject noise at all levels, some

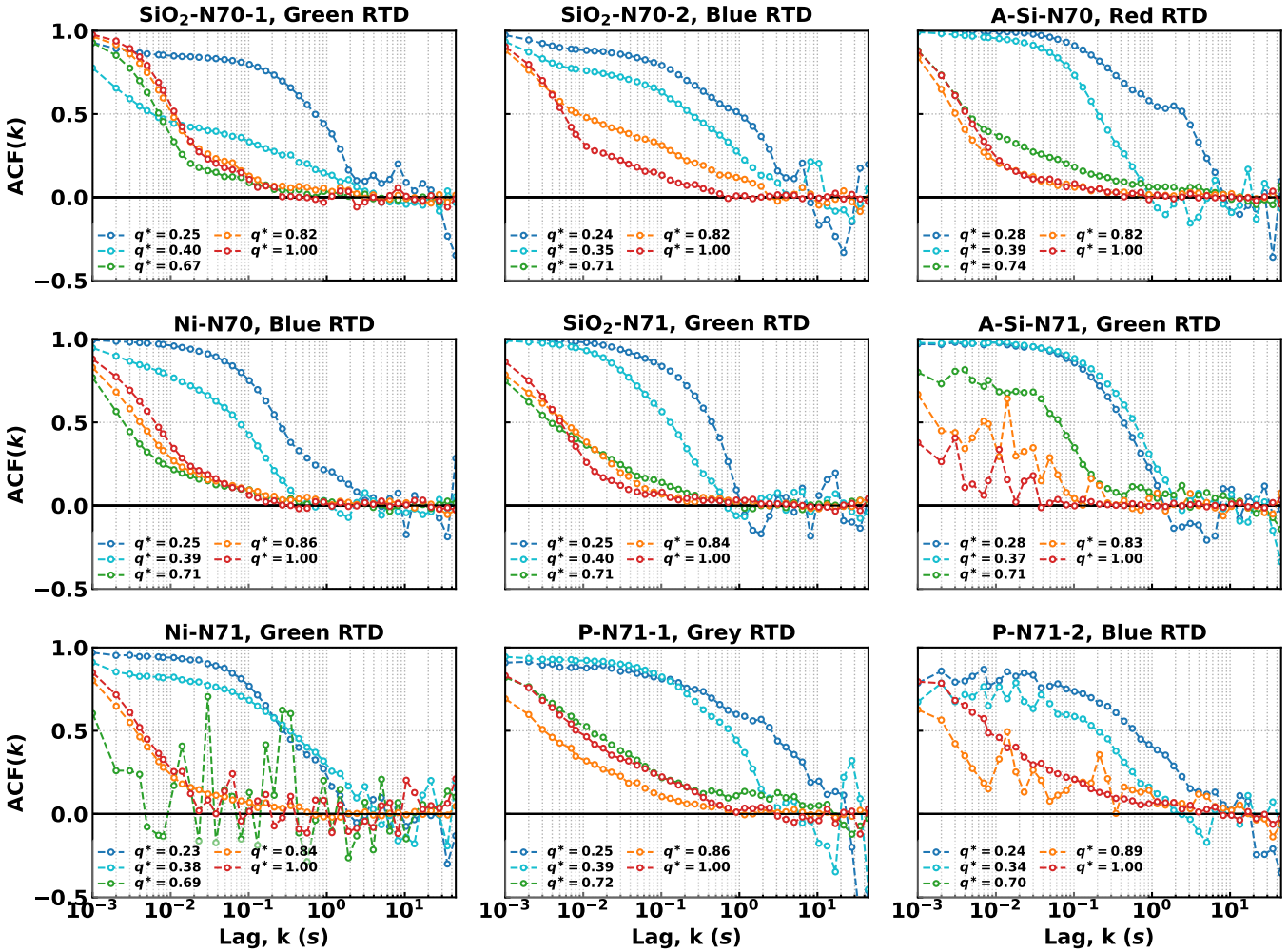

Figure 4.17: Decay in Auto-Correlation Functions (ACF) across all experiments. For each experiment, ACF(k) is plotted for an arbitrarily chosen RTD at $q^* \simeq 0.25$ (blue), 0.4 (cyan), 0.7 (green), 0.85 (orange) and 1.0 (red).

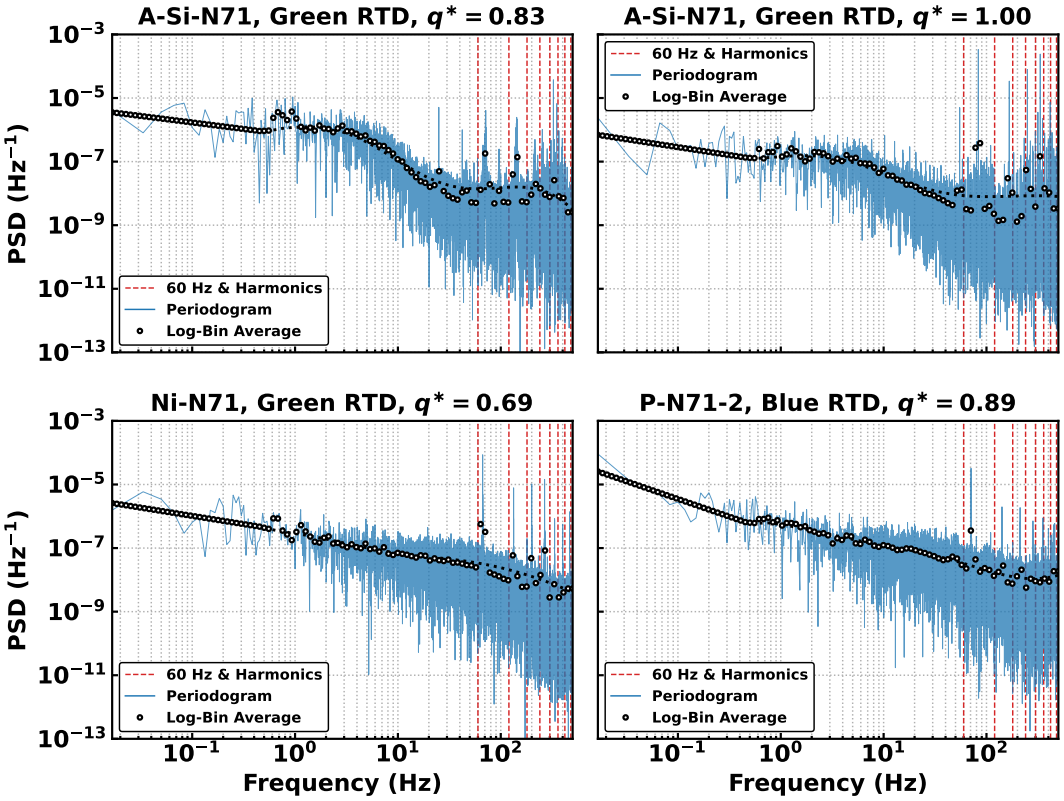

Figure 4.18: PSDs of temperature fluctuations that show scatter in ACF(k) vs. k plots in Figure 4.17. Significant noise is present at various frequencies.

temperature fluctuations still showed significant peaks. Notwithstanding the few noisy temperature fluctuations, the change in the decay of ACF(k) of temperature fluctuations suggests that long-term correlations are present in temperature fluctuations at high heat fluxes close to dry-out. In the next section, characterizing these long-term correlations while rejecting the noise in temperature fluctuations (when present) is discussed.

4.5 Hurst Exponent Analysis

As was noted in the last section, the computation of ACF(k) is sensitive to noise present in the temperature fluctuations. The ACF(k) also strongly fluctuates around zero when

the lags, k, are large. Therefore, it is unreliable to make deductions from ACF(k) about long-term correlations if they are weakly present. Instead, long-term correlations are characterized using the Hurst Exponent, H.

The Hurst Exponent, H, is a measure of the extent of long-range dependence in a time series. Its interpretation may best be understood by examining how it is estimated using a method called **Detrended Fluctuation Analysis (DFA)**.

4.5.1 Interpretation and Estimation of the Hurst Exponent

To calculate H given a time series x_i, $i = 1, ..., N$, the series is first mean-adjusted to remove a constant trend as

$$\widetilde{x_i} = x_i - \bar{x}$$

The mean-adjusted time series is then integrated to get a partial sum series, y_i, $i = 1, ..., N$ as

$$y_i = \sum_{j=1}^{i} \widetilde{x_i}$$

Mean-adjusting the time series has the effect of transforming the values of the time series into positive or negative values relative to the mean, such that they either increase or decrease the partial sum, when integrated. A time series that has positive ACK(k) for small lags, k, is more *likely* (i.e. with a high statistical probability) to have positive or negative values clustered together, which would cause the partial sum to stray away from the origin. On the other hand, a time series that has negative ACF(k) for small lags k would cause the partial sum series to revert to the mean (or origin for a mean-adjusted time series).

For an uncorrelated time series, however, where ACF(k) $\simeq 0$ for all $k > 0$, like for

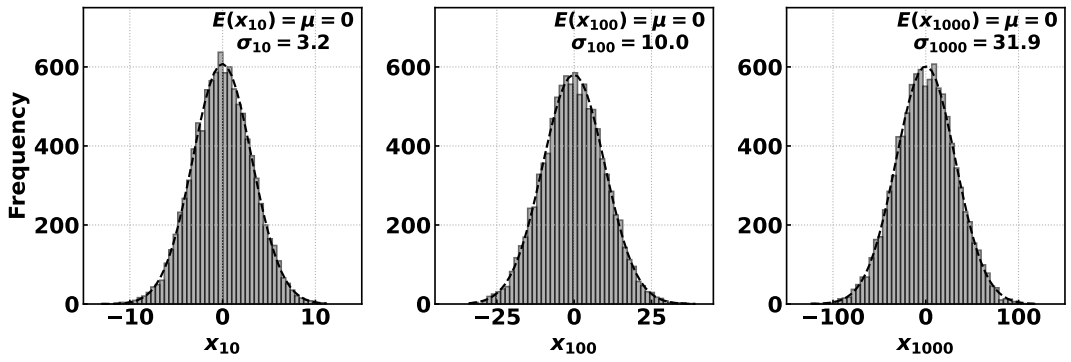

Figure 4.19: Distribution of the x_{10} (left), x_{100} (center), and x_{1000} (right) for 10,000 realizations of random walk. The mean of the distribution does not change but the distribution spreads out and the standard deviation scales as $i^{1/2}$.

white noise, the likelihood of a positive or negative value following any other value is equal. Integrating a mean-adjusted white noise series to get the partial sum series has the effect of creating a random walk series. The i-th element of the random walk series represents the location of a random walker relative to the origin after i steps.

Since the random walk series is created as the partial sum series of mean-adjusted white noise, the expected value of a random walk series at any step i is 0, $E(y_i) = 0$, $i = 1, ..., N$, as adding i randomly, positive or negative numbers should result in 0. This result in trivial but is illustrated in Figure 4.19, which shows distributions of x_{10}, x_{100}, and x_{1000} for 10,000 realizations of random walk. The distributions are Gaussian centered around 0, but the standard deviations of the distributions increase (note the increase in the scaling of the x-axis) as i increases. In fact, $\sigma_{1000}/\sigma_{100} = \sigma_{100}/\sigma_{10} = 10^{1/2}$. This scaling law is a well-known property of random walks and implies that the standard deviation of the distribution of values of a one-dimensional random walk process after i steps scales as $i^{1/2}$.

The scaling law also implies non-stationarity. If a single realization of random walk series of length N, which has a standard deviation of σ_N, is segmented into an arbitrary

number of smaller segments of length w, the distribution of the standard deviations of the smaller segments will center around $\sigma_N(w/N)^{1/2}$. In general, the standard deviation depends on the length of time series such that one can write $\sigma \sim t^{1/2}$, where t is the time of observation. The estimation of the Hurst Exponent found by using the Detrending Fluctuation Analysis (DFA) method is based on this scaling law of a random walk.

In DFA, the partial sum series $y_i, i = 1, ..., N$ is split into $N_w = \text{int}(N/w)$ non-overlapping segments of size w starting from the beginning and another N_w non-overlapping segments of size w starting from the end of the time series, for a total of $2N_w$ segments[8]. In order to remove any local trends in the segments due to non-stationarities, a local linear fit $\bar{y}_i$ is made to each segment y_i and the structure function, F_w^2, for a given segment size w, is calculated as

$$F_w^2 = \frac{1}{2N_w} \sum_{i=1}^{2N_w} \left(\frac{1}{w} \sum_{j=1}^{w} \left(y_j - \bar{y}_j \right)^2 \right)^{1/2}$$

Based on the definition above, the structure function is the average value (across all $2N_w$ segments) of the root-mean-square-error of the partial sums about the local linear fit. The Hurst Exponent, H, is estimated as the slope of the linear regime on a double-logarithmic plot of F_w^2 for each span sizes w.

Figure 4.20 shows the scaling of the structure function against the segment size, w, for a synthetically generated sine wave (periodic signal) and for white noise, and for RTD temperature fluctuations at $q^* = 0.48$ and 1.0 from the boiling experiment of SiO_2 in Novec 7100. The structure function of the periodic signal stays constant. This is because the partial sum series of a periodic signal will also be periodic, and, even though the sum, $\sum \left(y_i - \bar{y}_i \right)^2$, increases as w increases, the increase is by the same factor such that the value of the structure function stays constant. Therefore, a periodic signal is characterized by $H = 0$.

[8]This way, neither data at the end or the beginning were neglected.

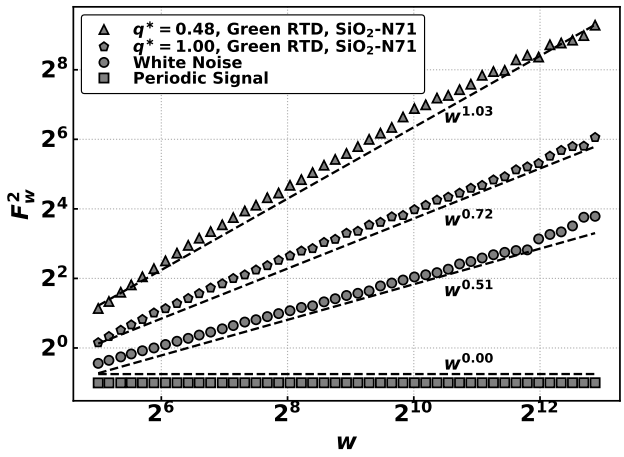

Figure 4.20: Comparison in scaling of Structure Functions, F_w^2, with segment size, w, for a synthetically generated sine wave (periodic signal) and white noise, and RTD temperature fluctuations at $q^* \simeq 0.5$ and 1.0 from one of the RTDs of the boiling experiment of a SiO_2 surface in Novec 7100 (SiO_2-N71).

The structure function of random walk scales as $w^{1/2}$ for the reason discussed beforehand, hence, $H = 0.5$. Therefore, $H = 0.5$ indicates that the original time series is **uncorrelated**. The range of $0 < H < 0.5$ corresponds to long-term anti-correlations and implies that the original time series has a propensity to revert to the mean, with the strength of mean reversion being higher as H approaches 0. In the original series x_i, positive fluctuations (about the mean) are likely (i.e., with high statistical probability) to be followed by negative fluctuations. Time series with $H < 0.5$ are called **anti-persistent**.

A value of $H > 0.5$ implies long-term positive correlations. As discussed before, for a positively correlated series, positive or negative fluctuations (about the mean) are likely to cluster together such that the partial sum series spends more time straying away from the mean than does a random walk series. Therefore, time series with $H > 0.5$ are called **persistent**. The higher the value of H, the more persistent is the time series.

It should be noted that while $H > 0.5$ implies persistence and positive or negative fluctuations clustering together, the reverse is not true. For instance, for a periodic signal like a pure sine wave sampled at a rate faster than its time period, positive and negative fluctuations cluster together, but $H = 0$ for the reason explained earlier. Therefore, persistence should only be deduced from the estimation of H.

4.5.2 Crossover in Scaling of Structure Functions and Range of Segment Sizes in Evaluation of H

Short-term correlated time series are characterized by a finite characteristic correlation decay time, $t_\times$, beyond which all correlations are destroyed. This leads to a crossover in the scaling behavior of the structure functions of the partial sum series. While $H > 0.5$ is observed (indicating correlations) over a range of segment sizes, w, the asymptotic behavior (for large segment sizes w) is always characterized by $H \to 0.5$, since all correlations have decayed. There may also exist time series with both short-term and long-term correlations since crossovers in the scaling behavior of time series may also be caused by different regulation mechanisms (that generate the time series) on fast and slow time scales. Therefore, one has to be careful in choosing the range of segment sizes w over which H is estimated.

Small deviations in the structure function scaling from the scaling law occurs for small segment sizes, w. These deviations are intrinsic to the DFA method, as the scaling behavior is approached only asymptotically. The deviations limit the capability of DFA to determine the correct correlation behavior in very short records and in the regime of small w. If the regime of small w is used in the fitting procedure to determine H, it will result in an overestimation. In addition to this, noise present in the RTD temperature fluctuations at high frequencies (peaks in the PSD at $f \geq 60$ Hz) also affect the scaling behavior since it is periodic and causes an underestimation of H[9]. The effect of small

[9]This is because for purely periodic signals, $H = 0$

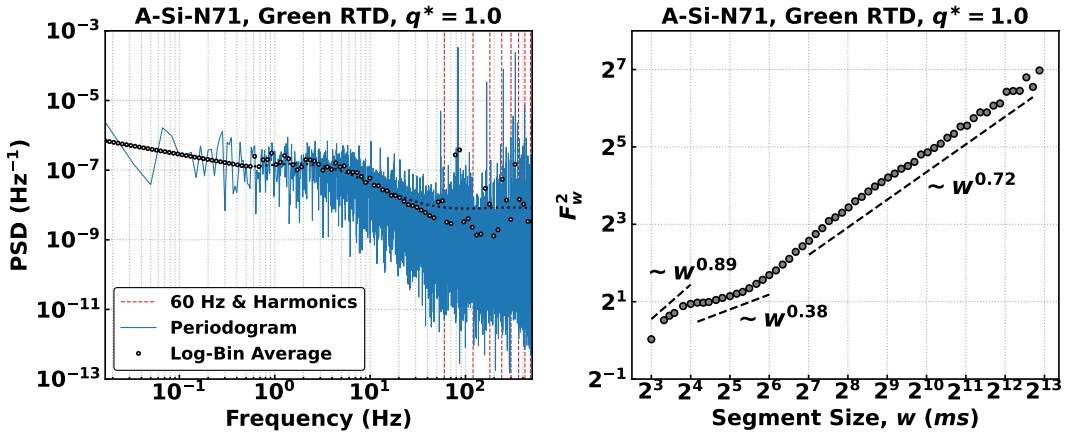

Figure 4.21: (Left) PSD of temperature fluctuations from the Green RTD in the boiling experiment of A-Si in Novec 7100 (A-Si-N71) which shows significant peaks at $f \gtrsim 60$ Hz corresponding to noise. (Right) Deviations in the scaling of the structure function at small $w < 2^7$ ms $= 128$ ms.

segment size, w, and noise in RTD temperature fluctuations in overestimating and underestimating H, respectively, are shown in Figure 4.21. The temperature fluctuation chosen was from the boiling experiment of A-Si in Novec 7100 (A-Si-N71) for $q^* = 1.0$, which had a very significant level of noise at $f \gtrsim 60$ Hz, as can be seen in the PSD on the left. Note that in the figure on the right, the structure function, F_w^2, first scales as $w^{0.89}$ until $w = 2^4$ ms $= 16$ ms, then as $w^{0.38}$ until $w = 2^6$ ms $= 64$ ms before it converges to scaling as $w^{0.72}$ for (2^7 ms $= 128$ ms $< w < 2^{13}$ ms $= 8.192$ s). The initial steep increase at $w^{0.89}$ is attributed to the small segment size resulting in overestimation of H. The slow increase as $w^{0.38}$ in the range 16 ms $< w <$ 128 ms is attributed to the periodic noise, the earliest, most significant peak of which is observed at $f \approx 55$ Hz in the PSD. A frequency of 55 Hz corresponds to a time period of $1/f = 18$ ms, which coincides with the point where the scaling exponent changes from 0.89 to 0.38. It is not until $w = 128$ ms that F_w^2 begins scaling as $w^{0.72}$ up to the largest segment size of $w = 8.129$ s.

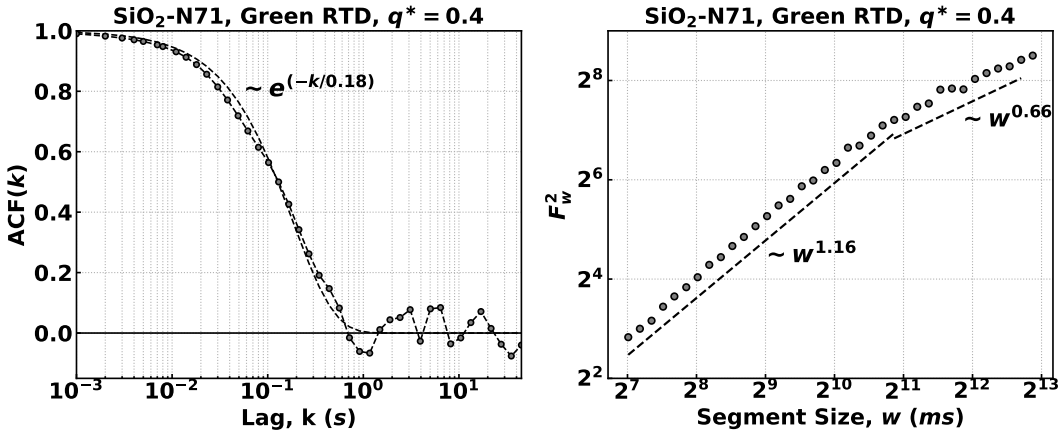

Figure 4.22: (Left) Decay of ACF(k) in temperature fluctuations from the Green RTD in the boiling experiment of SiO_2 in Novec 7100 (SiO_2-N71) which suggests short-term correlations are destroyed around $k \approx 1$ s. (Right) Deviations in the scaling of the structure function at large $w > 2.048$ s.

At the higher end of segment sizes, the results of DFA become statistically unreliable for segment sizes, w, larger than one-fourth the length of the time series. For instance, for $w = N/4$, there are only four segments of the time series over which the structure function is calculated. This results in a bad estimation in F_w^2 for large w and is evident in the scatter present in Figure 4.21 for $w > 2^{12}$ ms $= 4.096$ s. For this reason, the segment sizes were limited to $w = N/4$.

Since correlations are destroyed for short-term correlated time series beyond a crossover time, the structure function scaling changes to $H \to 0.5$ for large w. This can be seen in Figure 4.22. The exponential decay of ACF(k) suggests that all correlations are destroyed for $k \gtrsim 1$ s. Subsequently, the scaling of the structure function changes from $w^{1.16}$ to $w^{0.66}$ beyond $w = 2^{11}$ ms $= 2.048$ s.

Note that at both small and large w, the change in the scaling law occurs gradually over a short span of w such that the effects are delayed. Based on the observations above, H was estimated as the scaling exponent of F_w^2 over the range of w in 128 ms$< w < 2.048$

s. The choice of the lower bound of 128 ms was informed by the intermittent presence of noise around $f \gtrsim 60$ Hz in a few of the temperature fluctuations, while the upper bound of 2.048 s was selected based on Figure 4.17, which showed that the earliest time beyond which short-term correlations were destroyed was 1 s for the short-term correlated time series at low and moderate q^* values in the boiling experiment of a SiO_2 surface in Novec 7100 (SiO_2-N71).

A final note regarding the error in estimation of H by DFA: The accuracy of H determined by DFA was studied as a function of the length N of the time series by Bashan et al. (2008) [90]. They synthetically generated series with known values of H using a process called Fourier Filtering[10] and compared values of H estimated from DFA to the known values. Their results showed that statistical standard errors in estimation of H (one standard deviation) were approximately 0.1 for $N = 500$, 0.05 for $N = 3{,}000$, and reach 0.03 for $N = 10{,}000$. Since $N = 60{,}000$ for the RTD temperature fluctuations, the error in estimation of H is less than 0.03.

4.5.3 Results of Hurst Exponent Analysis

The evolution of H as a function of q^* is shown in Figure 4.23 for all surface experiments performed. For all the working RTDs in every experiment, H was calculated as the scaling exponent of F_w^2 with w ($F_w^2 \sim w^H$) in the range of 128 ms $< w <$ 2.048 s. Also shown is the mean value of H at every q^*. The steady decrease in H from values of 1.6 to ~ 0.8 suggests that as the surface conditions proceeded toward dry-out, the degree of persistence of temperature fluctuations is reduced. At $q^* > 0.75$ the evolution of H plateaued and hovered around 0.8 in most experiments.

Figure 4.24 plots the mean value curves of H from all the experiments on two plots for comparison. The general trend is that $H > 1.0$ for low q^*, implying a high degree of persistence in the time series, and at high q^*, H converges to a value of 0.8 at dry-out.

[10] Refer to Kantelhardt (2008) [91] for more information on Fourier Filtering.

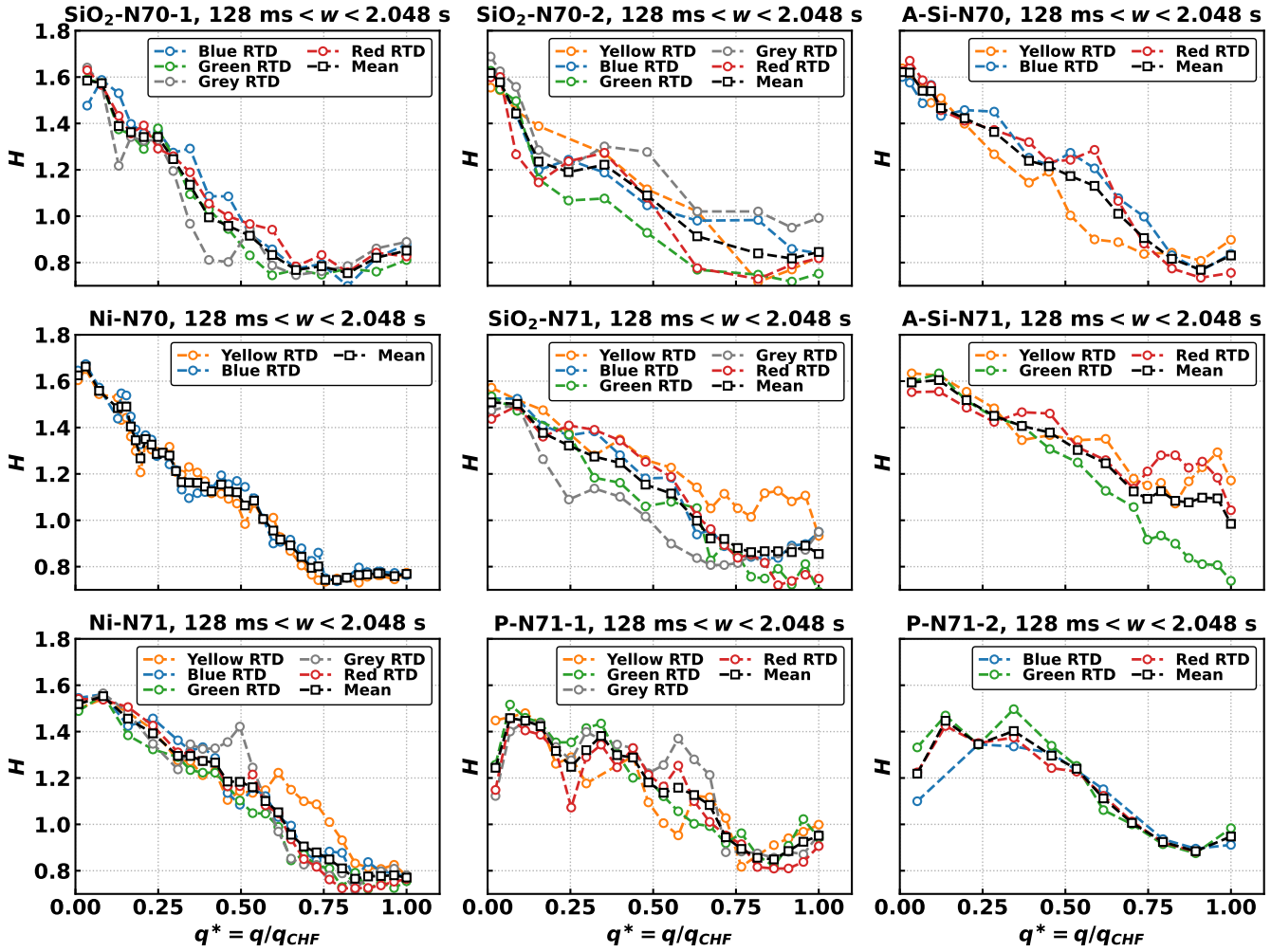

Figure 4.23: Evolution of H as a function of q^* for all surface experiments performed. H was calculated as the scaling exponent of F_w^2 with w ($F_w^2 \sim w^H$) in the range of 128 ms $< w <$ 2.048 s.

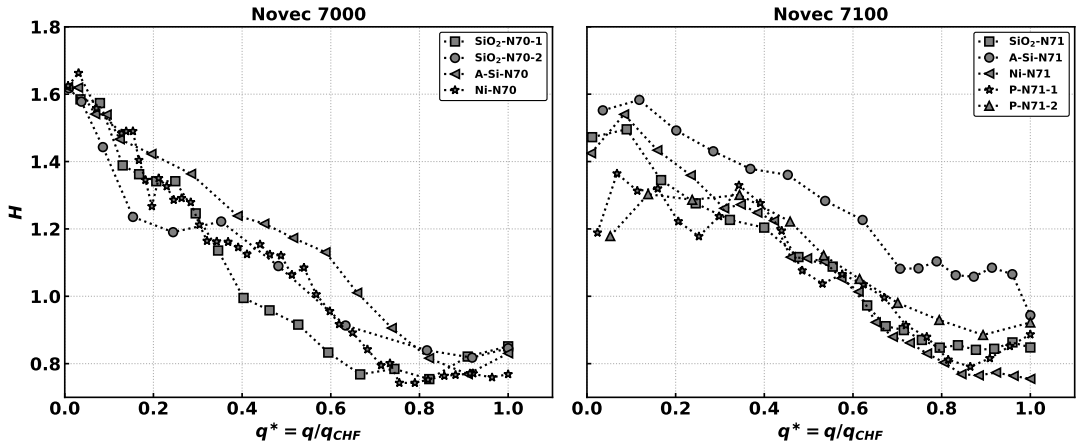

Figure 4.24: Comparison of evolution of H with q^* for all surface experiments performed. H was calculated as the scaling exponent of F_w^2 with w ($F_w^2 \sim w^H$) in the range of 128 ms $< w <$ 2.048 s.

The H evolution curve for the experiment of A-Si in Novec 7100 (A-Si-N71) does not collapse so well as do the other curves. This is most likely due to the significant level of noise in the fluctuations but it nevertheless follows the general trend of convergence at dry-out. Figure 4.23 (middle-right) shows that while the Green RTD followed the trend displayed in other experiments, despite the noise, the curves of the other two RTDs weighted the mean value curve to higher values. Regardless, the convergence at $q^* = 1.0$ suggests that the estimation of H by DFA is capable of working reasonably well with noisy data.

4.5.4 Relationship of Hurst Exponent to Autocorrelation Decay

When a persistent time series ($H > 0.5$) is long-term correlated such that ACF(k) $\sim k^{-\gamma}$, H satisfies the following relationship:

$$2H = 2 - \gamma \qquad 0.5 < H < 1 \tag{4.1}$$

where $0 < \gamma < 1$ is the exponent of the rate of decay of ACF(k). The above relation is not valid when $H \geq 1$ as that implies $\gamma < 0$, i.e., ACF(k) increases with k. DFA estimates the value of H to characterize the self-affinity of the data, and not the autocorrelation decay. Therefore, when $H \geq 1$, the interpretation is that the data have a high degree of persistence in the range of w over which H is calculated.

As $H \to 0.5$, Equation (4.1) implies that $\gamma \to 1$. Therefore, for power-law correlations decaying faster than $1/k$, we have $H = 1/2$ for large w values, as when data are uncorrelated.

To summarize, $H > 0.5$ implies persistence of time series and $0.5 < H < 0.1$ implies long-term correlations in addition to persistence.

Chapter 5

Results - Wire Pool Boiling Experiments

5.1 Experimental Runs

To obtain a wide range of CHF values, wire pool boiling experiments were performed in various fluids. Table 5.1 lists the set of experiments performed, the corresponding fluid used and its saturation temperature at atmospheric pressure, the observed value of CHF from the experiment, and an identifier assigned to the experimental run for reference in the results that follow.

As can be seen in Figure 5.1, the observed values of CHFs spanned a wide range of values. The two nanofluid solutions that exhibited the highest CHF values were 0.01% and 0.1% silica nanoparticles in DI water. Experimental results from tests in each fluid were compared for repeatability of results at least once.

It should be noted here that the observed value of CHF for DI water (~ 46.5 W/cm^2) was well below 110 W/cm^2, the value predicted by Zuber's hydrodynamic model. However,

S.No.	Boiling Fluid	Identifier	T_{sat} at 1 atm (°C)	Observed CHF (W/cm^2)
1	Novec 7000	N70-Run 1	34	15.85
2		N70-Run 2		16.85
3		N70-Run 3		18.92
4	Novec 7100	N71-Run 1	61	19.49
5		N71-Run 2		14.06
6	DI Water	DIW-Run 1	100	45.81
7		DIW-Run 2		47.54
8	0.01% Silica-Nanofluid	0.01%NF-Run 1	100	107.52
9		0.01%NF-Run 2		98.53
10	0.1% Silica-Nanofluid	0.1%NF-Run 1	100	88.95
11		0.1%NF-Run 2		90.09

Table 5.1: List of wire pool boiling experiments performed.

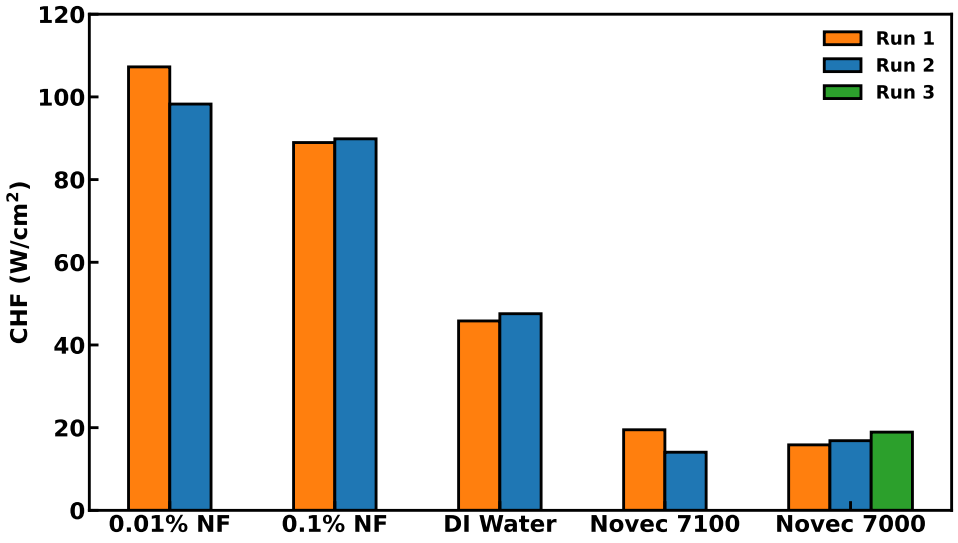

Figure 5.1: Observed CHF values for wire pool boiling experiments.

Zuber's model is applicable only to flat horizontal surfaces, and lower values of CHFs on wires with small diameters, such as the 0.1 mm platinum wire used in the present experiments, has been reported in Van Stralen and Sluyter (1969) [92], Sun and Lienhard (1970) [93], and Mohan Rao and Andrews (1976) [94]. Therefore, the reduced values

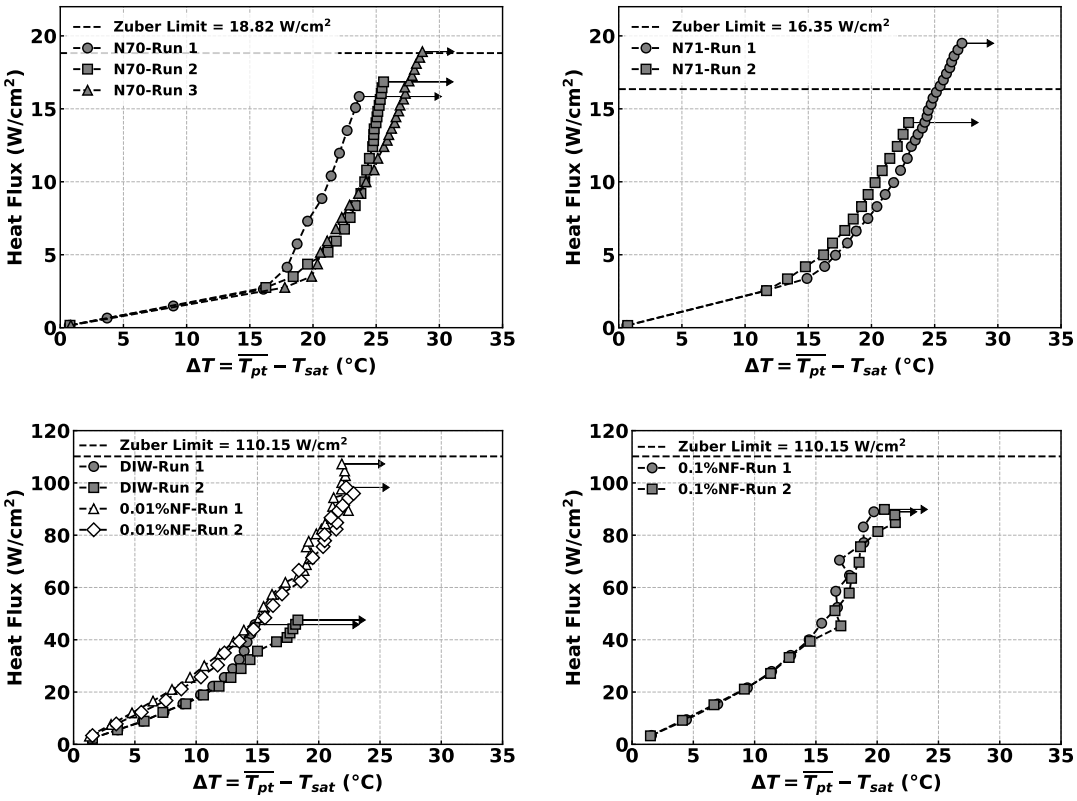

Figure 5.2: Boiling curves for wire experiments performed in Novec 7000 (top-left), Novec 7100 (top-right), DI Water and nanofluid solution with 0.01% silica nanoparticles by volume (bottom-left), and nanofluid solution with 0.1% silica nanoparticles by volume (bottom-right). The arrows represent the last data point before dry-out occurred.

of CHF for DI water is consistent with the general behavior as predicted by Zuber's model.

In the foregoing sections, only the results of the analysis are presented. For the details of these analyses performed, the reader is referred to Chapter 4.

5.2 Statistical Distributions

Figure 5.3 shows the PDFs of the wire temperature fluctuations for all but two experiments at non-dimensional heat flux values of $q^* \approx 0.30$, 0.50, 0.70, 0.85 and 1.0. The PDFs of boiling experiments with Novec 7000-Run 2 and DI Water-Run 1 are not shown due to space constraints, but they were similar to the PDFs of Novec 7000-Runs 1 & 3, and DI Water-Run 2, respectively. This can be verified from Figure 5.4, which shows the evolution of the standard deviation ($\mu_2^{1/2} = \sigma$), skewness ($\mu_3/\mu_2^{3/2}$), and kurtosis (μ_4/μ_2^2 as a function of q^* for all the experiments.

The PDFs for refrigerants Novec 7000 and Novec 7100 are more spread out at the lowest q^* value of 0.30 (blue) than at larger q^*. In fact, as can be seen in Figure 5.4 (top-left), the standard deviation for the experiments in the refrigerants have a maxima around $q^* = 0.15$, which marks the onset of nucleate boiling (ONB), and then decreases from that point forward. Hence, the PDFs for the refrigerants tend to narrow as q^* increases.

The PDFs for the refrigerants at $q^* = 1.0$ (red) are also positively skewed. This is reflected in the skewness of the refrigerants (Figure 5.4 (middle-left)) which consistently increases with q^*. This trend is similar to that observed for RTD temperature fluctuations and is ascribed large positive excursions at high q^* values. However, since wire temperature fluctuations represent the average temperature of the surface of the wire at a given time, local excursions are likely to be dampened due to averaging over the entire length of the wire. This would explain why the PDFs are not as skewed (with the exception of the PDF for N70-Run 3 at $q^* = 1.0$ (red)) as they were for RTD temperature fluctuations.

The evolutions in the PDFs for DI water and nanofluids have the opposite characteristics. The PDFs spread as q^* increases, as indicated by the increase in σ with q^*. Additionally, the PDFs for only experiments with DI water become positively skewed as q^* increases, while for the nanofluid experiments, the PDFs stay mostly symmetric

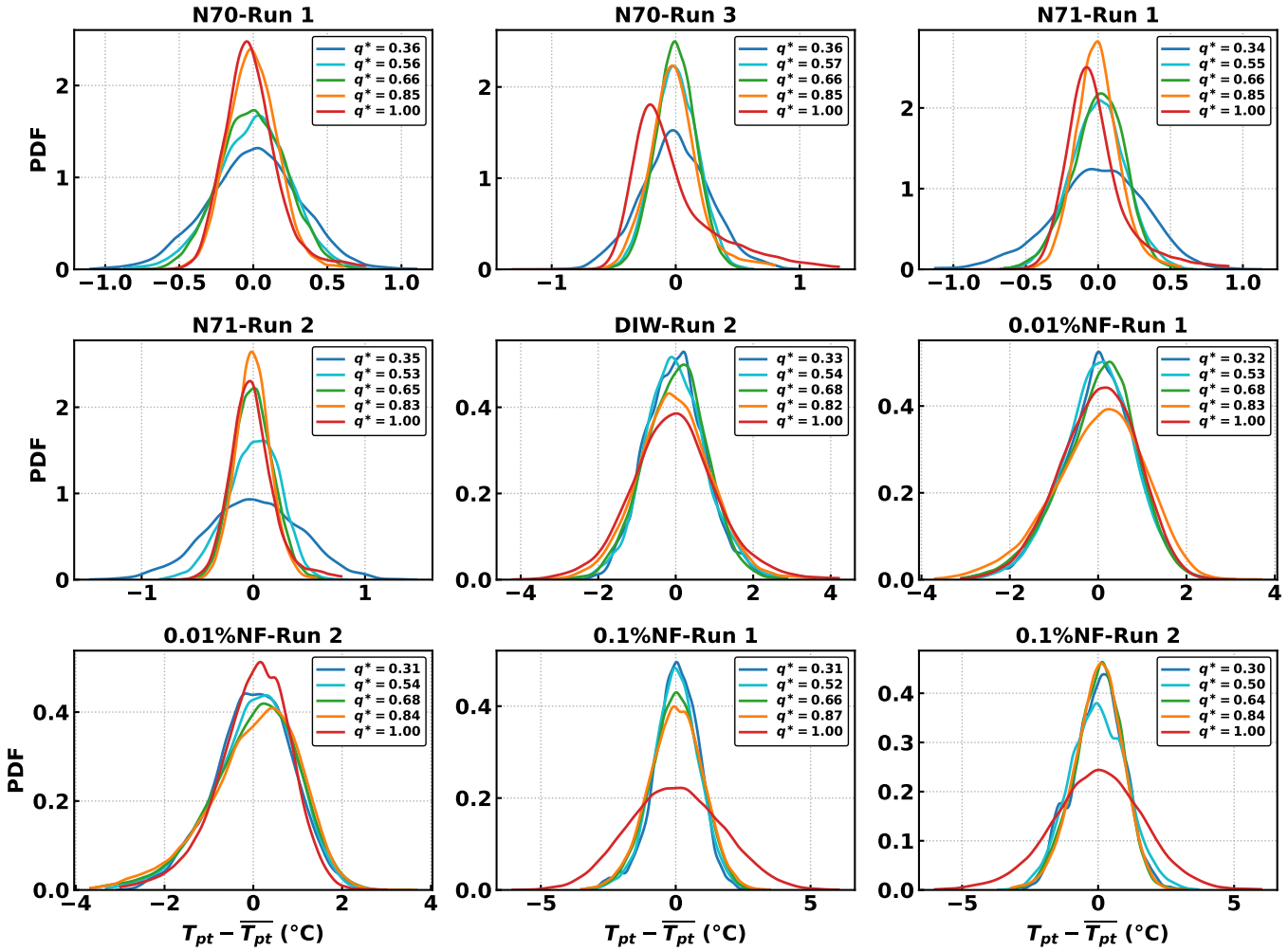

Figure 5.3: PDFs of wire temperature fluctuations from for each experiment at non-dimensional heat flux values ($q^* = q/q_{\mathrm{CHF}}$) ranging from ~ 0.4 to 1.0.

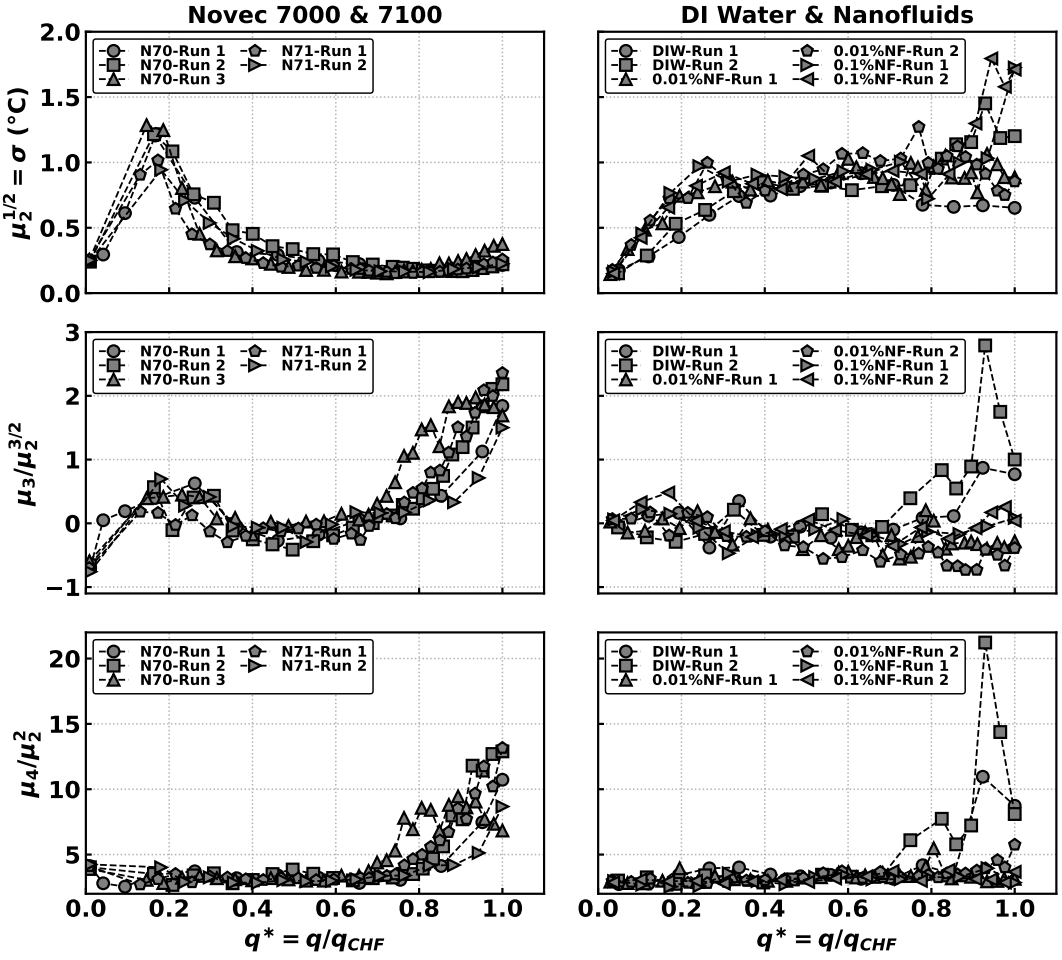

Figure 5.4: Evolution of statistical central moments of orders 2, 3 and 4 (standard deviation, skewness, and kurtosis, respectively) along the boiling curve.

or negatively skewed. The positive skewness of the PDFs of DI water at high q^* are due to large positive excursions ($\sim$ 10 K) near dry-out. These were absent in the nanofluid experiments. The large positive excursions also explain the large spikes in evolution of skewness ($\mu_3/\mu_2^{3/2}$) and the kurtosis (μ_4/μ_2^2) for DI water experiments in Figure 5.4 (middle-right and bottom-right).

For all the time series, the Kolmogorov-Smirnov (KS) tests [89] was performed to test

if the time series were sampled from Gaussian distributions. Without exception, the test result for all the time series concluded that the PDFs of the time series were not Gaussian.

5.2.1 Variation of Statistical Moments with Segment Size

Figures 5.5 5.6 show the variation in mean, standard deviation ($\mu_2^{1/2} = \sigma$), and kurtosis (μ_4/μ_2^2) with segment size for non-dimensional heat flux values of ~ 0.5, 0.75, and 1.0. The choice of time series from which the experimental runs to analyze were arbitrary in either figure. Note that the segment size refers to the duration of time (in s) that a segment spanned. Since the wire temperatures were sampled at 1000 Hz, a segment of 1000 data points, for instance, spanned 1 s.

As can be seen, the average of each segment mean did not vary for even the smallest span of 8 ms considered for q^*. While the standard deviations converge for all six time series shown, the kurtoses for N71-Run 1, $q^* = 1.0$, in Figure 5.5 and DIW-Run 1, $q^* = 1.0$ in Figure 5.6, do not converge. While this violates the strict definition of stationarity, time series for which the mean and standard deviation do not change with time are also considered stationary, in the weak sense.

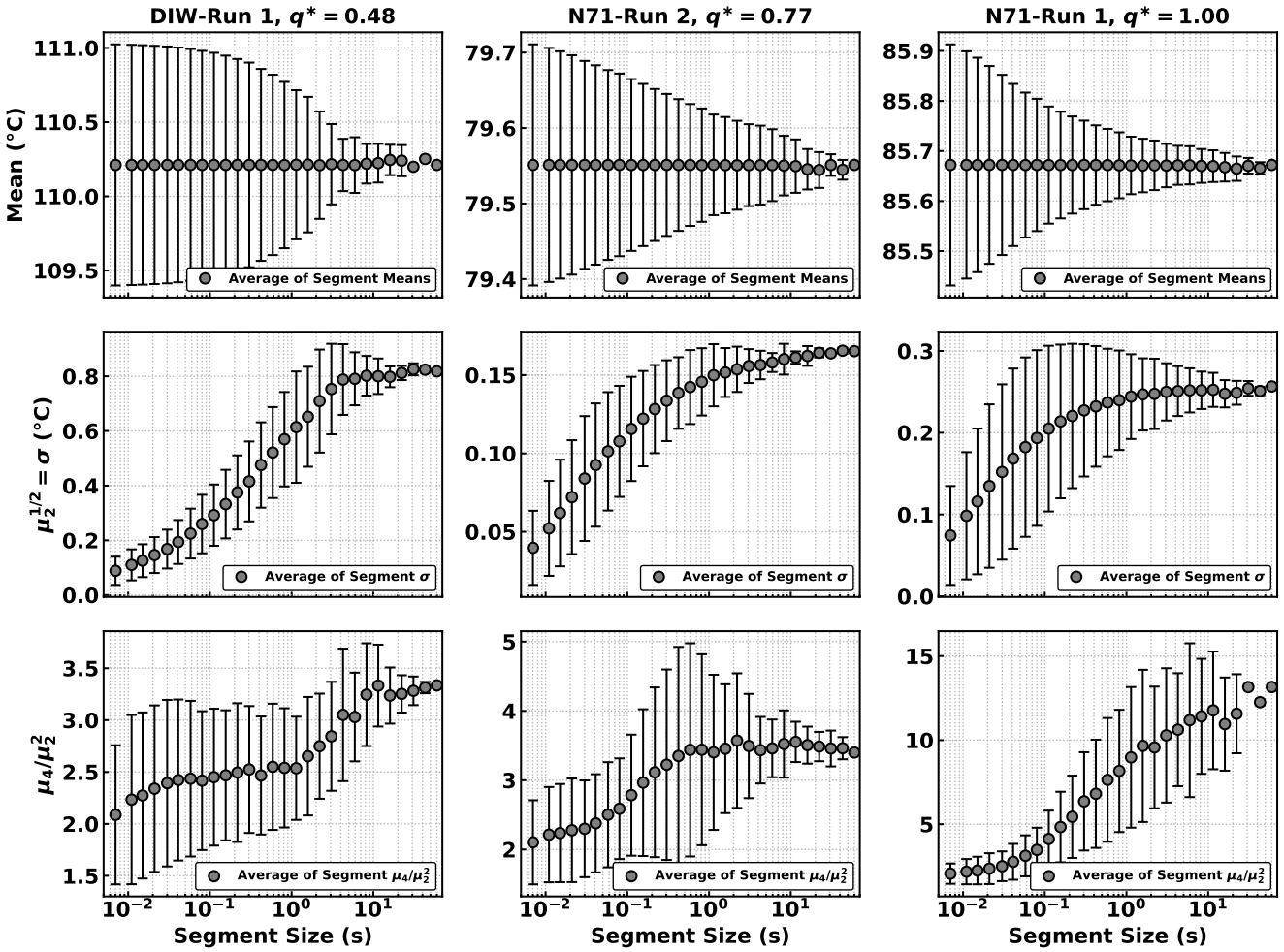

Figure 5.5: Variation in mean (top row), standard deviation (middle row) and kurtosis (bottom row) of temperature fluctuations with segment size at $q^* \simeq 0.50$, 0.75, and 1.0. Each column corresponds to temperature fluctuations from an arbitrarily chosen wire experimental run.

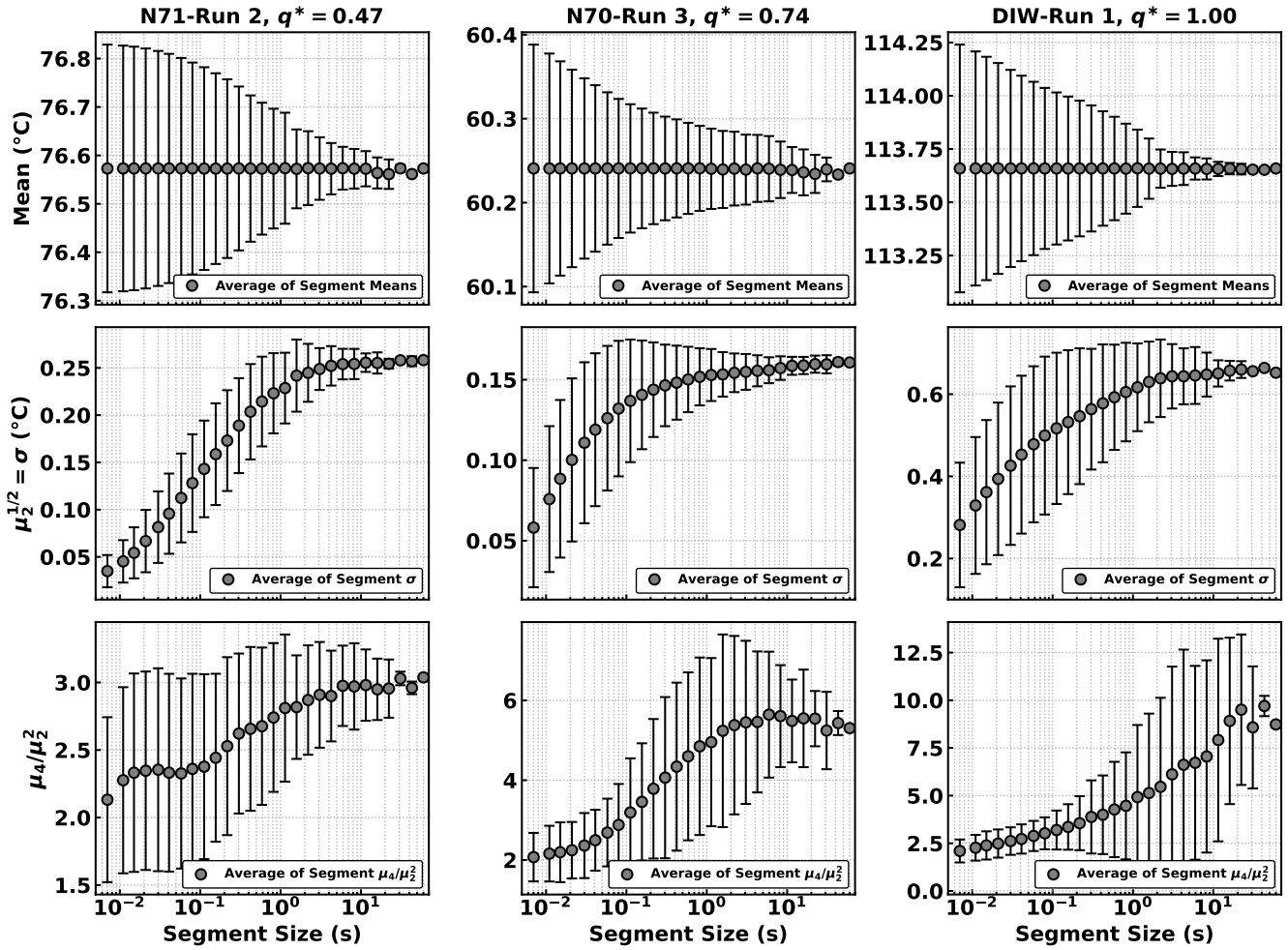

Figure 5.6: Variation in mean (top row), standard deviation (middle row) and kurtosis (bottom row) of temperature fluctuations with segment size at $q^* \simeq 0.50$, 0.75, and 1.0. Each column corresponds to temperature fluctuations from an arbitrarily chosen wire experimental run.

5.3 Frequency Spectrum Analysis

Figure 5.7 shows a representative 2-s segments of wire temperature fluctuations and the corresponding Power Spectral Densities (PSDs) at low and moderate q^* values of 0.31 and ~ 0.66 from wire boiling experiments in a 0.1 % Nano-fluid solution with $q_{\text{CHF}} = 88.96$ W/cm^2. It is interesting that even though the wire temperature fluctuations represent the temperature of the wire averaged over the entire length, the 2-s segment for $q^* = 0.31$ show multiple cycles of the typical, aperiodic and intermittent sawtooth-like rise and fall of temperature under a nucleating bubble. The 2-s segment for $q^* = 0.66$ also shows the sawtooth-like waves but with a more noise-like behavior along the entire segment. This is reflected in values of the PSDs at $f > 60$ Hz, which are higher for $q^* = 0.66$, even though the slope of the drop-off of the PSD is more steep (PSD $\sim f^{-2.88}$) than the same for $q^* = 0.31$ (PSD $\sim f^{-2.54}$).

Figure 5.8 shows representative 2-s segments of wire temperature fluctuations and the corresponding Power Spectral Densities (PSDs) at low and moderate q^* values of 0.35 and 0.76 from the wire boiling experiment in Novec 7000 with $q_{\text{CHF}} = 16.85$ W/cm^2. The sawtooth-like rise and fall of temperature fluctuations are not as easy to ascertain for these time series.

Just as for RTD temperature fluctuations, the scale-free nature of the temperature fluctuations is evident from the PSDs in Figures 4.12 and 5.7. Figure 5.9 compares the evolution of the power law drop-off exponent from all experiments, with the curves for experiments in refrigerants and non-refrigerants plotted separately to avoid clutter. The drop-off exponent was estimated by considering only the PSDs in the range of 6 Hz$\leq f \leq 60$ Hz that spanned a decade. This was because the PSD flattened (or started to) at $f \geq 60$ Hz in some experiments (see Figure 5.8). This also had the desired effect of neglecting line noise and harmonics, which affected only 60 Hz or higher frequencies, if and when present.

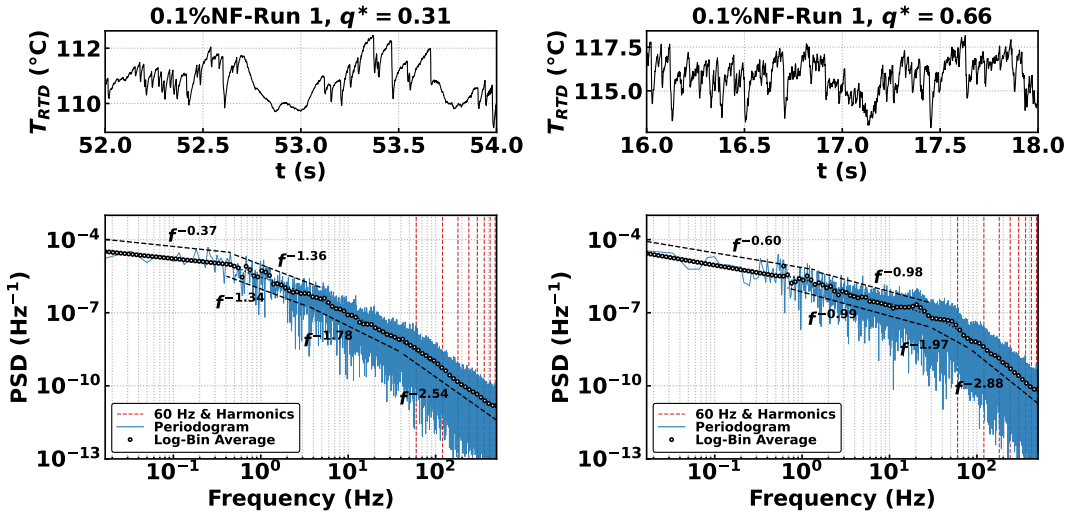

Figure 5.7: Representative Power Spectral Densities. The temperature fluctuations were taken from the boiling experiment in 0.1 % Nanofluid - Run 1, $q_{\mathrm{CHF}} = 88.96$ W/cm^2.

The PSD drop-off curves for experiments in refrigerants first drop to values below -2.0 after which they start increasing. Note that the first few points in all experiments

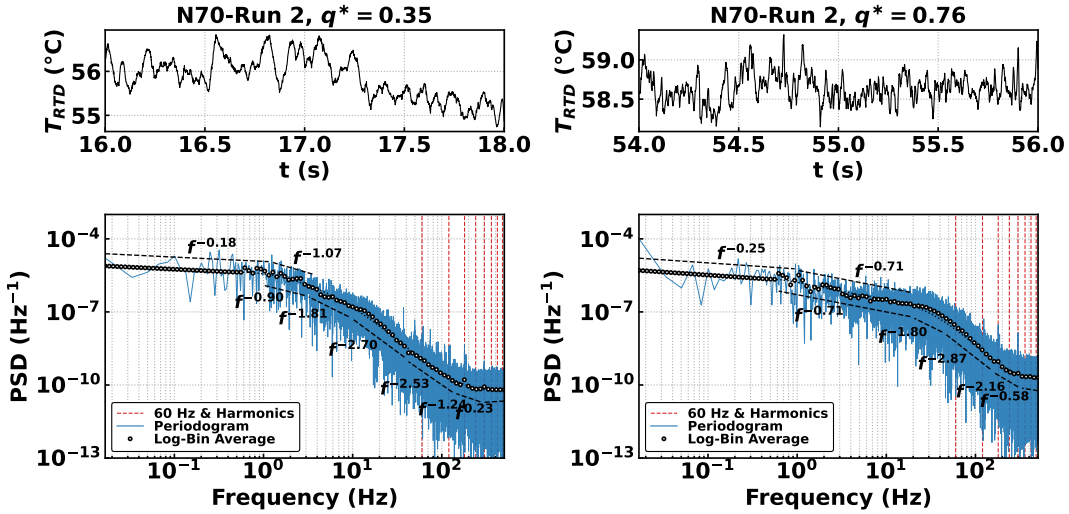

Figure 5.8: Representative Power Spectral Densities. The temperature fluctuations were taken from the boiling experiment in Novec 7000 - Run 2, $q_{\mathrm{CHF}} = 16.85$ W/cm^2.

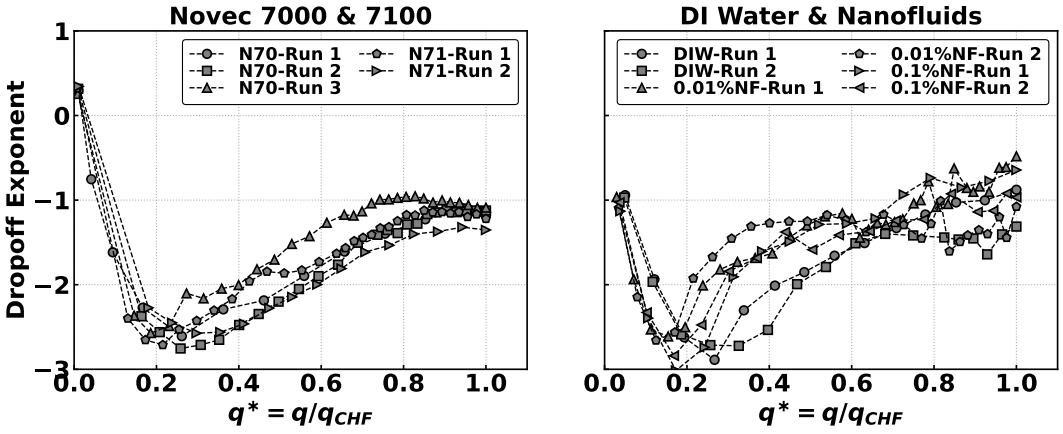

Figure 5.9: The evolution of the scaling exponent of PSD vs frequency (PSD $\sim f^m$) in the range 6 Hz $\leq f \leq$ 60 Hz for all wire experiments.

correspond to the natural convection regime with no bubble nucleation. After the Onset of Nucleate Boiling (ONB, at $q^* \sim 0.1$), the drop-off exponents increase and converge to the value of $\sim$ -1.0 at dry-out.

The PSD drop-off exponent curves for experiments in DI water and nanofluid solutions also follow the same trend but do not collapse so well as they do for the experiments in refrigerants. Nevertheless, the PSD drop-off exponent for these experiments also converge to a value of $\sim$ -1.0 at dry-out.

5.4 Auto-Correlation Function Analysis

Figure 5.10 illustrates a representative decay of ACF(k) for wire temperature fluctuations at low and high q^* values. It is evident that the ACF(k) for temperature fluctuations at $q^* = 0.24$ decay exponentially ($\sim \exp(-k)$). For $q^* = 1.0$, however, ACF(k) declines as a power-law ($\sim k^{-\gamma}$) until $\sim$ 3 s and then drops off sharply.

Figure 5.11 shows the change in the nature of ACF(k) decay across five values of $q^* \simeq$ 0.25, 0.4, 0.7, 0.85, and 1.0 for all but two of the wire experiments. The ACFs of

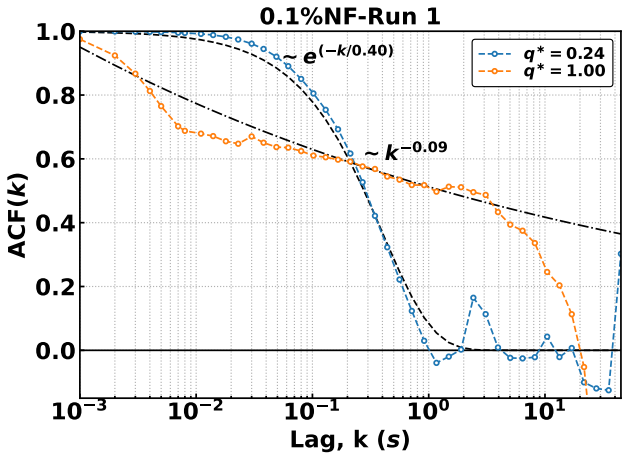

Figure 5.10: Decay of ACF(k) for wire temperature fluctuations at low and high q^* values. The temperature fluctuations were taken from the boiling experiment in 0.1% Silica Nano-fluid solution, $q_{\text{CHF}} = 88.96$ W/cm^2.

boiling experiments in Novec 7000-Run 2 and DI Water-Run 1 are not shown due to space constraints, but they behave similarly to other ACF trends. The general trend across all experiments is that at low q^* values of 0.25 and 0.4, ACF(k) decays exponentially, indicating that the temperature fluctuations are short-term correlated. At moderate and high values of q^* in most experiments, ACF(k) appears to decay exponentially at low lags ($k < 0.02$ s) but then decay as a power-law, indicating long-term correlations in the time series. Even though the wire temperature fluctuations represent length-averaged temperature fluctuations, the change in decay of ACF(k) of temperature fluctuations suggests that long-term correlations are present in surface-averaged temperature fluctuations at high heat fluxes when close to dry-out.

5.5 Hurst Exponent Analysis

Similar to the Hurst Exponent estimation for RTD temperature fluctuations, H was estimated as the scaling exponent of F_w^2 over the range of w in 128 ms$< w <$ 2.048 s. The choice of the lower bound of 128 ms was informed by the intermittent presence of

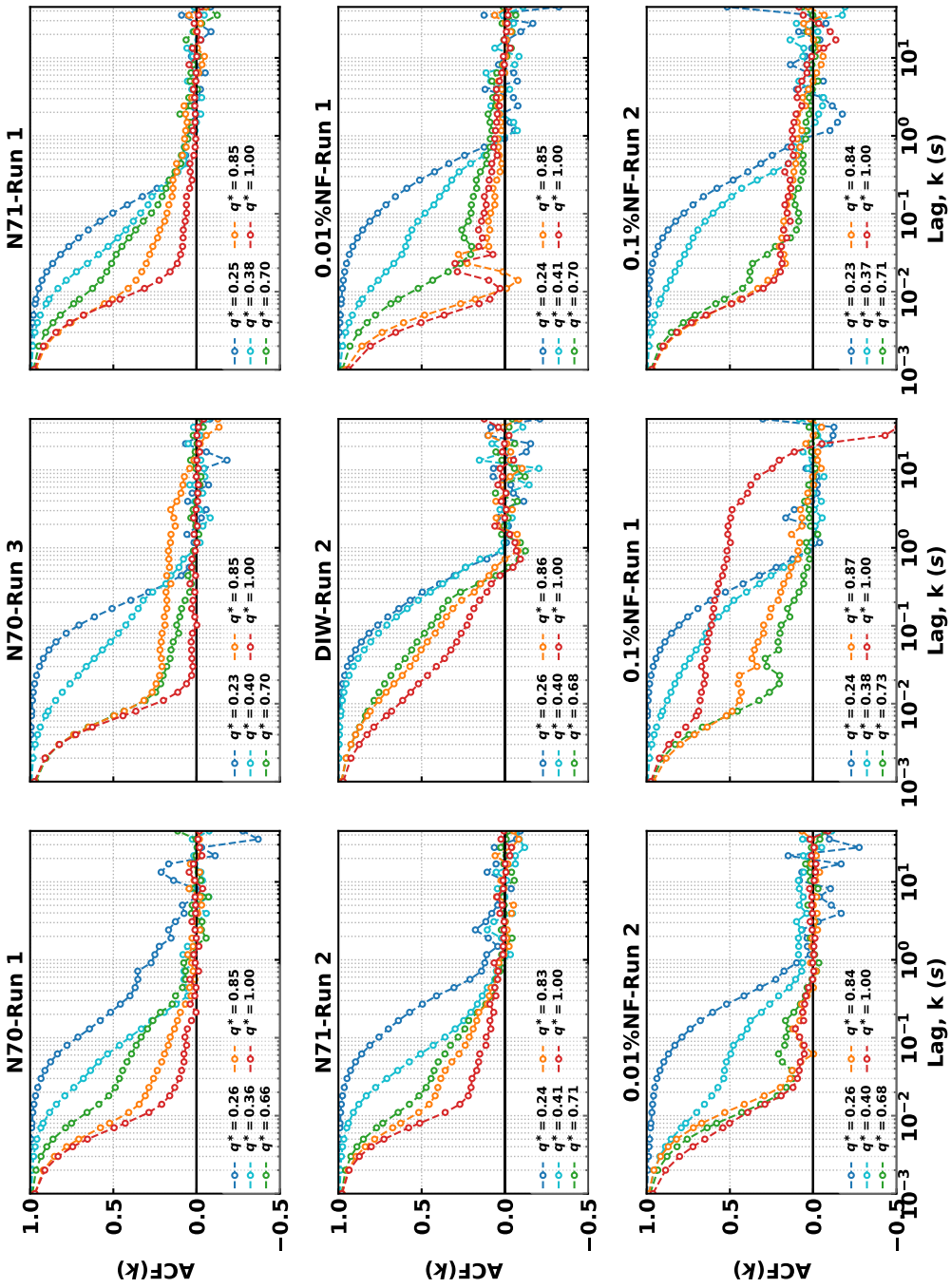

Figure 5.11: Decay in Auto-Correlation Functions (ACF) across all wire experiments.

noise around $f \gtrsim 60$ Hz in a few of the temperature fluctuations, while the upper bound of 2.048 s was selected based on Figure 5.11, which showed that the earliest time beyond which short-term correlations were destroyed was 1 s for the short-term correlated time series at low and moderate q^* values across all experiments.

Figure 5.12 plots the evolution of H with q^* from all the wire experiments on two plots for comparison. The general trend is similar to that observed for RTD temperature fluctuations: $H > 1.0$ for low q^*, implying a high degree of persistence with no long-term correlations in the time series. At high q^*, H tends to converge to a value of 0.8 at dry-out. The H evolution curves for refrigerants collapse well but there is considerable scatter across the evolution curves for DI water and Nano-fluids. However, closer analysis shows that the evolution curves for DI water experiments are the general outliers. As was noted earlier, the DI water experiments exhibited very large positive excursions in temperature fluctuations ($\sim$ 10 K) at high q^*. This is likely to have affected the estimation of H as the contribution of large positive excursions $(x - \bar{x})$ is going to be high to the structure function (since $F_w^2 \sim \left(x - \bar{x}\right)^2$).

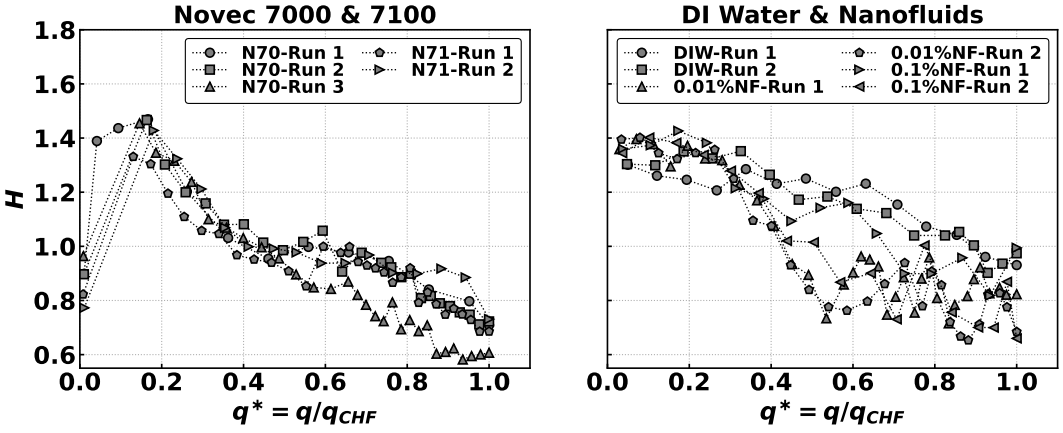

Figure 5.12: Comparison of evolution of H with q^* for all wire experiments performed. H was calculated as the scaling exponent of F_w^2 with w ($F_w^2 \sim w^H$) in the range of 128 ms $< w <$ 2.048 s.

5.6 Comparison of Hurst Exponent Evolution for Surface and Wire Experiments

Figure 5.13 plots the evolution of H with q^* for the surface experiment of Ni in Novec 7000 (Ni-N70) and the first wire experiment in 0.1% Silica Nano-fluid solution (0.1%NF-Run 1) for comparison. As has been stated earlier, wire temperature fluctuations represented the length-averaged temperature fluctuations of the entire wire while the RTD temperature fluctuations represent local fluctuations in the surface temperature. Nevertheless, evolution of H follows the same trend along q^*. Note the large difference in observed CHF values across the two experiments. Additionally, $H < 1.0$ at $q^* \gtrsim 0.5$ suggests long-term correlations in temperature fluctuations. This was also confirmed by the decay of Auto-Correlation Functions ACF(k) for both the RTD and wire temperature fluctuations.

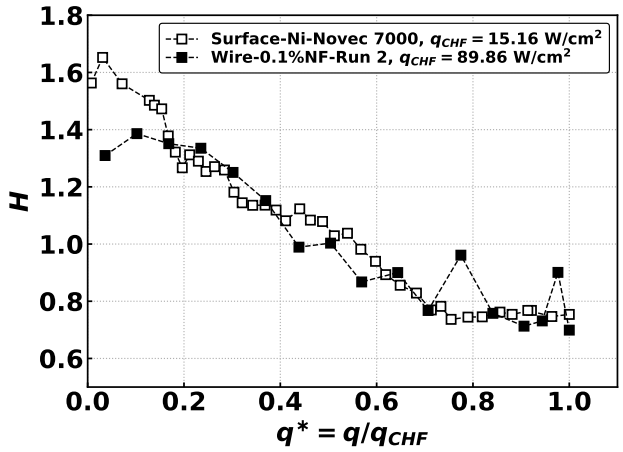

Figure 5.13: Comparison of evolution of H with q^* for wire and surface experiments. The surface experiment chosen for comparison was Ni in Novec 7000 with an observed CHF of 15.16 W/cm^2. The wire experiment shown was 0.1% Silica Nano-fluid with an observed CHF of 89.86 W/cm^2.

Chapter 6

Results - Boiling Experiments in Microgravity

The methodology of detecting and characterizing long-term correlations is applied to publicly available data [95] from the Multiheater Array Boiling Experiments (MABE) which were conducted on the International Space Station (ISS) with the aim of understanding the effects of gravity level, heater size, subcooling and system pressure on CHF. The boiling curves based on the area-averaged heat flux and wall superheat have been reported in several articles [82, 96, 97]. Here, the focus is on the behavior of thermal fluctuations, which have not been previously analyzed.

The experiments were performed using a sapphire substrate maintained at a uniform surface temperature, T_s, by 96 independently controlled platinum resistance heaters (Figure 6.1 (Left)). Each platinum heater (of size 0.7×0.7 mm) was also used as a resistance thermometer. Complete details of the data acquisition and reduction processes are available elsewhere [98]; here we merely note that a high-frequency feedback loop (sampling at 15 kHz) that maintained the heater surface temperatures constant,

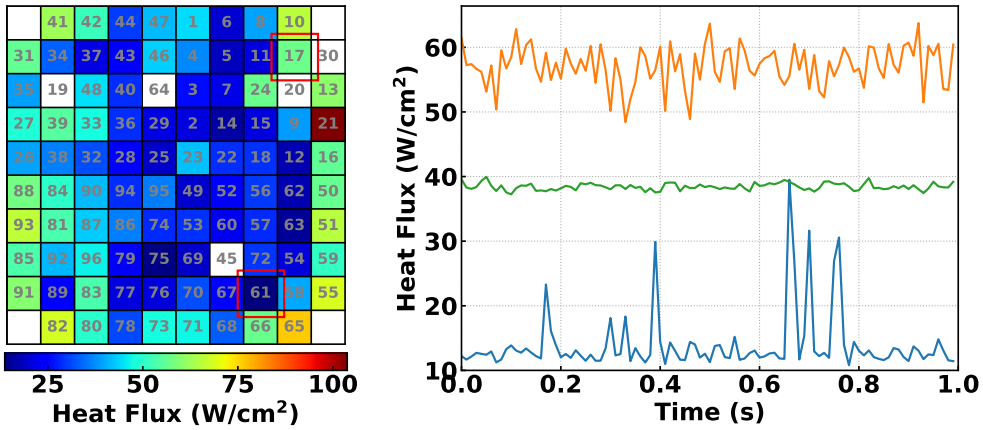

Figure 6.1: (Left) Time-averaged heat map (with heater numbering) for an experiment carried out at 1 atm. $T_s = 87.5$ °C, $\Delta T_{sub} = 26$ °C in micro-gravity. Heaters dissipating the minimum and maximum heat flux (heaters 17 and 61, discounting the edge heaters) are highlighted. Inactive heaters are colored white. (Right) Time series of the minimum (blue) and maximum (orange) heat flux dissipating heaters. Also shown is the space averaged heat flux time series (green).

and power (heat flux) measurements that were taken at 100 Hz for approximately 30 s in each run. Experiments were performed with n-perfluorohexane (saturation temperature, T_{sat}, of 56 °C at 1 atmosphere) at multiple pressures (0.58, 1, 1.38, 1.6, and 1.86 atm) and levels of bulk liquid subcooling below saturation temperature ($\Delta T_{\text{sub}} = 1$, 11, 21, 26 °C). The surface temperatures were incremented in steps of 5 °C and caused the surface to exhibit multiple boiling regimes ranging from the bubble incipience regime through fully developed nucleate boiling, past the boiling crisis and into transition boiling. Terrestrial experiments were also performed using an identical setup using FC-72, which is near-identical to n-PFH in the relevant transport properties. The sampling rate in terrestrial experiments was 300 Hz and the power measurements were taken for approximately 5 s in each run.

In reporting the experimental data along the boiling curve, the non-dimensional temperature T^* is used, which is defined in terms of the surface temperature, T_s, as

$$T^* = \frac{T_s - T_{\text{sat}}}{T_{\text{CHF}} - T_{\text{sat}}}$$

where T_{CHF} is the surface temperature at which the boiling crisis occurs, as inferred from [98]. Figure 6.1 (Left) shows an example of a time-averaged heat flux distribution for $T^* = 1.0$ at 1 atm. Considerable spatial variation in surface heat flux is evident, attesting to the likely non-uniform coverage of liquid film and nucleation sites.

Figure 6.1 (Right) shows a 1-s interval of the heat flux signal from heaters with maximum and minimum heat dissipation, as well as the surface area-averaged value. Note the highly intermittent signal from the heater with the lowest power dissipation, which is likely the result of intermittent nucleation. In subsequent plots, data are presented for the behavior of the heater with minimum power dissipation, though the results are similar to those for other heaters.

6.1 Statistical Distributions

The central moments of heat flux fluctuations along the boiling curve are first analyzed. A typical Probability Density Function (PDF) of heat flux fluctuations for a fixed pressure in micro-gravity (Figure 6.2(a)) suggests that at low surface temperatures ($T^* = 0.52$), the fluctuations have a relatively narrow amplitude, with two peaks on either side of the mean. This may reflect the heating and cooling cycles associated with bubble departure. As the wall temperature (and hence the heat flux) increases ($T^* = 0.68$, 0.92), larger excursions from the mean are observed on both sides, as the system approaches CHF. However, once the surface has crossed the CHF point and is in the transition boiling regime ($T^* = 1.24$), the PDF is narrow and peaked, likely reflecting the absence of bubble nucleation cycles. Figure 6.2(b) and Figure 6.2(c) show

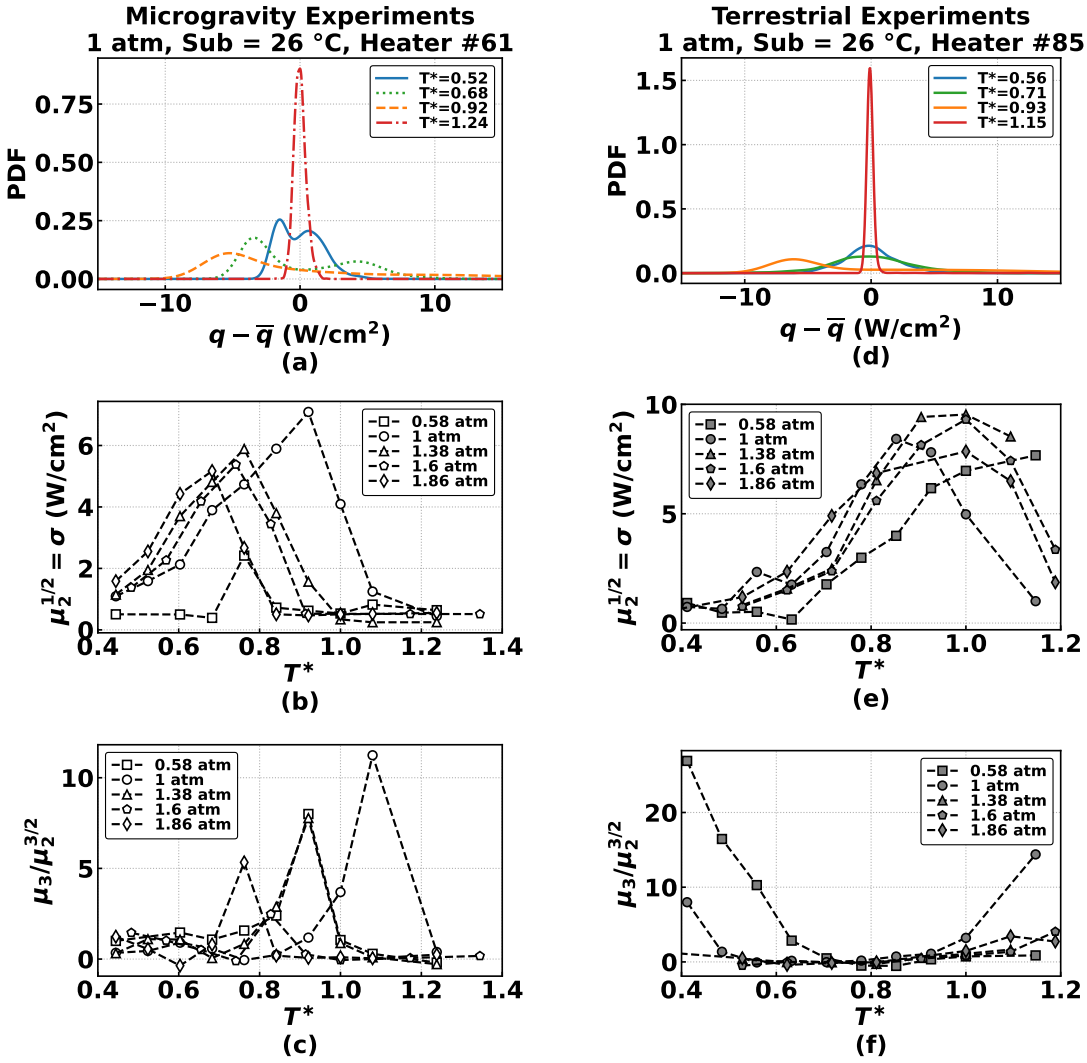

Figure 6.2: Probability Density Functions of heat flux time series for (a) microgravity and (b) terrestrial experiments. (b,e) Standard deviations ($\mu_2^{1/2} = \sigma$), and (c,f) Skewness ($\mu_3/\mu_2^{3/2}$) of heat flux time series from heater with minimum heat flux dissipating for multiple pressures as a function of T^*.

the behavior of the standard deviation and skewness (2$^{\text{nd}}$ and 3$^{\text{rd}}$ order moments) of fluctuations for multiple pressures. In each case, the moment reaches a maximum at wall temperatures well before CHF, and drops to nearly zero past CHF. Note, however,

that there is some uncertainty in the exact value of wall temperature at which CHF occurs, since temperature was incremented in steps of 5 °C during the experiment.

The corresponding plots for terrestrial data are shown in Figure 6.2(d-f). The trends for the PDF are seen to be qualitatively similar, i.e., broad amplitudes of fluctuations with a secondary peak at low values of T^*, and the absence of large fluctuations in the transition boiling regime. The behavior of the standard deviation is also similar, reaching larger values as T^* is increased towards CHF before sharply decreasing past CHF. The skewness of heat flux fluctuations, on the other hand is quite different, with large values at low values of T^* that drop to nearly zero as T^* is increased, reflecting more symmetric distributions for large T^*.

6.2 Frequency Spectrum Analysis

Figure 6.3(b) charts the evolution of PSD drop-off exponents of heat flux fluctuations in micro-gravity and terrestrial conditions as the wall temperature is increased from low superheats towards $T^* = 1.0$. For clarity, we first consider the PSD in micro-gravity at two values, $T^* = 0.44$ and 1.0, corresponding to the nucleate boiling regime and the onset of the boiling crisis (Figure 6.3(a)). The scale-free behavior of the spectra is evident for both values of T^* as power-law exponents of -1.7 and -0.25 are observed for these values of T^*. The corresponding data for terrestrial experiments, taken under the same pressure and subcooling, and at the same values of T^* are shown in Figure 6.3(a), and again appear qualitatively similar despite significant differences in actual heat fluxes between ISS and terrestrial experiments. Note that the sampling frequency of 100 Hz used in the microgravity experiments is expected to be sufficient for micro-gravity data due to the relatively longer time scales. However, for terrestrial experiments marked by strong ebullition, this sampling frequency may introduce some aliasing, which may explain the presence of some peaks in the power spectrum, though these do not appear to carry significant energy.

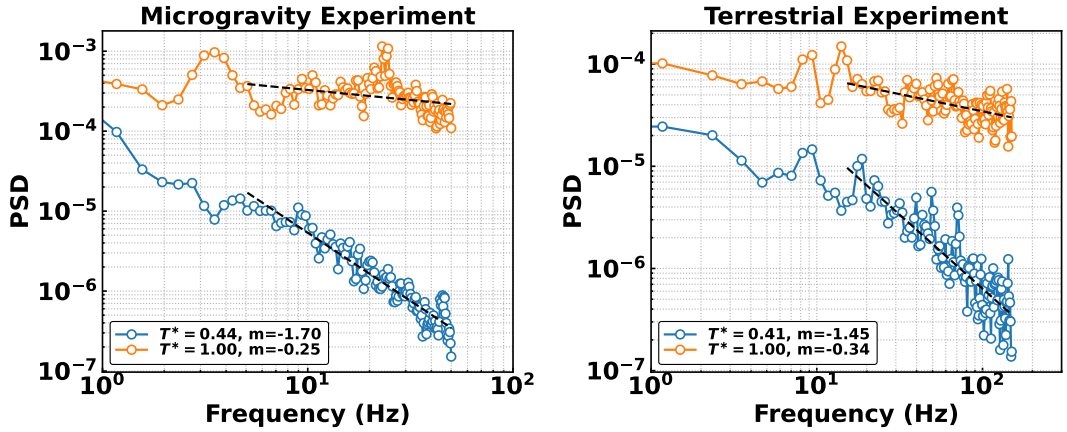

(a) PSD of heat flux fluctuations at $T^* \sim 0.4$ and $T^* = 1.0$ for (Left) MABE and (Right) Ground measurements. Data in microgravity and terrestrial experiments was acquired at a sampling rate of 100 Hz and 300 Hz, respectively.

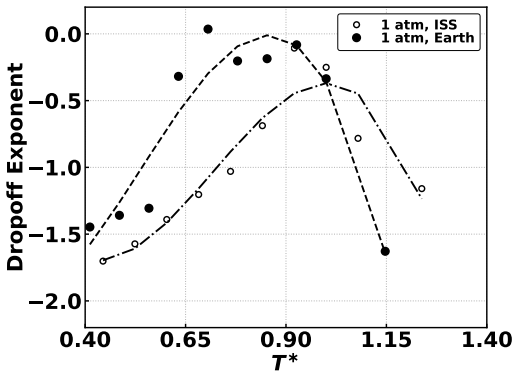

(b) Dropoff exponent of PSD power-law along the boiling regime for microgravity and terrestrial data.

Figure 6.3: Frequency Spectrum Analyses of MABE Experiments.

The variations of the drop-off exponents of the heat flux fluctuations are shown in Figure 6.3(b). For both micro-gravity and terrestrial experiments, the scaling exponent of the spectra decreases in magnitude in a continuous manner, varying from near 1.5 to smaller value between zero and 0.5 near the boiling crisis. There appears to be differences in the exact behavior of the exponent as T^* is varied; however the exponents reach a value close to 0.5 at $T^* = 1.0$, before dropping to lower values in the

transition boiling regime. This is in contrast to earlier observations in surface and wire boiling experiments where the drop-off exponent converged to a value of -1.0 at dry-out. Nevertheless, it is interesting to note that even under micro-gravity conditions, nucleate boiling is characterized by a range of time scales spanning orders of magnitude. Further, the terrestrial data show no obvious discrete frequencies with large amplitudes corresponding to bubble departure, pointing to a lack of support for scale-based mechanistic modeling.

6.3 Auto-Correlation Function Analysis

Figure 6.4 shows the change in the nature of ACF(k) decay across five values of $T^* \simeq$ 0.4, 0.55, 0.7, 0.85, and 1.0 for micro-gravity (left column) and terrestrial experiments (right column) at 1 atm (top row), 1.38 atm (middle row) and 1.6 atm (bottom row). The reason for choosing $T^* = 0.4$ as the lowest value was because data for lower T^* values were not available. In fact, the lowest T^* value at which data were available for terrestrial experiments at 1.38 atm and 1.6 atm was $T^* = 0.53$ in both cases. Also notice the slightly different scales on the x-axis for the two sets of experiments. This is because the terrestrial data were sampled at 300 Hz.

The general trend across all experiments is that at low and moderate T^* values of 0.4, 0.55 and 0.7, ACF(k) decayed as a power law (ACF(k) $\sim k^{-\gamma}$) indicating long-term correlations in the heat flux time series. At $T^* = 0.85$, ACF(k) decayed as a power-law in some cases (1 atm and 1.6 atm in μg, and 1.38 atm and 1.6 atm in 1g), and in the remaining cases, the time series appears entirely uncorrelated even at the lowest values of lags. At $T^* = 1.0$, all but one heat flux time series (1.6 atm in μg) appears uncorrelated. This is in contrast to observation from surface and wire experiments where ACF(k) at low q^* decayed exponentially suggesting short-term correlations, and at dry-out, the temperature fluctuations exhibited long-term temporal correlations due to the decay of ACF(k) as a power-law.

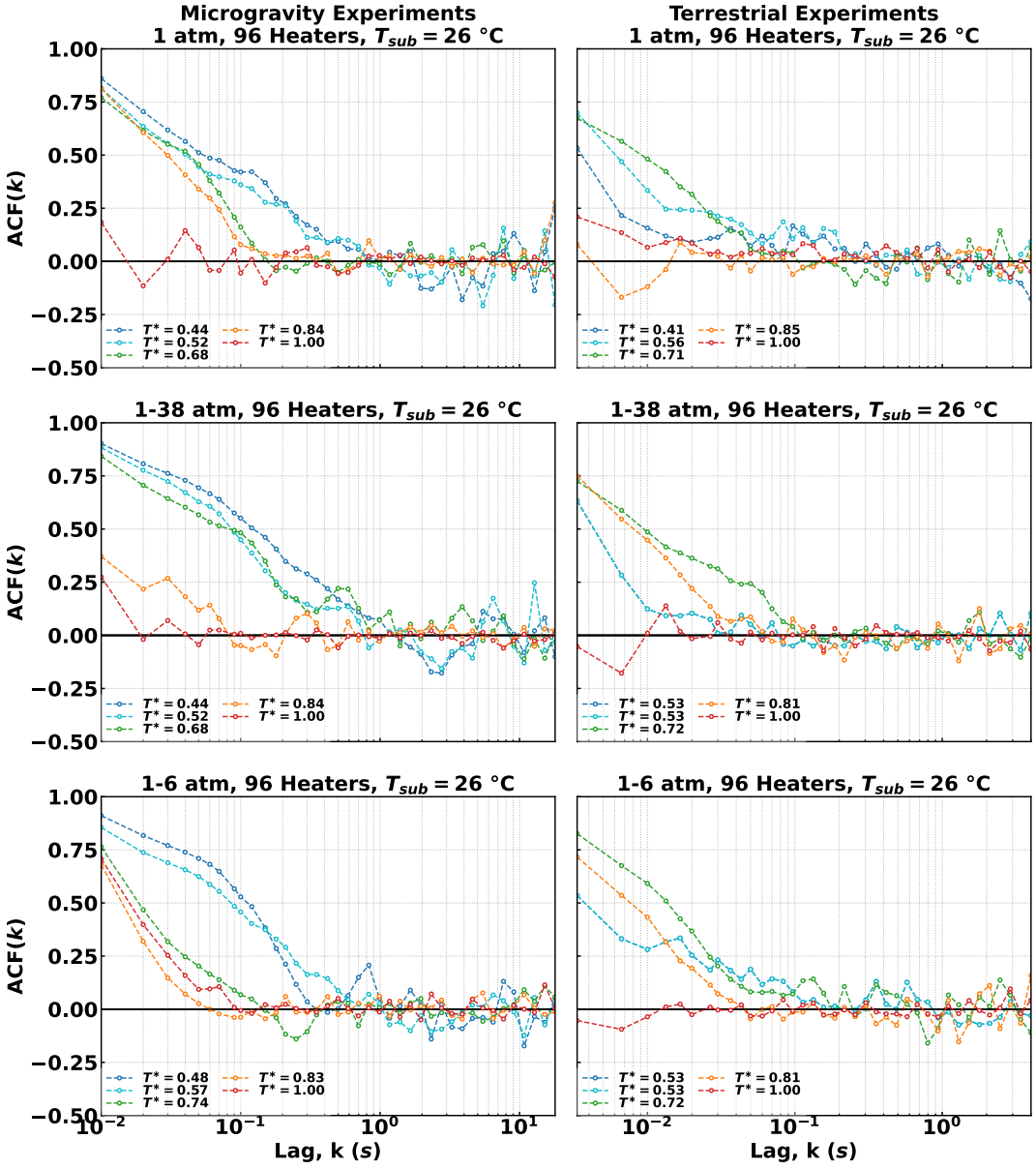

Figure 6.4: Decay in Auto-Correlation Functions (ACF) across all MABE micro-gravity and terrestrial experiments.

6.4 Hurst Exponent Analysis

For microgravity and terrestrial experiments, H was calculated as the scaling exponent of F_w^2 with w ($F_w^2 \sim w^H$) in the ranges of 160 ms $< w <$ 3.62 s and 106 ms $< w <$ 853 ms, respectively. The lower upper limit for terrestrial experiments was due to the short time period ($\lesssim$ 5 s) over which the heat flux fluctuations were sampled. It should also be noted that the low number of data points in the time series ($\sim$ 3000) for the MABE experiments meant statistical standard errors in the estimation of H using DFA were as large as 0.05.

Figure 6.5 (Left) shows the trend of the Hurst exponent, H, along the nucleate boiling curve for a microgravity experiment carried out at 1 atm and ΔT_{sub} = 26 °C, for the heaters with lowest and largest heat dissipation at T^* = 1.0. Clearly, there is a consistent trend across one heater to the next, with H decreasing from large values in the nucleate boiling regime (low T^* values) to values in the range of $0.5 - 0.6$ at the boiling crisis (T^* = 1.0). Cases with $H \approx 0.5$ at hight T^* confirm the ACF analysis

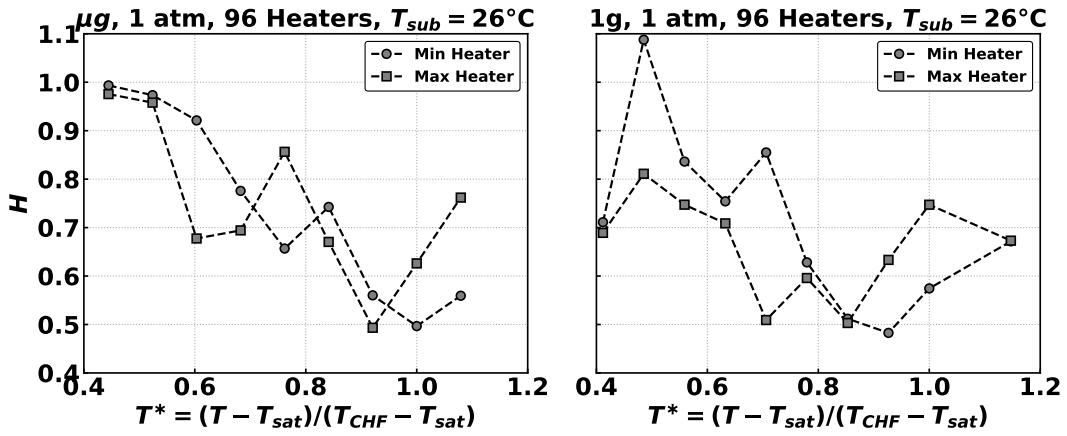

Figure 6.5: Evolution of H for heaters dissipating minimum and maximum heat flux at T_{CHF} for 1 atm for a (Left) microgravity experiment, and (Right) terrestrial experiment. The time series analyzed in all the figures were recorded by the heaters dissipating the lowest heat fluxes at T_{CHF}.

that the heat flux fluctuations are uncorrelated.

The results of such an analysis with terrestrial data for the same conditions are examined as well. Figure 6.5 (right) shows that the behaviors of H for the maximum and minimum power dissipating heaters overlap less than in the microgravity data. Both heaters appear to reach a minimum value of H in the range $T^* = 0.8 - 1.0$, before displaying larger values in the transition boiling regime, for a given system pressure and subcooling. A value of 0.5 would match well with the observations of frequency-independent noise in the frequency spectra in Figure 6.3a; however the results must be interpreted with caution due to the lower number of points in the time series.

To test the universality of this behavior, data sets corresponding to multiple system pressures, and multiple levels of subcooling were interrogated. While mechanistic theories typically account for the effects of system pressure through a capillary/bubble length scale which depends on the difference in liquid and vapor density, there is no consensus on how to model the effects of subcooling. In Figure 6.6 (Left), evolution of H, is plotted for multiple system pressures ranging from 1 to 1.6 atm in micro-gravity

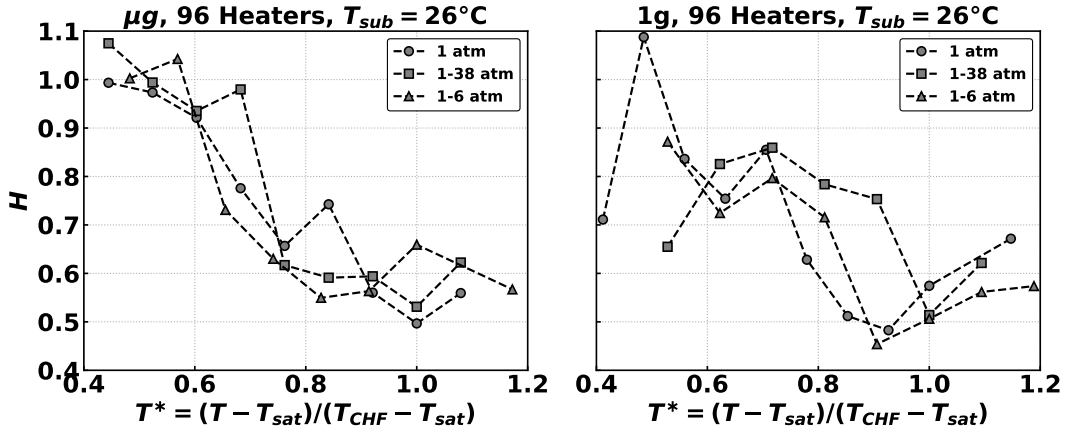

Figure 6.6: Hurst exponent evolution for experiments carried out at different pressures with $T_{\text{sub}} = 26$ °C for (a) microgravity and (b) terrestrial experiments.

and a fixed subcooling level of $\Delta T_{\text{sub}} = 26$ °C. The overall trend of H is the same for multiple values of pressure with low variability. Figure 6.6 (right) plots the corresponding data for terrestrial experiments and shows a consistent trend over all pressures, albeit with some significant scatter in the data.

Finally, Figure 6.7 plots the evolution of H for a fixed pressure of 1 atm, with multiple subcooling levels of $\Delta T_{\text{sub}} = 26$ °C, 11 °C, and 1 °C in micro- and earth-gravity. Clearly, the same trend is followed in all levels of subcooling in the terrestrial data set, with the curves converging to a value of $0.5 - 0.6$ near CHF. The curve for micro-gravity and $\Delta T_{\text{sub}} = 26$ °C is also plotted and matches well with the terrestrial data. Overall, these plots indicate that there is much greater consistency among the MABE data, with curves of H behaving relatively independent of heater location, system pressure and subcooling.

The universal behavior in the evolution of H with T^* appears to be surprisingly robust. While the low sampling rate and the low number of data points contribute to some

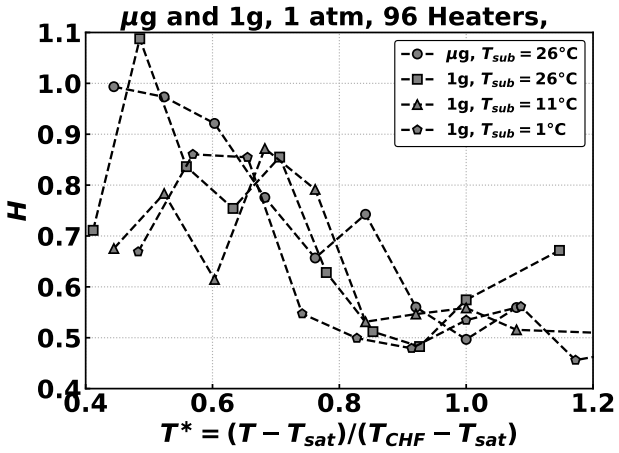

Figure 6.7: Comparison of H evolution for experiments carried out in migrogravity and earth at 1 atm. The time series analyzed in all the figures were recorded by the heaters dissipating the lowest heat flux at T_{CHF}.

ambiguity in the inference, the overall trend of H^2 is surprisingly independent of several factors (pressure, subcooling, spatial location, gravity level) and appears to depend only on the 'state' of the system, which can be associated with the location along the boiling curve. The observation that all heaters on the surface display a similar trend for H^2 is not altogether surprising, if we regard the boiling phenomenon as a system with coupling between large and small scales, and incorporate ideas from chaos theory, which state that the qualitative behavior of all state variables in a nonlinear dynamic system should follow similar behavior.

Chapter 7

Conclusion

In this study, long-term correlations in temperature and heat flux fluctuations on surfaces undergoing boiling were studied. This was motivated by evidence of intermittent nucleation site behavior, nucleation site interactions and scale-free behavior in boiling in the literature, which all suggested analyzing boiling as a complex dynamical system. Data series generated by complex dynamical systems are known to follow scaling relations over several orders of magnitude. In this context, the Hurst Exponent, which characterizes the self-similar or fractal appearance of time series and can also be interpreted as a measure of long-term correlations in a time series was explored as an indicator of a boiling system proceeding towards dry-out. Two types of temperature fluctuations were obtained through experiments: local surface temperature fluctuations from micro-scale Resistance Temperature Detectors (RTDs) deposited on flat surfaces undergoing boiling, and surface-averaged temperature fluctuations from platinum wires undergoing boiling. Boiling experiments were performed in various fluids such that the observed CHF values spanned approximately one order of magnitude. The same analysis was applied to publicly available data for boiling experiments performed in micro-gravity aboard the International Space Stations (ISS).

In summary, the main findings of this work are:

- All thermal fluctuations in boiling exhibit fluctuations on a wide spectrum of frequencies suggesting scale-free behavior.
- Auto-Correlation Function (ACF) analysis of temperature fluctuations of RTD and wire temperature fluctuations revealed a change in the decay of ACF from exponential decay at low heat flux values to power-law like decay at moderate and high heat flux values.
- Local and surface-averaged temperature fluctuations exhibit long-term correlations close to dry-out.
- The trend in the evolution of the Hurst Exponent, a measure of persistence or anti-persistence of a time series, along the boiling curve is the same for local and surface-averaged temperature fluctuations. The trend also extends to heat flux fluctuations in surface temperature-controlled boiling experiments in microgravity.

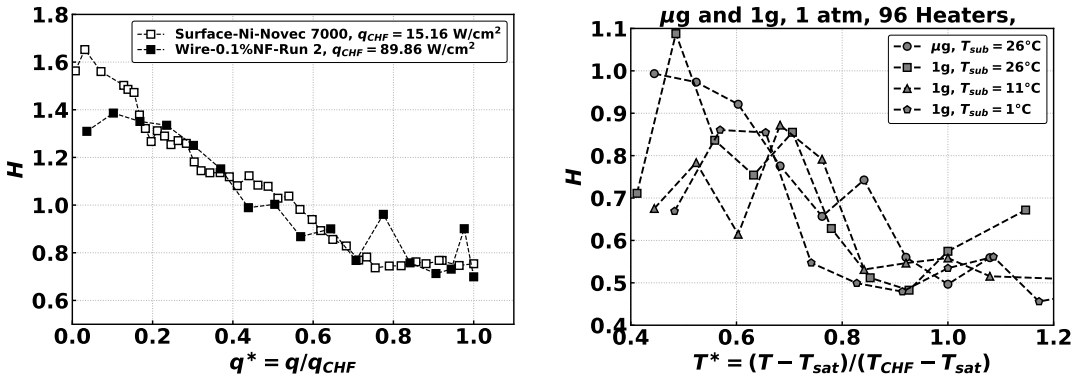

Figure 7.1: Decrease in the Hurst Exponent, H, along the boiling curve for (left) temperature fluctuations on a heat-flux controlled surface, and (right) heat flux fluctuations on a temperature-controlled surface. Note the different linear scales along the y-axis. While the values of Hurst Exponents do not match, there is a general trend of decrease in the persistence of thermal fluctuations as a system proceeds towards dry-out.

The implications of this result suggest that there are new physics to be explored that can be deduced from temperature fluctuations. Additionally, in practical applications in which surfaces undergo fouling, the ability to assess the safety margin from CHF by using a single sensor that continuously measures thermal fluctuations, may offer significant benefits. Further studies on this aspect may enable the adoption of the many high-performance surfaces developed in the last decade by the heat transfer community.

7.1 Recommended Future Work

At the conclusion of this study, the following are recognized as possible avenues of future work:

1. For local surface temperature fluctuations, the observed CHF values did not span a wide range due to the higher power requirement of the 4 cm^2 chips to achieve dry-out in fluids other than the refrigerants used. Scaling down the chip surface area to 1 cm^2 would make it possible to achieve dry-out at lower powers for fluids like pentane, methanol, and DI water. Demonstrating that H behaves similarly along the boiling curve for fluids with higher values of CHF will lend credence to the idea that the trend exhibited in the evolution of H is universal.

2. Having established long-term temporal correlations in temperature fluctuations, investigation of spatial cross-correlations from simultaneous measurements of temperature fluctuations from linearly spaced RTDs would help investigate length scales over which the dynamics of an active nucleation site is effective.

3. Establishing the presence of long-term correlations in fluctuations of other measurable quantities in boiling would further lend credence to the framework of treating boiling as a complex dynamical system. Fluctuations in acoustic emissions, near-wall pressure, void area fraction and contact line length, where such measurements are possible, are likely to exhibit persistent behavior similar to the temperature fluctuations discussed

herein.

4. The effectiveness of using the Hurst Exponent as an indicator of a surface's proximity to dry-out could be demonstrated by operating a surface close to dry-out conditions and introducing nano-particles into the fluid such that the likelihood of dry-out in the enhanced working fluid decreases. This should be accompanied by an increase in the persistence of temperature fluctuations, and hence, the Hurst Exponent.

References

[1] U.S. Energy Information Administration. Short-Term Energy Outlook (Washington, DC: U.S. Department of Energy, 2024). https://www.eia.gov/outlooks/steo/.

[2] Melanie Tetreault-Friend et al. "Critical heat flux maxima resulting from the controlled morphology of nanoporous hydrophilic surface layers". In: *Applied Physics Letters* 108.24 (2016).

[3] Susmita Dash, Leonid Rapoport, and Kripa K Varanasi. "Crystallization-Induced Fouling during Boiling: Formation Mechanisms to Mitigation Approaches". In: *Langmuir* 34.3 (2017), pp. 782–788.

[4] DC Groeneveld et al. "Lookup tables for predicting CHF and film-boiling heat transfer: past, present, and future". In: *Nuclear Technology* 152.1 (2005), pp. 87–104.

[5] Winfried Beck et al. "Nuclear Fuel Safety Criteria Technical Review". In: (2012).

[6] Masahiro Shoji. "Chaos in boiling on a small-size heater". In: *Proceedings of the Fourth ASME-JSME Thermal Joint Conference, Maui, 1995*. Vol. 2. 1995, pp. 225–232.

[7] V Sathyamurthi et al. "Measurement of the fractal order of wall void fraction during nucleate boiling". In: *International Journal of Heat and Fluid Flow* 29.1 (2008), pp. 207–218.

[8] Vijaykumar Sathyamurthi and Debjyoti Banerjee. *Investigation of pool boiling dynamics on a rectangular heater using nano-thermocouples: is it chaotic or stochastic?* July 2009.

[9] H Bruce Stewart and AN Lansbury. *Forecasting catastrophe by exploiting chaotic dynamics*. Tech. rep. Brookhaven National Lab., Upton, NY (USA), 1990.

[10] Agostino Accardo et al. "Use of the fractal dimension for the analysis of electroencephalographic time series". In: *Biological cybernetics* 77.5 (1997), pp. 339–350.

[11] Jonas Olsson, Janusz Niemczynowicz, and Ronny Berndtsson. "Fractal analysis of high-resolution rainfall time series". In: *Journal of Geophysical Research: Atmospheres* 98.D12 (1993), pp. 23265–23274.

[12] LG Moyano, J De Souza, and SM Duarte Queirós. "Multi-fractal structure of traded volume in financial markets". In: *Physica A: Statistical Mechanics and its Applications* 371.1 (2006), pp. 118–121.

[13] M Sadegh Movahed et al. "Multifractal detrended fluctuation analysis of sunspot time series". In: *Journal of Statistical Mechanics: Theory and Experiment* 2006.02 (2006), P02003.

[14] Luca Pietrasanta. "Experimental analysis of two-phase flows in the context of Pulsating Heat Pipes for space applications". PhD thesis. University of Brighton, 2018.

[15] BB Mikic. "Bubble growth rates in non-uniform temperature field". In: *Progress in Heat and Mass Transfer* (1969), pp. 283–293.

[16] Han Chi-Yeh and Peter Griffith. "The mechanism of heat transfer in nucleate pool boiling—Part I: Bubble initiaton, growth and departure". In: *International Journal of Heat and Mass Transfer* 8.6 (1965), pp. 887–904.

[17] E. A. Ibrahim and R. L. Judd. "An Experimental Investigation of the Effect of Subcooling on Bubble Growth and Waiting Time in Nucleate Boiling". In: *Journal of Heat Transfer* 107.1 (Feb. 1985), pp. 168–174.

[18] Craig Gerardi et al. “Infrared thermometry study of nanofluid pool boiling phenomena”. In: *Nanoscale research letters* 6 (2011), pp. 1–17.

[19] MG Cooper and AJP Lloyd. “The microlayer in nucleate pool boiling”. In: *International Journal of Heat and Mass Transfer* 12.8 (1969), pp. 895–913.

[20] SJD Van Stralen et al. “Bubble growth rates in pure and binary systems: combined effect of relaxation and evaporation microlayers”. In: *International Journal of Heat and Mass Transfer* 18.3 (1975), pp. 453–467.

[21] Ho Sung Lee and Herman Merte Jr. “Spherical vapor bubble growth in uniformly superheated liquids”. In: *International Journal of Heat and Mass Transfer* 39.12 (1996), pp. 2427–2447.

[22] Renwei Mei, Wenchin Chen, and James F Klausner. “Vapor bubble growth in heterogeneous boiling—I. Formulation”. In: *International Journal of Heat and Mass Transfer* 38.5 (1995), pp. 909–919.

[23] Gihun Son, Vijay K Dhir, and N Ramanujapu. “Dynamics and heat transfer associated with a single bubble during nucleate boiling on a horizontal surface”. In: *Journal of Heat Transfer* 121.3 (1999), pp. 623–631.

[24] Gihun Son, Nm Ramanujapu, and Vijay K Dhir. “Numerical simulation of bubble merger process on a single nucleation site during pool nucleate boiling”. In: *Journal of Heat Transfer* 124.1 (2002), pp. 51–62.

[25] A Mukherjee and VK Dhir. “Study of lateral merger of vapor bubbles during nucleate pool boiling”. In: *Journal of Heat Transfer* 126.6 (2004), pp. 1023–1039.

[26] Van P Carey. *Liquid-vapor phase-change phenomena: an introduction to the thermophysics of vaporization and condensation processes in heat transfer equipment.* CRC Press, 2020.

[27] Jungho Kim. “Review of nucleate pool boiling bubble heat transfer mechanisms”. In: *International Journal of Multiphase Flow* 35.12 (2009), pp. 1067–1076.

[28] P Stephan and J Hammer. “A new model for nucleate boiling heat transferEin neues Modell für den Wärmeübergang beim Blasensieden”. In: *Heat and Mass Transfer* 30.2 (1994), pp. 119–125.

[29] SS Kutateladze. “Hydromechanical model of heat transfer crisis in pool liquid boiling”. In: *Journal of Technical Physics* 20.11 (1950), pp. 1389–1392.

[30] Gangtao Liang and Issam Mudawar. “Pool boiling critical heat flux (CHF)–Part 1: Review of mechanisms, models, and correlations”. In: *International Journal of Heat and Mass Transfer* 117 (2018), pp. 1352–1367.

[31] Novak Zuber. “On the stability of boiling heat transfer”. In: *Transactions of the American Society of Mechanical Engineers* 80.3 (1958), pp. 711–714.

[32] Y Haramura and Y Katto. “A new hydrodynamic model of critical heat flux, applicable widely to both pool and forced convection boiling on submerged bodies in saturated liquids”. In: *International Journal of Heat and Mass Transfer* 26.3 (1983), pp. 389–399.

[33] Richard Francis Gaertner. “Photographic study of nucleate pool boiling on a horizontal surface”. In: *Journal of Heat Transfer* 87.1 (1965), pp. 17–27.

[34] Vadim S Nikolayev and Daniel A Beysens. “Boiling crisis and non-equilibrium drying transition”. In: *Europhysics Letters* 47.3 (1999), p. 345.

[35] VS Nikolayev et al. “Growth of a dry spot under a vapor bubble at high heat flux and high pressure”. In: *International Journal of Heat and Mass Transfer* 44.18 (2001), pp. 3499–3511.

[36] VS Nikolayev et al. “Experimental evidence of the vapor recoil mechanism in the boiling crisis”. In: *Physical Review Letters* 97.18 (2006), p. 184503.

[37] Satish G Kandlikar. “A theoretical model to predict pool boiling CHF incorporating effects of contact angle and orientation”. In: *Journal of Heat Transfer* 123.6 (2001), pp. 1071–1079.

[38] TG Theofanous et al. "The boiling crisis phenomenon: Part I: nucleation and nucleate boiling heat transfer". In: *Experimental Thermal and Fluid Science* 26.6-7 (2002), pp. 775–792.

[39] Theo G Theofanous and True-Nam Dinh. "High heat flux boiling and burnout as microphysical phenomena: mounting evidence and opportunities". In: *Multiphase Science and Technology* 18.3 (2006).

[40] H Jeremy Cho et al. "Nanoengineered materials for liquid–vapour phase-change heat transfer". In: *Nature Reviews Materials* 2.2 (2017), p. 16092.

[41] Renkun Chen et al. "Nanowires for enhanced boiling heat transfer". In: *Nano Letters* 9.2 (2009), pp. 548–553.

[42] Kuang-Han Chu, Ryan Enright, and Evelyn N Wang. "Structured surfaces for enhanced pool boiling heat transfer". In: *Applied Physics Letters* 100.24 (2012), p. 241603.

[43] Amy Rachel Betz, James Jenkins, Daniel Attinger, et al. "Boiling heat transfer on superhydrophilic, superhydrophobic, and superbiphilic surfaces". In: *International Journal of Heat and Mass Transfer* 57.2 (2013), pp. 733–741.

[44] Navdeep Singh Dhillon, Jacopo Buongiorno, and Kripa K Varanasi. "Critical heat flux maxima during boiling crisis on textured surfaces". In: *Nature Communications* 6 (2015), p. 8247.

[45] JY Chang and SM You. "Enhanced boiling heat transfer from microporous surfaces: effects of a coating composition and method". In: *International Journal of Heat and Mass Transfer* 40.18 (1997), pp. 4449–4460.

[46] Chen Li and GP Peterson. "Parametric study of pool boiling on horizontal highly conductive microporous coated surfaces". In: *Journal of Heat Transfer* 129.11 (2007), pp. 1465–1475.

[47] In Cheol Bang and Soon Heung Chang. "Boiling heat transfer performance and phenomena of Al2O3–water nano-fluids from a plain surface in a pool". In: *International Journal of Heat and Mass Transfer* 48.12 (2005), pp. 2407–2419.

[48] Sung Joong Kim et al. “Surface wettability change during pool boiling of nanofluids and its effect on critical heat flux”. In: *International Journal of Heat and Mass Transfer* 50.19-20 (2007), pp. 4105–4116.

[49] Johnathan S Coursey and Jungho Kim. “Nanofluid boiling: The effect of surface wettability”. In: *International Journal of Heat and Fluid Flow* 29.6 (2008), pp. 1577–1585.

[50] Dwight Cooke and Satish G Kandlikar. “Effect of open microchannel geometry on pool boiling enhancement”. In: *International Journal of Heat and Mass Transfer* 55.4 (2012), pp. 1004–1013.

[51] Arvind Jaikumar and Satish G Kandlikar. “Ultra-high pool boiling performance and effect of channel width with selectively coated open microchannels”. In: *International Journal of Heat and Mass Transfer* 95 (2016), pp. 795–805.

[52] Shoji Mori and Yoshio Utaka. “Critical heat flux enhancement by surface modification in a saturated pool boiling: a review”. In: *International Journal of Heat and Mass Transfer* 108 (2017), pp. 2534–2557.

[53] Ho Seon Ahn et al. “Effect of liquid spreading due to nano/microstructures on the critical heat flux during pool boiling”. In: *Applied Physics Letters* 98.7 (2011), p. 071908.

[54] Bong June Zhang and Kwang J Kim. “Effect of liquid uptake on critical heat flux utilizing a three dimensional, interconnected alumina nano porous surfaces”. In: *Applied Physics Letters* 101.5 (2012), p. 054104.

[55] Md Mahamudur Rahman, Emre Olceroglu, and Matthew McCarthy. “Role of wickability on the critical heat flux of structured superhydrophilic surfaces”. In: *Langmuir* 30.37 (2014), pp. 11225–11234.

[56] Joel L Plawsky et al. “Review of the effects of surface topography, surface chemistry, and fluid physics on evaporation at the contact line”. In: *Chemical Engineering Communications* 196.5 (2008), pp. 658–696.

[57] Fujio Tachibana, Mamoru Akiyama, and Hiroshi KAWAMURA. "Non-hydrodynamic aspects of pool boiling burnout". In: *Journal of Nuclear Science and Technology* 4.3 (1967), pp. 121–130.

[58] Mehmet Arik and Avram Bar-Cohen. "Effusivity-based correlation of surface property effects in pool boiling CHF of dielectric liquids". In: *International Journal of Heat and Mass Transfer* 46.20 (2003), pp. 3755–3764.

[59] In Cheol Bang et al. "Measurement of key pool boiling parameters in nanofluids for nuclear applications". In: *Journal of Power and Energy Systems* 2.1 (2008), pp. 340–351.

[60] RL Judd and A Chopra. "Interaction of the nucleation processes occurring at adjacent nucleation sites". In: *Journal of Heat Transfer* 115.4 (1993), pp. 955–962.

[61] DBR Kenning. "Wall temperature patterns in nucleate boiling". In: *International Journal of Heat and Mass Transfer* 35.1 (1992), pp. 73–86.

[62] DBR Kenning and Youyou Yan. "Pool boiling heat transfer on a thin plate: features revealed by liquid crystal thermography". In: *International Journal of Heat and Mass Transfer* 39.15 (1996), pp. 3117–3137.

[63] Jocelyn Bonjour, Marc Clausse, and Monique Lallemand. "Experimental study of the coalescence phenomenon during nucleate pool boiling". In: *Experimental Thermal and Fluid Science* 20.3-4 (2000), pp. 180–187.

[64] Masahiro Shoji. "Nonlinear bubbling and micro-convection at a submerged orifice". In: *Tsinghua Science and Technology* 7.2 (2002), pp. 97–108.

[65] Masahiro Shoji and Yuto Takagi. "Bubbling features from a single artificial cavity". In: *International journal of heat and mass transfer* 44.14 (2001), pp. 2763–2776.

[66] Masahiro Shoji. "Studies of boiling chaos: a review". In: *International Journal of Heat and Mass Transfer* 47.6-7 (2004), pp. 1105–1128.

[67] Lei Zhang and Masahiro Shoji. "Nucleation site interaction in pool boiling on the artificial surface". In: *International Journal of Heat and Mass Transfer* 46.3 (2003), pp. 513–522.

[68] Robert Mallozzi, Ross Leonard Judd, and Narayanaswamy Balakrishnan. "Investigation of randomness, overlap and the interaction of bubbles forming at adjacent nucleation sites in pool boiling". In: *International Journal of Heat and Mass Transfer* 43.18 (2000), pp. 3317–3330.

[69] Patrick E McSharry et al. "Spatio-temporal analysis of nucleate pool boiling: identification of nucleation sites using non-orthogonal empirical functions". In: *International Journal of Heat and Mass Transfer* 45.2 (2002), pp. 237–253.

[70] VG Jukanti and V Srinivasan. "Modeling the chaotic dynamics of bubble growth under hydrodynamic interactions in pool boiling". In: *International Journal of Heat and Mass Transfer* 234 (2024), p. 126114.

[71] David Kenning et al. "Mechanistic models for pool nucleate boiling heat transfer: input and validation". In: *Thermal Sciences 2004. Proceedings of the ASME-ZSIS International Thermal Science Seminar II*. Begel House Inc. 2004.

[72] Vyacheslav Nikolaevich Skokov et al. "Low-frequency fluctuations with 1/f α power spectrum in transient modes of water boiling on a wire heater". In: *High Temperature* 48 (2010), pp. 706–712.

[73] Pol Lloveras et al. "Boiling crisis as a critical phenomenon". In: *Physical Review Letters* 108.21 (2012), p. 215701.

[74] Thomas Charignon et al. "Criticality in the slowed-down boiling crisis at zero gravity". In: *Physical Review E* 91.5 (2015), p. 053007.

[75] Lenan Zhang et al. "Boiling crisis due to bubble interactions". In: *International Journal of Heat and Mass Transfer* 182 (2022), p. 121904.

[76] Limiao Zhang et al. "A unifying criterion of the boiling crisis". In: *Nature Communications* 14.1 (2023), p. 2321.

[77] P Sadasivan, C Unal, and R Nelson. "Perspective: issues in CHF modeling—the need for new experiments". In: *Journal of Heat Transfer* 117.3 (1995), pp. 558–567.

[78] C-K Peng et al. "Long-range anticorrelations and non-Gaussian behavior of the heartbeat". In: *Physical Review Letters* 70.9 (1993), p. 1343.

[79] Armin Bunde et al. "Correlated and uncorrelated regions in heart-rate fluctuations during sleep". In: *Physical Review Letters* 85.17 (2000), p. 3736.

[80] Vineeth Nair and RI Sujith. "Multifractality in combustion noise: predicting an impending combustion instability". In: *Journal of Fluid Mechanics* 747 (2014), pp. 635–655.

[81] Ankit Saini and Vinod Srinivasan. "Multifractality and universality of thermal fluctuations in terrestrial and microgravity pool boiling". In: *Journal of Heat Transfer* 143.8 (2021), p. 081601.

[82] Rishi Raj, Jungho Kim, and John McQuillen. "Pool boiling heat transfer on the international space station: experimental results and model verification". In: *Journal OF Heat Transfer-Transactions of the ASME* 134.10 (2012).

[83] JR Lloyd and WR Moran. "Natural convection adjacent to horizontal surface of various planforms". In: *Journal of Heat Transfer* 96.4 (Nov. 1974), pp. 443–447.

[84] E Radziemska and WM Lewandowski. "Heat transfer by natural convection from an isothermal downward-facing round plate in unlimited space". In: *Applied Energy* 68.4 (2001), pp. 347–366.

[85] 3M. "Novec™ 7000 Engineered Fluid," Technical Datasheet, Sept. 2021.

[86] Texas Instruments, "REF200 Dual Current Source and Current Sink", SBVS020C datasheet, Sept. 2000 [Revised Feb. 2020].

[87] Weiming Lv et al. "Role of micro-nano fabrication process on the temperature coefficient of resistance of platinum thin films resistance temperature detector". In: *Materials Letters* 309 (2022), p. 131313.

[88] David W Scott. *Multivariate density estimation: theory, practice, and visualization*. John Wiley & Sons, 2015.

[89] Wikipedia contributors. *Kolmogorov–Smirnov test — Wikipedia, The Free Encyclopedia*. [Online; accessed 20-November-2024]. 2024. URL: https://en.wikipedia.org/w/index.php?title=Kolmogorov%E2%80%93Smirnov_test&oldid=1245231697.

[90] Amir Bashan et al. "Comparison of detrending methods for fluctuation analysis". In: *Physica A: Statistical Mechanics and its Applications* 387.21 (2008), pp. 5080–5090.

[91] Jan W Kantelhardt. "Fractal and multifractal time series". In: *arXiv preprint arXiv:0804.0747* (2008).

[92] SJD Van Stralen and WM Sluyter. "Investigations on the critical heat flux of pure liquids and mixtures under various conditions". In: *International Journal of Heat and Mass Transfer* 12.11 (1969), pp. 1353–1384.

[93] Kauo-Hwa Sun and John H Lienhard. "The peak pool boiling heat flux on horizontal cylinders". In: *International Journal of Heat and Mass Transfer* 13.9 (1970), pp. 1425–1439.

[94] PK Mohan Rao and DG Andrews. "Effect of heater diameter on the critical heat flux from horizontal cylinders in pool boiling". In: *The Canadian Journal of Chemical Engineering* 54.5 (1976), pp. 403–412.

[95] NASA Physical Sciences Informatics System. URL: https://psi.nasa.gov.

[96] Rishi Raj, Jungho Kim, and John McQuillen. "Subcooled pool boiling in variable gravity environments". In: *Journal OF Heat Transfer-Transactions of the ASME* 131.9 (2009).

[97] Rishi Raj and Jungho Kim. "Heater size and gravity based pool boiling regime map: transition criteria between buoyancy and surface tension dominated boiling". In: *Journal OF Heat Transfer-Transactions of the ASME* 132.9 (2010).

[98] J. Kim and R. Raj. "Gravity and Heater Size Effects on Pool Boiling Heat Transfer". In: (2014), NASA/CR–2014–216672.

[99] ML McGlashan. "The international temperature scale of 1990 (ITS-90)". In: *The Journal of Chemical Thermodynamics* 22.7 (1990), pp. 653–663.

[100] RL Magin et al. "Transition temperatures of the hydrates of Na2SO4, Na2HPO4, and KF as fixed points in biomedical thermometry". In: *Journal of Research of the National Bureau of Standards* 86.2 (1981), p. 181.

[101] Umesh Madanan. "High-Rayleigh-number thermal convection of compressed gases in inclined rectangular enclosures of varied aspect ratios". In: *Ph. D. Thesis* (2019).

Appendix A

Calibrating the Standard Platinum Resistance Thermometer

A Standard Platinum Resistance Thermometer (SPRT) was used as the primary standard to calibrate the thermocouples used in the experiments. The SPRT itself was calibrated using two fixed temperatures as reference standards - the triple point of water (T_{tpw} = 273.16 K), and the transition temperature of anhydrous Sodium Sulfate to its decahydrate form ($Na_2SO_4 \cdot 10H_2O$, T_{salt} = 305.5148 K) in a saturated water solution.

The International Temperature Scale of 1990 (ITS-90) [99] defines a list of fixed temperatures, which are known to be thermodynamically reproducible, between 13.8033 K (triple point temperature of hydrogen) and 1234.49 K (melting point of silver) as reference standards for calibrating an SPRT. It also recommends what fixed temperatures to use as reference standards to calibrate an SPRT for different temperature sub-ranges

within the aforementioned range. For instance, for the sub-range of 273.15 K – 429.7485 K (0 °C – 156.5985 °C), the recommended reference standards are the triple point of water (273.16 K) and the melting point of Indium (429.7485 K), respectively. Since the SPRT was used to calibrate type-T thermocouples in the range of 5 °C (278.15 K) – 100 °C (373.15 K), as explained in Appendix B, the SPRT was calibrated for this sub-range. While the triple point of water was reproduced in the lab (Appendix A.1) using a Water Triple Point Cell (Water-TPC), the melting point of Indium, however, could not be reproduced in the lab due to unavailability of a Indium Fixed-Point Cell which is needed to achieve the melting point accurately. Instead, the transition temperature of anhydrous Sodium Sulfate to its decahydrate form in a saturated water solution was used as a substitute reference standard.

As per ITS-90 standards, to read a temperature using an SPRT, the resistance of the SPRT is first measured, and a resistance ratio, $W(T)$, is calculated as

$$W(T) = \frac{R(T)}{R_0} \tag{A.1}$$

where R_0 is the resistance of the SPRT at the triple point of water, one of the reference temperatures at which the SPRT has to be calibrated. Next, the reference value of the resistance ratio, $W_r(T)$, is calculated using deviation functions, which are defined by ITS-90 for different ranges, and sub-ranges. For the range of 273.15 K – 1234.49 K, the deviation function is defined as

$$\begin{aligned} W(T) - W_r(T) = a\,(W(T) - 1) + b\,(W(T) - 1)^2 + c\,(W(T) - 1)^3 + \\ d\,(W(T) - W(933.473\text{ K}))^2 \end{aligned} \tag{A.2}$$

where a, b, c, and d are constants whose values are determined by calibrating the SPRT at the fixed temperatures. For smaller sub-ranges of interest, and particularly 273.15 K – 429.7485 K (0 °C – 156.5985 °C), $b = c = d = 0$. In this sub-range, the deviation

function simplifies to

$$W(T) - W_r(T) = a\,(W(T) - 1) \qquad 273.15\ \text{K} \leq T \leq 429.7485\ \text{K} \tag{A.3}$$

The reference value of the resistance ratio, $W_r(T)$, at any given temperature T is the ideal value that should be measured from an SPRT as per ITS-90. ITS-90 defines reference functions for all ranges which relates the reference value $W_r(T)$ to the temperature T. For the range of interest, ITS-90 defines the reference function as

$$W_r(T) = C_0 + \sum_{i=1}^{9} C_i \left(\frac{T - 754.15\ \text{K}}{481\ \text{K}} \right)^i \qquad 273.15\ \text{K} \leq T \leq 1234.93\ \text{K} \tag{A.4}$$

ITS-90 also defines an inverse function for the equation above, which is accurate to within 0.13 mK. It is given by

$$T = 273.15\ \text{K} + D_0 + \sum_{i=1}^{9} D_i \left(\frac{W_r(T) - 2.64}{1.64} \right)^i \tag{A.5}$$

The values of constants C_0, C_i, D_0, and D_i in Equations (A.4) and (A.5) are listed in Table A.1 (taken from [99]).

i	C_i	D_i
0	2.78157254	439.932854
1	1.64650916	472.418020
2	−0.13714390	37.684494
3	−0.00649767	7.472018
4	−0.00234444	2.920828
5	0.00511868	0.005184
6	0.00187982	−0.963864
7	−0.00204472	−0.188732
8	−0.00046122	0.191203
9	0.00045724	0.049025

Table A.1: Values of constants in Equations (A.4) and (A.5).

Since no two SPRTs can give the exact same measurement at any temperature, or have the same resistance-temperature dependence, the deviation function given by Equation (A.3) is used as a correction to calculate the reference value ($W_r(T)$) from the resistance ratio ($W(T)$). Once $W_r(T)$ is calculated, the temperature can be backed out using Equation (A.5).

Note that to calibrate the SPRT in the range of 273.15 K – 429.7485 K, only one other fixed temperature besides the triple point of water needs to be reproduced to determine the value of the constant a in Equation (A.3). As stated earlier, the transition temperature of anhydrous Sodium Sulfate to its decahydrate form in a saturated water solution was used for this purpose. This temperature is known to be thermodynamically reproducible in laboratories and may be used as a reference standard for calibrating thermometers [100] despite not being listed as a fixed temperature by ITS-90. Reproducing this temperature in a lab is convenient, as explained in Appendix A.2.

During calibration of the SPRT at the second reference temperature, $T_{salt} = 305.5148$ K, the resistance ratio $W(T_{salt})$ was measured, and the reference function definition in Equation (A.4) was used to calculate $W_r(T_{salt})$. Then, the value of constant a was calculated as

$$a = \frac{W(T_{salt}) - W_r(T_{salt})}{W(T_{salt}) - 1} \tag{A.6}$$

The above process of calculating a and the associated uncertainty is outlined in greater detail in Appendix A.3.

A.1 Triple Point of Water

The triple point of water is one of the fixed temperatures listed by ITS-90. It was reproduced in the lab using a Water-TPC, a glass instrument with pure water in a

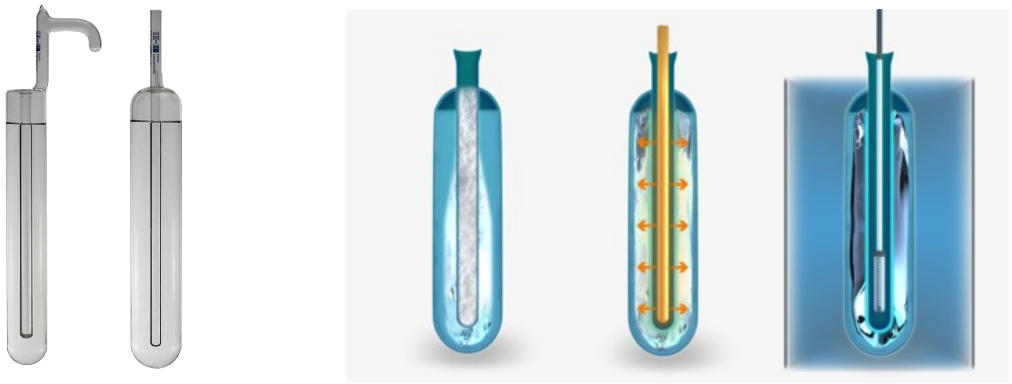

(a) (b)

Figure A.1: (a) Water-TPC, and (b) ice forming inside the TPC (left), melting the ice so that it may float freely inside the TPC (middle), and the TPC with the SPRT inside an ice bath.

sealed and hollow cylindrical shell as shown in Figure A.1a. The well in the center holds the SPRT during calibration.

To achieve the triple point of water, the TPC was first pre-chilled by placing it in an ice bath to bring the temperature of the water in the cell as close to the triple point as possible. Then, 4–5 drops of isopropyl alcohol (2-propanol, shortened to IPA) were put into the well followed by dry ice (solid carbon dioxide). The purpose of the IPA was to improve heat transfer between the wall of the well and the dry ice, so that the water inside the TPC began to solidify faster to form ice. Dry ice was poured up to the level of the water in the TPC so that ice formed all along the walls of the well. During this, the dry ice continued to vaporize and rise through the well, and it was constantly replaced to maintain the level of dry ice. Care was also taken to ensure that *ice bridges* did not form inside the TPC. Ice bridge is a structure that results when the water inside the TPC anywhere along the length of the well solidifies such that the two glass walls in the annular region are connected by a *bridge of ice*. Ice bridges are known to result in causing the TPC to break. Hence, ice bridges, when observed, may be melted by

locally warming the TPC where the ice bridge are observed using body heat generated from hands.

A constant level of dry ice was maintained in the well until a roughly 1-cm thick layer of ice formed around the well all along its length. The TPC was carefully dipped in a beaker of water to remove the parallax when determining the thickness of the layer of ice. Once the desired thickness of ice had been achieved, any remaining dry ice inside the well was removed by carefully holding the TPC upside-down. A metal rod at room temperature, with an appropriate diameter to slip easily into the well, was then inserted into the well to melt the ice inside the TPC just enough so that the ice structure did not stick to the wall and floated freely about the well. Before this, the metal rod was cleaned thoroughly with acetone, IPA, and de-ionized (DI) water. Once the ice inside the TPC began to float freely about the well, the SPRT was placed inside the well, and the entire arrangement was placed inside a insulated ice bath to maintain the triple point of water for as long as possible.

Once the TPC, with the SPRT in the well, was placed inside the ice bath, data was not taken for several hours to give time for the TPC and the SPRT to stabilize. Then, the resistance of the SPRT was measured by a digital multimeter (DMM) using the 4-wire resistance measurement technique. Additionally, the DMM was configured to make offset compensation to account for any thermal EMFs (electromotive force) due to the use of dissimilar metals in the connections made between the SPRT and the DMM. When offset compensating, the DMM takes two measurements of the voltage drop across the resistance-under-test with two different levels of source current, the second one being the lowest current source the DMM can supply. By taking two measurements, the DMM offsets the effect of thermal emfs as follows

$$\begin{aligned} V_{m1} &= V_{temf} + I_{s1} \cdot R \\ V_{m2} &= V_{temf} + I_{s2} \cdot R \\ V_{m1} - V_{m2} &= I_{s1} \cdot R - I_{s2} \cdot R \\ \Rightarrow R &= \frac{V_{m1} - V_{m2}}{I_{s1} - I_{s2}} \end{aligned} \tag{A.7}$$

where V_{m1} and V_{m2} are the two voltage measurements, I_{s1} and I_{s2} are the two different levels of source currents supplied by the DMM, V_{temf} is the thermal EMF which remains unchanged regardless of the source current, and R is the resistance-under-test.

300 resistance measurements were taken at 5-second time intervals over a period of roughly 30 minutes. The mean value of the resistances was taken as the best estimate of the resistance of the SPRT at the triple point of water, R_0, and the standard deviation of the measurements was used to calculate the measurement uncertainty with 95% confidence as

$$U_R = \frac{t_{95\%,N-1} \cdot s}{\sqrt{N}} \tag{A.8}$$

where $N = 300$ is the sample size, $t_{95\%,N-1}$ is the two-sided t-value for a 95% confidence interval with $N - 1 = 299$ degrees of freedom, and s is the sample standard deviation. For $N - 1 = 299$, $t_{95\%,N-1} = 1.968$. In this way, the value of R_0 obtained, and the associated uncertainty with 95% confidence were

$$R_0 \pm U_{R_0} = 25.5637 \pm 1.045 \times 10^{-5}\ \Omega$$

A.2 Transition Temperature of Decahydrate of Sodium Sulfate

As mentioned earlier, the temperature at which anhydrous sodium sulfate (Na_2SO_4) transitions to its decahydrate form ($Na_2SO_4 \cdot 10H_2O$) in a saturated solution in water was used as the second reference temperature to calibrate the SPRT. This transition is known to occur at $T_{salt} = 305.5148$ K, is thermodynamically reproducible, and has been used for calibrating thermometers [100].

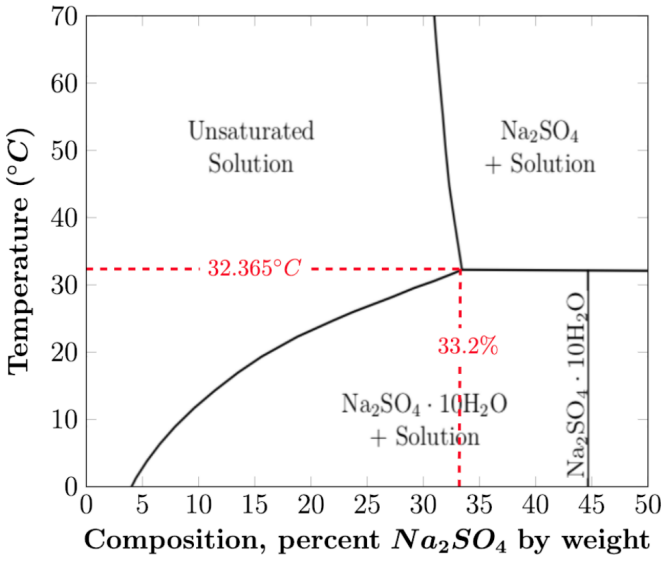

Figure A.2: Phase Diagram of the Na_2SO_4:H_2O system.

Figure A.2 shows the phase diagram of the Na_2SO_4:H_2O system, taken from [101]. Note that for a mixture of over 33.2% of Na_2SO_4 by weight in water, at 40 °C, the solution is completely saturated with some Na_2SO_4 that remains undissolved in the mixture. At this temperature, all Na_2SO_4 is in the anhydrous form. However, when the mixture cools to $T_{salt} = 32.3648$ °C, the anhydrous Na_2SO_4 transitions into its crystalline decahydrate form, $Na_2SO_4 \cdot 10H_20$. The mixture stays at that temperature until either the anhydrous salt or water is exhausted. This was used to calibrate the SPRT at 32.3648 °C.

A mixture of anhydrous Na_2SO_4 in distilled water, 40 % by weight, was prepared in a beaker and heated to just over 40 °C on a hot plate. The amount of solution prepared was enough to allow for more than 20 cm of the SPRT to be immersed in the solution. This is the recommended minimum immersion depth for an SPRT. The hot plate was then turned off and the solution was allowed to cool down to the transition temperature. During this time, the resistance of the SPRT was monitored by a DMM using the 4-wire resistance measurement technique with offset compensation for thermal EMFs (see Appendix A.1 for details). Eventually, the solution cooled down to the transition temperature, and stayed at that temperature for an hour. During that time period, 300 resistance measurements of the SPRT were recorded by the DMM, spaced 8-seconds apart. Figure A.3 shows the measurements, the mean, and the 95% confidence interval.

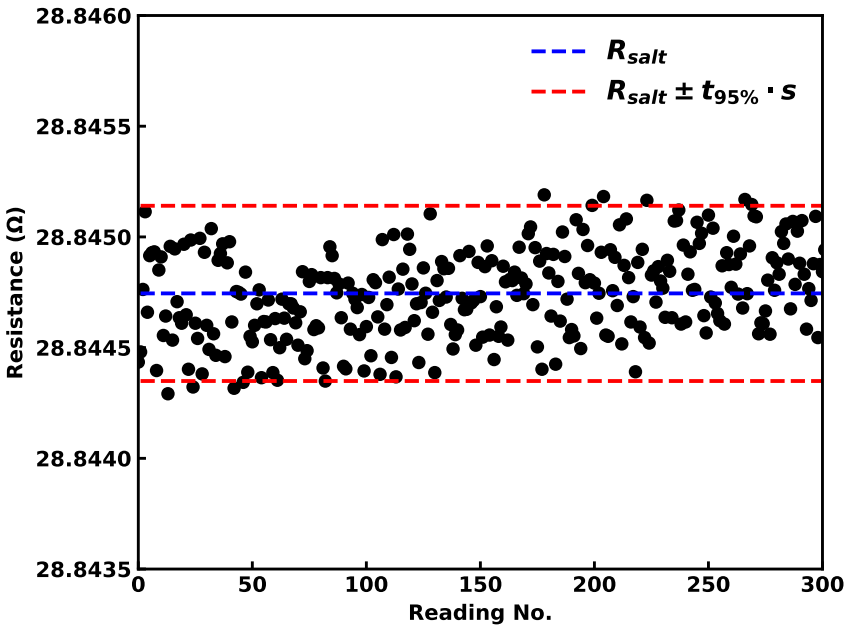

Figure A.3: Resistance measurements of the SPRT at T_{salt} = 305.5148 K. The mean (dashed blue line) is taken as the best estimate of R_{salt}. Also shown is the 95% confidence interval.

The 95% confidence interval shown in Figure A.3 is an interval defined for the sample

population of $N = 300$ measurements. Since the mean of the sample population is taken as the best estimate of R_{salt}, the associated uncertainty in the measurement for R_{salt} is much smaller than the confidence interval and is given by Equation (A.8). This is because the means of sample populations are distributed more closely about the population mean than individual samples. Therefore, the value of R_{salt} obtained, and the associated uncertainty with 95% confidence were

$$R_{salt} \pm U_{R_{salt}} = 28.845 \pm 3.957 \times 10^{-4}\ \Omega$$

A.3 Error Propagation and Uncertainty Analysis

Having taken measurements at the two reference temperatures, the resistance ratio at T_{salt} was calculated as

$$W(T_{salt}) = \frac{R_{salt}}{R_0} = 1.1283$$

The associated uncertainty in the above estimation of $W(T_{salt})$ was calculated by propagating uncertainties associated with measuring R_0 and R_{salt} as

$$U_{W(T_{salt})} = \sqrt{\left(\frac{1}{R_0}\right)^2 (U_{R_{salt}})^2 + \left(\frac{R_{salt}}{(R_0)^2}\right)^2 (U_{R_0})^2}$$

$$\Rightarrow U_{W(T_{salt})} = 9.940 \times 10^{-7}$$

The reference value of the resistance ratio at T_{salt}, $W(T_{salt})$, was then calculated using Equation (A.4), with the values of constants taken from Table A.1, as

$$W_r(T_{salt}) = C_0 + \sum_{i=1}^{9} C_i \left(\frac{T_{salt} - 754.15\ \text{K}}{481\ \text{K}}\right)^i$$

$$\Rightarrow W_r(T_{salt}) = 1.1284$$

Since the above equation is defined by ITS-90, there is no corresponding uncertainty associated with it. Finally, the values of a was calculated using Equation (A.6) as

$$a = \frac{W(T_{salt}) - W_r(T_{salt})}{W(T_{salt}) - 1}$$
$$\Rightarrow a = -5.148 \times 10^{-4}$$

And the corresponding uncertainty in estimation of a, U_a, was calculated by propagating $U_{W(T_{salt})}$ in the above equation as

$$U_a = \frac{W_r(T_{salt}) - 1}{(W(T_{salt}) - 1)^2} U_{W(T_{salt})}$$
$$\Rightarrow U_a = 7.749 \times 10^{-6}$$

Appendix B

Calibrating type-T Thermocouples

The purpose of the thermocouple calibration was to obtain a single calibration curve that could be applied to any thermocouple taken from a given spool of thermocouple wire. For this, 10 lenghts of wire (each $\sim$ 3-ft long) were taken from a single spool of AWG 30 type-T thermocouple wire and the sensing junctions were formed by spot welding one end of the wires[1]. The sensing junctions of the 10 thermcouples, along with an SPRT, were then immersed in an isothermal bath filled with silicone oil[2] while the reference junctions of the thermocouples were placed in an ice bath. The isothermal bath was set to temperatures between 5 °C and 140 °C, at intervals of 5 °C, and measurements taken from the SPRT and the 10 thermocouples to obtain a total of 28 calibration data points.

At each set temperature, the isothermal bath was given time to reach steady state. Measurements from the SPRT were taken continuosly at regular intervals as the isothermal

[1]This was done using the equipment available in the author's lab.
[2]The melting point of the oil was reported to be greater than 140 °C by the manufacturer.

bath heated up, and steady state was assumed to have been reached when the standard deviation of the last 100 readings fell below a threshold value. Once steady state had been reached, sequential measurements of the SPRT resistance and thermocouple EMFs from the 10 thermocouples were taken. This was repeated 250 times, for a total of 2750 measurements. Therefore, the sample size of measurements from the SPRT and the thermocouples was 250, and the sample means were taken to represent the true values of the measurements.

The sample means of resistance measurements from the SPRT were used to calculate the reference temperatures using the relevant equations from Appendix A, summarized here for convenience:

$$\begin{aligned} W(T) &= \frac{R(T)}{R_0} \\ W_r(T) &= W(T) - a\big(W(T) - 1\big) \\ T &= 273.15\ \text{K} + D_0 + \sum_{i=1}^{9} D_i \left(\frac{W_r(T) - 2.64}{1.64} \right)^i \end{aligned} \tag{B.1}$$

where $R(T)$ was the sample mean of the resistance measurements, $R_0 = 25.5637\ \Omega$ and $a = -5.148 \times 10^{-4}$ from the SPRT calibration, and D_i were values of constants from Table A.1. The uncertainty in the measurements of the SPRT resistances $R(T)$ was calculated as

$$U_{R(T)} = t_{95\%, N_{\text{meas}}-1} \frac{s}{\sqrt{N_{\text{meas}}}}$$

where s was the sample standard deviation of the measurements, $N_{\text{meas}} = 250$, and $t_{95\%, N_{\text{meas}}-1} = 1.970$ was the two-sided value for student's t distribution for a 95% confidence interval with $N_{\text{meas}} - 1 = 249$ degrees of freedom. This measurement uncertainty, along with the uncertainty in the value of the constant a estimated from the SPRT

calibration ($U_a = 7.749 \times 10^{-6}$), was propagated through Equation (B.1) to get the uncertainty in the reference temperatures. These uncertainties were of the order 1 mK.

The 10 sample means of thermocouple EMF measurements at any reference temperature were assumed to be normally distributed about the population mean because the population was the set of all thermocouples that could be made from the spool being calibrated, and the 10 thermocouples represented the 10 samples taken from the population. Therefore, the mean value and sample standard deviations of the sample means was used as the best estimates of the population mean and standard deviation. Appendix B compares the standard deviations of measurements from the 10 thermocouples and the standard deviation of the 10 sample means (s_{sm}) at every reference temperature. As expected, the standard deviations of the 10 sample means were usually larger than the 10 standard deviations of measurements from the thermocouples at all reference temperatures.

Appendix B shows the mean values of the 10 samples means at every reference temperature. The uncertainty in mean thermocouple EMFs (U_{EMF}) was calculated using the standard deviation of the sample means (s_{sm}) as

$$U_{\text{EMF}} = t_{95\%,N_{\text{tcs}}-1} \frac{s_{\text{sm}}}{\sqrt{N_{\text{tcs}}}}$$

where $N_{\text{tcs}} = 10$ was the number of thermocouples used in the calibration and $t_{95\%,N-1} = 2.262$ was the two-sided value for student's t distribution for a 95% confidence interval with $N_{\text{tcs}} - 1 = 9$ degrees of freedom. The uncertainty in the mean thermcouple EMFs in the calibration was of the order of 0.01%.

To obtain the calibration curve, a second-order polynomial ($a_1T^2 + a_2T + a_3$) was fit to the calibration data points using the method of least squares. A second-order polynomial fit was used because it was visibly a better choice than a first-order polynomial fit

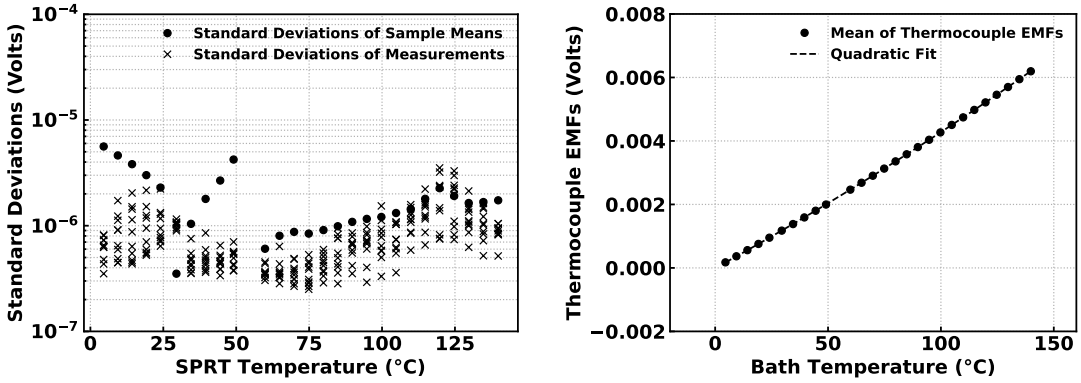

Figure B.1: (Left) Comparing standard deviation of sample means and standard deviation of measurements, and (Right) Mean values of thermocouple EMFs versus reference temperatures.

while higher-order polynomial fits were avoided because inverting the fit to get the temperature as a function of the thermocouple EMF becomes increasingly complicated. Table B.1 lists the values of the coefficients and the associated uncertainties estimated from the fitting process. The standard error in the estimates of the coefficients was used to calculate the 95% confidence intervals as

$$U_{a_i} = t_{95\%,N-1}\frac{se_{a_i}}{\sqrt{N}}$$

where se_{a_i} was the standard error in the coefficient estimate, $N = 28$ was the number of calibration data points, and $t_{95\%,N-1} = 2.052$ was the two-sided value of the student's

Coefficient	Units	Predicted Value	Standard Error of Estimate (se_{a_i})	95% Confidence Interval (U_{a_i})
a_1	Volt/°C^2	3.8579×10^{-8}	2.8790×10^{-10}	1.1368×10^{-10}
a_2	Volt/°C	3.8980×10^{-5}	4.2581×10^{-8}	1.6814×10^{-8}
a_3	Volt	-6.2977×10^{-6}	1.3141×10^{-6}	5.1892×10^{-7}

Table B.1: Results from fitting a second-order polynomial ($a_1T^2 + a_2T + a_3$) using method of least squares.

t distribution for a 95% confidence interval with $N-1=27$ degrees of freedom.

To calculate the temperature if the thermocouple EMF is known, the calibration curve was inverted as

$$T\big(\mathrm{EMF}\big)=\frac{-a_2+\sqrt{a_2^2-4a_1\big(a_3-\mathrm{EMF}\big)}}{2a_1} \tag{B.2}$$

The goodness of the fit may be evaluated by estimating the uncertainty of the fit with 95% confidence interval (U_{fit}) as

$$U_{\mathrm{fit}}=t_{95\%,N-1}\frac{se_{\mathrm{y}}}{\sqrt{N}}\ \text{ where}$$

$$se_{\mathrm{y}}=\sqrt{\frac{\sum_{i=1}^{N}\big(T-T\big(\mathrm{EMF}\big)\big)^2}{N-3}}$$

where $N=28$ was the number of calibration data points and $t_{95\%,N-1}=2.052$ was the two-sided value for the student's t distribution for a 95% confidence interval with $N-1=27$ degrees of freedom. For the calibration, $U_{\mathrm{fit}}=3.789$ mK.

To calculate the uncertainty in temperature measurement using the calibration curve with 95% confidence interval, the following equation, derived by error propagation, was used:

$$U_{T(\mathrm{EMF})}=\left\{\left(\frac{U_{\mathrm{EMF}}^2+U_{a3}^2}{a_2^2-4a_1\big(a_3-\mathrm{EMF}\big)}\right)+\left(-1+\frac{a_2}{\sqrt{a_2^2-4a_1\big(a_3-\mathrm{EMF}\big)}}\right)^2\left(\frac{U_{a_2}}{2a_1}\right)^2+\left(\frac{-a_3+\mathrm{EMF}}{a_1\sqrt{a_2^2-4a_1\big(a_3-\mathrm{EMF}\big)}}-\frac{-a_2+\sqrt{a_2^2-4a_1\big(a_3-\mathrm{EMF}\big)}}{2a_1^2}\right)^2U_{a_1}^2\right\}^{1/2} \tag{B.3}$$

where $U_{T(\mathrm{EMF})}$ was the uncertainty in the measurement of thermocouple EMF, and U_{a_1}, U_{a_2}, and U_{a_3} are the uncertainties in the estimates of the coefficients a_1, a_2, and a_3 with

95% confidence interval, respectively, listed in Table B.1.

Appendix C

Micro-Fabrication of RTDs on Sapphire Subtrates

This section provides a brief outline of steps taken in the micro-fabrication process to prepare the surfaces used in the surface pool boiling experiments. The substrates used were double side polished, 4-inch diameter, 600 μm-thick Sapphire wafers.

Step 1: Cleaning the Wafers - The sapphire wafers were cleaned in a two-step process. In the first step, the wafers were rinsed by spraying the following solvents on them in order: Acetone, Iso-Propyl Alcohol (IPA), and DI Water. Care was taken to move quickly from Acetone to IPA, and then to DI Water so that the dilute solvents (Acetone and IPA) did not have time to evaporate off the wafer. After the final rinse using DI water, the wafers were blow-dried using an N_2 gun.

In the second step, the wafers were cleaned in a UV (Ultraviolet) Ozone cleaner for 30 minutes to remove any remaining organic contaminants. Inside the chamber of the UV Ozone cleaner, the wafers had to be placed flat on a surface, rendering the side placed flat down unclean. Therefore, care was taken while handling to distinguish the clean,

top side of the wafer from the bottom side.

Step 2: Deposition of the Platinum thin-film heater - A physical vapor deposition process called sputtering was used to deposit a 75-nm thick layer of platinum as a thin-film heater on the clean side of the wafer. To ensure good adhesion of the Platinum thin-film to the substrate, a 5-nm thick layer of Titanium was deposited first as an adhesive layer, followed by the 75-nm thick layer of Platinum.

Step 3: Re-Cleaning the Wafers - After depositing the thin-film heater, the other side of the wafer needed to be cleaned before proceeding to deposit RTDs on it. The same process as in Step 1 was followed with a greater focus to clean the side of wafer without the thin-film heater on it. In the rest of this section, the thin-film heater side and the RTD side of the wafer will be referred to as backside and topside, respectively.

Step 4: Photolithography for RTDs - Before depositing Platinum to serve as RTDs, a mask was deposited on the topside of the wafer using Optical Photolithography. The photoresist used was Futurrex NR71-1500P, a negative photoresist. The following recipe was followed:

Step 4.1: Spin coat the wafer with NR71-1500P over two steps: 1) 300 rpm for 3 s, and 2) 3000 rpm for 45 s.

Step 4.2: Soft bake the wafer on a hotplate at 150 °C for 3 minutes.

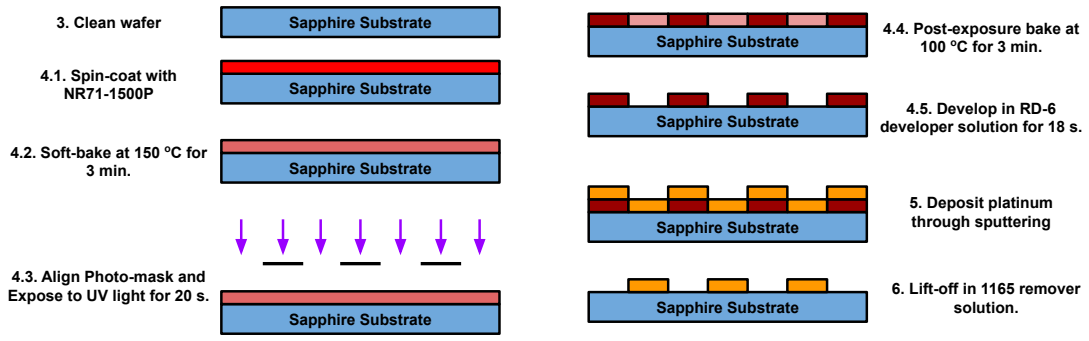

Figure C.1: Schematic representing steps 3-6 in the micro-fabrication of RTDs.

Step 4.3: Using a photomask, expose the wafer to UV light (12 mJ/m^2) in a Contact Aligner for 20 s.

Step 4.4: Post-exposure, bake the wafer on a hotplate at 100 °C for 3 minutes.

Step 4.5: Develop the wafer in RD-6 developer solution for 18 s.

Step 4.6: Rinse the wafer in DI water for 2 minutes.

Note: It is very important to clean the hotplates thoroughly so that the backside of the wafer makes good thermal contact with the hotplate surface. For the final result of the photolithography process to be good, it is critical for the wafers to be uniformly heated. Even trace amounts of non-visible residue on the hotplate surface will affect the uniformity of heating and affect the final result.

Step 5: Deposition of Platinum RTDs - Similar to Step 2, sputtering was used to deposit a 75-nm thick layer of platinum (with a 5-nm layer of Ti to serve as an adhesion layer) to the topside of the wafer.

Step 6: Liftoff I - The remaining photoresist was stripped off (in a process called "Liftoff") by immersing the wafer in a crystallizing dish filled with Microposit Remover 1165 solution, and placing the dish in a ultrasonic sonicator maintained at 60 °C for $\sim$ 4 hours.

Step 7: Thermal Annealing - After the platinum thin-film heater and platinum RTDs had been deposited, the wafers were thermally annealed at 450 °C for 4 hours to release residual stresses in the thin films.

Step 8: Photolithography for Final Layer - The photolithography process was repeated to deposit a photoresist mask on 50-µm-by-50-µm areas on the topside of the wafer which were to serve as the bond pands. NR71-1500P was used as the photoresist.

Step 9: Deposition of Final Layer - The final 2-µm layer of SiO_2/A-Si/Ni was deposited using the appropriate vapor deposition process. Sputtering was used to deposit

Ni while High Density Plasma Enhanced Chemical Vapor Deposition (HD-PCVD) process was used to deposit SiO_2 or A-Si. ***Note:*** To prepare Parylene-C surfaces, the final layer of Parylene-C was deposited after the chips had been assembled on the PCBs.

Step 10: Liftoff II - After deposition of the final layer, the photoresist was stripped off again by immersing the wafer in a crystallizing dish filled with Microposit Remover 1165 solution, and placing the dish in a ultrasonic sonicator maintained at 60 °C for $\sim$ 4 hours. After this step, only the bond pads of the RTDs were left uncovered by the final layer.

Step 11: Dicing - Before dicing the 20-mm-by-20-mm square chips out of the wafers, the entire topside was covered with a photoresist mask. This was to protect the surface from getting contaminated by wafer dust during the dicing process. After the dicing process, the photoresist mask was stripped off using Microposit Remover 1165 solution.

The chips were now ready to be assembled onto PCBs.

Appendix D

Acronyms

Care has been taken in this thesis to minimize the use of jargon and acronyms, but this cannot always be achieved. This appendix contains a table of acronyms and their meaning.

D.1 Acronyms

Table D.1: Acronyms

Acronym	Meaning
ACF	Auto-Correlation Function
CHF	Critical Heat Flux
DFA	Detrended Fluctuation Analysis
DI Water	De-Ionized Water
DMM	Digital Multimeter
EMF	Electro-Motive Force

Continued on next page

Table D.1 – Continued from previous page

Acronym	Meaning
FFT	Fast Fourier Transform
GHE	Generalized Hurst Exponent
HTC	Heat Transfer Coefficient
IPA	Isopropyl Alcohol or 2-propanol
ITS-90	International Temperature Scale of 1990
MABE	Micro-heater Array Boiling Experiment
ONB	Onset of Nucleate Boiling
PSD	Power Spectral Density
RTD	Resistance Temperature Detector
SPRT	Standard Platinum Resistance Thermometer
TPC	Triple Point Cell